Evolution of dislocation structures following a change in loading conditions studied by in situ high resolution reciprocal space mapping

Wejdemann, Christian

Publication date:
2011

Document Version
Publisher's PDF, also known as Version of record

Evolution of dislocation structures following a change in loading conditions studied by in situ high resolution reciprocal space mapping

Risø-PhD-Report

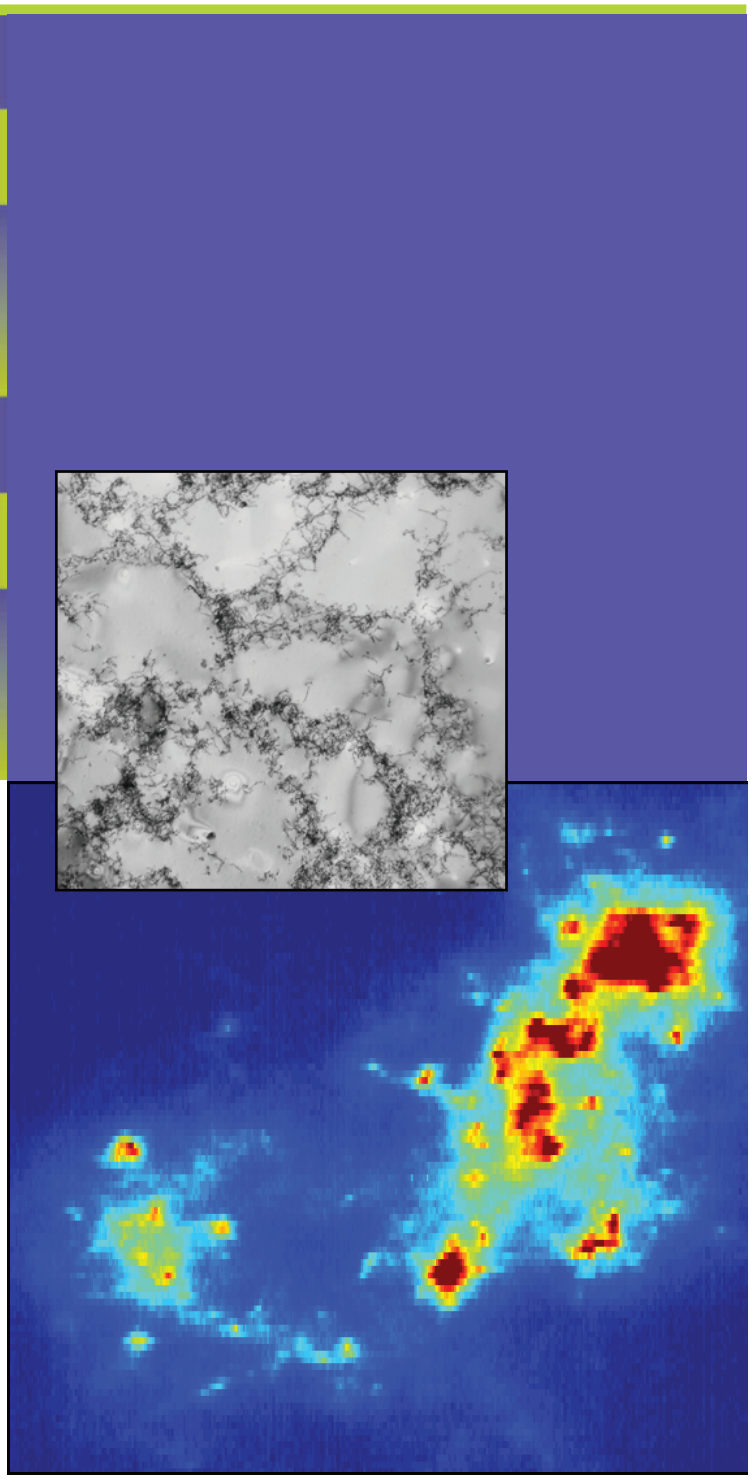

Christian Wejdemann
Risø-PhD-74(EN)
March 2011

Risø DTU
National Laboratory for Sustainable Energy

Evolution of dislocation structures following a change in loading conditions studied by in situ high resolution reciprocal space mapping

PhD thesis written by Christian Wejdemann

Supervisors: Wolfgang Pantleon (main supervisor) and Henning F. Poulsen

Center for Fundamental Research: Metal Structures in Four Dimensions
Materials Research Division
Risø National Laboratory for Sustainable Energy
Technical University of Denmark
P.O.Box 49, DK-4000 Roskilde, Denmark

Risø-PhD-74(EN)
March 2011

ISBN 978-87-550-3888-2

Abstract

This thesis presents the results of a study aimed at investigating the evolution of dislocation structures in individual grains in copper polycrystals following a strain path change or a change in temperature.

Copper samples were pre-deformed in tension to a strain of 5 % at room temperature or to a strain of 7 % at a temperature of -196 °C, and the samples were characterized by electron microscopy and mechanical tests. Transmission electron microscopy showed that the pre-deformation produced a characteristic dislocation cell structure consisting of regions with relatively high dislocation density, called dislocation walls, enclosing regions with very low dislocation density, called subgrains. The mechanical tests showed that a tension-tension strain path change leads to an increase in the yield stress if the change in strain path is sufficiently severe, and to a transient phase with a reduced work hardening rate.

The main part of the study consisted of a number of X-ray diffraction experiments in which the pre-deformed samples were further deformed in tension in situ at the APS synchrotron (the Advanced Photon Source at Argonne National Laboratory), for some samples along an axis different from the pre-deformation axis. In the X-ray diffraction experiments a technique was employed with which it is possible to obtain high-resolution reciprocal space maps from individual bulk grains. The high-resolution reciprocal space maps contain features related to the dislocation structure in the grains: A spread-out 'cloud' of low intensity caused by diffraction from the dislocation walls and a number of sharp peaks of high intensity caused by diffraction from the individual subgrains. By acquiring reciprocal space maps at a number of different strain levels the evolution of the dislocation structures can be studied, and by analyzing the sharp peaks information about the strain in the individual subgrains and about the intra-granular stresses can be obtained. For the analysis of the reciprocal space maps a mathematical method was developed to partition the intensity distribution into two components corresponding to the contributions from the subgrains and the walls.

The analysis showed that the morphology of the dislocation structures is almost unchanged during the micro-plastic range of the in situ deformation, and during the macro-plastic range the evolution occurs in a gradual manner without any sudden major changes and with no indications that intermittent dynamics plays a major role in the evolution of the dislocation structures.

An analysis of the position of the radial profiles from the individual subgrains revealed a substantial variation in the elastic back-strain in the subgrains and showed that the distribution of the elastic back-strain in the subgrains can be well approximated by a Gauss distribution. Furthermore, it was found that on average the elastic back-strain is larger in the larger subgrains than in the smaller subgrains.

The analysis also showed that, following a strain path change, the intra-granular stresses are substantially redistributed during the micro-plastic range. In a few individual subgrains it was possible to follow the evolution of the elastic back-strain from the tensile to the compressive case. Following an increase in temperature from -196 °C to room temperature, both the average intra-granular stress and the variation in the intra-granular stresses go through an initial phase of decrease or stagnation.

An analysis of the width of the radial profiles from the individual subgrains showed that the dislocation density in the subgrains remains constant at a low level during the deformation.

Finally, an analysis of the radial profiles from the individual grains indicated that a change in loading conditions leads to a less ordered dislocation structure in the walls.

Dansk resumé

Denne afhandling præsenterer resultaterne af et studium hvis mål var at undersøge udviklingen af dislokationsstrukturer i individuelle korn i polykrystaller af kobber efter en ændring i tøjningsvejen eller temperaturen.

Kobberprøver blev præ-deformeret i træk til en tøjning på 5 % ved stuetemperatur eller en tøjning på 7 % ved en temperatur på -196 °C, og prøverne blev undersøgt med elektronmikroskopi og mekaniske test. Transmissions-elektronmikroskopi viste at præ-deformationen producerede en karakteristisk dislokationsstruktur bestående af områder med en relativt høj dislokationstæthed, kaldet dislokationsvægge, som omslutter områder med en meget lav dislokationstæthed, kaldet subkorn. De mekaniske test viste at en træk-træk ændring af tøjningsvejen fører til en forøgelse af flydespændingen hvis ændringen i tøjningsvejen er tilstrækkelig stor og til en forbigående reduktion i deformationshærdningsraten.

Hovedparten af studiet bestod af en række røntgendiffraktionseksperimenter i hvilke de præ-deformerede prøver blev yderligere deformeret i træk in situ ved APS-synkrotronen (Advanced Photon Source ved Argonne National Laboratory), for nogle prøvers vedkommende langs en akse forskellig fra præ-deformationsaksen. I røntgendiffraktionseksperimenterne blev der benyttet en teknik med hvilken det er muligt at frembringe kort over det reciprokke rum med høj opløsning fra dybtliggende individuelle korn. De højtopløste kort over det reciprokke rum indeholder træk der er relateret til dislokationsstrukturen i kornene: En udbredt "sky" med en lav intensitet forårsaget af diffraktion fra dislokationsvæggene og en række skarpe toppe med en høj intensitet forårsaget af diffraktion fra de individuelle subkorn. Ved at frembringe kort over det reciprokke rum ved en række forskellige tøjningsniveauer er det muligt at studere udviklingen af dislokationsstrukturerne, og ved at analysere de skarpe toppe er det muligt at opnå viden om tøjningen i de individuelle subkorn og om de intra-granulære spændinger. Til analysen af kortene over det reciprokke rum blev der udviklet en matematisk metode til at skille intensitetsfordelingen i to dele svarende til bidragene fra subkornene og væggene.

Analysen viste at morfologien af dislokationsstrukturerne næsten ikke ændrer sig i det mikro-plastiske område af in situ-deformationen, og i det makro-plastiske område sker ændringerne i morfologien af dislokationsstrukturerne gradvist og uden pludselige voldsomme forandringer og uden tegn på at intermitterende dynamik spiller en væsentlig rolle i udvilklingen af dislokationsstrukturerne.

En analyse af positionen af de radielle profiler fra de individuelle subkorn afslørede en betydelig variation i den elastiske baglænsrettede tøjning i subkornene og viste at fordelingen af den elastiske baglænsrettede tøjning i subkornene kan approksimeres med en Gauss-fordeling. Endvidere viste analysen at der i gennemsnit er en større elastisk baglænsrettet tøjning i de store subkorn end i de små subkorn.

Analysen viste også at efter en ændring i tøjningsvejen bliver de intra-granulære spændinger betydelig omfordelt i det mikro-plastiske område. I nogle få individuelle subkorn var det muligt at følge udviklingen i den elastiske baglænsrettede tøjning fra træk til kompression. Efter en ændring i temperaturen fra -196 °C til stuetemperatur gennemgår både den gennemsnitlige intra-granulære spænding og variationen i de intra-granulære spændinger en indledende fase med formindskelse eller stagnation.

En analyse af bredden af de radielle profiler fra de individuelle subkorn viste at dislokationstætheden i subkornene forbliver konstant på et lavt niveau under deformationen.

Endelig indikerede en analyse af de radielle profiler fra de individuelle korn at en ændring i deformationsbetingelserne fører til en mindre ordnet dislokationsstruktur i væggene.

Preface

This thesis is submitted to the Technical University of Denmark (DTU) in partial fulfillment of the requirements for the degree of Doctor of Philosophy (PhD) in physics.

The work presented in the thesis was performed while I was employed at the Center for Fundamental Research: Metal Structures in Four Dimensions at Risø National Laboratory for Sustainable Energy, Technical University of Denmark between March 2007 and September 2010. The X-ray diffraction experiments were carried out at the Advanced Photon Source (APS) at Argonne National Laboratory.

Funding for the work was provided by the Danish National Research Foundation via the Center for Fundamental Research: Metal Structures in Four Dimensions. Use of the Advanced Photon Source was supported by the U.S. Department of Energy, Office of Science, Basic Energy Sciences under Contract No. DE-AC02-06CH11357.

My supervisors were Wolfgang Pantleon (main supervisor) and Henning F. Poulsen from Risø DTU, and our collaborator at APS was Ulrich Lienert. I am very grateful for the help they have all given me during the project.

I would like to thank Hans B. Nielsen from the department of Informatics and Mathematical Modelling (IMM) at DTU for his help in the development of the partitioning method described in chapter 6.

A number of other people also deserve a word of thanks: Bo Jakobsen, Matthew P. Miller, Mesut Varlioglu, Peter Kenesei, and Jette Oddershede for their assistance during the beam times, Lars Lorentzen for preparing the samples, Preben Olesen and Oleg Mishin for characterizing the samples with electron backscatter diffraction, Gitte Christiansen and Naoya Kamikawa for characterizing the samples with transmission electron microscopy, and Frank Adrian for performing the mechanical tests. Brian Ralph from Brunel University is thanked for reading through the almost finished version of the thesis and correcting some of the errors.

Finally, I would like to thank my wife, Annelise, for her support throughout the project, particularly during the long and difficult period in which the thesis was written.

Christian Wejdemann
Roskilde, March 2011

Contents

Chapter 1

Introduction

Metals are a very important class of materials which are used in almost all aspects of modern technology from simple beverage cans to sophisticated jet fighters. In order to save resources it is desirable to develop ways of making metals stronger. This will reduce the amount of metal needed for a particular application, and because smaller components will be lighter they can be transported with a reduced consumption of fuel, thereby saving oil resources and reducing the impact on the climate.

The metals used in most applications are composed of a number of small crystals called grains, and the shapes, sizes and orientations of the grains along with the distribution of the crystal defects within the individual grains have a large influence on the mechanical properties of the metal. So, with a detailed understanding of the relationship between microstructure (the structure that can be observed under high magnification such as different phases, grains and crystal defects) and mechanical properties it is possible to improve the mechanical properties, for instance increasing the strength, by processing the metal in a way that produces an optimal microstructure with respect to the desired properties.

One way of modifying the microstructure is by plastic deformation. In many metals plastic deformation primarily takes place through the motion of one-dimensional crystal defects called dislocations. As the metal is deformed, the density of dislocations increases and in many cases the dislocations form heterogeneous structures consisting of almost dislocation-free regions (called subgrains) separated by regions with high dislocation density (called dislocation walls). These dislocation structures are not static, and as the deformation proceeds the scale of the structures decreases. Furthermore, the morphology of the structures depends on the deformation conditions, and a change in the deformation conditions can induce a change from one type of structure to another.

One particular type of change in deformation conditions is a strain path change, in which the main axes of the deformation are changed. A simple example is a change in deformation axis during tensile deformation. As all shaping processes involve several changes in the strain path, an understanding of the processes responsible for the transient mechanical response following a strain path change is of immense practical importance for industrial metal forming, and because the mechanical properties are strongly influenced by the organization of the dislocation structure in the metal, such an understanding requires knowledge about the dynamical reorganization of the dislocation structure following a strain path change.

However, a fundamental understanding of the formation and evolution of dislocation structures is still lacking, in large part because in situ observations of the evolution of dislocation

structures during deformation have not been possible with the available experimental techniques. Transmission electron microscopy (TEM) can be used to produce high resolution images of dislocation structures, but it is a destructive technique and in situ observations in the bulk of a sample are impossible. Traditional X-ray diffraction techniques are non-destructive and can be used to perform in situ bulk measurements, but the X-rays probe a large volume of the metal which contains many grains, and measurements on individual subgrains are not possible.

Recently a new X-ray diffraction technique was developed (Jakobsen, Poulsen, Lienert, Almer, Shastri, Sørensen, Gundlach & Pantleon 2006) with which it is possible to study the evolution of dislocation structures in individual grains and even the properties of individual subgrains in situ during deformation. With this technique it is possible to obtain reciprocal space maps with high resolution from individual grains. Reciprocal space maps contain information about the distribution of orientations and elastic strains within the investigated volume and can be used to study the dislocation structure in the investigated grains. One disadvantage of the technique is that it can not give spatial information and the interpretation of the reciprocal space maps is not as straightforward as generally believed for the images obtained by TEM.

The aim of the work presented in this thesis was to study the evolution of dislocation structures, particularly the changes occurring right after a change in loading conditions. Most of the experiments carried out focused on the effects of a tension-tension strain path change (an abrupt change in loading axis during tensile deformation), but samples subjected to a change in temperature and reference samples that were not subjected to any change in loading conditions were also investigated.

Polycrystalline copper samples with a mean grain size of approximately 20 μm were pre-deformed in tension and then subsequently further deformed in tension in situ at the APS synchrotron. By using the technique mentioned above to obtain a sequence of high resolution reciprocal space maps, the evolution of the dislocation structures could be studied. Copper has a face centered cubic (fcc) crystal structure and was chosen as a model material for the wide range of fcc metals forming a type of dislocation structure known as a cell structure. The experiments were performed at relatively low levels of deformation, focusing on the processes occurring right after a change in loading conditions. The samples were pre-deformed to a strain of 5 % at room temperature or to a strain of 7 % at a temperature of -196 °C and further deformed (along a different axis for some of the samples) to a strain of less than 5 % (about 1 % for most sample) at the synchrotron.

The main part of the thesis is organized as follows: Chapter 2 introduces dislocations and the structures they form during plastic deformation as well as the effects of a change in strain path or temperature. Chapter 3 describes the basics of X-ray diffraction from crystals and the use of X-ray diffraction techniques to study dislocation structures. Chapter 4 presents the preparation of the samples used in the experiments and their characterization by electron microscopy and mechanical tests. Chapter 5 contains a detailed description of the experimental technique and of the procedure for a typical experiment along with an overview of the X-ray experiments carried out during the project. Chapter 6 presents the analysis of the X-ray diffraction data and contains a description of a method developed to partition the reciprocal space maps into two components corresponding to the contributions from the subgrains and the dislocation walls. Chapter 7 contains a presentation and a discussion of the results of the data analysis. Finally, chapter 8 contains a summary of the main points and a brief outlook.

Chapter 2

Background: Dislocations and dislocation structures

As mentioned in the previous chapter, the motion of dislocations is the main process responsible for plastic deformation in many metals, and as a result of plastic deformation the dislocations may form heterogeneous structures. With a focus on copper polycrystals deformed in tension, this chapter gives a brief introduction to dislocations and their role in plastic deformation, deformation-induced dislocation structures, and the effects of a change in strain path or temperature.

2.1 Dislocations and plastic deformation of fcc metals

This section briefly summarizes the basic elements of physical metallurgy relevant to the work presented in this thesis. For more details the reader is referred to the literature, e.g. the books by Honeycombe (1968), Hirth & Lothe (1992), Hosford (1993), Hull & Bacon (2001), and Abbaschian, Abbaschian & Reed-Hill (2010).

2.1.1 The fcc crystal structure and dislocations

Metals have a crystalline atomic structure in which, disregarding unavoidable defects, the atoms are arranged in a periodic pattern extending over regions that are large compared to interatomic distances.

A crystalline structure can be described as a lattice with an identical atomic arrangement (a basis) attached to each lattice point. A lattice is the set of all points whose distance from the origin is given by a lattice vector defined as a vector of type $\boldsymbol{R} = n_1\boldsymbol{a}_1 + n_2\boldsymbol{a}_2 + n_3\boldsymbol{a}_3$, where n_1, n_2, and n_3 are integers and $\boldsymbol{a}_1$, $\boldsymbol{a}_2$, and $\boldsymbol{a}_3$ are the fundamental lattice vectors describing the lattice. In a cubic lattice the fundamental lattice vectors are mutually orthogonal and have the same length which is called the lattice constant and is denoted by a. The crystal axes are lines parallel to $\boldsymbol{a}_1$, $\boldsymbol{a}_2$, or $\boldsymbol{a}_3$.

Many metals, among these copper, have an fcc crystal structure. The atomic arrangement of an ideal fcc crystal is illustrated in figure 2.1. It can be described as a cubic lattice with a basis consisting of four atoms positioned at the positions $(0, 0, 0)$, $(a/2, a/2, 0)$, $(a/2, 0, a/2)$, and $(0, a/2, a/2)$ relative to each lattice point.

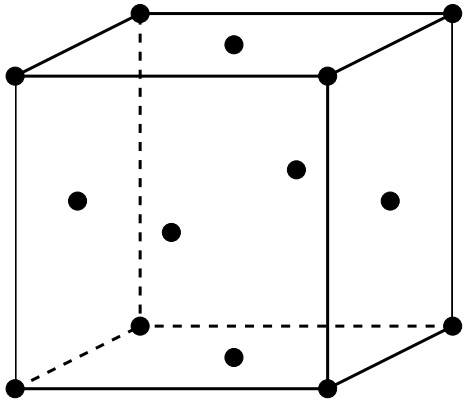

Figure 2.1: The atomic arrangement of an fcc crystal.

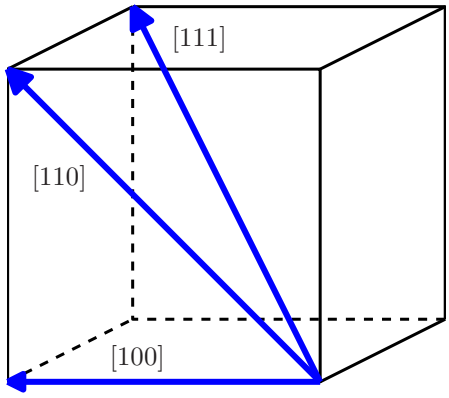

Figure 2.2: The directions [100], [110], and [111] in a cubic lattice.

To describe directions and planes in a lattice, Miller indices are used. A particular direction is described by finding a vector which is parallel to the direction, and whose projections on the crystal axes are the smallest possible integer multiples, ua, va, and wa, of the lattice constant. The direction is then denoted by $[uvw]$. For a cubic lattice the directions [100], [110], and [111] are illustrated in figure 2.2. Because of the symmetry of an fcc crystal, certain directions are symmetrically equivalent, such as [100] and [010]. The notation $\langle uvw \rangle$ is used to denote all directions equivalent to $[uvw]$ by symmetry.

For a cubic lattice, a family of lattice planes (a set of parallel planes with constant spacing, d, between adjacent planes) is described by the projection of a vector with length a^2/d, which is normal to the planes, onto the crystal axes. If the projections of this vector are ha, ka, and la, the lattice plane family is denoted by (hkl), and the lattice plane spacing is denoted by d_{hkl}. For planes, the notation $\{hkl\}$ is used to denote all lattice plane families symmetrically equivalent to (hkl). For a cubic lattice, the lattice plane spacing is given by $d_{hkl} = a/\sqrt{h^2 + k^2 + l^2}$.

Crystalline solids in which the periodic arrangement of atoms extend throughout the entire solid are called single crystals. Single crystals are difficult to produce, and most metallic solids are polycrystals, which means that they are composed of many small crystals with different crystallographic orientations. The individual crystals are called grains, and they meet along two-dimensional surfaces, called grain boundaries, at which the periodic atomic pattern breaks down. The distribution of the crystallographic orientation of the grains is called the texture of the polycrystal.

There are also defects in the crystal structure within individual grains (and within single crystals). One very important type is the dislocation, which is a one-dimensional defect in the crystal structure. A precise description of dislocations requires the concepts of a Burgers circuit and a Burgers vector: A Burgers circuit is any atom-to-atom path which forms a closed loop in the crystal. If the Burgers circuit encloses a dislocation, then the same atom-to-atom sequence traced in a perfect crystal will not form a closed loop, but will begin and end at different atomic positions. The vector required to complete the circuit in the perfect crystal is called the Burgers vector of the dislocation. An example of a Burgers circuit and the

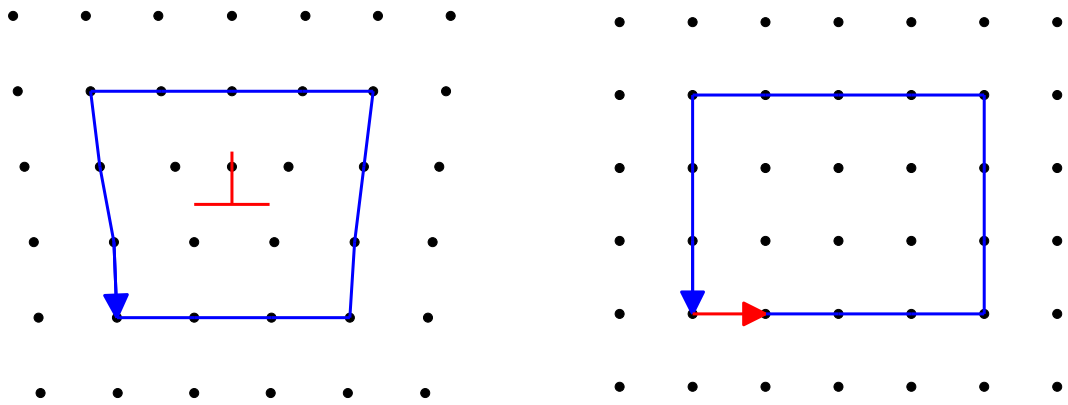

Figure 2.3: Left: The atomic arrangement and a Burgers circuit around an edge dislocation. Right: The same atom-to-atom path with the dislocation Burgers vector (red) required to close the circuit in a perfect crystal.

corresponding Burgers vector is shown in figure 2.3. If the Burgers circuit does not enclose a dislocation, there will be no closure failure in the perfect crystal. A dislocation is thus a one-dimensional crystal defect, around which there is a Burgers circuit closure failure.

A dislocation is characterized by its direction (the dislocation line vector) and its Burgers vector. If the Burgers vector is parallel to the dislocation line vector, the dislocation is called a screw dislocation, and if the Burgers vector is perpendicular to the dislocation line vector (as in figure 2.3 where the dislocation line vector points out of the figure), the dislocation is called an edge dislocation. In general, any configuration between these two extremes can occur, even for the same dislocation, because the dislocation line vector may be different at different points along the dislocation.

The crystal is distorted around a dislocation, and stress and strain fields are associated with dislocations. A dislocation placed in the stress field from another dislocation experiences a force, and in this way the stress fields give rise to long-range interactions between dislocations. Other interactions are possible when two dislocations intersect or pass within a few Burgers vector lengths of each other. In this case it is possible for (parts of) the dislocations to combine and produce dislocation segments whose Burgers vector is the sum of the Burgers vectors of the individual dislocations. This may lead to either annihilation if the resulting Burgers vector is zero or to dislocation segments with restricted mobility. These short-range interactions involving topological changes of the dislocation configuration can be very complicated and difficult to analyze, even in the case of only a few interacting dislocations.

It is not possible for a dislocation to end within a crystal. It must either extend to the crystal surface or a grain boundary, form a closed loop, or branch into other dislocations. Such branching points are called nodes and they may form as a result of short-range dislocation interactions. The dislocations in a crystal are thus arranged in a complicated network consisting of components of possibly curved dislocation lines connected to each other through nodes, where some line segments extend to the crystal boundary. These components may range in complexity from simple loops to complex networks extending throughout the crystal. The dislocation content of the crystal is quantified by the dislocation density, ρ, defined as the total length of dislocation line per unit volume of the crystal.

2.1.2 Elastic and plastic deformation and dislocation glide

A metallic solid deforms when it is subjected to external stresses. For sufficiently small stress levels the deformation is elastic: When the external stress is removed, the solid recovers its original shape, and for many materials stress and strain are approximately linearly related. For uniaxial tension, elasticity is expressed by Hooke's law:

$$\sigma = E\varepsilon, \tag{2.1}$$

where σ is the uniaxial stress along the tensile axis, E is Young's modulus, and ε is the strain along the tensile axis. Perpendicular to the tensile axis the Poisson effect produces an elastic strain, which is given by $\varepsilon_\perp = -\nu\varepsilon$, where ν is Poisson's ratio.

For larger stress levels the deformation becomes plastic: The solid does not recover its original shape when the external stress is removed, and the relation between stress and strain is non-linear. As the amount of plastic deformation increases, work hardening is commonly observed for most metals, which means that the stress required for further plastic deformation (the flow stress) increases. A generic curve of stress versus strain for a tensile experiment showing elastic and plastic behavior is shown in figure 2.4. Plastic deformation is accompanied by an amount of elastic strain given by $\varepsilon = \sigma/E$, which is recovered when the external stress is removed.

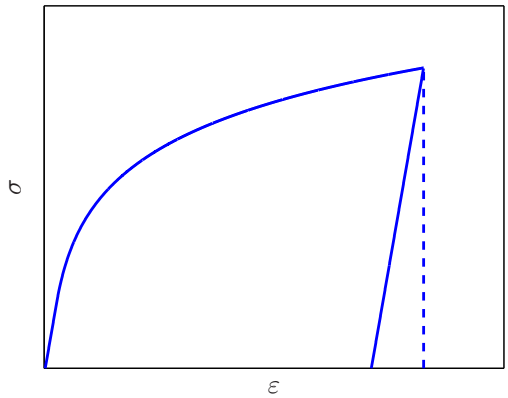

Figure 2.4: A generic stress-strain curve for tensile deformation. The curve is initially linear during the elastic range, and then the sample deforms plastically while the flow stress gradually increases. Finally the sample is unloaded along the solid line. The dashed line indicates the sum of the plastic and elastic strain just before unloading.

The main process by which an fcc crystal deforms plastically is dislocation glide. This is the motion of dislocations on a plane that contains both the dislocation line vector and the Burgers vector. Such a plane is called a slip plane, the direction of the Burgers vector is called the slip direction, and the combination of a particular slip plane and a particular slip direction is called a slip system. Each crystal structure has a specific set of slip systems. For an fcc crystal the slip planes are of type $\{111\}$, and the possible Burgers vectors are parallel to the $\langle 110\rangle$ directions and have length $a/\sqrt{2}$. When a dislocation glides through the crystal, the parts of the crystal on either side of the slip plane are displaced relative to each other by the Burgers vector of the dislocation, and on the slip plane the dislocation marks

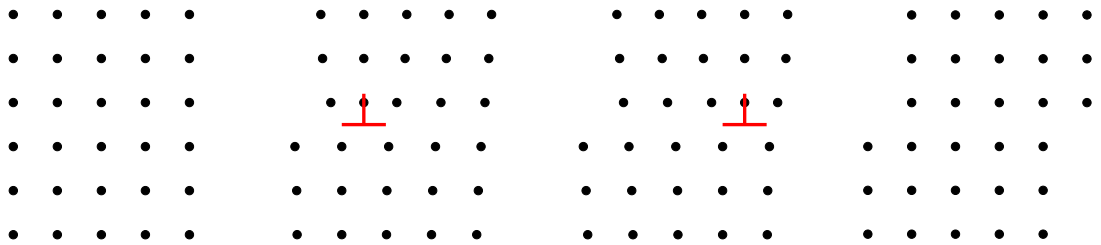

Figure 2.5: A schematic illustration of plastic deformation by the movement of an edge dislocation through part of a crystal. From left to right: The crystal is initially perfect, but as the dislocation enters from the left and moves to the right on a horizontal slip plane the crystal structure is distorted until the dislocation exits to the right and leaves the crystal with a perfect crystal structure and a change in shape.

the boundary between slipped and non-slipped areas of the crystal as illustrated in figure 2.5. Deformation by dislocation glide only takes place on slip planes, and as a consequence, in order to deform compatibly, grains in a polycrystal are forced to rotate during deformation because of geometrical constraints imposed by neighboring grains.

During plastic deformation new dislocations are formed, the dislocation density increases, and each dislocation interacts with an increasing number of other dislocations through both short-range and long-range interactions. The increase in dislocation density combined with the restricting effect on dislocation motion of these interactions is the standard explanation for work hardening. Besides raising the flow stress, the complex interactions may cause the dislocations to form heterogeneous structures as described in section 2.2.

In a heterogeneous dislocation structure the local flow stress depends on the local dislocation density, and in order to ensure that regions with different dislocation density deform compatibly the local stress must vary in the structure. In the case of uniaxial tensile deformation, regions with a high dislocation density experience a local tensile stress which is higher than the mean tensile stress, and regions with a low dislocation density experience a local tensile stress which is lower than the mean tensile stress.

In the dislocation-rich regions this results in a tensile elastic strain which is higher than the mean tensile elastic strain along the tensile direction, and, because of the Poisson effect, a compressive elastic strain which is higher than the mean compressive elastic strain in the directions perpendicular to the tensile axis. The dislocation-rich regions are said to experience a tensile elastic forward-strain along the tensile direction and a compressive elastic forward-strain in the perpendicular directions.

Similarly, in the dislocation-poor regions the tensile elastic strain is lower than the mean tensile elastic strain along the tensile direction, and the compressive elastic strain is lower than the mean compressive elastic strain in the perpendicular directions. The dislocation-poor regions are said to experience a compressive elastic back-strain along the tensile direction and a tensile elastic back-strain in the perpendicular directions.

Upon loading, internal stresses (deviations from the average stress) are built up as a result of the motion of dislocations through the most easily deformable parts of the structure. This range of deformation, where isolated parts of the crystal have begun to deform plastically while other parts still deform elastically is called the micro-plastic range. In contrast, the range of macroscopic plastic deformation, where the plastically deforming regions are connected

throughout the crystal is called the macro-plastic range. The internal stresses created in this way remain in the crystal after unloading.

In a crystal that contains a dislocation structure and related internal stresses, thermally activated processes can gradually clean up the dislocation structure by removing and rearranging some of the dislocations produced during plastic deformation and possibly reducing the internal stresses. This phenomenon is called recovery.

2.2 Dislocation structures

The structures formed by dislocations during plastic deformation have been studied extensively by TEM, e.g. by Essmann (1963), Basinski (1964), Steeds (1966), Essmann, Rapp & Wilkens (1968), Mughrabi (1971), and Göttler (1973). This section describes a particular type of ordered dislocation structure, called a cell structure in this thesis, which forms in many metals, including copper, for a wide range of deformation conditions. For a general overview of dislocation structures formed during plastic deformation the reader is referred to the paper by Hughes & Hansen (2004).

The system consisting of many dislocations interacting through both short-range and long-range interactions is very complex, and although the literature contains many modeling attempts using various methods, a fundamental understanding of the formation and evolution of dislocation structures is still lacking. The papers by Kubin (1993, 1996) and Bulatov (2002) provide an overview of the various modeling approaches.

2.2.1 Cell structures

The particular morphology of a dislocation structure depends on various parameters, e.g. the material, the deformation mode, the orientation of the grain, and the strain level. Generally, cell structures form during plastic deformation when the three-dimensional dislocation mobility is sufficiently high (Hughes & Hansen 2004). The main contribution to the three-dimensional mobility of dislocations is cross slip (the process whereby a screw dislocation changes slip plane, which it can do because its Burgers vector and line vector are parallel). The ease of cross slip depends on the material, the strain rate and the temperature. When the three-dimensional dislocation mobility is low, the dislocations form simpler structures with more homogeneous dislocation distributions.

Cell structures consist of regions with relatively high dislocation density enclosing regions with very low dislocation density. Examples of cell structures are shown in figures 2.6 and 2.7. The regions with a high dislocation density are commonly called (dislocation) walls or boundaries, and the regions with a low dislocation density are commonly called subgrains or cell interiors (the former indicating that they are regions of almost perfect crystal). The subgrains on each side of a wall are slightly rotated with respect to each other by an angle called the misorientation angle, which is on the order of $1\,^{\circ}$. In many cases cell structures are found to be hierarchical, with groups of cells, called cell blocks (Bay, Hansen, Hughes & Kuhlmann-Wilsdorf 1992), separated by walls with larger misorientation angles. In general, it has been found that the misorientation angle increases with increasing strain (Hughes, Liu, Chrzan & Hansen 1997) and the cell size and wall thickness decrease with increasing stress (Raj & Pharr 1986, Knoesen & Kritzinger 1982).

The walls between cell blocks are different from the walls between individual subgrains within a cell block. The former are called geometrically necessary boundaries (GNBs) and

the latter are called incidental dislocation boundaries (IDBs) (Kuhlmann-Wilsdorf & Hansen 1991). The GNBs are planar, and they are assumed to form between regions where the slip activity is distributed differently among the available slip systems. The IDBs are usually more curved, and they are assumed to form as a result of random mutual trapping of dislocations.

2.2.2 Dislocation structures in copper deformed in tension

In the case of copper polycrystals deformed in tension, the dislocation structures have been studied in detail with TEM for strains between 5 % and 30 % by Huang and coauthors (Huang 1998, Huang, Borrego & Pantleon 2001, Huang & Winther 2007). Their results show that the dislocation structure in each grain belongs to one of three different morphological types. The primary parameter determining which type of structure is present in a given grain is the orientation of the grain with respect to the tensile axis. The three different types are shown in figure 2.6 together with the orientation of the grains in which they are observed.

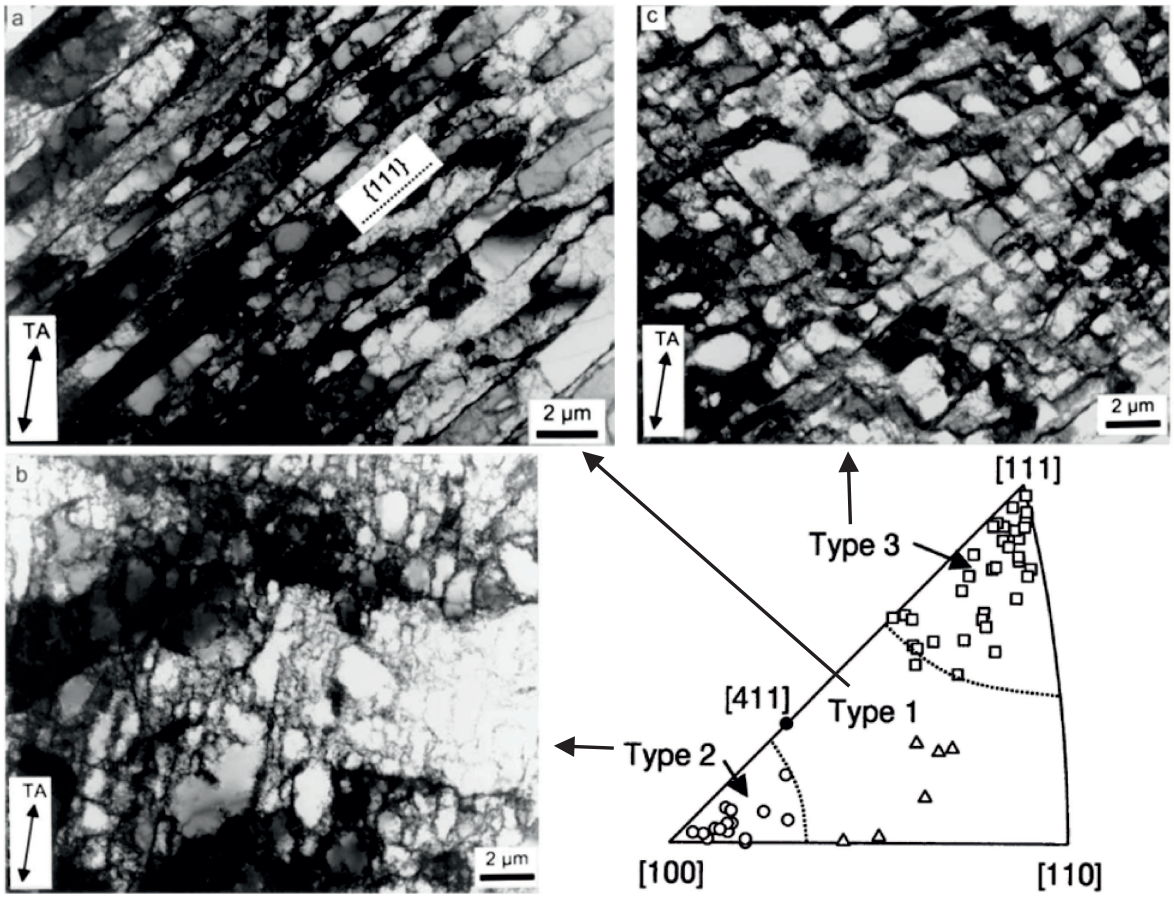

Figure 2.6: TEM images of the three morphological types of dislocation structure observed in copper polycrystals deformed in tension. The stereographic triangle shows the connection between the type of structure observed and the direction of the tensile axis with respect to the crystal in each of the investigated grains. Modified from Huang et al. (2001).

One type of structure is found in grains for which the tensile axis points toward the central part of the stereographic triangle. This structure consists of a set of extended planar walls separating regions containing short, curved walls. Each of the planar walls is oriented almost parallel to a (111) plane. This is type 1 in figure 2.6.

A second type of structure is found in grains for which the tensile axis is almost parallel to (within 15 ° of) a [100] direction. This structure contains no planar walls, but is composed of cells which are slightly elongated along the tensile axis and essentially equiaxed in the cross section. This is type 2 in figure 2.6.

The third type of structure is found in grains for which the tensile axis is almost parallel to (within 20 ° of) a [111] direction. This structure is similar to the first structure, but the extended walls in this structure are less planar and deviate more from a (111) plane. Typically two crossing sets of extended walls are present. This is type 3 in figure 2.6.

2.3 Effects of a change in loading conditions

The morphology of a dislocation structure formed during plastic deformation depends on the deformation conditions, for tensile deformation particularly the orientation of the grain with respect to the tensile axis, and if the loading conditions are changed during deformation the dislocation structure may change in order to accommodate the new loading conditions. This section considers the effects of two types of change in loading conditions: A change in strain path and a change in temperature.

2.3.1 Strain path changes

A strain path change is a change in the normalized deviatoric strain rate tensor during deformation, such as a change from rolling to tensile deformation or a change in the orientation of the tensile axis during tensile deformation.

A strain path change can be conveniently represented by the strain path change parameter, α, introduced by Schmitt, Aernoudt & Baudelet (1985). It is defined by

$$\alpha = \mathbf{N}_1 : \mathbf{N}_2, \tag{2.2}$$

where $\mathbf{N}_1$ and $\mathbf{N}_2$ are the normalized deviatoric strain rate tensors for the first and second strain paths, respectively. Schmitt, Shen & Raphanel (1994) have shown that α appears to be a good indicator of the mechanical effects of a strain path change for various loading sequences, in the sense that different loading sequences with the same value for α results in the same mechanical response. In their experiments, the effects of a strain path change (as measured by the ratio of the reloading yield stress to the stress reached in monotonic straining) was largest for $\alpha = 0$ (called an orthogonal strain path change). The extreme cases $\alpha = 1$ and $\alpha = -1$ correspond to monotonic deformation and complete strain reversal (called a reverse strain path change), respectively.

For tension-tension sequences with a rotation of the tensile axis by an angle ψ, the normalized deviatoric strain rate tensors before and after the strain path change can be represented as

$$\mathbf{N}_1 = \sqrt{\frac{2}{3}} \begin{pmatrix} 1 & 0 & 0 \\ 0 & -1/2 & 0 \\ 0 & 0 & -1/2 \end{pmatrix} \tag{2.3}$$

and

$$\mathbf{N}_2 = \sqrt{\frac{2}{3}} \begin{pmatrix} \cos^2(\psi) - 1/2 \sin^2(\psi) & 3/2 \cos(\psi)\sin(\psi) & 0 \\ 3/2 \cos(\psi)\sin(\psi) & \sin^2(\psi) - 1/2 \cos^2(\psi) & 0 \\ 0 & 0 & -1/2 \end{pmatrix}, \tag{2.4}$$

which leads to

$$\alpha = \mathbf{N}_1 : \mathbf{N}_2 = 3/2 \cos^2(\psi) - 1/2. \tag{2.5}$$

From equation (2.5) it follows that for tension-tension sequences, values of α between $-1/2$ and 1 can be realized. Table 2.1 shows the value of α for some values of ψ.

Table 2.1: Values of the angle of rotation, ψ, of the tensile axis and the corresponding strain path change parameter, α, for a tension-tension strain path change.

ψ :	0 °	35 °	55 °	90 °
α :	1	1/2	0	−1/2

2.3.2 Effects of a strain path change in general

Brief summaries of the effects of a strain path change on the mechanical properties and the dislocation structure can be found in the papers by Aernoudt, Van Houtte & Leffers (1993), Peeters, Kalindindi, Van Houtte & Aernoudt (2000), and Bouvier, Alves, Oliveira & Menezes (2005). In general, compared to monotonic deformation a strain path change results in an increase or decrease in the yield stress followed by a transient phase with a reduced work hardening rate. The orthogonal strain path change results in the largest increase in the yield stress, and the reverse strain path change results in the largest decrease in the yield stress. Both types of strain path change lead to a reduction in the work hardening rate, in some cases to the extent that work softening is observed.

TEM observations of dislocation structures after a strain path change show that generally the structures formed during pre-deformation change to the structure corresponding to the second strain path after a transient phase. For a reverse strain path change a partial dissolution or disintegration of the structure is often observed before the new structure is formed. For an orthogonal strain path change, microbands are sometimes observed to form, penetrating the old structure.

In a reverse strain path change most of the slip systems that were active during the first strain path are also active during the second strain path, but they are operating in the opposite sense. The decrease in the yield stress observed in this case is commonly attributed to the ease of backward dislocation motion due to the effects of internal stresses.

In an orthogonal strain path change most of the slip systems that were active during the first strain path are inactive during the second strain path and new slip systems are activated. The increase in the yield stress observed in this case is commonly attributed to the effects of interactions between the existing dislocation structure and the new dislocations, where the structure formed during the first strain path may act as an obstacle to slip on the new slip systems.

The reduction in the work hardening rate observed in all cases is commonly attributed to the formation of microbands forming channels for easy transport of dislocations through the old structure or to an increase in the rate of annihilation reactions due to interactions between the existing dislocation structure and the new dislocations.

2.3.3 Effects of a strain path change on polycrystalline copper

The effects of a tension-tension strain path change on polycrystalline copper with a mean grain size of 20 μm have been studied by Schmitt, Fernandes, Gracio & Vieira (1991), who investigated the mechanical response for values of ψ between 0 ° and 90 ° and true pre-strain levels between 6 % and 18 %. They found that after a strain path change an increase in the yield stress was followed by a transient phase with a reduced work hardening rate compared to monotonic tensile deformation (along the direction corresponding to the second strain path). The increase in the yield stress was largest for values of ψ between 45 ° and 60 °, and the decrease in the work hardening rate was largest for ψ = 90 °. The effects on both the yield stress and the work hardening rate were larger if the level of pre-strain was increased.

For ψ-values of 15 °, 45 °, and 90 °, they also investigated the effects on the dislocation structures with TEM. For a pre-strain of 5 % and higher, a well-developed cell structure was observed (figure 2.7, top left). For ψ = 45 ° and ψ = 90 ° the structure changed after the strain path change: The dislocation walls created during the pre-deformation tended to disappear, the walls thickened, and the dislocation density in the walls seemed to decrease. After a strain

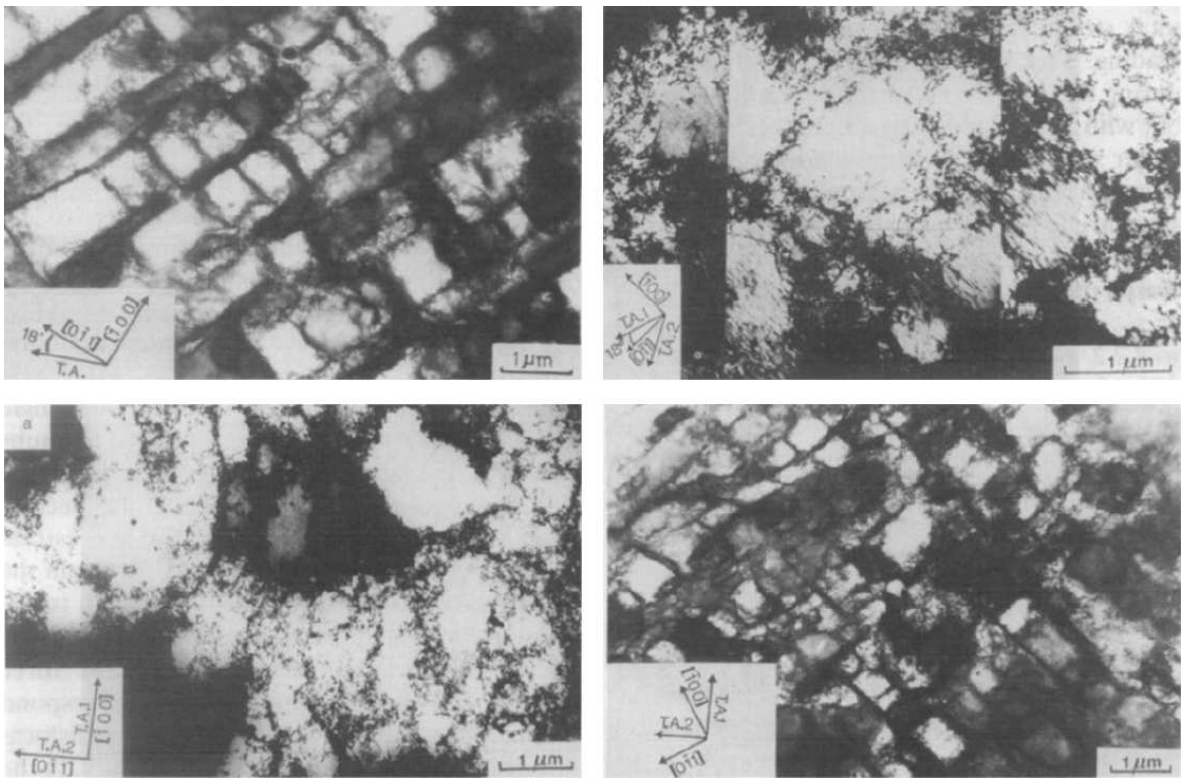

Figure 2.7: TEM images of the effect of a tension-tension strain path change on dislocation structures in copper. Top left: Cell structure after monotonic deformation to a strain of 15 %. Top right: Unorganized dislocation structure after a pre-strain of 12 % and further deformation to a strain of 2.5 % along an axis with ψ = 45 °. Bottom left: Partial disappearance of dislocation walls after a pre-strain of 12 % and further deformation to a strain of 2.5 % along an axis with ψ = 90 °. Bottom right: Development of a new structure after a pre-strain of 12 % and further deformation to a strain of 26 % along an axis with ψ = 90 °. Note that the images are from grains in different samples because the samples must be destroyed for TEM investigations. From Schmitt et al. (1991).

of 2.5 % along the second strain path the structure was unorganized and more homogeneous in most grains (figure 2.7, top right). For $\psi = 90°$ dissolution was observed in a few grains (figure 2.7, bottom left). The structural evolution took place over a wide strain interval (at least 10 % for a pre-strain of 12 %), but eventually new walls appeared, forming a structure compatible with the new deformation conditions (figure 2.7, bottom right).

Christodoulou, Woo & MacEwen (1986) performed reverse strain path changes (compression-tension and tension-compression) on polycrystalline copper with a mean grain size of 20 μm. They investigated true pre-strain levels between 2 % and 33 %. In all cases they observed a decrease in the yield stress followed by a transient phase with a reduced work hardening rate. TEM investigations of the dislocation structure showed evidence of cell walls being dissolved or partially reduced to tangles upon stress reversal.

Fernandes, Gracio & Schmitt (1993) performed rolling-tension strain path changes on polycrystalline copper samples with different grain sizes (20 μm and 250 μm) with pre-strain levels between 10 % and 50 %. After the strain path change they observed microbands in the large grains but not in the small grains. This indicates that the formation of microbands is not relevant for the grains investigated in the study presented in this thesis.

2.3.4 Effects of a change in temperature

If two identical metals samples are deformed at two different temperatures, but under otherwise identical conditions, the sample deformed at the lower temperature exhibits a higher flow stress (Schmid & Boas 1935).

According to Cottrell & Stokes (1955) the increase in flow stress can be interpreted as a result of two effects: First, due to the suppression of thermally activated recovery processes at low temperatures the dislocation density increases faster with strain at the lower temperature, leading to an increase in the flow stress compared to the sample deformed at the higher temperature. Second, because of the temperature dependence of the elastic constants, there are reversible changes in the flow stress when the temperature is changed.

Experiments designed to quantify the reversible effect by measuring the change in flow stress as the temperature is cycled between different temperatures were carried out on aluminum single crystals by Cottrell & Stokes (1955) and on copper single crystals by Adams & Cottrell (1955). In both experiments an additional irreversible effect was observed when the deformation was interrupted at the lower temperature and resumed at the higher temperature. In this case, for sufficiently high strain levels, an abrupt decrease in the flow stress (work softening) was observed. This is shown for the experiments on copper in figure 2.8.

This effect was interpreted in terms of the destruction of immobile dislocation configurations due to the combined effect of thermally activated processes (due to the higher temperature) and stress. During deformation at the lower temperature short-range dislocation interactions may lead to dislocation configurations which are unable to move and thus act as obstacles to dislocation glide. The stress required to destroy such obstacles depends on the temperature, and when the temperature is raised, the increased rate of thermally activated processes leads to the destruction of the least stable obstacles, making dislocation glide easier and reducing the flow stress.

The effects of the temperature on the morphology of dislocation structure in copper have been studied by Swann (1963), Staker & Holt (1972), and Prinz & Argon (1980). The studies show that for lower temperatures the cell size decreases and the dislocation structure appear less well defined.

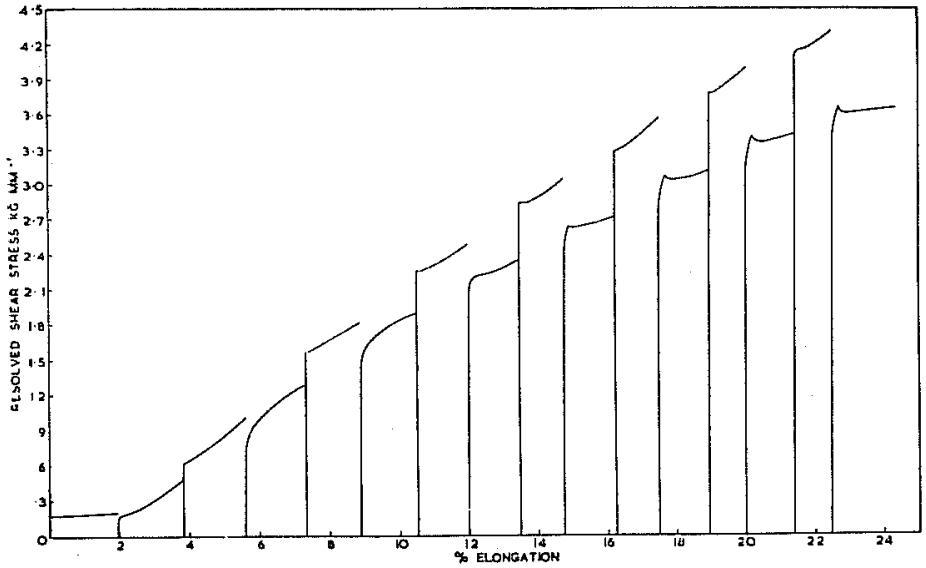

Figure 2.8: The stress as a function of the strain for the deformation of a copper single crystal deformed alternately at two different temperatures (-183 °C and 200 °C). The sections with a high flow stress corresponds to the lower temperature. At sufficiently high strain, work softening is observed when the temperature is changed from the lower temperature to the higher temperature. From Adams & Cottrell (1955).

Chapter 3

Background: X-ray diffraction used to study dislocation structures

X-ray diffraction offers an alternative to TEM for studying dislocation structures. Unlike TEM, X-ray diffraction can be used to study grains embedded in the bulk of a polycrystalline sample nondestructively during deformation. This chapter first describes the basics of X-ray diffraction from crystals and introduces reciprocal space maps. Radial profiles and methods for obtaining information about dislocation structures from them are introduced next. The last section presents two recently-developed X-ray diffraction techniques and results on dislocation structures in copper obtained with their use.

3.1 X-ray diffraction from crystals

This section presents the basics of monochromatic X-ray diffraction from crystals. For more details the reader is referred to the literature, e.g. the books by Warren (1990), Guinier (1994), Als-Nielsen & McMorrow (2001), and Cullity & Stock (2001).

3.1.1 Reciprocal space

In an X-ray diffraction experiment with a monochromatic beam, the intensity of the diffracted beam in a given direction depends on the relative orientation of the sample and the wave vectors of the incoming and the outgoing beams. The wave vector of a monochromatic beam is a vector, $\boldsymbol{k}$, pointing along the beam with length $|\boldsymbol{k}| = 2\pi/\lambda$, where λ is the wavelength of the radiation. The wavelength is related to the beam energy, E, by the relation $\lambda = hc/E$, where h is Planck's constant, and c is the speed of light in vacuum. The scattering angle, 2θ, is the angle between the wave vector of the incoming beam, $\boldsymbol{k}_{\mathrm{in}}$, and the wave vector of the outgoing beam $\boldsymbol{k}_{\mathrm{out}}$. The scattering vector, $\boldsymbol{q}$, is the difference between the wave vectors of the incoming and the outgoing beams: $\boldsymbol{q} = \boldsymbol{k}_{\mathrm{out}} - \boldsymbol{k}_{\mathrm{in}}$. This thesis only deals with elastic scattering, where the wavelength of the beam is unchanged by the diffraction. In this case the length of the scattering vector is given by

$$q = |\boldsymbol{q}| = \frac{4\pi}{\lambda}\sin(\theta). \tag{3.1}$$

The scattering plane is the plane containing $\boldsymbol{k}_{\mathrm{in}}$ and $\boldsymbol{k}_{\mathrm{out}}$ (and $\boldsymbol{q}$). The relations between the wave vectors, the scattering angle and the scattering vector are illustrated in figure 3.1.

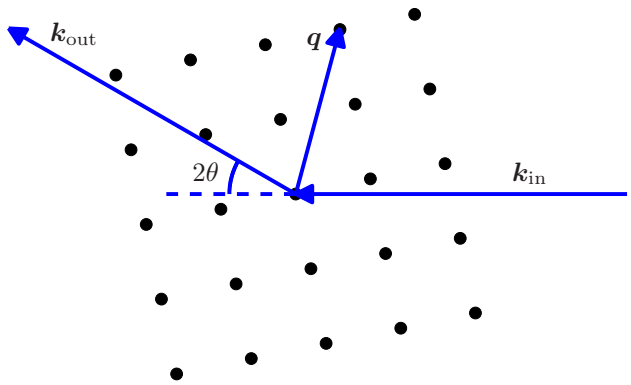

Figure 3.1: An illustration of the relations between the wave vectors, $\boldsymbol{k}_{\text{in}}$ and $\boldsymbol{k}_{\text{out}}$, the scattering angle, 2θ, and the scattering vector, $\boldsymbol{q} = \boldsymbol{k}_{\text{out}} - \boldsymbol{k}_{\text{in}}$. A number of reciprocal lattice points are shown to illustrate the fulfillment of Laue's condition for diffraction.

The intensity of the diffracted beam is proportional to the square of the norm of the structure factor, $F(\boldsymbol{q})$, which is given as a sum over all the atoms in the diffracting volume:

$$F(\boldsymbol{q}) = \sum_j f_j(\boldsymbol{q}) e^{i\boldsymbol{q}\cdot\boldsymbol{r}_j}, \tag{3.2}$$

where $f_j(\boldsymbol{q})$ is a parameter called the atomic form factor for the j'th atom, and $\boldsymbol{r}_j$ is the position vector for the j'th atom. Equation (3.2) shows that the structure factor, and therefore the diffracted intensity, depends on the orientation and length of the scattering vector. The space of all possible scattering vectors is called reciprocal space, and the diffracted intensity can be perceived as an intensity in reciprocal space.

For a perfect crystal the structure factor can be split into a sum over all lattice points and a sum over the atoms in the basis:

$$F_{\text{crystal}}(\boldsymbol{q}) = \sum_n e^{i\boldsymbol{q}\cdot\boldsymbol{R}_n} \times \sum_l f_l(\boldsymbol{q}) e^{i\boldsymbol{q}\cdot\boldsymbol{r}_l}. \tag{3.3}$$

Here the sum over n is over all lattice points in the crystal, and $\boldsymbol{R}_n$ is the lattice vector corresponding to the n'th lattice point. The sum over l is over all atoms in the basis, and $f_l(\boldsymbol{q})$ and $\boldsymbol{r}_l$ are the atomic form factor and the position vector for the l'th basis atom, respectively.

3.1.2 Diffraction from ideal and real crystals

For ideal crystals, which have an infinite size and a perfect crystal structure, evaluation of equation (3.3) shows that $F_{\text{crystal}}(\boldsymbol{q})$ is zero unless $\boldsymbol{q}$ is equal to a vector of the type $\boldsymbol{g}_{hkl} = h\boldsymbol{a}_1^* + k\boldsymbol{a}_2^* + l\boldsymbol{a}_3^*$, where h, k, and l are integers, and

$$\boldsymbol{a}_1^* = 2\pi\frac{\boldsymbol{a}_2 \times \boldsymbol{a}_3}{\boldsymbol{a}_1 \cdot (\boldsymbol{a}_2 \times \boldsymbol{a}_3)}, \quad \boldsymbol{a}_2^* = 2\pi\frac{\boldsymbol{a}_3 \times \boldsymbol{a}_1}{\boldsymbol{a}_2 \cdot (\boldsymbol{a}_3 \times \boldsymbol{a}_1)}, \quad \text{and} \quad \boldsymbol{a}_3^* = 2\pi\frac{\boldsymbol{a}_1 \times \boldsymbol{a}_2}{\boldsymbol{a}_3 \cdot (\boldsymbol{a}_1 \times \boldsymbol{a}_2)}. \tag{3.4}$$

When the condition

$$\boldsymbol{q} = \boldsymbol{g}_{hkl}, \tag{3.5}$$

which is called Laue's condition and is illustrated in figure 3.1, is fulfilled, the observed reflection is called an hkl-reflection. The set of vectors $\boldsymbol{g}_{hkl}$ generate a lattice called the reciprocal lattice, and the vectors $\boldsymbol{a}_1^*$, $\boldsymbol{a}_2^*$, and $\boldsymbol{a}_3^*$ are the fundamental reciprocal lattice vectors. The reciprocal lattice vector $\boldsymbol{g}_{hkl}$ is perpendicular to the lattice planes (hkl) and its length is given by $|\boldsymbol{g}_{hkl}| = 2\pi/d_{hkl}$. From this it follows that Laue's condition is equivalent to Bragg's law, which states that for diffraction to occur from a family of lattice planes, (hkl), the scattering vector must be normal to the planes, and the equation

$$\lambda = 2d_{hkl}\sin(\theta) \tag{3.6}$$

must be fulfilled.

Bragg's law shows that the scattering angle is the same for diffraction from all symmetrically equivalent lattice plane families, and in the case of diffraction from a large number of randomly oriented small crystals (for instance a crystalline powder or a polycrystal with many small randomly oriented grains) the diffracted beams from all $\{hkl\}$ planes form a cone and give rise to a ring, called an hkl Debye-Scherrer ring, on an area detector.

If the crystal is rotated, the reciprocal lattice rotates with the crystal lattice, and the direction of the scattering vector corresponding to each reflection changes in the same manner. This corresponds to a shift of the reflection in a direction perpendicular to the scattering vector. Such a direction is called an azimuthal direction, and the plane perpendicular to the scattering vector is called the azimuthal plane.

If the crystal is strained isotropically and elastically, the fundamental reciprocal lattice vectors change in length, and the reciprocal lattice contracts or expands isotropically. From Laue's condition it follows that the length of the scattering vector corresponding to each reflection changes in length. This corresponds to a shift of the reflection along a straight line passing through the origin. This direction (parallel to the scattering vector) is called the radial direction. A non-isotropic straining of the crystal may produce rotations of the lattice planes, causing an additional azimuthal shift.

For real crystals, which have a finite size and contain defects, diffraction may occur even though Laue's condition is not exactly fulfilled. In this case the reciprocal space intensity is spread out around the reciprocal lattice points. The effect of a finite size or a distribution of lattice spacings (elastic strains) introduced by defects is a broadening of the reflection in all directions in reciprocal space. The effect of a distribution of orientations introduced by defects is a broadening of the reflection in the azimuthal directions. As a consequence, when a crystal is deformed and the dislocation density increases, it generally results in a broadening of the reflections which increases with increasing deformation.

3.1.3 Reciprocal space maps

As described above, the broadening of an X-ray reflection is related to the size, the strain distribution, and the orientation distribution of the crystal. Because of this, measurement and analysis of the diffracted intensity can be used to obtain information about the crystal size and defects, particularly the density and organization of dislocations. A map of the intensity in some region of reciprocal space is called a reciprocal space map.

One way to obtain a reciprocal space map is to measure the diffracted intensity in different directions either by use of an area detector or by point-wise sampling with a point detector. This produces a map of the intensity on a surface in reciprocal space. If the sample is then rotated (and with it the reciprocal space coordinate system) and the measurement is

repeated, a different surface in reciprocal space is mapped, and by continuing this process a three-dimensional reciprocal space map is gradually constructed.

Besides depending on the scattering vector, the diffracted intensity also depends on the volume of the crystal that is illuminated by the incoming X-ray beam. The reciprocal space maps presented in this thesis are all obtained from individual grains in a polycrystal, and in this case it is important to keep the grain fully within the X-ray beam when the sample is rotated during acquisition.

Traditional methods for investigation of reciprocal space have measured the projection of the intensity onto the radial direction (obtaining what is called a radial profile) or onto an azimuthal direction (obtaining what is called a rocking curve). A radial profile contains information about the distribution of elastic strains, and a rocking curve contains information about the distribution of orientations in the diffracting volume. The term 'radial profile' is used in this thesis, but in the literature the terms 'radial peak profile', 'peak profile' or 'line profile' are also used.

3.2 Radial profiles

Because a radial profile contains information about the distribution of elastic strains in a crystal, the analysis of radial profiles is an important method for obtaining quantitative information about the density and organization of dislocations and the internal stresses in the crystal. This section briefly describes the most important factors that influence the position, width and asymmetry of a radial profile. For an overview of the analysis of radial profiles the reader is referred to the papers by Ungár (1999), Ungár (2001), and Ungár, Gubicza, Ribarik & Borbély (2001).

3.2.1 The position of radial profiles

A radial profile is defined as the projection of the intensity distribution in reciprocal space onto the radial direction:

$$I_{\mathrm{r}}(q) = \int_{q'=q} I(\boldsymbol{q}')\,\mathrm{d}\tilde{S}', \tag{3.7}$$

where $\mathrm{d}\tilde{S}'$ is a surface element in reciprocal space on a sphere with radius q centered at the origin, and the integral is over a surface in reciprocal space covering the entire azimuthal spread of the reflection. The prime on $\mathrm{d}\tilde{S}'$ indicates that $\boldsymbol{q}'$ is the variable of integration.

The position of a radial profile is related to the radial elastic strain (the elastic strain along the direction parallel to the scattering vector). From equations (3.1) and (3.6) it follows that $q = 2\pi/d_{hkl}$, which shows that the length of the scattering vector is inversely proportional to the lattice plane spacing. A radial elastic strain, ε_{r}, corresponds to a change in the lattice plane spacing from the reference value d_{hkl0} to d_{hkl}, and the radial elastic strain can be expressed as

$$\varepsilon_{\mathrm{r}} = \frac{d_{hkl} - d_{hkl0}}{d_{hkl0}} = -\frac{q - q_0}{q} = \frac{q_0}{q} - 1, \tag{3.8}$$

where q_0 is the q-value corresponding to the reference lattice plane spacing d_{hkl0}.

3.2.2 The width of radial profiles

The width of a radial profile is related to the size of the coherently scattering domains in the sample (regions in which the periodic atomic pattern is not severely disturbed), the distribution of radial elastic strains, and experimental conditions such as beam divergence and beam energy spread. Other factors that may influence the width, such as planar defects in the crystal, are ignored here. The shape of the measured radial profile is the result of a convolution of the profiles representing the effects of size, strain, and instrumental conditions. These effects are discussed below.

The width, Δq, of a radial profile which is broadened only by size effects is given by the equation (Scherrer 1918)

$$\Delta q = \frac{2\pi k}{t}, \tag{3.9}$$

where t is the thickness of the coherently scattering domains (in the direction parallel to the scattering vector), and k is a constant called the Scherrer constant which depends on the chosen measure of width and the crystal shape, but is generally not far from unity (Langford & Wilson 1978). Commonly used measures of width are the full width at half maximum intensity (FWHM) and the integral width (the total area below the profile divided by the maximum intensity).

Warren & Averbach (1950) derived an expression for the Fourier coefficients of a profile which is only broadened by strain effects:

$$A(L) = \exp\left(-\frac{1}{2}q_0^2 L^2 \left\langle \varepsilon_{\boldsymbol{q},L}^2 \right\rangle\right). \tag{3.10}$$

Here q_0 is the mean q-value, and $\langle \varepsilon_{\boldsymbol{q},L}^2 \rangle$ is the (spatially averaged) mean square strain. This expression is exact if the relative atomic displacements are Gauss distributed and a valid approximation if they are very small. From this the profile can be found by the Fourier transformation:

$$I(\delta q) = \int_{-\infty}^{\infty} A(L) \exp\left(iL\delta q\right) \mathrm{d}L, \tag{3.11}$$

where $\delta q = q - q_0$ measures the distance from the mean q-value along the radial direction.

For evaluation of the Fourier coefficients a model of the mean square strain is needed. Warren & Averbach (1950) treated $\langle \varepsilon_{\boldsymbol{q},L}^2 \rangle$ as a constant which leads to a Gauss profile. Krivoglaz & Ryaboshapka (1963) realized that the atomic displacements must be calculated from the displacements caused by dislocations. Assuming randomly distributed straight parallel screw dislocations they found an approximate expression for the mean square strain, which, however, depends on the crystal size. Introducing the concept of a restricted random distribution of dislocations, Wilkens (1970*a*, 1970*b*) later described a model in which the dependence on crystal size was absent. Wilkens' model is described below.

Apart from the explicit dependence on the length of the scattering vector in equation (3.10), the Fourier coefficient, and hence the width of the profile, also depends on the scattering vector through the $\boldsymbol{q}$-dependence of $\langle \varepsilon_{\boldsymbol{q},L}^2 \rangle$. This is called strain anisotropy, and it is quantified by a parameter called the contrast factor, which depends on the elastic constants of the crystal and the relative orientation of the scattering vector and the line vector and the Burgers vector of the dislocations.

To characterize the instrumental contribution to profile broadening, measurements must be performed with a standard sample for which the effects of size broadening and strain

broadening are negligible or known. From such measurements the effects of instrumental broadening can in principle be removed from the measured profiles by deconvolution.

3.2.3 Wilkens' model of radial profiles

Wilkens (1970*a*, 1970*b*) introduced the concept of a restricted random distribution of dislocations: The cross section of a cylindrical crystal is subdivided into a number of sub-areas of equal size, and each of the sub-areas is intersected by the same number of dislocations parallel to the crystal axis and randomly distributed across each sub-area, such that the net Burgers vector of the dislocations intersecting each sub-area is zero, and such that the stress field is screened to zero at the boundary of each sub-area. Based on this model the mean square strain is given by

$$\langle \varepsilon^2_{\boldsymbol{q},L} \rangle = \left(\frac{b}{2\pi}\right)^2 \pi\rho C f\left(\frac{L}{R}\right), \tag{3.12}$$

where b is the length of the Burgers vector, ρ is the dislocation density, C is the contrast factor, and R is a parameter characterizing the cross sectional area of the subregions. The function f is given by

$$f\left(\frac{L}{R}\right) = f^*(\eta), \tag{3.13}$$

where $\eta = \frac{1}{2}\exp\left(-\frac{1}{4}\right)\frac{L}{R}$, and

$$f^*(\eta) = \begin{cases} -\ln(\eta) + \frac{7}{4} - \ln(2) + \frac{512}{90\pi\eta} + \\ \quad \frac{2}{\pi}\left(1 - \frac{1}{4\eta^2}\right)\int_0^\eta \frac{\arcsin(V)}{V}\,\mathrm{d}V - \\ \quad \frac{1}{\pi}\left(\frac{769}{180\eta} + \frac{41\eta}{90} + \frac{2\eta^3}{90}\right)\sqrt{1-\eta^2} - \\ \quad \frac{1}{\pi}\left(\frac{11}{12\eta^2} + \frac{7}{2} + \frac{\eta^2}{3}\right)\arcsin(\eta) + \frac{\eta^2}{6} & \text{for } \eta \le 1 \\ \\ \frac{512}{90\pi\eta} - \left(\frac{11}{24} + \frac{1}{4}\ln(2\eta)\right)\frac{1}{\eta^2} & \text{for } \eta > 1 \end{cases} \tag{3.14}$$

This model results in a symmetric profile, which is called a Wilkens profile in this thesis. Instead of R, the parameter $M = R\sqrt{\rho}$, called the dislocation arrangement parameter, is often used to describe the Wilkens profile. The value of M characterizes the arrangement of the dislocations and the length of the profile tails: A larger value of M corresponds to a weaker screening of the dislocation strain fields (or equivalently a weaker correlation between the dislocations – a more disordered structure) and to shorter profile tails, and a smaller value of M corresponds to a stronger screening of the dislocation strain fields (or equivalently a stronger correlation between the dislocations – a more ordered structure) and to longer profile tails (Ungár et al. 2001). In the literature, the parameters R and M are sometimes defined to be a factor of e^2 larger than the definitions used in this thesis.

The width of a Wilkens profile increases with both ρ and M. For a given value of ρ the width is approximately proportional to $\ln(M)$, and for a given value of M the width is proportional to $\sqrt{\rho}$ (Wilkens 1970*a*). However, if the coordinate δq is normalized with the width, the shape of the profile depends only on M, with smaller values of M corresponding to longer profile tails and larger values of M corresponding to shorter profile tails. Figure 3.2 shows how the profile width increases when the dislocation density is increased and the dislocation arrangement parameter is kept constant, and figure 3.3 shows how the length

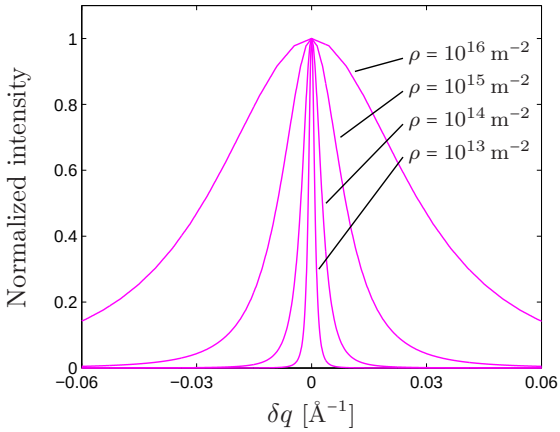

Figure 3.2: Wilkens profiles for $M = 0.2$ and different values of ρ (indicated in the figure). The profiles are normalized to have a maximum value of 1.

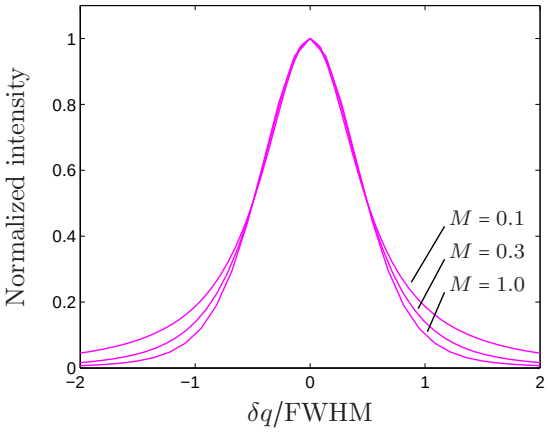

Figure 3.3: Wilkens profiles for $\rho = 10^{14}$ m^{-2} and different values of M (indicated in the figure). The profiles are normalized to have a maximum value and a FWHM of 1.

of the profile tails increases when the dislocation arrangement parameter is decreased. The profiles were calculated using equations (3.10) to (3.14).

3.2.4 The asymmetry of radial profiles and the composite model

The models for the mean square strain mentioned above all give rise to symmetric profiles, but in some cases asymmetric profiles are measured, for instance from samples containing heterogeneous dislocation structures. This was first observed by Ungár and coauthors (Ungár, Mughrabi & Wilkens 1984, Ungár, Mughrabi, Rönnpagel & Wilkens 1984, Mughrabi, Ungár, Kienle & Wilkens 1986), who interpreted the asymmetry in terms of different elastic strains in the subgrains and the walls as described by a composite model introduced by Mughrabi (1979, 1983), called the classical composite model in this thesis.

The model describes the dislocation structure as a composite consisting of a soft and a hard phase (the subgrains and walls, respectively). When the structure is deformed, the model assumes that the subgrains yield easier than the walls, and because of the requirement for compatible deformation intra-granular stresses develop as described in section 2.1.2. In uniaxial tensile deformation, this results in intra-granular stresses parallel to the tensile axis with the result that the stress in the walls is larger than the stress in the subgrains.

Due to these intra-granular stresses, the elastic strain in the subgrains (relative to the mean elastic strain) is compressive along the tensile axis and, because of the Poisson effect, tensile along the perpendicular directions. Similarly, the relative elastic strain in the walls is tensile along the tensile axis and compressive along the perpendicular directions.

In other words, along the tensile axis the subgrains experience a compressive elastic back-strain, and the walls experience a tensile elastic forward-strain. Along the directions perpendicular to the tensile axis, the subgrains experience a tensile elastic back-strain, and the walls experience a compressive elastic forward-strain. The intra-granular stresses and the corresponding elastic strains are illustrated in figure 3.4. In the figure and the discussion above the walls perpendicular to the tensile axis are ignored.

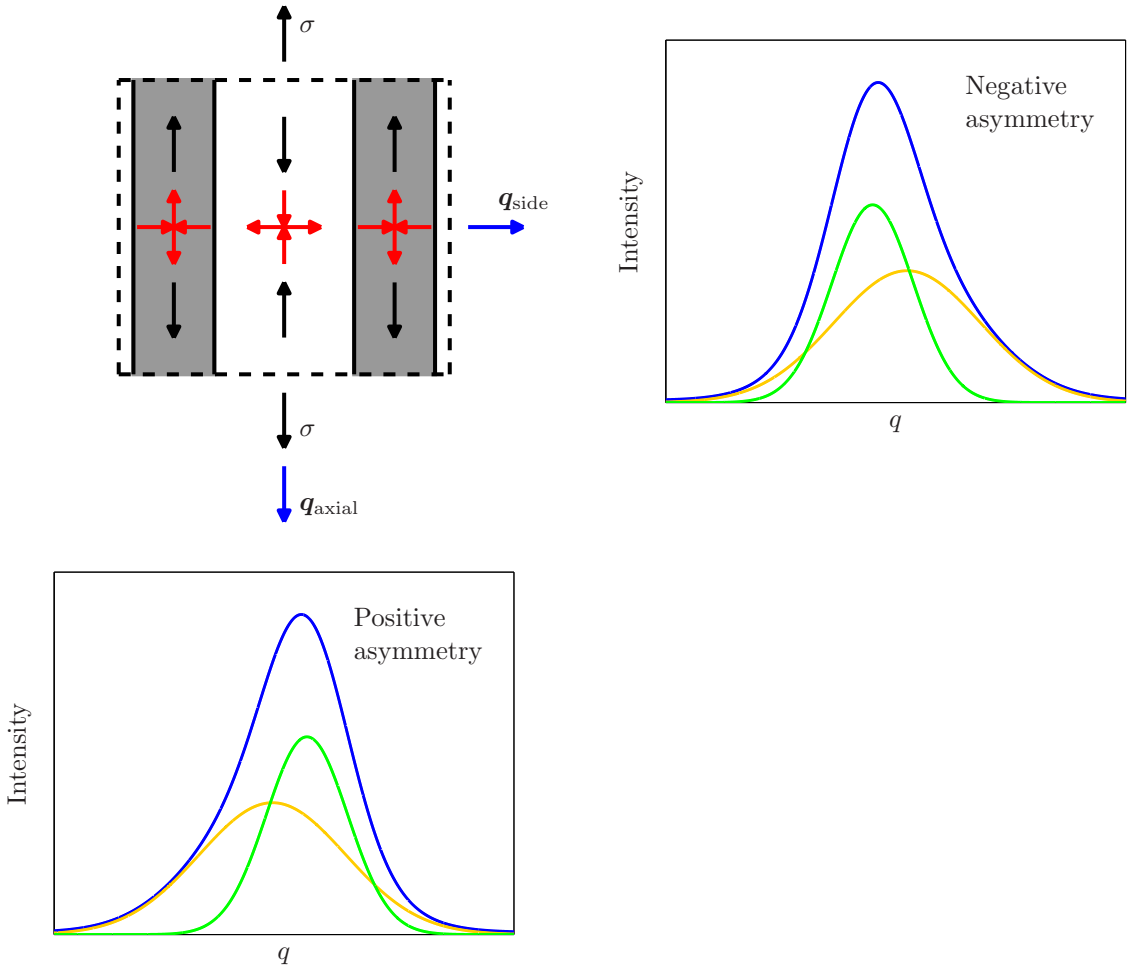

Figure 3.4: Top left: A schematic illustration of the classical composite model. The white region represents a subgrain with a low dislocation density and the grey regions represent walls with a high dislocation density. The black arrows indicate the relative intra-granular stresses and the red arrows indicate the corresponding relative elastic strains. The system is subjected to an external stress in the vertical direction. The blue arrows represent the scattering vector in the axial case and the side case. Bottom left: The radial profiles from the subgrains (green), the walls (yellow), and the total profile (blue) in the axial case, illustrating a positive asymmetry. Top right: The radial profiles from the subgrains (green), the walls (yellow), and the total profile (blue) in the side case, illustrating a negative asymmetry.

The origin of the intra-granular stresses can also be understood in terms of dislocations. When a load is applied to the structure, dislocation glide is first initiated in the subgrains where the dislocation density and therefore the resistance to dislocation motion is low. When the dislocations encounter a dislocation wall, they are stopped because of the high dislocation density. This means that only the subgrains deform plastically at first (the micro-plastic range). As more and more dislocations get stopped at the walls in this manner, the stress in the walls is gradually increased above the average stress, while the stress in the subgrains is decreased. At some point the stress in the walls reaches a level where dislocation glide in (and through) the walls is possible, and the walls start to deform plastically as well.

In the classical composite model the radial profile from the structure is described as the sum of two subprofiles, one from the subgrains and one from the walls. The width of both subprofiles is assumed to be determined by the dislocation content of the two phases of the composite, and because of the higher dislocation density in the walls, the subprofile from the walls is assumed to be wider than the subprofile from the subgrains. The position of the subprofiles is determined by the average elastic strain in the two phases of the composite, and as a result of the different elastic strains in the subgrains and the walls, the position of the two subprofiles are shifted in opposite directions. This relative shift of two subprofiles with different width produces an asymmetry of the total profile, which depends on the orientation of the scattering vector with respect to the tensile axis.

If the sample is oriented with the scattering vector parallel to the tensile axis (this means that the elastic strains parallel to the tensile axis are probed and is called the axial case) the compressive elastic back-strain in the subgrains causes a shift of the narrower subgrain subprofile towards larger q-values, and the tensile elastic forward-strain in the walls causes a shift of the wider wall subprofile towards smaller q-values. The result is an asymmetric profile with a longer tail on the low-q side (called a positive asymmetry).

If the sample is oriented with the scattering vector perpendicular to the tensile axis (this means that the elastic strains perpendicular to the tensile axis are probed and is called the side case) the situation is the opposite: The tensile elastic back-strain in the subgrains causes a shift of the narrower subgrain subprofile towards smaller q-values, and the compressive elastic forward-strain in the walls causes a shift of the wider wall subprofile towards larger q-values. In this case the result is an asymmetric profile with a longer tail on the high-q side (called a negative asymmetry). Figure 3.4 illustrates the asymmetry observed in the axial case and the side case.

In general, the observed asymmetry depends on the relative strain in the subgrains and the walls a long a direction parallel to the scattering vector, and for orientations of the scattering vector between the two extreme cases discussed above the observed asymmetry will be smaller and in some cases zero.

3.3 Two recently-developed techniques

Traditionally X-ray diffraction has been applied to the investigation of dislocation structures by measurement of radial profiles or rocking curves from single crystals or by averaging over many grains in polycrystalline materials. In both cases the diffracting volume contains a large number of subgrains. With developments of new X-ray diffraction techniques it has become possible to obtain information about relatively few and in some cases even individual subgrains. This section presents two recently-developed techniques: One that uses high angular resolution to separate diffraction signals from subgrains based on their orientation differences and one that uses high spatial resolution to measure diffraction from individual subgrains.

3.3.1 High angular resolution three-dimensional X-ray diffraction

Jakobsen et al. (2006) studied the properties of individual subgrains in polycrystalline copper with a technique called high angular resolution three-dimensional X-ray diffraction. They used a 52 keV X-ray beam with high flux, narrow energy spread and low divergence to obtain reciprocal space maps with high angular resolution from individual grains in the bulk of 300 μm thick polycrystalline copper samples that were deformed in tension in situ up to a

strain of 4.2 %. The reciprocal space maps were centered around 400 reflections with the scattering vector nearly parallel to the tensile axis, and they were obtained with an area detector positioned 4 m from the sample by rotating the sample as described in section 3.1.3. The selected grains were smaller than the beam size (which was $14\,\mu\text{m} \times 14\,\mu\text{m}$) and were fully illuminated at all times. The reciprocal space resolution corresponding to one pixel on the detector was reported to be $5 \cdot 10^{-4}$ Å^{-1}.

The observed reciprocal space intensity distributions were composed of individual high-intensity peaks on a background cloud of enhanced intensity (see figure 3.5). The authors interpreted the individual peaks as the diffracted intensity from individual subgrains and the cloud as the diffracted intensity from the dislocation walls. This interpretation was supported by three findings:

- The individual peaks were very sharp (with a FWHM between $1 \cdot 10^{-3}$ Å^{-1} and $3 \cdot 10^{-3}$ Å^{-1}) in all directions in reciprocal space, indicating a very low dislocation density.
- The size of the diffracting volumes calculated from the integrated intensity in the individual peaks was in the range 1 μm to 3 μm in good agreement with TEM measurements of subgrain sizes.
- Most of the individual peaks originated from just one position in the sample.

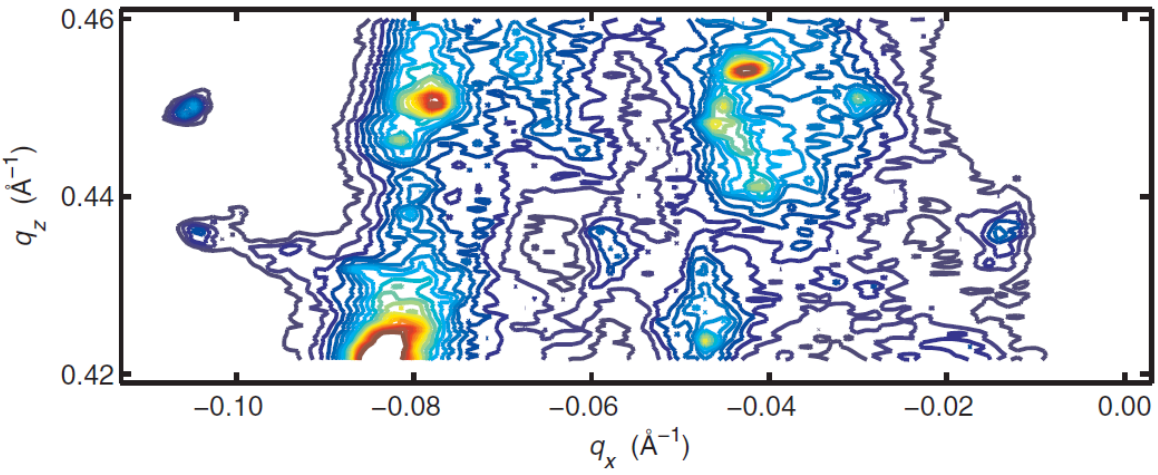

Figure 3.5: A projection onto the azimuthal directions of a reciprocal space map from an individual grain in a sample deformed to a strain of 3.49 % in tension. The structure consisting of individual high-intensity peaks on a background cloud of enhanced intensity is apparent. From Jakobsen et al. (2006).

One sample was continuously deformed from the undeformed state to a strain of 3 %, and reciprocal space maps obtained during the deformation showed that subgrains formed shortly after the onset of plastic deformation. Reciprocal space maps obtained while keeping the strain at 3 % showed no significant changes, indicating that the dislocation structure was not affected by the interruption of the deformation.

For a second sample the strain was increased incrementally from 3 % to 4.2 % in steps of 0.04 %, and a reciprocal space map was obtained at each strain level. The evolution of

the reciprocal space maps (and of the dislocation structure in the investigated grain) as a function of strain showed examples of intermittent dynamics: Appearance and disappearance of individual peaks during deformation and the temporary splitting of a peak into two peaks and their subsequent recombination. No permanent splitting corresponding to a subdivision of a subgrain was observed.

The radial elastic strain in the subgrains was investigated by calculating radial profiles from the individual peaks. The positions of the profile centers were clearly separated, indicating that the subgrains experienced quite different elastic strains.

Using the same technique, Jakobsen, Poulsen, Lienert & Pantleon (2007) investigated the distribution of radial elastic strains in the subgrains in more details. A reciprocal space map was obtained from a fully-illuminated grain in a polycrystalline copper sample deformed to a strain of 2 % in tension, and radial profiles were calculated both for the entire grain and for 14 individual peaks. The profile from the entire grain was asymmetric as expected from the classical composite model. Analysis of the profiles from the individual peaks showed that:

- They were significantly narrower (with a mean FWHM of $2.0 \cdot 10^{-3}$ Å^{-1}) than the profile from the entire grain (with a FWHM of $6.4 \cdot 10^{-3}$ Å^{-1}).

- Their average position was shifted (by $6.0 \cdot 10^{-4}$ Å^{-1}) relative to the mean position of the profile from the entire grain in the direction predicted by the classical composite model (towards larger q-values).

- Their positions were spread around the position of maximum intensity of the radial profile from the entire grain (with a standard deviation of $1.0 \cdot 10^{-3}$ Å^{-1}).

3.3.2 Scanning-monochromatic differential-aperture X-ray microscopy

Levine, Larson, Yang, Kassner, Tischler, Delos-Reyes, Fields & Liu (2006) studied the distribution of strains in individual subgrains in copper single crystals with a technique called scanning-monochromatic differential-aperture X-ray microscopy (Yang, Larson, Ice, Tischler, Budai, Chung & Lowe 2003). They used a highly focused monochromatic X-ray beam (approximately $0.5\,\mu\text{m} \times 0.5\,\mu\text{m}$ in size) for high spatial resolution in the directions perpendicular to the beam. An area detector was used to measure the diffracted intensity. Depth resolution was provided by incrementally translating a platinum wire in steps of $0.5\,\mu$m through the diffracted beam parallel to the sample surface while measuring the change in the diffraction pattern as a function of the wire position. A triangulation-based method was then used to determine the depth in the sample from which the diffracted X-rays originated. To obtain a reciprocal space map from a selected $0.5\,\mu\text{m} \times 0.5\,\mu\text{m} \times 0.5\,\mu\text{m}$ voxel in real space, the wire-scanning was combined with a scanning of the wavelength of the incoming beam. The strain resolution was reported to be 10^{-4}, and the depth limit was reported to be approximately $50\,\mu$m.

Observations on samples deformed to a true strain of approximately 30 % in tension or compression and then unloaded showed that the observed intensity distribution (influenced by variations in the diffracted intensity in both real space and reciprocal space) consisted of localized areas of high intensity superimposed on a smeared-out intensity distribution, similar to the (pure reciprocal space) observations by Jakobsen et al. (2006). The high-intensity areas were interpreted as diffraction from individual subgrains, and the low-intensity smeared-out

contribution as a combination of diffraction from dislocation walls, small subgrains and size broadening.

With the high spatial resolution of the method the authors were able to focus on the high-intensity regions and characterize the diffraction from individual subgrains. They observed that the spatially-integrated radial profile showed the characteristic asymmetry expected for heterogeneous dislocation structures, and that the position of the profiles from the individual subgrains were all shifted towards larger q-values in the sample deformed in tension and towards smaller q-values in the sample deformed in compression. Furthermore, they reported a 'dramatic variation' of the elastic strain from subgrain to subgrain and suggested that a similar variation must exist for the elastic strains in the walls.

In a similar study Levine, Larson, Tischler, Geantil, Kassner, Liu & Stoudt (2008) analyzed the radial profiles from 52 individual subgrains from a copper single crystal deformed in compression to a true strain of 28 % and then unloaded. For all the subgrains the position of the profile was shifted towards smaller q-values. The elastic strain in the subgrains determined from the profiles ranged from $0.3 \cdot 10^{-4}$ to $16 \cdot 10^{-3}$ with a mean value of $5.3 \cdot 10^{-4}$. The width of the profiles (FWHM, corrected for instrumental broadening) ranged from $7.2 \cdot 10^{-4}$ to $2.5 \cdot 10^{-3}$ in units of strain with a mean of $1.58 \cdot 10^{-3}$.

3.3.3 Modifications to the classical composite model

In the classical composite model, the subprofile caused by diffraction from the subgrains is broadened by the dislocation density in the subgrains. Haasen (1993) and Argon & Haasen (1993) have pointed out that TEM investigations have not revealed the required dislocation density in the subgrains. They note that the dislocation density in the subgrains, when measured by TEM, is many orders of magnitude less than the dislocation density in the walls. From the width of the radial profiles from the individual subgrains, Jakobsen et al. (2007) estimated that the maximum dislocation density in the subgrains was $1.2 \cdot 10^{13}\,\mathrm{m}^{-2}$, which suggests that the dislocation density in the subgrains indeed is very low as TEM observations indicate.

The small width and the significant spread in the position of the radial profiles from the individual subgrains have lead Pantleon, Wejdemann, Jakobsen, Lienert & Poulsen (2010) to propose a modified composite model in which the dislocation density in the subgrains is lower than suggested by the classical model, and in which the distribution of strain in the subgrains contributes significantly to the shape and width of the radial profile from the entire grain.

In the modified composite model the subgrains are assumed to be virtually dislocation-free, and the radial profile from each subgrain is consequently very narrow. As in the classical composite model the subgrains on average experience an elastic back-strain, but variations in the strain between different subgrains means that the narrow profiles are shifted relative to each other. The subprofile from the subgrains is the sum of these narrow profiles, and its width is predominantly determined by the spread in the position of the profiles from the individual subgrains and not by the dislocation density in the subgrains. The profiles from the individual subgrains, the walls, and the entire grain as described by the modified composite model are illustrated in figure 3.6, which should be compared with figure 3.4.

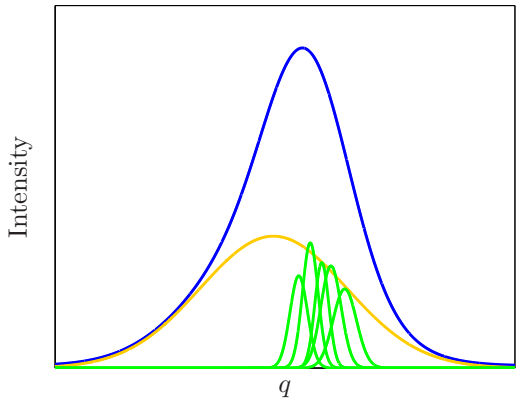

Figure 3.6: A schematic illustration of the radial subprofiles as described by the modified composite model. The green profiles are from individual subgrains, the yellow profile is from the walls, and the blue profile is from the entire grain.

Chapter 4

Samples: Preparation and characterization

To study the effects of a change in loading conditions on dislocation structures, copper samples were prepared for TEM investigations, for characterization of the mechanical properties, and for in situ tensile deformation in X-ray diffraction experiments. This chapter describes how the samples were prepared and characterized by electron backscatter diffraction, TEM, and mechanical tests, all carried out at Risø DTU.

4.1 Preparation of samples

As described in section 2.3, a change in strain path or temperature during deformation may result in changes in the mechanical properties and in the dislocation structure. To study such changes and the processes involved, copper samples were prepared with a dislocation structure produced by uniaxial tensile deformation. This initial deformation will be called the pre-deformation, and its purpose was to produce a dislocation structure, corresponding to one particular set of loading conditions, which might become unstable during continued deformation under changed loading conditions.

Samples were prepared for TEM investigations (described in section 4.2), mechanical characterization (described in section 4.3), and for X-ray diffraction experiments (described in chapter 5). The samples were given names starting with a letter indicating the use of the sample: 't' for the samples studied with TEM, 'm' for the samples used for mechanical characterization, and 'x' for the samples used for X-ray diffraction experiments. The properties of the samples are summarized in table A.1 in appendix A. As explained in the appendix (and in section 5.3) the 'x'-samples have been grouped into eight different groups, and in the thesis different colors will be used when writing these sample names (and when showing results in figures) to make it easier for the reader to distinguish between the different groups and identify them in the figures.

4.1.1 The sample material

The samples were prepared from oxygen-free high conductivity copper with a purity of at least 99.99 %. The material was originally cold rolled from the as-received thickness of 40 mm to 2.2 mm and stored at -18 °C for several years. Following this, a piece of the material was

annealed in vacuum at a temperature of 550 °C for two hours and cold rolled to a sheet with a thickness of approximately 0.32 mm by nine rolling passes. The rolling direction referred to below is the direction of rolling in this step of the preparation.

A number of pieces were then cut from the sheet (the largest with dimensions of 300 mm × 50 mm × 0.32 mm and the smallest with dimensions of 48 mm × 35 mm × 0.32 mm) and annealed in vacuum at a temperature of 450 °C for two hours.

4.1.2 Characterization by electron backscatter diffraction

To characterize the microstructure of the samples electron backscatter diffraction was used. This is a technique used to obtain information about the shape and size of the grains and the texture of the sample by using the electron beam in a scanning electron microscope to measure the crystallographic orientation at a number of points arranged in a regular grid on the sample surface. To obtain a reliable result the sample surface must be very smooth, which was ensured by first polishing it mechanically and electrochemically. Figure 4.1 shows a map of the crystallographic orientation obtained from a piece of the material after pre-deformation to a strain of 5 %.

The characterization showed that the material was fully recrystallized with a mean grain size of approximately 20 μm and a texture close to random. This was the case for all samples except xe1, xe2, and xe3 which were prepared separately from the other samples and had a relatively strong cube texture (a texture where a large proportion of the grains are oriented with the ⟨100⟩ directions parallel to the rolling direction and the direction normal to the sheet). Figure 4.1 also shows twins in a significant number of the grains.

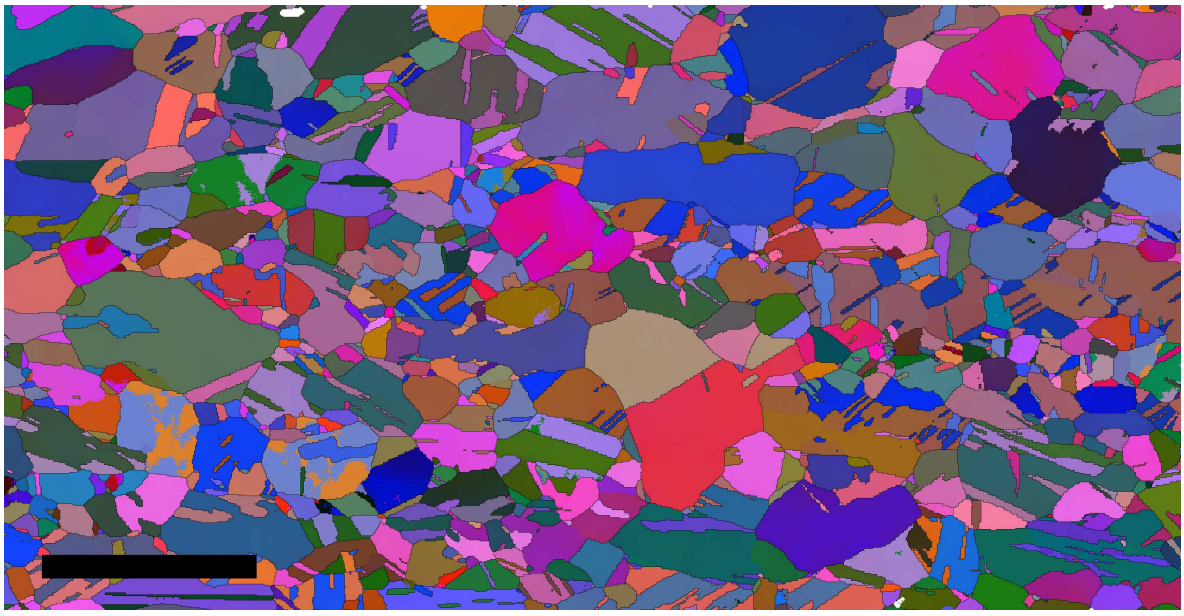

Figure 4.1: A map of the crystallographic orientation from a cross section of a piece of material after pre-deformation to a strain of 5 %. Black lines show grain boundaries with a misorientation angle of at least 10 °. The map covers an area of 550 μm × 290 μm. The horizontal direction is parallel to the rolling direction and the vertical direction is across almost the entire thickness of the sample. The length of the black scale bar in the lower left corner corresponds to 100 μm.

4.1.3 Pre-deformation and cutting

Most of the pieces of the recrystallized material were pre-deformed in uniaxial tension to a plastic strain of 5 %. The deformation took place at room temperature, and the pre-deformation axis was parallel to the rolling direction. ψ_1 is used to denote the angle between the pre-deformation axis and the rolling direction, so for these samples $\psi_1 = 0\,°$.

Samples designed for further uniaxial tensile deformation were then spark cut from the pre-deformed material in two different shapes: Dog-bone shaped samples with a gauge length of 8 mm and a gauge width of 3 mm for the X-ray diffraction experiments, and rectangular samples with a length of 48 mm and a width of 8 mm for the mechanical tests. The sample shapes are shown in figure 4.2.

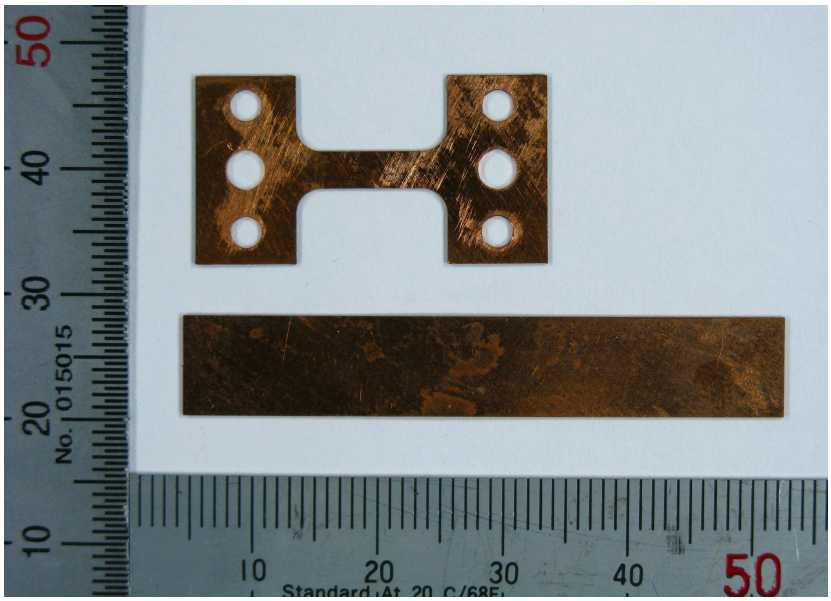

Figure 4.2: A picture of a dog-bone shaped sample used in the X-ray diffraction experiments and a rectangular sample used for the mechanical tests.

For most of the samples the second deformation axis was different from the pre-deformation axis, and these samples were used to study the effects of a strain path change. ψ_2 is used to denote the angle between the second deformation axis and the rolling direction. Samples were prepared with ψ_2-values of 0 °, 35 °, 55 °, and 90 ° corresponding to values of the strain path change parameter, α, of 1, $^1/_2$, 0, and $-^1/_2$, respectively (calculated from equation (2.5)). The samples for which $\psi_2 = 0\,°$ served as reference samples. A sketch of the orientation of the dog-bone shaped samples used to study the effects of a strain path change is shown in figure 4.3.

A number of rectangular reference samples were also spark cut directly from the recrystallized material. These samples were only subjected to a single tensile deformation. For these samples ψ_1 is used to denote the angle between the deformation axis and the rolling direction. Samples were prepared with ψ_1-values of 0 °, 35 °, 55 °, and 90 °.

To study the effects of a change in temperature a few dog-bone shaped samples were spark cut directly from the recrystallized material and pre-deformed in tension to a plastic strain of 7 % while submerged in liquid nitrogen with a temperature of -196 °C. For these

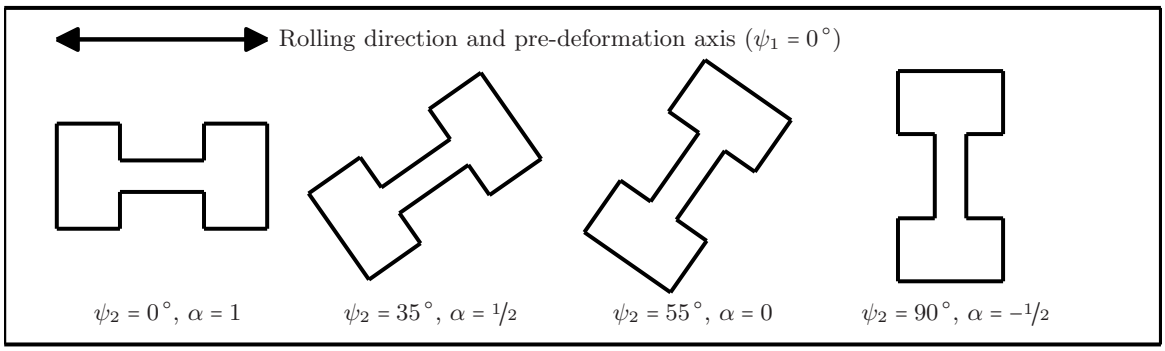

Figure 4.3: The orientation of the dog-bone shaped samples with respect to the pre-deformation axis. The samples were pre-deformed to a strain of 5 % in tension parallel to the rolling direction. The value of ψ_2 and α are indicated for each sample. For all the samples $\psi_1 = 0\,^\circ$.

samples the pre-deformation axis was parallel to the rolling direction ($\psi_1 = 0\,^\circ$). After the pre-deformation, the samples were placed in liquid nitrogen as quickly as possible for storage until the second tensile deformation along the same axis ($\psi_2 = 0\,^\circ$). One of the samples was shipped to the APS synchrotron in a dry shipper, keeping it at cryogenic temperatures.

4.2 TEM

To investigate the morphology of the dislocation structure in the samples TEM was used. This was not a comprehensive study, and relatively few grains were investigated, partly because of difficulties with preparation of thin foils of adequate quality.

4.2.1 TEM and dislocations

TEM produces high-resolution images from thin foils with the use of electromagnetic lenses and a focused electron beam which penetrates and interacts with the sample. Because of the distortion of the crystal near a dislocation, the scattering of electrons is affected by the presence of dislocations, and this produces a contrast in the image and allows dislocations to be observed with TEM.

For observation of dislocation structures, however, the technique has some disadvantages related to the fact that thin foils must be used. Preparation of thin foils may lead to stress relaxation and changes in the dislocation structure from that in a bulk sample. Furthermore, in situ TEM investigations of dislocation structures in thin foils are very difficult, and the observations may not be representative of bulk behavior because of image forces from the free surfaces.

4.2.2 The morphology of the dislocation structures

Thin foils were prepared from a piece of the recrystallized material deformed in uniaxial tension to a strain of 5 %, from one sample deformed along the same axis to an additional strain of 4 %, and from four samples which were deformed along a perpendicular axis to an additional strain of 1 %, 2 %, 5 %, and 10 %, respectively. For many of the foils it was only possible to observe the dislocation structure in very few and small regions because of problems

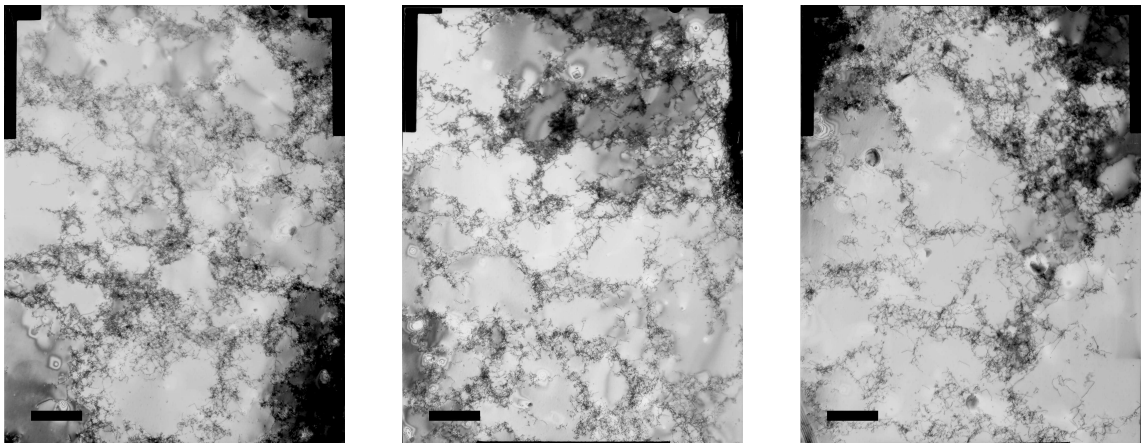

Figure 4.4: Dislocation structures in two grains from a piece of the recrystallized material deformed in uniaxial tension to a strain of 5 %. The length of the scale bar corresponds to 1 μm.

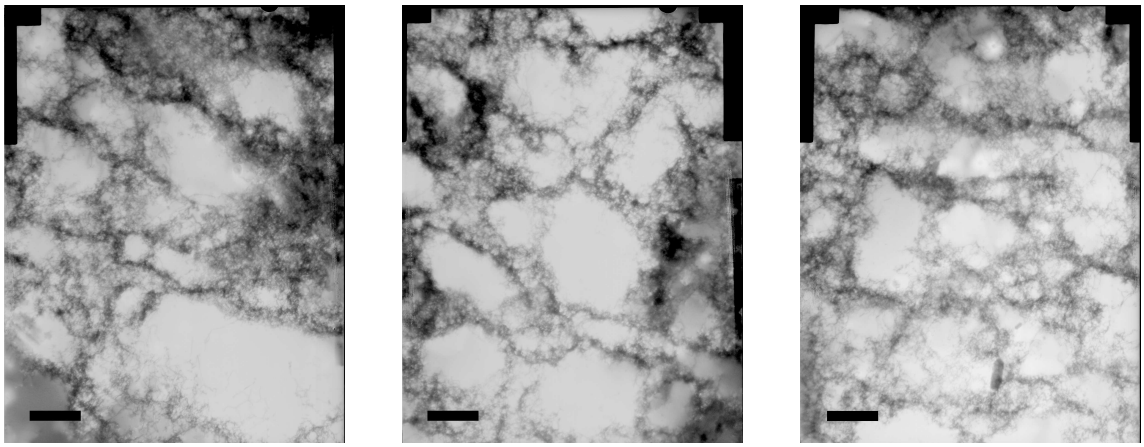

Figure 4.5: Dislocation structures in one grain from sample t1 deformed to a strain of 5 % + 4 % with $\alpha = 1$. The length of the scale bar corresponds to 1 μm.

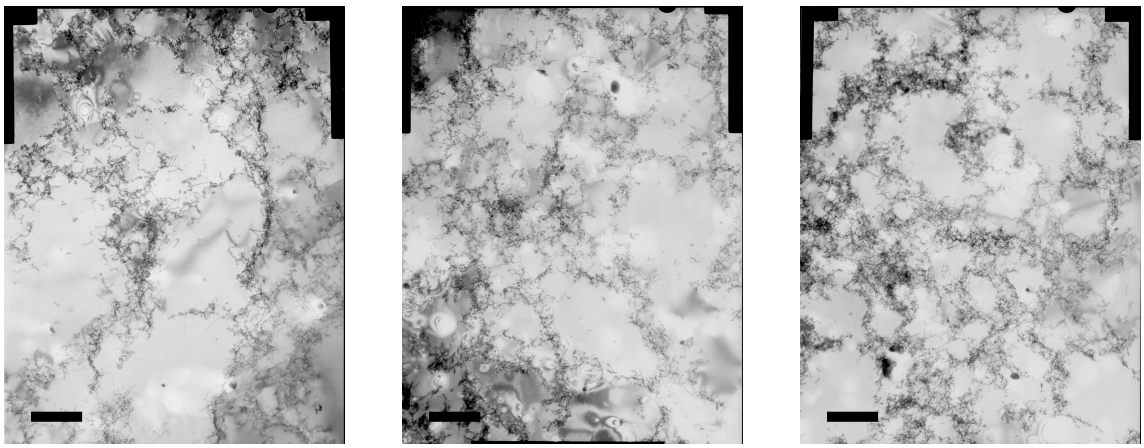

Figure 4.6: Dislocation structures in two grains from sample t2 deformed to a strain of 5 % + 1 % with $\alpha = -0.5$. The length of the scale bar corresponds to 1 μm.

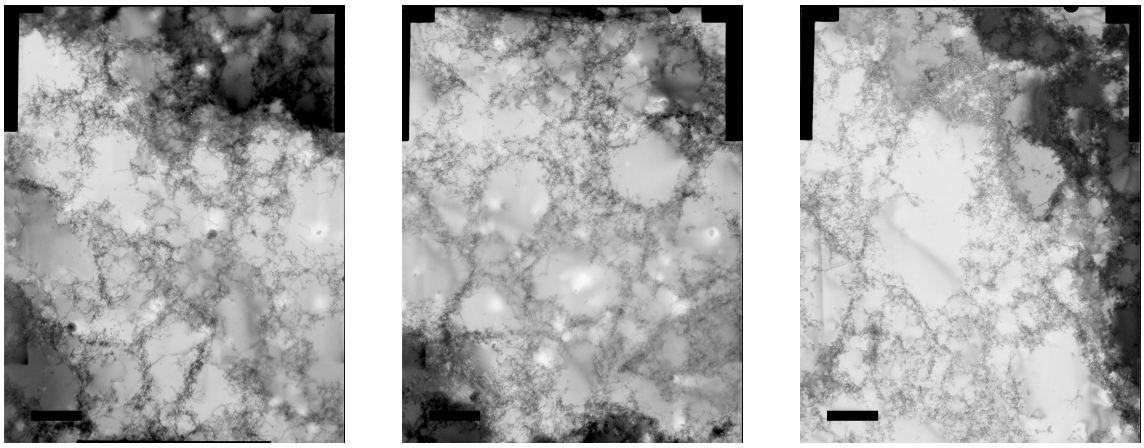

Figure 4.7: Dislocation structures in two grains from sample t3 deformed to a strain of 5 % + 2 % with $\alpha = -0.5$. The length of the scale bar corresponds to 1 μm.

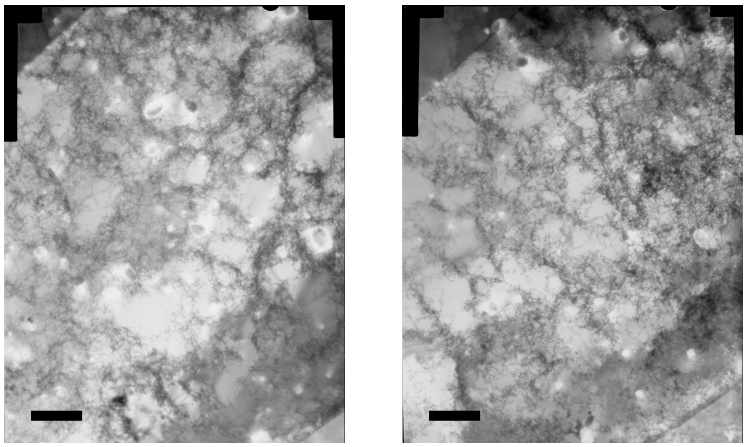

Figure 4.8: Dislocation structures in one grain from sample t4 deformed to a strain of 5 % + 5 % with $\alpha = -0.5$. The length of the scale bar corresponds to 1 μm.

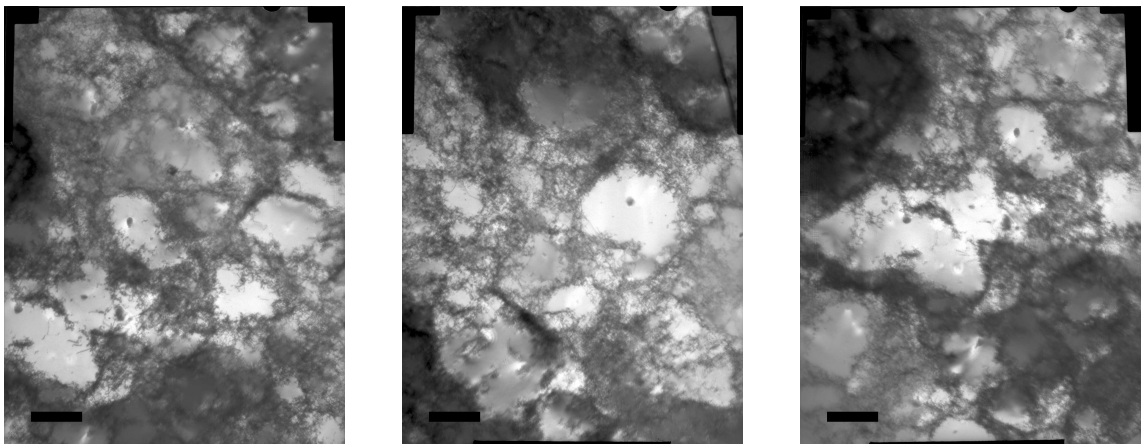

Figure 4.9: Dislocation structures in one grain from sample t5 deformed to a strain of 5 % + 10 % with $\alpha = -0.5$. The length of the scale bar corresponds to 1 μm.

with the thin foil quality. The TEM images are shown in figures 4.4 to 4.9. The scale is the same in all the images.

For all the observations, the plane of the thin foil contains both the original rolling direction and the direction(s) of tensile deformation. The tensile axes and the viewing axis were all within 15 ° of a [100] direction. A JEOL 2000FX microscope operating at 200 kV was used for the investigations. The structures were observed under multi-beam diffraction conditions to reveal most of the individual dislocations and dislocation boundaries.

Figures 4.4 and 4.5 show the dislocation structure produced by uniaxial tensile deformation. An equiaxed dislocation cell structure is observed for the grains, as expected for grains deformed with the tensile direction close to a [100] direction (see section 2.2.2). When the strain is increased from 5 % to 9 %, the dislocation density in the walls increases, and the walls appear sharper and more well defined. For each of the observed grains the subgrain size varies significantly.

Figures 4.6 to 4.9 show the effect of further tensile deformation along a perpendicular axis after pre-deformation to a strain of 5 %. No qualitative difference is observed in the morphology of the structure after a stain of 1 % or 2 % along the new axis. After a strain of 5 % along the new axis, the walls appear thicker and less well defined, and the structure looks more homogeneous. This is also the case after a strain of 10 % along the new axis, but in this case the dislocation density appears to be higher. These observations suggest that the morphology of the dislocation structure becomes different from that in grains deformed in uniaxial tension after an additional strain of more than 2 % and less than 5 % along the second tensile axis, and that the strain path change affects the morphology in a strain interval with a length of at least 5 %. These results are consistent with the observations reported by Schmitt et al. (1991) (presented in section 2.3.3).

4.3 Mechanical characterization

To characterize the mechanical effects of a strain path change, a number of the pre-deformed samples and the undeformed reference samples were deformed in tension. A servo-hydraulic testing machine with a 1 kN load cell was used for the tests. The strain was measured with a video extensometer, using strips of white tape placed on the gauge section of the samples as markers. The setup is shown in figure 4.10. For all the deformations the strain rate was approximately 10^{-4} s^{-1}.

4.3.1 Mechanical effects of a strain path change

The values of the load, F, and the strain, ε, recorded during the tests were converted to values of true stress, $\sigma_t = F/A = (1+\varepsilon) \cdot F/A_0$, and true strain, $\varepsilon_t = \ln(1+\varepsilon)$. Here A is the instantaneous cross sectional area of the gauge section, and A_0 is the cross sectional area before the test (after the pre-deformation for the pre-deformed samples). The value of A_0 was determined for each sample from measurements of the width and the thickness at different points with a digital caliper. From these repeated measurements it is estimated that the uncertainty in the determination of the cross sectional area is approximately ±2 %.

Figure 4.11 shows the true stress-true strain curves for the reference samples cut along different directions in the rolled sheet and deformed without a change in strain path. The difference between the curves is most likely an effect of the different orientation of the samples with respect to the rolling direction and the texture of the material.

Figure 4.10: A picture of the setup used for the mechanical tests. The sample can be seen between the grips on the left, and the video extensometer can be seen on the right.

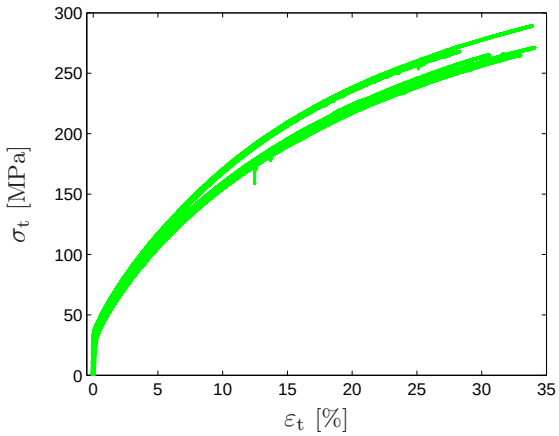

Figure 4.11: True stress-true strain curves for the reference samples cut along different directions in the rolled sheet and deformed without a change in strain path (samples m1, m2, m5, m6, m10, m11, m15, and m16).

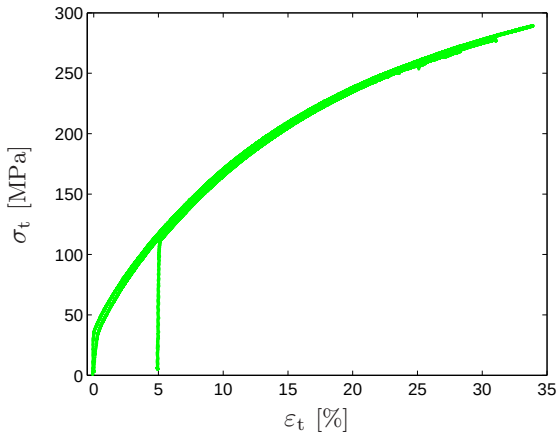

Figure 4.12: True stress-true strain curves for samples m1, m2, m3, and m4 deformed in tension along an axis parallel to the rolling direction without a change in strain path. Samples m3 and m4 were pre-deformed along the same axis to a strain of 5 %.

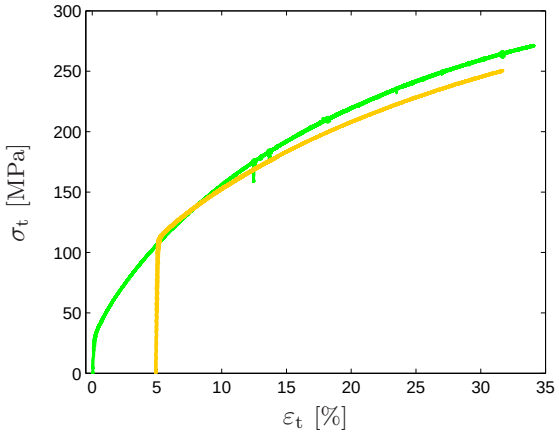

Figure 4.13: True stress-true strain curves for samples m5, m6, m7, m8, and m9 deformed in tension along an axis making an angle of 35 ° with the rolling direction. The yellow curves correspond to the samples subjected to a strain path change with $\alpha = 1/2$. The green curves correspond to samples deformed without a change in strain path.

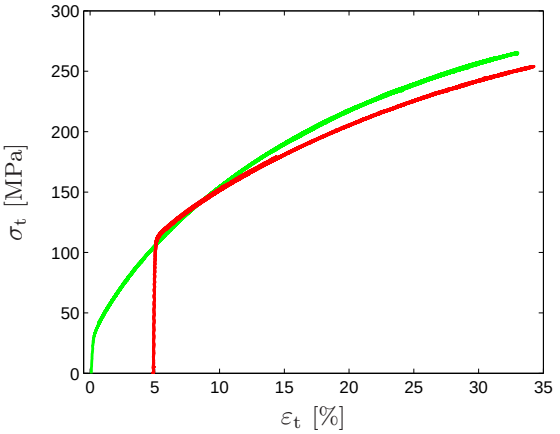

Figure 4.14: True stress-true strain curves for samples m10, m11, m12, m13, and m14 deformed in tension along an axis making an angle of 55 ° with the rolling direction. The red curves correspond to the samples subjected to a strain path change with $\alpha = 0$. The green curves correspond to samples deformed without a change in strain path.

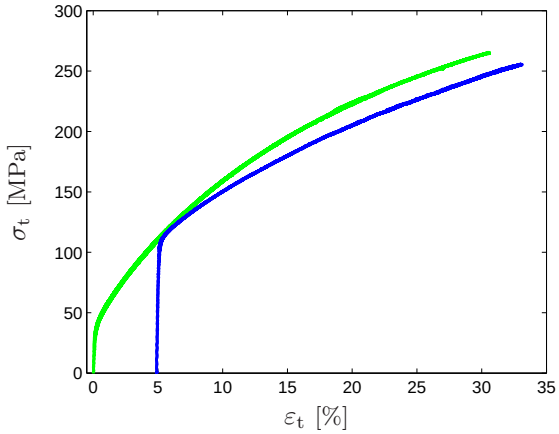

Figure 4.15: True stress-true strain curves for samples m15, m16, m17, and m18 deformed in tension along an axis making an angle of 90 ° with the rolling direction. The blue curves correspond to samples subjected to a strain path change with $\alpha = -1/2$. The green curves correspond to samples deformed without a change in strain path.

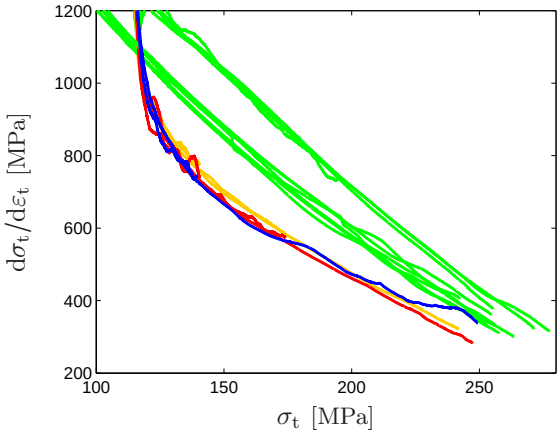

Figure 4.16: The work hardening rate for samples m1 to m18 as a function of the true stress.

True stress-true strain curves arranged according to the direction of the last deformation are shown in figures 4.12 to 4.15. In each of the figures the pre-deformed samples are compared to reference samples, such that the second tensile axis for the pre-deformed samples is parallel to the tensile axis for the reference samples (which means that ψ_2 for the pre-deformed samples is equal to ψ_1 for the reference samples). This removes trivial effects of the texture, and should ensure that any observed difference between the samples is caused by the strain path change.

When the curves are arranged in this way, each figure contains the curves corresponding to one particular value of the strain path change parameter α ($\alpha = 1$ in figure 4.12, $\alpha = 1/2$ in figure 4.13, $\alpha = 0$ in figure 4.14, and $\alpha = -1/2$ in figure 4.15). For each pre-deformed sample the curve has been shifted to start at a strain level equal to the true plastic strain at the end of the pre-deformation. More than one sample of each type was tested, and the corresponding true stress-true strain curves coincide, showing that the results are reproducible. This is also shown by the fact that the curves for the reference samples and for the pre-deformed samples coincide in figure 4.12.

The figures show that for $\alpha = 1/2$ and $\alpha = 0$ the yield stress is increased compared to the corresponding reference curves. The increase appears to be larger for $\alpha = 0$. For $\alpha = -1/2$, the yield stress is unchanged compared to the reference curve. For $\alpha = 1/2$, $\alpha = 0$, and $\alpha = -1/2$ the strain path change is followed by a reduced work hardening rate compared to the corresponding reference curves.

For a few of the samples values of load and strain were recorded during unloading, and from these data the value of Young's modulus was estimated from a linear approximation. The results were in the range 100 GPa to 110 GPa. The uncertainty was estimated to be at least ±10 GPa. These values are reasonable for polycrystalline copper with an almost random texture. Young's modulus is usually reported to be around 130 GPa for polycrystalline copper with a random texture and smaller for crystals with a cube texture (Noyan & Cohen 1987, Hosford 1993).

The work hardening rate was calculated from the curves in figures 4.12 to 4.15 by locally approximating each curve with a straight line around each data point. The results are shown in figure 4.16 as a function of the true stress. For the reference samples the work hardening rate decreases approximately linearly and there is a difference in the level of the work hardening rate between some of the samples, which is most likely an effect of the combination of the texture of the material and the different orientation of the samples. For the samples subjected to a strain path change the method did not produce reliable estimates of the work hardening rate for stresses below 120 MPa. Above this level, the work hardening rate is lower than for the reference samples. It also decreases approximately linearly, but the decrease is slower, and the difference in work hardening rate between the two sets of samples decreases with increasing true stress. If the linear behavior in the figure is extrapolated to higher stresses, the different curves would reach the same work hardening rate at a stress around 300 MPa. This indicates that the strain path change leads to a transient phase with a reduced work hardening rate. The figure shows no significant difference between the three samples subjected to a strain path change.

As described in section 2.3.2, the increase in yield stress observed for $\alpha = 1/2$ and $\alpha = 0$ can be interpreted as a result of interactions between dislocations created on new slip systems and the dislocations produced during pre-deformation. The reason that the yield stress is not increased for $\alpha = -1/2$ is that in this case anisotropic internal stresses make it easier for dislocations to penetrate the old structure, offsetting the effect. In all three cases interactions between the new dislocations and the old structure leads to an increase in the rate of

annihilation reactions which can explain the observed reduction in the work hardening rate.

The observed change in yield stress and the transient phase with a reduced work hardening rate are consistent with the results reported by Schmitt et al. (1991), who, however, also observed an effect of α on the decrease in the work hardening rate which is not seen in figure 4.16.

4.3.2 Mechanical effects of a change in temperature

As mentioned in section 4.1.3 a few dog-bone shaped samples were pre-deformed at a temperature of -196 °C. For this purpose the sample and the grips were surrounded by a tube filled with liquid nitrogen, and strain measurements with the video extensometer were not possible. After the pre-deformation the samples were stored in liquid nitrogen.

Four of the samples were used to investigate the mechanical effects of a change in temperature. After storage in liquid nitrogen, they were kept at room temperature over night and deformed in tension along the pre-deformation axis at room temperature. However, due to problems with the video extensometer the strain measurements were useless. An attempt was made to estimate the strain based on the motion of the grips, but the results were not believable.

One of the samples pre-deformed at a low temperature was shipped to the APS synchrotron. For this sample the pre-deformation strain was estimated from a measurement of the sample length after the pre-deformation. The sample originally had a length of 12 mm, and after the pre-deformation the length was 12.75 mm. The elongation of 0.75 mm was then divided by the effective gauge length of 11 mm to get an estimate of the strain of approximately 7 %. The reason for using an effective gauge length of 11 mm is that the sample also deforms outside the 8 mm long gauge length. The value of 11 mm was determined based on measurements of the elongation of other samples for which the strain had been measured with a strain gauge.

Chapter 5

X-ray diffraction experiments: Technique and procedure

The dog-bone shaped samples (see section 4.1.3) were brought to the APS synchrotron for investigation with X-ray diffraction at beamline 1-ID-XOR. The samples were investigated with a technique, briefly described in section 3.3.1, with which it is it possible to obtain high-resolution reciprocal space maps from individual bulk grains while deforming the samples in tension. This chapter first gives a detailed description of the experimental technique as it was used in the study presented in this thesis and of the procedure for a typical experiment. This is followed by an overview of the grains investigated during the experiments and a presentation of an experiment addressing the reproducibility of the results.

5.1 The experimental technique

This section contains a description of the setup used in the experiments and the procedure for acquiring reciprocal space maps followed by an estimate of the experimental resolution.

5.1.1 The setup

The experimental setup included an X-ray optical system, which consisted of a bent double-Laue pre-monochromator, a set of collimating compound refractive lenses, a four-reflection flat-crystal high-resolution monochromator, and a set of saw-tooth lenses for vertical focusing (Shastri, Fezzaa, Mashayekhi, Lee, Fernandez & Lee 2002, Shastri 2004, Shastri, Almer, Ribbing & Cederström 2007). A sketch of the X-ray optical system is shown in figure 5.1. The purpose of the focusing was to increase the flux at the sample and reduce the acquisition time required to get an acceptable signal-to-noise ratio. The resulting beam was highly monochromatic with a relative energy spread of $7 \cdot 10^{-5}$. The beam energy was 52 keV, which corresponds to a penetration depth of approximately 500 μm in copper.

To control the size of the beam hitting the sample a set of slits with a horizontal and vertical opening of 30 μm was placed approximately 19 m from the focusing lenses and 20 cm in front of the sample. In the horizontal direction the beam was much wider than the slit opening, so the horizontal beam profile behind the slits was approximately box-shaped. In the vertical direction the beam was narrower due to the focusing, so the slits only cut the tails of the beam, and the vertical beam profile behind the slits was more bell-shaped. The

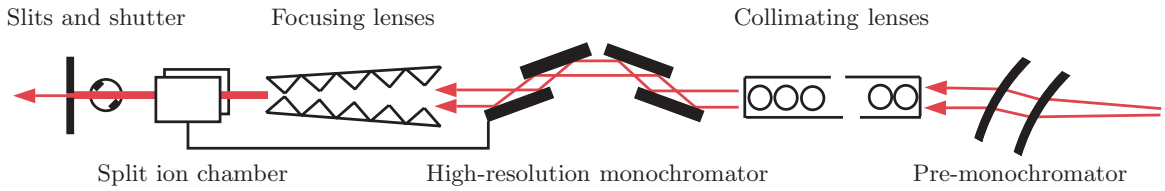

Figure 5.1: A sketch of the X-ray optical system. The X-ray beam passed through a pre-monochromator, a set of collimating lenses, and a high-resolution monochromator before it was focused vertically and cut to its final size by horizontal and vertical slits. A split ion chamber measured the vertical beam position and was connected to the high-resolution monochromator with a feedback loop. Modified from Jakobsen et al. (2006).

horizontal beam divergence was approximately 11 μrad, and the vertical beam divergence was approximately 17 μrad. The slits were used to reduce the beam size to ensure that only a small volume of the sample was illuminated. This minimized the amount of overlap between reflections from different grains and made it possible to investigate reflections from individual grains.

To monitor the vertical position of the beam a split ion chamber was placed in front of the slits on the same optical table. A feedback loop connected the split ion chamber to the high-resolution monochromator and adjusted the vertical beam position continuously during acquisition to eliminate any vertical drift of the beam. A fast shutter was placed between the split ion chamber and the slits to accurately control the timing of the illumination.

The sample chosen for investigation was fitted with a resistive strain gauge glued onto the gauge area and mounted in a position-controlled, screw-driven load frame, allowing the sample to be deformed in tension in situ while measuring the strain and the applied load. The sample was mounted for investigation in transmission. The load frame was placed on three perpendicular translation stages and mounted in a three-axis Euler cradle (see figure 5.2). The Euler cradle was mounted on the same optical table as the slits and the split ion chamber in order to eliminate any drift of the beam position in the sample, and its center of rotation was centered with respect to the beam. A beam stop with a Si PIN diode was placed behind the sample to measure the transmitted intensity.

Two area detectors were included in the setup, both oriented with the detector plane vertical. One was placed near the sample (approximately 680 mm away) and was used to find suitable grains. This was a GE Revolution 41RT with 2048×2048 pixels and a pixel size of 200 μm. It was positioned to cover the entire 400 Debye-Scherrer ring for copper. The other detector was placed far from the sample (approximately 3650 mm away) and was used to obtain high resolution reciprocal space maps. It was placed at a height corresponding to the reflection of interest. This was a Mar CCD165 with 2048×2048 pixels, a pixel size of 79 μm and a point spread function width (FWHM) of 100 μm. The large distance from the sample to the detector in combination with the low energy spread and the low beam divergence results in a high angular resolution (see section 5.1.5). The near detector was mounted on a horizontal translation stage, so it could be moved out of the beam path when the far detector was used. The experimental hutch is shown in figure 5.3. The values of the most relevant experimental parameters are summarized in table 5.1.

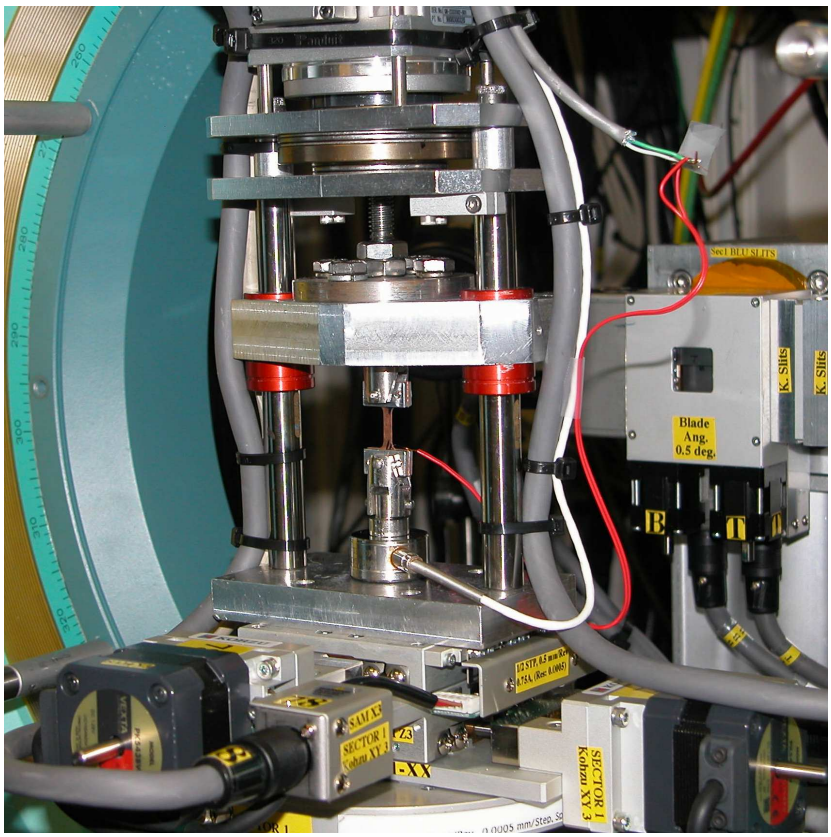

Figure 5.2: A picture of the sample mounted in the load frame on top of the horizontal translation stages. The slits can be seen in the right part of the picture.

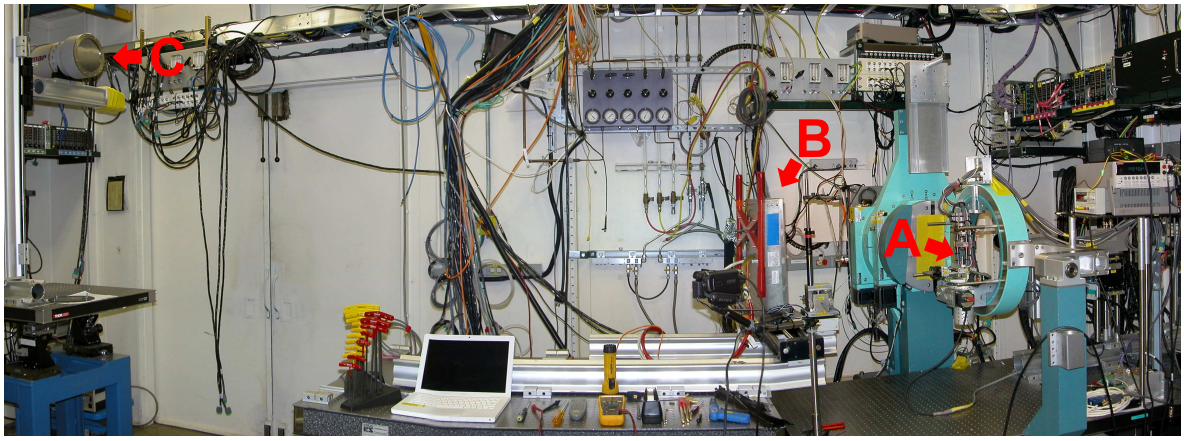

Figure 5.3: A picture of the experimental hutch including the sample (A) centered in the Euler cradle, the near detector (B) used to find suitable grains, and the far detector (C) used to obtain high resolution reciprocal space maps. The X-ray beam entered from the right.

Table 5.1: Values of the most relevant experimental parameters.

Parameter	Value
Beam energy, E	52 keV
Relative beam energy spread, $\Delta E/E$	$7 \cdot 10^{-5}$
Horizontal beam size (defined by slits)	30 μm
Vertical beam size (FWHM, defined by focusing)	$\sim$ 25 μm
Horizontal beam divergence, d_h	11 μrad
Vertical beam divergence, d_v	17 μrad
Scattering angle for the 222 reflection from copper, 2θ	13.12 °
Scattering angle for the 400 reflection from copper, 2θ	15.16 °
Horizontal pixel size for far detector	79 μm
Vertical pixel size for far detector	79 μm
Horizontal point spread function width for far detector, Δx_psf	100 μm
Vertical point spread function width for far detector, Δy_psf	100 μm
Horizontal distance from sample to far detector, z_det	3650 mm
ω rocking interval, $\Delta\omega$	0.005 ° to 0.015 °

5.1.2 Coordinate systems

In this thesis, the position of the sample, the detectors, and the beam are described in a Cartesian coordinate system fixed with respect to the laboratory. The x-axis is horizontal and positive to the left when looking along the beam. The y-axis is vertical and positive upwards. The z-axis is parallel to the beam and positive in the direction of the beam (see figure 5.4). The origin of the laboratory coordinate system coincides with the center of rotation of the Euler cradle.

The Euler cradle had three orthogonal rotation axes. Angular coordinates ω, χ, and ϕ are used to describe the rotation around the three axes. ω measures the rotation (in a left-handed sense) around the outer rotation axis, χ measures the rotation (in a right-handed sense) around the middle rotation axis, and ϕ measures the rotation (in a right-handed sense) around the inner rotation axis. When ω, χ, and ϕ are all zero, the ω-axis is parallel to the x-axis, the χ-axis is parallel to the z-axis, and the ϕ-axis is parallel to the y-axis (see figure 5.4). Because it is the outer rotation axis, the ω-axis is fixed with respect to the laboratory and is always parallel to the x-axis, but the orientation of the χ- and ϕ-axes change when ω and χ are changed. The ϕ-axis is always parallel to the in situ deformation axis.

The position of a pixel on the far detector can be described by its coordinates in the laboratory system or by the direction to the center of the pixel from the origin of the laboratory system. In the latter case, the angular coordinates η and 2θ are used (see figure 5.4). They are related to the laboratory coordinates of the pixel by

$$\eta = \arctan\left(\frac{-x}{y}\right), \tag{5.1}$$

and

$$2\theta = \arctan\left(\frac{\sqrt{x^2 + y^2}}{z_{\text{det}}}\right), \tag{5.2}$$

where z_{det} is the horizontal distance from the origin of the laboratory system to the detector. The coordinate 2θ is just the scattering angle introduced in section 3.1.

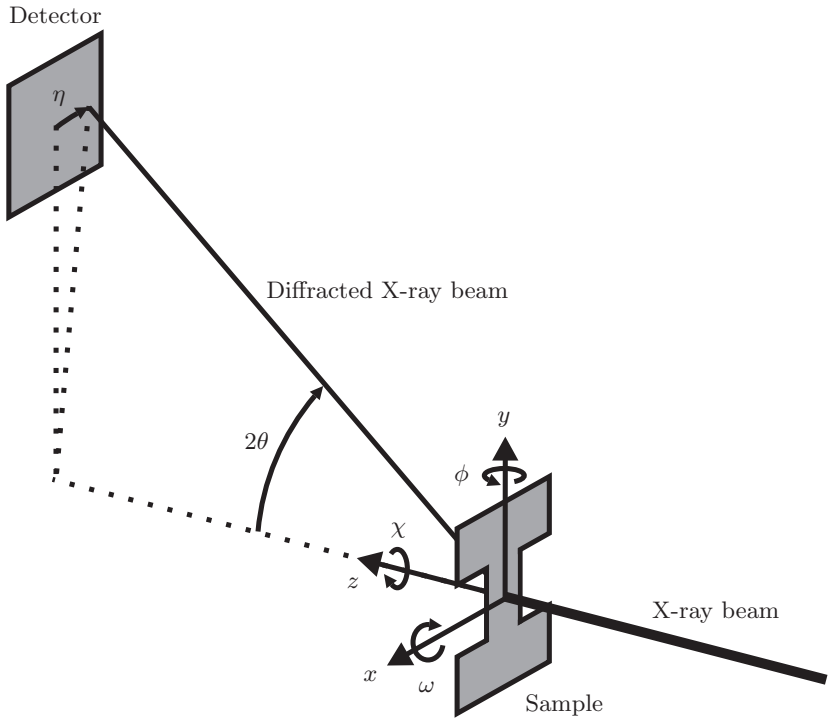

Figure 5.4: A sketch showing the various coordinates and the diffraction geometry when the far detector is used. In the sketch the sample is oriented so the rotation axes of the Euler cradle are parallel to the axes of the laboratory system.

5.1.3 Acquisition of reciprocal space maps

Three-dimensional reciprocal space maps were acquired by combining the two-dimensional detector images with rotations of the sample around the ω-axis. The two-dimensional images (examples are shown in figure 5.8 later) were acquired on the far detector while rocking the sample (rotating it with a constant angular velocity) through small angle intervals around the ω-axis (always perpendicular to the X-ray beam). For most of the samples a rocking interval of 0.015 ° was used, but for a few samples the rocking interval was 0.005 ° or 0.007 °.

Each two-dimensional image corresponds to a map of a surface in reciprocal space. Because the sample (and with it the reciprocal space) was rotated between the acquisition of each image, the images correspond to maps of different surfaces in reciprocal space. By stacking several images acquired over successive ω-intervals, a three-dimensional reciprocal space map is constructed, where two dimensions are the horizontal (the x-direction) and vertical (the y-direction) directions on the detector, and the third dimension (the ω-direction) arises from subsequent rocking intervals. Each value in the reciprocal space map represents the diffracted intensity integrated over a voxel in reciprocal space.

5.1.4 Coordinates in reciprocal space

The three coordinates used in reciprocal space are denoted by q, $\tilde{x}$, and $\tilde{\omega}$. q is the length of the scattering vector:

$$q = \frac{4\pi}{\lambda}\sin(\theta). \tag{5.3}$$

The direction parallel to y (the vertical detector direction) corresponds to a direction in reciprocal space which is almost parallel to the scattering vector (the radial direction). The angle between the two is close to θ (exactly θ when η is zero).

The coordinate $\tilde{x}$ measures the distance in reciprocal space along a curve corresponding to the direction parallel to x (the horizontal detector direction). When η is small, this corresponds to a direction in reciprocal space almost in the azimuthal plane perpendicular to the scattering plane, and a small distance along the x-direction corresponds approximately to a small change, $\Delta\eta$, in η and to a small distance, $\Delta\tilde{x}$, in reciprocal space given by

$$\Delta\tilde{x} = -|\boldsymbol{k}_{\text{out}}|\sin(2\theta)\Delta\eta, \tag{5.4}$$

where $|\boldsymbol{k}_{\text{out}}|\sin(2\theta)$ is the projection of the wave vector of the outgoing beam onto the x-y plane, and the minus sign is included to make the $\tilde{x}$-axis and the x-axis point the same way. Therefore the coordinate $\tilde{x}$ is approximately given by

$$\tilde{x} = -\frac{2\pi\sin(2\theta)}{\lambda}(\eta - \eta_0), \tag{5.5}$$

where η_0 is the value of η at the point on the curve chosen as reference (zero) point.

The coordinate $\tilde{\omega}$ measures the distance in reciprocal space along a curve corresponding to the direction parallel to ω (the rocking direction). When η is small, this corresponds to a direction in reciprocal space in the azimuthal plane and approximately in the scattering plane, and a small distance, $\Delta\omega$, along the ω-direction corresponds approximately to a small distance, $\Delta\tilde{\omega}$, in reciprocal space given by

$$\Delta\tilde{\omega} = |\boldsymbol{q}|\Delta\omega. \tag{5.6}$$

Therefore the coordinate $\tilde{\omega}$ is approximately given by

$$\tilde{\omega} = \frac{4\pi\sin(\theta)}{\lambda}(\omega - \omega_0), \tag{5.7}$$

where ω_0 is the value of ω at the point on the curve chosen as reference (zero) point.

5.1.5 The experimental resolution

In this section the resolution of the technique is estimated, both for the angular coordinates 2θ, η, and ω, for the reciprocal space coordinates q, $\tilde{x}$, and $\tilde{\omega}$, and for measurements of radial elastic strains. For convenience, the resolution is estimated for an ideal 400 reflection from copper ($2\theta_0 = 15.16\,^\circ$) in a vertical scattering plane ($\eta_0 = 0\,^\circ$).

The resolution of the technique is influenced by the detector resolution (point spread function width), the beam properties (divergence and energy spread), and the geometry of the setup (distance and direction to the detector and the size of the rocking interval).

From equations (5.1) and (5.2) it follows that for small values of x, a horizontal and vertical detector resolution of Δx_{psf} and Δy_{psf}, respectively, correspond to a resolution in η and 2θ of

$$\Delta\eta_{\mathrm{psf}} = \frac{\Delta x_{\mathrm{psf}}}{z_{\mathrm{det}} \tan(2\theta_0)}, \tag{5.8}$$

and

$$\Delta 2\theta_{\mathrm{psf}} = \frac{\Delta y_{\mathrm{psf}}}{z_{\mathrm{det}} \left(1 + \tan^2(2\theta_0)\right)}. \tag{5.9}$$

A small horizontal beam divergence of d_{h} corresponds to a resolution in η of

$$\Delta\eta_{\mathrm{div}} = \frac{\Delta x_{\mathrm{div}}}{z_{\mathrm{det}} \tan(2\theta_0)} = \frac{d_{\mathrm{h}}}{\tan(2\theta_0)}, \tag{5.10}$$

and a vertical beam divergence of d_{v} corresponds directly to a resolution in 2θ of

$$\Delta 2\theta_{\mathrm{div}} = d_{\mathrm{v}}. \tag{5.11}$$

From equation (3.6) and the fact that $\Delta E/E = -\Delta\lambda/\lambda$ it follows that an energy spread of ΔE for the beam corresponds to a resolution in 2θ of

$$\Delta 2\theta_{\mathrm{es}} = \frac{\Delta E}{E} 2\tan(\theta_0). \tag{5.12}$$

The energy spread has no effect on the resolution in η, and therefore the contribution to the horizontal resolution can be ignored when η is close to zero.

The resolution in ω is directly given by the rocking interval $\Delta\omega$.

From equation (5.3) it follows that the resolution in q is given by

$$\Delta q = \frac{2\pi}{\lambda} \cos(\theta_0) \Delta 2\theta. \tag{5.13}$$

From equations (3.8) and (5.13) it follows that the resolution in radial elastic strain is given by

$$\Delta\varepsilon_{\mathrm{r}} = \frac{\Delta\theta}{\tan(\theta_0)}. \tag{5.14}$$

The resolution in $\tilde{x}$ and $\tilde{\omega}$ is given by equations (5.4) and (5.6).

Table 5.2 contains calculated values of the experimental resolution, both for the angular coordinates, for the reciprocal space coordinates, and for the radial elastic strain. For each coordinate an estimate of the total resolution is given as an interval. The upper bound has been calculated by a linear addition of the separate contributions. The lower bound has been calculated by a quadratic addition of the separate contributions. The resolution in the three directions is comparable and the different contributions are all of the same order of magnitude.

With a pixel size of 79 μm and a rocking interval between 0.005 ° and 0.015 °, each voxel (close to an ideal 400 reflection from copper) corresponds to a rectangular box in reciprocal space with side lengths

$$\Delta q = 5.3 \cdot 10^{-4}\,\text{Å}^{-1}, \tag{5.15}$$

$$\Delta\tilde{x} = 5.5 \cdot 10^{-4}\,\text{Å}^{-1}, \text{ and} \tag{5.16}$$

$$6.1 \cdot 10^{-4}\,\text{Å}^{-1} < \Delta\tilde{\omega} < 18.2 \cdot 10^{-4}\,\text{Å}^{-1}. \tag{5.17}$$

Table 5.2: The experimental resolution calculated for $2\theta_0 = 15.16\,^\circ$ and $\eta_0 = 0\,^\circ$.

	Angular coordinates	Reciprocal space
Vertical point spread	$\Delta 2\theta_{\mathrm{psf}} = 0.0015\,^\circ$	$\Delta q_{\mathrm{psf}} = 6.7 \cdot 10^{-4}$ Å^{-1}
Vertical divergence	$\Delta 2\theta_{\mathrm{div}} = 0.0010\,^\circ$	$\Delta q_{\mathrm{div}} = 4.4 \cdot 10^{-4}$ Å^{-1}
Relative energy spread	$\Delta 2\theta_{\mathrm{es}} = 0.0011\,^\circ$	$\Delta q_{\mathrm{es}} = 4.9 \cdot 10^{-4}$ Å^{-1}
Total radial resolution	$0.0021\,^\circ < \Delta 2\theta < 0.0035\,^\circ$	$9.4 \cdot 10^{-4}$ Å^{-1} $< \Delta q < 16 \cdot 10^{-4}$ Å^{-1}
Radial elastic strain		$1.4 \cdot 10^{-4} < \Delta\varepsilon_{\mathrm{r}} < 2.4 \cdot 10^{-4}$
Horizontal point spread	$\Delta\eta_{\mathrm{psf}} = 0.0058\,^\circ$	$\Delta\tilde{x}_{\mathrm{psf}} = 7.0 \cdot 10^{-4}$ Å^{-1}
Horizontal divergence	$\Delta\eta_{\mathrm{div}} = 0.0023\,^\circ$	$\Delta\tilde{x}_{\mathrm{div}} = 2.8 \cdot 10^{-4}$ Å^{-1}
Total horizontal resolution	$0.0062\,^\circ < \Delta\eta < 0.0081\,^\circ$	$7.5 \cdot 10^{-4}$ Å^{-1} $< \Delta\tilde{x} < 9.8 \cdot 10^{-4}$ Å^{-1}
Rocking angle	$0.005\,^\circ < \Delta\omega < 0.015\,^\circ$	$6.1 \cdot 10^{-4}$ Å^{-1} $< \Delta\tilde{\omega} < 18.2 \cdot 10^{-4}$ Å^{-1}

5.2 Procedure for a typical experiment

A number of different experiments were carried out with the technique described above. The experiments differed with respect to the type of sample, the type of reflection investigated, the number of samples studied, the number of grains investigated from each sample, the number of reciprocal space maps obtained from each grain, and the strain levels for the different reciprocal space maps. An overview of the experiments can be found in section 5.3 and in appendix A. In this section the procedure for a typical experiment is described.

5.2.1 Aligning and sample mounting

Before each experiment the setup was aligned. The optical table was shifted vertically and horizontally to center the ϕ- and χ-axes of the Euler cradle on the X-ray beam. After this the slits, the split ion chamber, and the fast shutter were all centered on the beam. The near detector was then placed at the right distance from the Euler cradle, and the far detector was placed at the height corresponding to the chosen reflection (the distance to the far detector was fixed by the position of the vertical rail on which it was mounted).

The sample was fitted with a strain gauge, which was glued onto the gauge area, and mounted in the load frame. The sample was kept in place by two pins, one at each end, going through holes in the grips and the sample, allowing self-alignment of the sample with the tensile axis. To stabilize the sample a small load corresponding to a stress of approximately 30 MPa and a strain of approximately 0.03 % was then applied.

For most of the experiments the sample was rotated around the ω-axis to $\omega = \theta_0$ (where θ_0 is half the reference scattering angle for the chosen reflection) in order to bring the in situ deformation axis parallel to the scattering vector corresponding to an ideal reflection in a vertical scattering plane. Two of the samples were rotated around the χ-axis to $\chi = 55\,^\circ$, resulting in an angle of approximately $55\,^\circ$ between the in situ deformation axis and the scattering vector for the investigated grains in these samples.

5.2.2 Grain hunting

The process of finding grains suitable for reciprocal space mapping was quite time consuming and took up a large part of the beam times. The near detector was used for this purpose, and first its position with respect to the beam was determined so the value of 2θ and η could be calculated for each diffraction spot. A series of images were then acquired, covering different ω-intervals, with a slit opening of $50\,\mu$m. Figure 5.5 shows an image from the near detector. The sample was then moved a distance of $50\,\mu$m, and a new series of images were acquired from a new part of the sample. By repeating this procedure for a number of sample positions arranged in a regular grid, all grains in a relatively large part of the sample were illuminated, and with the help of software able to identify the reflection spots in the images (written around the Peaksearch routine from the software package ImageD11 [http://sourceforge.net/apps/trac/fable/wiki/imaged11]) it was possible to produce maps containing information about the distribution of reflections in reciprocal space and the relative position of the corresponding grains perpendicular to the beam direction. These maps were then used to identify suitable candidates for the high resolution reciprocal space mapping.

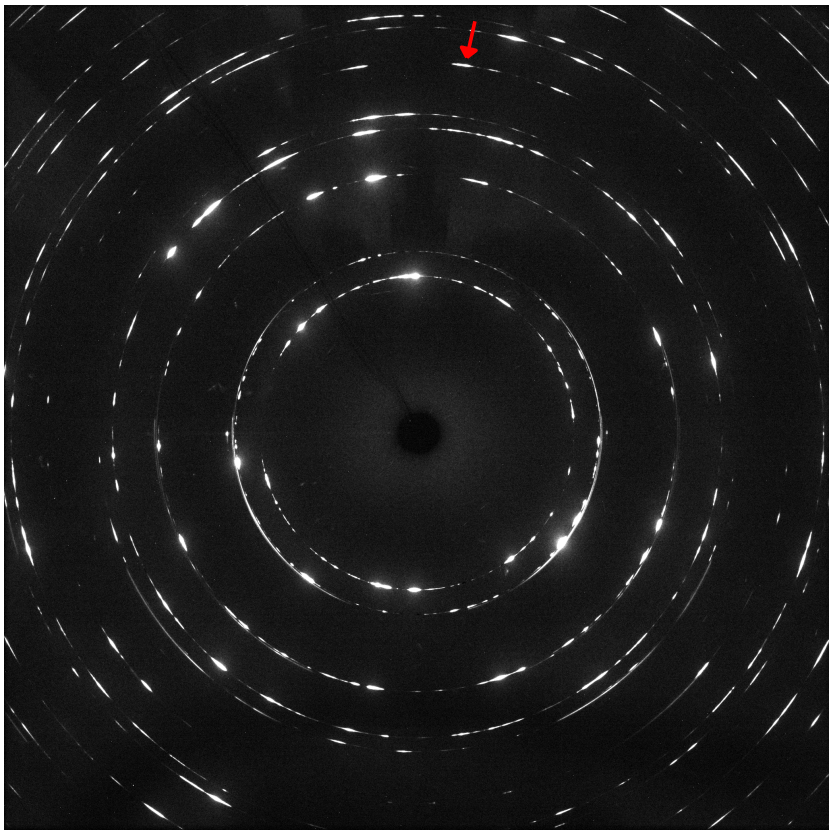

Figure 5.5: An example of an image from the near detector showing reflections arranged along the Debye-Scherrer rings. The red arrow indicates a 400 reflection near $\eta = 0$.

The candidates were investigated in further detail in a search for grains fulfilling five criteria:

- The chosen reflection should be well separated from reflections from other grains in the illuminated volume. For most of the samples a 400 reflection was chosen, but for samples xe1, xe2, and xe3, which had a relatively strong cube texture that resulted in overlap of the 400 reflections, a 222 reflection was chosen.

- The scattering vector should be almost parallel to (within 10 ° of) the in situ deformation axis. As mentioned above, for some grains the angle between the scattering vector and the in situ deformation axis was chosen to be close to (within 10 ° of) 55 °.

- The grain should be small enough to be completely illuminated by the beam. The grain size was estimated by scanning the grain through the beam while measuring the intensity of the reflection as a function of the sample position.

- The intensity profiles obtained by scanning the grain through the beam should be well behaved. Some grains were excluded because the scan through the beam produced a profile with two distinct intensity maxima indicating a twin lamella in the grain.

- The orientation spread in the ω-direction should be neither very small, indicating no interesting structure in the reciprocal space map, or very large, such that many images were required for each reciprocal space map.

From one to five grains were selected from each sample in this way (one in the initial experiments, more later). For most of these the position of the grain within the sample (and thereby the distance from the grain to the sample surface) was determined with the use of a geometric method developed during the project and described in appendix B.

Reciprocal space maps were only obtained at total strains below 12 % (including both pre-deformation and in situ deformation). For higher strains, the diffraction spots were very wide, and it was difficult to avoid overlap between reflections from different grains.

5.2.3 Data acquisition

One at a time the chosen reflection from each of the selected grains was rotated to the far detector by rotating the sample around the ω- and χ-axis, and a reciprocal space map was acquired as described in section 5.1.3. Most of the reciprocal space maps covered the entire ω-range of the reflection, but in some cases only partial reciprocal space maps were acquired. Before acquisition of each reciprocal space map the grain position was determined by scanning the grain through the beam, and the grain was centered in the beam to ensure full illumination.

The sample was then deformed in uniaxial tension (along a direction parallel to the ϕ-axis) with a strain rate of approximately $10^{-4}\,\mathrm{s}^{-1}$ and the strain and the applied load were continuously measured. At a number of different strain levels (between 6 and 31) the deformation was interrupted, and one at a time the grains were centered, and additional reciprocal space maps of the same reflections were acquired. A typical reciprocal space map required around 140 images and took about 60 minutes to acquire with an acquisition time of 20 seconds per image. During the experiments all parameters were written to a log file.

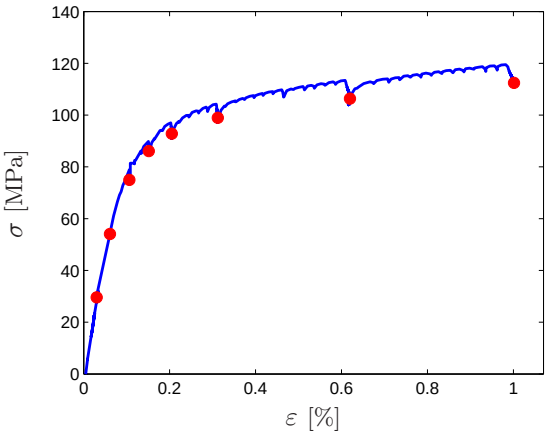

Figure 5.6: The stress-strain curve from the in situ deformation of sample xd2. Reciprocal space maps were obtained at the stress and strain values indicated by the red points.

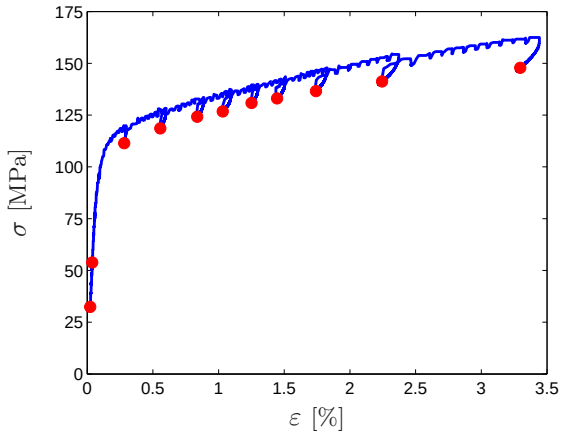

Figure 5.7: The stress-strain curve from the in situ deformation of sample xc1. Reciprocal space maps were obtained at the stress and strain values indicated by the red points.

Figure 5.6 shows a stress-strain curve from an experiment in which reciprocal space maps were obtained at eight different strain levels between 0 % and 1 %. The figure shows that during the holding periods the strain increased and the load decreased before the acquisition of each reciprocal space maps. This indicates that when the deformation was interrupted and the load frame was kept at a fixed displacement, a small amount of plastic deformation took place in the sample leading to a slight elongation of the sample and a drop in the load. Based on analysis of reciprocal space maps Jakobsen, Poulsen, Lienert, Bernier, Gundlach & Pantleon (2009) have shown that the stress relaxation does not significantly alter the morphology of the dislocation structure.

For three of the samples there were problems with measurements of the in situ strain. Figure 5.7 shows an example of this. The figure shows that during the holding periods the measured strain value decreases. This indicates that the strain gauge was gliding in the glue and means that the measured strain values are too small compared to the actual strain in the sample. This was observed for samples xb1, xc1, and xc3. When the elongation of these samples was measured after the experiments, it was found to be larger than the elongation expected on the basis of the measured strain values. Based on measurements of the length of the samples after the in situ deformation it is estimated that the measured strain values for these samples may be only half of the true values.

5.2.4 Detector images and interpretation

Figure 5.8 shows six examples of individual two-dimensional images from the far detector. The coordinates on the axes were calculated from equations (5.3) and (5.5) with an arbitrary reference point near the center of the image. The images are all from the same reciprocal space map from grain d2-1. Each image covers a different $\tilde{\omega}$-interval, all with a width of $1.8 \cdot 10^{-3}$ Å^{-1}, and the distance from one image to the next in the figure is $2.7 \cdot 10^{-2}$ Å^{-1}. The color scale, which is also used in other figures in this and the following chapters, shows low intensities in blue and high intensities in red.

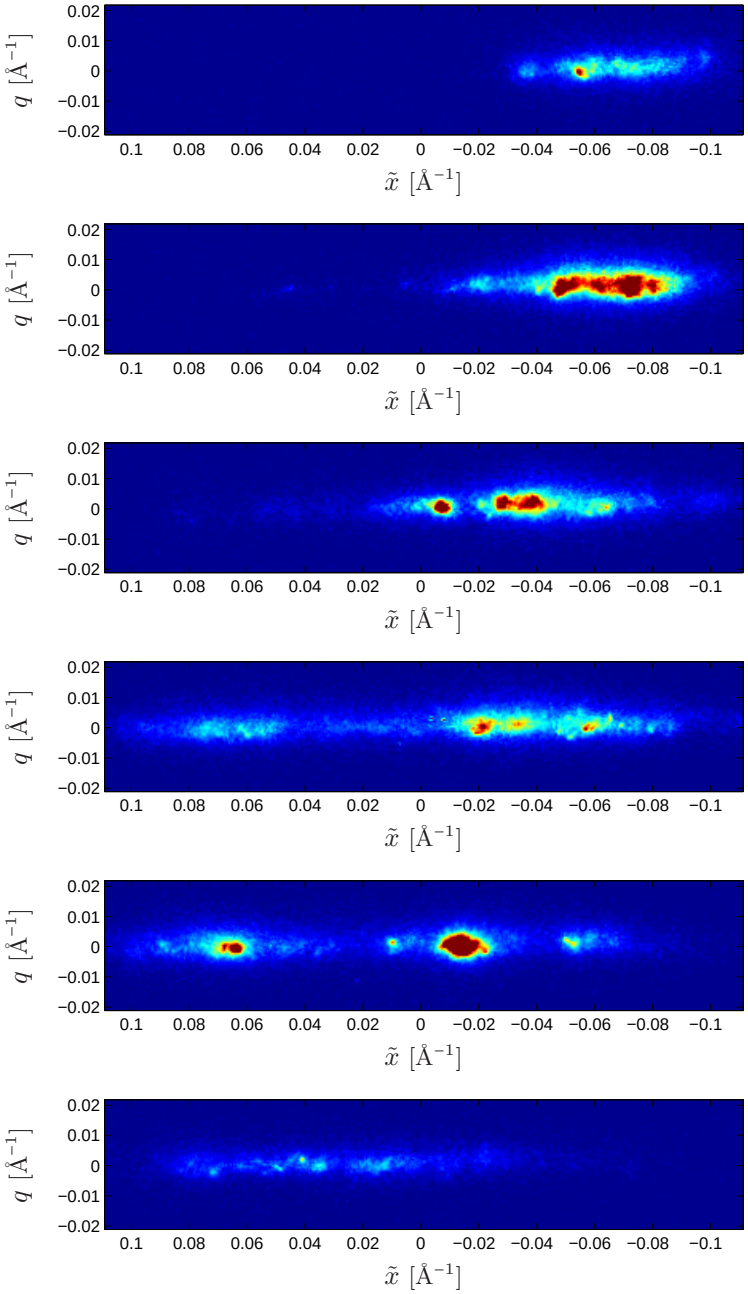

Figure 5.8: Examples of images from the far detector. The images are all from the same reciprocal space map from grain d2-1. The images cover the same range in q and $\tilde{x}$ and have the same color scale. Each image covers a different $\tilde{\omega}$-interval, all with a width of $1.8 \cdot 10^{-3}$ Å^{-1} and the distance from one image to the next is $2.7 \cdot 10^{-2}$ Å^{-1}.

Generally, the intensity distribution in the images can be described as being composed of two contributions: A spread-out, smoothly varying component (called the cloud) and a component consisting of a number of sharp high-intensity peaks. A comparison of images covering adjacent ω-intervals (not shown) reveals that the sharp peaks are narrow in all directions in reciprocal space. This is similar to the observations by Jakobsen et al. (2006), and as described in section 3.3 the interpretation of these features is that the spread-out cloud is caused by diffraction from dislocation-dense regions (the dislocation walls) and each sharp peak is caused by diffraction from an almost dislocation-free region (one or possibly more subgrains).

5.2.5 Stacking and visual check of azimuthal maps

For each reciprocal space map a region of interest containing the reflection was defined on the detector, and for each image only the region of interest was used in the data analysis. For each image the detector background was subtracted and the intensity values were normalized with the intensity measured at the beam stop to correct for fluctuations in the beam intensity (this will be described further in section 6.1).

The individual images were then stacked to produce a three-dimensional reciprocal space map, and the intensity distribution was projected onto the $\tilde{x}$-$\tilde{\omega}$-plane and visually checked to make sure the data quality was satisfactory. Because the intensity distribution is much wider in the $\tilde{x}$- and the $\tilde{\omega}$-directions than in the q-direction, much of the structure in the reciprocal space maps can be seen in such a projection, which will be called an azimuthal map. An azimuthal map shows the distribution within the grain of the crystallographic

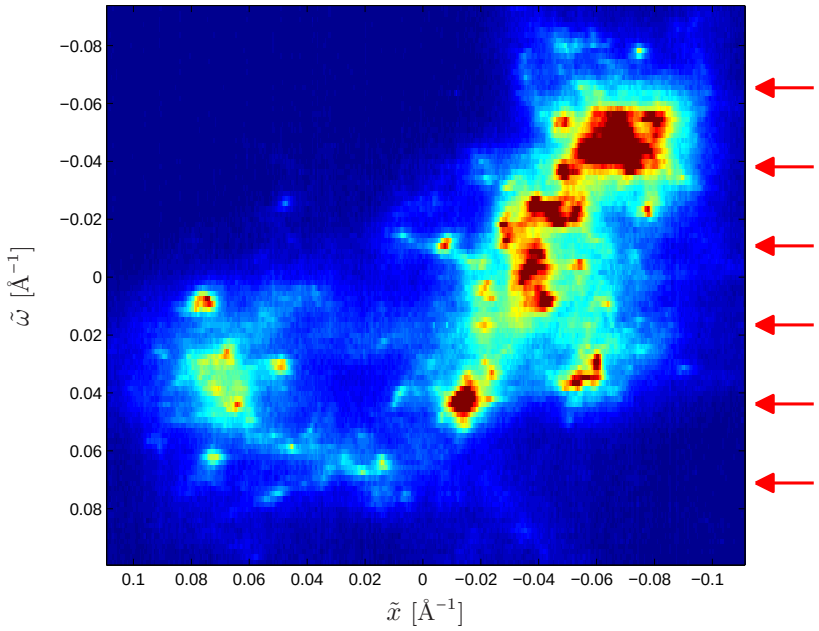

Figure 5.9: An example of an azimuthal map from grain d2-1 containing the images from figure 5.8. The $\tilde{\omega}$-values corresponding to the images in figure 5.8 are indicated by the red arrows.

direction corresponding to the investigated reflection. An example can be seen in figure 5.9, which shows an azimuthal map from the reciprocal space map containing the images from figure 5.8. The coordinates on the axes were calculated from equations (5.5) and (5.7) with an arbitrary zero point near the center of the map.

5.3 Overview of the X-ray diffraction experiments

The X-ray diffraction experiments presented in this thesis were carried out during five beam times, each lasting one or two weeks. The experiments can be conveniently categorized by the values of the following parameters:

- The type of reflection investigated (222 or 400).
- The orientation of the sample relative to the scattering vector (the angle, ξ, between the scattering vector and the in situ deformation axis).
- The strain path change parameter, α, for the sample (which depends on the relative orientation of the pre-deformation axis and the in situ deformation axis).
- The pre-deformation temperature (room temperature or -196 °C).

Depending on the value of these parameters, the studied grains are combined in eight different groups:

Grain group A consists of five grains from two samples with $\alpha = 1$ pre-deformed at room temperature to a strain of 5 %. From these grains a 400 reflection was observed with $\xi = 0°$.

Grain group B consists of a single grain from a sample with $\alpha = 1/2$ pre-deformed at room temperature to a strain of 5 %. From this grain a 400 reflection was observed with $\xi = 0°$.

Grain group C consists of five grains from three samples with $\alpha = 0$ pre-deformed at room temperature to a strain of 5 %. From these grains a 400 reflection was observed with $\xi = 0°$.

Grain group D consists of five grains from two samples with $\alpha = -1/2$ pre-deformed at room temperature to a strain of 5 %. From these grains a 400 reflection was observed with $\xi = 0°$.

Grain group E consists of three grains from three samples with $\alpha = -1/2$ pre-deformed at room temperature to a strain of 5 %. From these grains a 222 reflection was observed with $\xi = 0°$.

Grain group F consists of three grains from a single sample with $\alpha = 1$ pre-deformed at room temperature to a strain of 5 %. From these grains a 400 reflection was observed with $\xi = 55°$.

Grain group G consists of three grains from a single sample with $\alpha = 0$ pre-deformed at room temperature to a strain of 5 %. From these grains a 400 reflection was observed with $\xi = 55°$.

Grain group H consists of five grains from a single sample with $\alpha = 1$ pre-deformed at a temperature of -196 °C to a strain of 7 %. From these grains a 400 reflection was observed with $\xi = 0°$.

The color used for the grain group names in the list above is the color used in later chapters for the names of grains, grain groups and samples to make it easier for the reader to distinguish between the different grain groups and identify them in the figures.

A sketch of the relative orientation of the pre-deformation axis, the in situ deformation axis, and the scattering vector for the different grain groups is shown in figure 5.10. Tables A.2 and A.3 in appendix A summarize the properties for the grain groups and the individual grains.

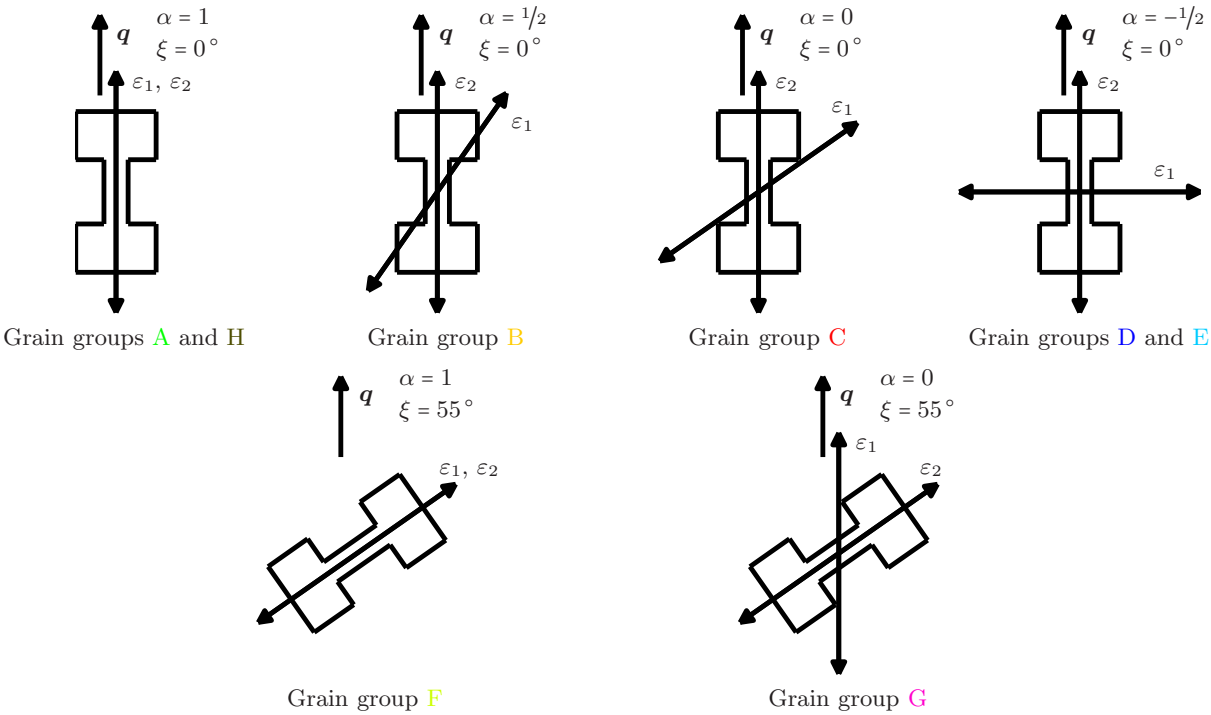

Figure 5.10: A sketch of the relative orientation of the pre-deformation axis, ε_1, the in situ deformation axis, ε_2, and the scattering vector, $\boldsymbol{q}$, for the different grain groups. The strain path change parameter, α, and the angle, ξ, between the scattering vector and the in situ deformation axis are indicated in the figure

5.4 Stability and reproducibility

As a test of the stability of the setup and the reproducibility of the results, eight reciprocal space maps were obtained from one grain from sample xh1 repeatedly without any adjustment to the setup. The eight reciprocal space maps were virtually identical after normalization with the beam intensity measured at the beam stop. This shows that the setup is very stable and that the results are reproducible. Figures 5.11 and 5.12 show the azimuthal maps from the first and last of the eight reciprocal space maps acquired over a period of ten hours.

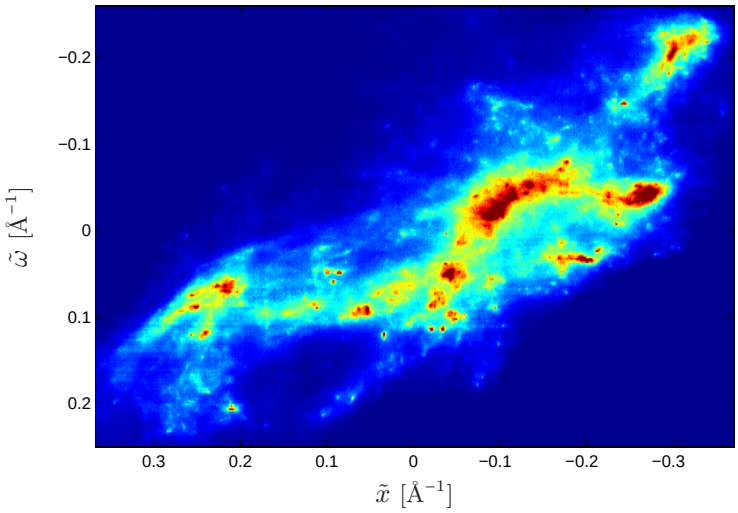

Figure 5.11: The azimuthal map from the first reciprocal space map acquired during a test of stability and reproducibility.

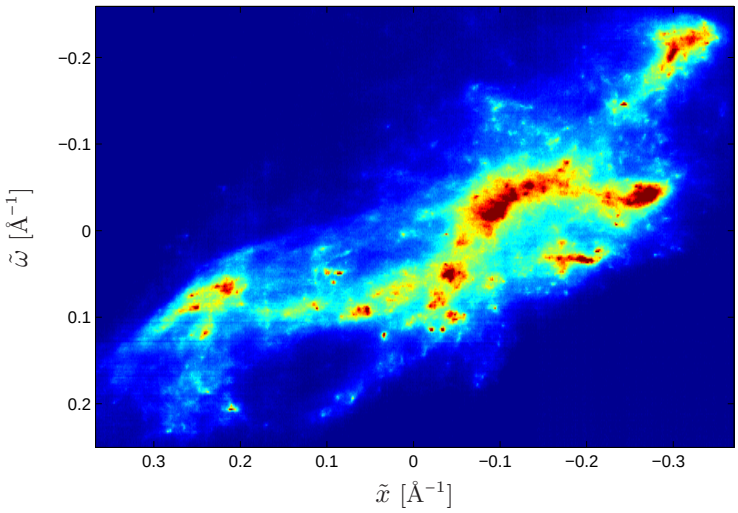

Figure 5.12: The azimuthal map from the last reciprocal space map acquired during a test of stability and reproducibility.

Chapter 6

X-ray diffraction experiments: Data analysis

The experimental technique described in chapter 5 is relatively new, and a substantial amount of work has been devoted to the development of methods and software for handling and analysis of the images acquired during the X-ray diffraction experiments. This chapter first describes the pre-processing of the images. This is followed by a description of how radial profiles were calculated from the reciprocal space maps and how they were characterized. After this a mathematical method developed to partition the intensity distributions of the reciprocal space maps into two components corresponding to the contributions from the subgrains and the walls is presented. The last section describes how the individual sharp peaks were identified and analyzed.

6.1 Pre-processing of the images

The images from the far detector were subjected to three pre-processing steps: The detector background was estimated and subtracted, the intensity values were normalized, and cosmic rays were removed. After these steps the reciprocal space maps were checked visually, and possible errors were corrected.

6.1.1 Background subtraction

The raw images from the far detector contain a contribution from the detector background. For each image the background level was estimated by calculating the mean intensity in two rectangular regions at the edges of the region of interest, above and below the reflection (with the same width as the region of interest and a height of 30 pixels as shown in figure 6.1). The mean intensity in these regions (ignoring pixels containing very large intensity values) was used as a measure of the background and subtracted from the intensity in the entire region of interest. For all the reciprocal space maps the background level had an average value of around 10 with a variation of around ±2. For comparison, typical intensity values are between 100 and 500 in the center of the cloud and 20 times larger in the intense peaks.

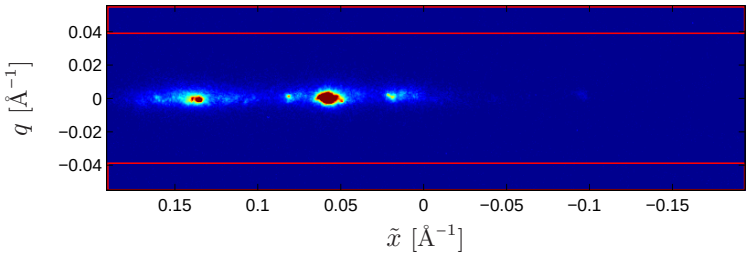

Figure 6.1: An example of the region of interest from an image from the far detector. The red rectangles indicate the regions used to estimate the level of the detector background.

6.1.2 Normalization

The intensity in each of the raw images is proportional to the beam intensity at the time of acquisition, which was measured at the beam stop behind the sample. The intensity in the X-ray beam fluctuated during the experiments, and to correct for this the intensity in each image (after subtraction of the background) was multiplied by a normalization factor given by the ratio of the mean beam intensity for the entire reciprocal space map to the beam intensity for the given image.

6.1.3 Removal of cosmic rays

Some images were contaminated by cosmic rays, which are streaks caused by muons (produced by high-energy cosmic particles hitting the atmosphere) hitting the detector during acquisition. Cosmic rays were identified by searching for pixels in which the intensity was at least a factor of 7 higher than the intensity in the same pixel in the neighboring images, and in which the intensity was larger than 50 (these values were conservative, and small cosmic rays may not have been removed). The cosmic rays found by this procedure were removed by linear interpolation between the images acquired before and after the contaminated image. Roughly a fraction of $2 \cdot 10^{-5}$ of the pixels in the regions of interest were affected by this.

6.1.4 Data check

After the steps described above the individual images were stacked to produce a three-dimensional reciprocal space map, and azimuthal maps of each reciprocal space map were inspected visually to check for errors. In a few cases bad or missing images (caused by experimental problems) were replaced or constructed by linear interpolating between neighboring images. For some of the grains (c2-1, f1-3, h1-1, h1-2, and h1-3), grain rotations during the experiment caused a reflection from another grain to appear in the mapped region of reciprocal space for the last few reciprocal space maps. In each case this only affected a small region near the edge of the mapped reflection where the intensity was very low, and the intensity in the affected pixels was set to zero.

6.2 Calculation and analysis of radial profiles

This section describes how radial profiles were calculated from the reciprocal space maps and how they were characterized, both by simple descriptive parameters and by fitting the

profiles with a Wilkens and a Gauss profile to quantify the density and arrangement of the dislocations.

For two grains (b1-1 and c2-1) not all the reciprocal space maps were included in the analysis because the shape of the radial profile was distorted due to a varying detector background. For this reason these reciprocal space maps are not included in the results presented in chapter 7.

6.2.1 Calculation of radial profiles

Radial profiles are projections of the intensity distribution in the reciprocal space maps onto the radial direction in reciprocal space as defined by equation (3.7). A measured profile is necessarily a discrete approximation obtained by averaging over q-intervals:

$$I_{\mathrm{r}}(q_n) = \frac{1}{\Delta q} \int_{|q'-q_n|<\frac{\Delta q}{2}} I(\boldsymbol{q}')\,\mathrm{d}\tilde{V}'. \tag{6.1}$$

Here q_n is the value of q at the center of the interval of width Δq, and $\mathrm{d}\tilde{V}'$ is a volume element in reciprocal space. The prime on $\mathrm{d}\tilde{V}'$ indicates that $\boldsymbol{q}'$ is the variable of integration. The integral is over part of a spherical shell in reciprocal space covering the entire azimuthal spread of the reflection. The integral can be approximated as a sum over all voxels in reciprocal space weighted by their relative volume inside the shell defined by $|q'-q_n| < \frac{\Delta q}{2}$. For the voxel with center coordinates $(q,\tilde{x},\tilde{\omega})$ this relative volume is denoted by $V(q,\tilde{x},\tilde{\omega})$, and the intensity is denoted by $I(q,\tilde{x},\tilde{\omega})$. Then

$$I_{\mathrm{r}}(q_n) \sim \frac{1}{\Delta q} \sum_{\text{all voxels}} V(q,\tilde{x},\tilde{\omega}) I(q,\tilde{x},\tilde{\omega}), \tag{6.2}$$

where $\sim$ means 'approximately proportional to'. Factors taking into account the normalization of the images and the rotation speed of the sample are ignored as they do not affect the position or the shape of the profile.

For the evaluation of equation (6.2), the q-width of one pixel ($5.3 \cdot 10^{-4}$ Å^{-1}, see equation (5.15)) was used for Δq. The value of $V(q,\tilde{x},\tilde{\omega})$ is equal to the relative area of the pixel covered by the Δq-shell as indicated in figure 6.2. This was approximated by first determining the values of q at the pixel corners, and then, assuming a locally linear relationship between q and $\tilde{x}$, calculating the area of the grey regions in the figure.

The radial profiles calculated from the entire reciprocal space maps in this way will be called grain profiles to distinguish them from the radial profiles calculated from the subgrain and wall components (called subgrain profiles and wall profiles, respectively) and from the individual sharp peaks (called individual subgrain profiles).

6.2.2 Calibration of the detector position

In order to calculate the radial profiles as described above, the value of q must be calculated at the corners of each pixel, and in order to do this the position of the detector with respect to the X-ray beam and the distance from the detector to the sample must be known. For this purpose images of Debye-Scherrer rings from a spinning LaB_6 powder were acquired during each beam time. LaB_6 powder is routinely used to calibrate peak positions because the crystallites are strain free, and the scattering angles are known with high precision. On the images acquired on the far detector segments of several Debye-Scherrer rings could be

observed, and from the horizontal position of the top of the rings (the point of the rings with the largest value of y) the horizontal position of the detector with respect to the X-ray beam was determined.

To determine the vertical position of the detector with respect to the X-ray beam, y_{det}, and the horizontal distance from the detector to the sample, z_{det}, a radial profile was calculated using the method described above with a reasonable estimate of the value of y_{det} and z_{det}. In the resulting profile, the Debye-Scherrer rings show up as sharp peaks, and the corresponding q-values were determined. The values of y_{det} and z_{det} were then adjusted to get the best possible agreement between the measured q-values and the reference values.

The beam position parameters were determined separately for each beam time. With the optimal values of the parameters the measured q-values had a relative deviation of less than 10^{-5} from the reference values. The position of the detector relative to the beam and the sample was determined with an accuracy of 0.1 mm.

6.2.3 Characterization of radial profiles

To characterize the position of the radial profiles the mean position, $\hat{q}$, is used. The mean position of a profile is the mean q-value of the profile weighted by the intensity values. This, however, depends on the range of q-values used for the radial profile due to the long tails of the profiles and their asymmetry. In this thesis the q-values used is the range of q-values around the position of maximum intensity, $q^{\max}$, in which the intensity is at least $1/50$ of the maximum intensity, and the position of a profile will always refer to the mean position unless stated otherwise. Figure 6.3 shows an example of a radial profile with the mean position indicated. The figure illustrates the used range of q-values.

To characterize the width of the radial profiles the integral width, β, is used. The integral width of a profile is defined as the total area below the profile (in the range of q-values defined above) divided by the maximum intensity. This is equivalent to the width of a rectangle with the same area and the same maximum intensity as the profile. The integral width is illustrated

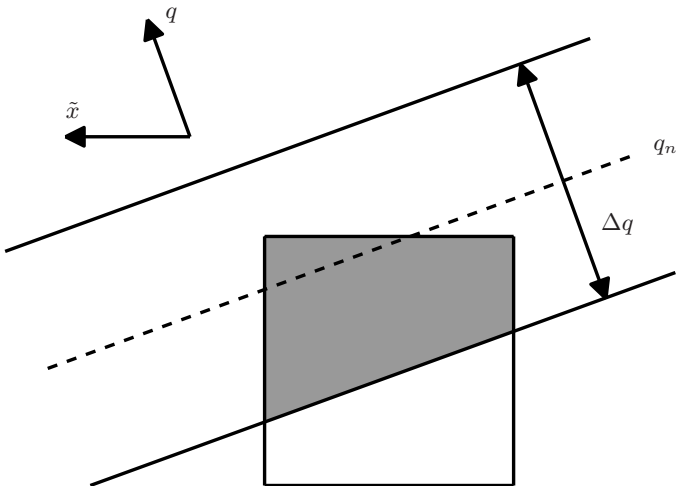

Figure 6.2: A sketch showing how $V(q, \tilde{x}, \tilde{\omega})$ was calculated as the relative area of a pixel covered by the Δq-shell.

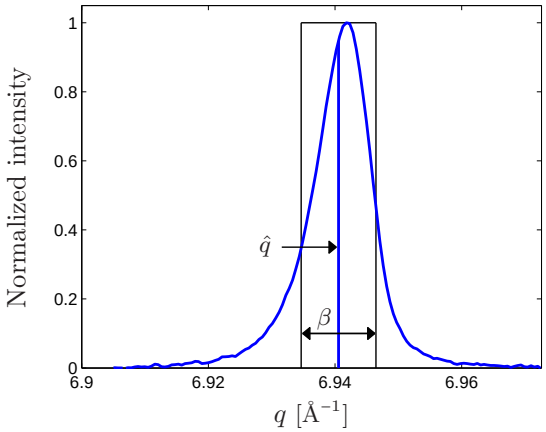

Figure 6.3: An example of a radial profile with the mean position and the integral width indicated. The profile is shown only for the q-range used for the calculation of the mean position and the integral width.

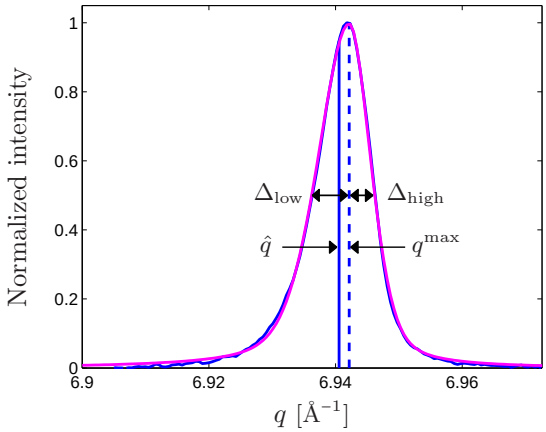

Figure 6.4: An example of fit with a split pseudo-Voigt profile (magenta) to the measured profile shown in figure 6.3 (blue). The mean position (solid line) of the measured profile, and the position of maximum intensity (dashed line) and the half widths of the split pseudo-Voigt profile are indicated.

for the profile in figure 6.3. In this thesis the width of a profile will always refer to the integral width unless stated otherwise.

To characterize the asymmetry of the profiles a split pseudo-Voigt profile was fitted to each profile. A pseudo-Voigt profile is a linear combination of a Gauss profile and a Lorentz profile (commonly with the same FWHM). A split pseudo-Voigt profile is a combination of two half pseudo-Voigt profiles, one on either side of the position of maximum intensity. This allows the profile to have different widths on either side and therefore to be asymmetric. A split pseudo-Voigt profile is given by

$$I(q) = I^{\mathrm{max}} \times \begin{cases} f_{\mathrm{L}}\left[1 + \left(\frac{q-q^{\mathrm{max}}}{\Delta_{\mathrm{low}}}\right)^2\right]^{-1} + (1-f_{\mathrm{L}})\left[\exp\left(-\frac{(q-q^{\mathrm{max}})^2}{\Delta_{\mathrm{low}}^2/\ln 2}\right)\right] & \text{for } q \le q^{\mathrm{max}} \\ f_{\mathrm{L}}\left[1 + \left(\frac{q-q^{\mathrm{max}}}{\Delta_{\mathrm{high}}}\right)^2\right]^{-1} + (1-f_{\mathrm{L}})\left[\exp\left(-\frac{(q-q^{\mathrm{max}})^2}{\Delta_{\mathrm{high}}^2/\ln 2}\right)\right] & \text{for } q > q^{\mathrm{max}} \end{cases} \tag{6.3}$$

Here I^{max} is the maximum intensity, f_{L} is the Lorentz fraction, q^{max} is the position of maximum intensity, and Δ_{low} and Δ_{high} are the half width at half maximum intensity on the low-q-side and high-q-side, respectively. An example of a fit with a split pseudo-Voigt profile is shown in figure 6.4. As illustrated in the figure the fits are typically not perfect, especially around the shoulders of the profiles, but they are adequate for determination of the position of maximum intensity and the two half widths.

As a measure of the asymmetry the parameter

$$\kappa = q^{\mathrm{max}} - \hat{q} \tag{6.4}$$

is used. q^{max} was determined from the split pseudo-Voigt profile fit and $\hat{q}$ was calculated from the measured profile (because of the Lorentz part of the split pseudo-Voigt profile the mean

position is not defined for the fitted profile). In figure 6.4 the difference between $q^{\max}$ and $\hat{q}$ is illustrated.

If the position of the radial profiles from the individual subgrains coincides with the position of maximum intensity of the grain profile (as indicated by the results of Jakobsen et al. (2007)), the asymmetry of the grain profile is equal to the radial shift of the individual subgrain profiles, and therefore proportional to the mean radial elastic strain in the subgrains.

An alternative measure of the asymmetry based on the half widths of the fitted split pseudo-Voigt profile is given by $\kappa_{rel} = (\Delta_{\text{low}} - \Delta_{\text{high}})/(\Delta_{\text{low}} + \Delta_{\text{high}})$. This parameter is independent of the absolute profile width and is called the relative asymmetry.

The uncertainty in the determined values of position, width, and asymmetry is estimated to be less than the q-width of one pixel which is $5.3 \cdot 10^{-4}$ Å^{-1}.

6.2.4 Fit with a Wilkens and a Gauss profile

The radial profiles from the 400 reflections were fitted with a Wilkens profile (described in section 3.2.3). The Wilkens profile was calculated by inverse Fourier transformation using equations (3.10) to (3.14). The density and range of the points used in the inverse Fourier transform was increased until further increase resulted in no significant change in the profile. For the calculation the following parameter values were used: $b = 2.556$ Å (the length of the Burgers vector in copper), $q_0 = 6.9523$ Å^{-1} (the length of the scattering vector for an ideal 400 reflection), and $C = 0.3$ (the contrast factor corresponding to an equal proportion of edge and screw dislocations (Ungár, Dragomir, Révész & Borbély 1999)). The position and maximum intensity of the profile, the dislocation density, and the dislocation arrangement parameter were adjusted to make the best fit.

Because the Wilkens profile is symmetric, it can not approximate asymmetric profiles very well. Figure 6.5 shows an example of the best fit to an asymmetric profile. The position of maximum intensity is off, and there is a systematic error around the shoulders of the profile because of the asymmetry.

The asymmetry is interpreted as a consequence of the relative shift of the two subprofiles from the subgrains and the walls. According to the classical composite model the shape and width of both subprofiles is determined by the dislocation density and arrangement in the respective parts of the crystal. According to this interpretation it would be more reasonable to fit the asymmetric profiles with a sum of two profiles representing the two subprofiles. This has been attempted by Scharfler, Simon, Bernstorff, Hanák, Tichy, Ungár & Zehetbauer (2005) who used two Wilkens profiles to approximate measured radial profiles.

In contrast, the modified composite model assumes a negligible dislocation density in the subgrains and explains the width of the subgrain profile as a consequence of variations in the elastic strain in the subgrains leading to a spread in the radial position of the narrow profiles from the individual subgrains. This suggests that the subgrain profile should not be fitted with a Wilkens profile. Assuming that the position of the profiles from the individual subgrains can be approximated by a Gauss distribution (as will be shown in section 7.4.2) it makes more sense to fit the subprofile from the subgrains with a Gauss profile.

Therefore the radial profiles were fitted with the sum of a Wilkens and a Gauss profile shifted with respect to each other:

$$I(q) = I_W^{\max} W(q - q_W, \rho, M) + I_G^{\max} \left[\exp\left(-\frac{(q - q_G)^2}{\Delta_{\text{FWHM}}/\ln 2} \right) \right]. \tag{6.5}$$

Here $W(q - q_W, \rho, M)$ is the Wilkens profile defined by equations (3.10) to (3.14). The arguments indicate that the profile depends on the center position, q_W, the dislocation density, ρ, and the dislocation arrangement parameter, M. The parameters adjusted to make the best fit were the position, q_W, the maximum intensity, $I_W^{\max}$, the dislocation density, ρ, and the dislocation arrangement arrangement, M, of the Wilkens profile, and the position, q_G, the maximum intensity, $I_G^{\max}$, and the width (FWHM), Δ_{FWHM}, of the Gauss profile. Figure 6.6 shows that this approach results in a fit to the measured profile which is significantly better than the fit in figure 6.5.

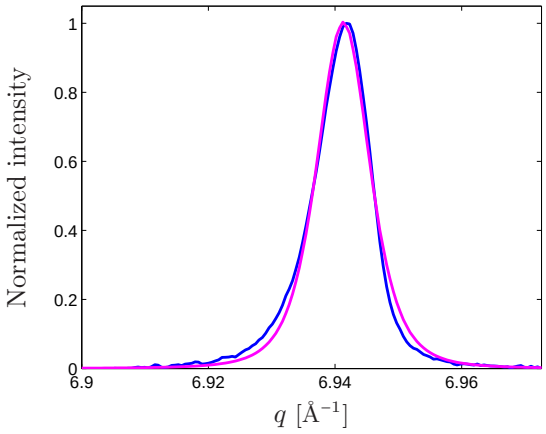

Figure 6.5: An example of a fit with a Wilkens profile (magenta) to the measured profile shown in figure 6.3 (blue).

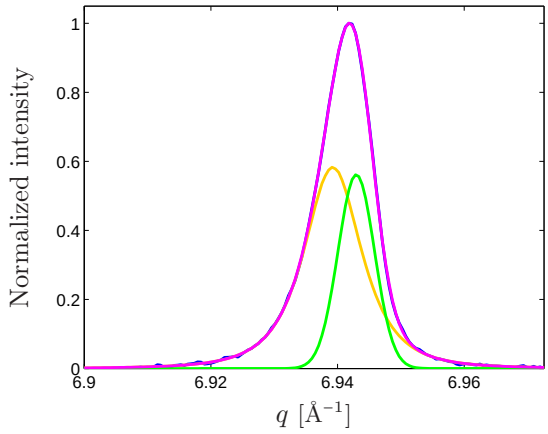

Figure 6.6: An example of a fit with the sum (magenta) of a Wilkens profile (yellow) and a Gauss profile (green) to the measured profile shown in figure 6.3 (blue).

It was difficult to select initial values of the parameters that resulted in convergence of the fit, particularly for the profiles which were almost symmetric, and to obtain a solution the initial values had to be close to the final values. However, within this range the found solutions were independent of the initial values.

6.3 Partitioning the intensity distributions

In section 5.2.4 it was described that the measured three-dimensional reciprocal space maps consist of a number of sharp high-intensity peaks (interpreted as being caused by diffraction from the subgrains) superimposed on a spread-out low-intensity cloud (interpreted as being caused by diffraction from the dislocation walls). A significant part of the work presented in this thesis was devoted to developing a mathematical method to partition the intensity distributions into two parts corresponding to these two components.

A method was developed that relies on approximating the cloud with a smooth function. The method uses an asymmetric measure of misfit to generate a fit that approximates the cloud only and ignores the high-intensity peaks as sketched in figure 6.7. The result of this is a model of the cloud (and therefore a model of the intensity contribution from the walls, called the wall component), which is subtracted from the total intensity distribution to give a model of the intensity contribution from the subgrains (called the subgrain component). This section describes the details of the method.

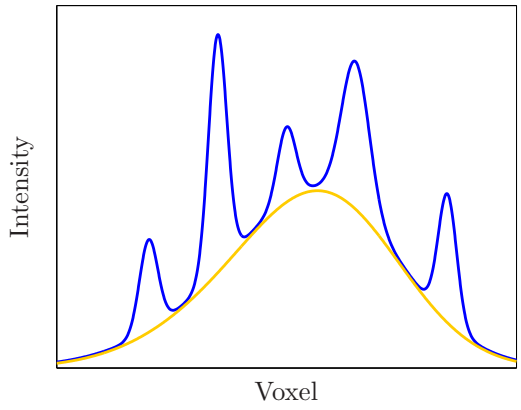

Figure 6.7: Sketch of the partitioning of the intensity distributions (blue) by approximation of the cloud with a smooth function (yellow).

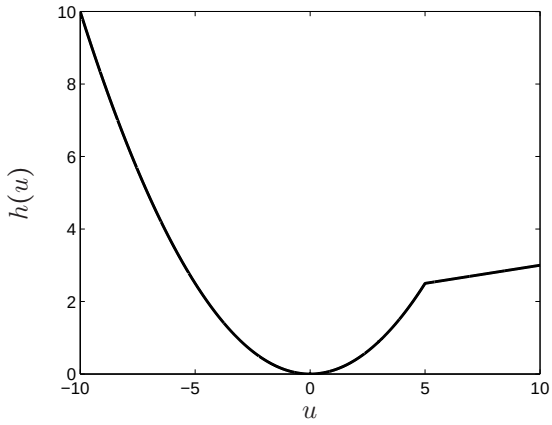

Figure 6.8: The asymmetric measure of misfit used in the partitioning method.

6.3.1 Fitting with splines

Because of the computational cost involved, the fitting was performed on individual $\tilde{x}$-$\tilde{\omega}$-layers (azimuthal layers with a thickness of one voxel), and the results were stacked to produce a three-dimensional model of the intensity contribution from the walls. The required computing time was reduced further by reducing the number of data points before the partitioning. This was done by dividing each azimuthal layer into a set of equal sized rectangles and replacing each rectangle with a single data point with the average intensity of the rectangle. Besides significantly reducing the required computing time, the data reduction also had the effect of smoothing the data, but since the aim of the method was to find a smooth function that approximated the cloud, this was not considered to be a problem. The rectangles were 6 voxels wide in the $\tilde{x}$-direction and 2 to 6 voxels wide in the $\tilde{\omega}$-direction (based on the size of the rocking interval to give approximately the same reciprocal space resolution in the two directions). The size of the rectangles was chosen to give a significant reduction in computing time without any significant effect on the resulting cloud model.

In the fit for each azimuthal layer a bicubic spline was used. A bicubic spline is a two-dimensional piecewise bicubic function which is continuous and has continuous first and second derivatives. The domain of each spline (the azimuthal layer) was divided into rectangles by a regular grid defined by a set of points, called knots, in each direction ($\tilde{x}$ and $\tilde{\omega}$), and in each of the rectangles the spline was given by an expression of the form

$$s(\tilde{x},\tilde{\omega}) = \sum_{i=0}^{3}\sum_{j=0}^{3} a_{ij}\tilde{x}^i\tilde{\omega}^j. \tag{6.6}$$

The coefficients a_{ij} were different in different rectangles. At the boundary of the domain the second derivative of the spline was set to zero.

The distance between the knots is an important parameter with a rather large effect on the resulting cloud model. The smaller the distance the better the spline is able to follow the variations in the intensity distribution. The distance between the knots was 30 voxels in the $\tilde{x}$-direction and 10 to 30 voxels in the $\tilde{\omega}$-direction (based in the size of the rocking interval to give

approximately the same reciprocal space resolution in the two directions). The distance was chosen based on visual inspection of one-dimensional intensity profiles through the reciprocal space maps and the corresponding cloud model. Because the spline is not able to perfectly follow the variations in the cloud, the subgrain component probably contains a small intensity contribution from the walls.

6.3.2 Fitting with an asymmetric measure of misfit

To make a good model of the cloud, the splines should follow the smoothly varying part of the intensity distribution and ignore the high-intensity peaks as in the sketch in figure 6.7. This was achieved by using an asymmetric measure of misfit, h, in the fit of the spline to the reduced data points. The function h is given by

$$h(u) = \begin{cases} u^2/2s & \text{for } u \le s \\ ru/s + s/2 - r & \text{for } u > s, \end{cases} \tag{6.7}$$

where u is the difference between the data value and the value of the spline. The function is shown in figure 6.8. This measure of misfit was inspired by the one-sided Huber methods described by Bandler, Chen, Biernacki, Gao, Madsen & Yu (1993) and Nielsen (1994), and differs from conventional least squares fitting for data points for which $u > s$. These are primarily the points in the sharp peaks, and compared to conventional least squares fitting they are assigned a much smaller measure of misfit and therefore do not influence the fit very much.

The value of the parameter s determines how intensity variations of different sizes are treated by the method. Data points for which $u \le s$ are treated as random variations (noise) in the cloud and data points for which $u > s$ are treated as sharp peaks whose influence on the resulting cloud model is minimized. This means that the method is unable to separate very small peaks from the cloud, and the resulting wall component probably contains an intensity contribution from very small subgrains. The value of s has only a small effect on the resulting could model. A value of 5 was used, which is approximately twice the standard deviation of the random pixel-to-pixel variation in the image background.

The value of the parameter r determines the relative influence of data points for which $u > s$ (points in the peaks). A larger value of r means that the points in the sharp peaks have a larger influence on the fit. The parameter r is the main contribution to the method made during the study presented in this thesis (for $r = s$ the method corresponds to the method described by Nielsen (1994)). The degree of freedom supplied by the parameter is important in order to use the method to produce reasonable models of the cloud. The value of r has a rather large effect on the resulting cloud model. A value of 0.5 was used. The chosen parameter values ($s = 5$ and $r = 0.5$) were based on a visual inspection of the results of the fit.

Based on the function h, the model of the intensity contribution from the walls (the wall component) is the solution obtained by varying the coefficients a_{ij} for the bicubic spline to minimize the sum $\sum_k h(u_k)$ over all the reduced data points. The algorithm that was used was developed by Madsen & Nielsen (1990), and the underlying software was written by H. B. Nielsen (from IMM, DTU). The solution was subtracted from the original reciprocal space map (not the reduced data) to give a model of the intensity contribution from the subgrains (the subgrain component). An example of the result is shown in figure 6.9. The figure shows the azimuthal map from figure 5.9 and azimuthal maps from the corresponding wall and subgrain components.

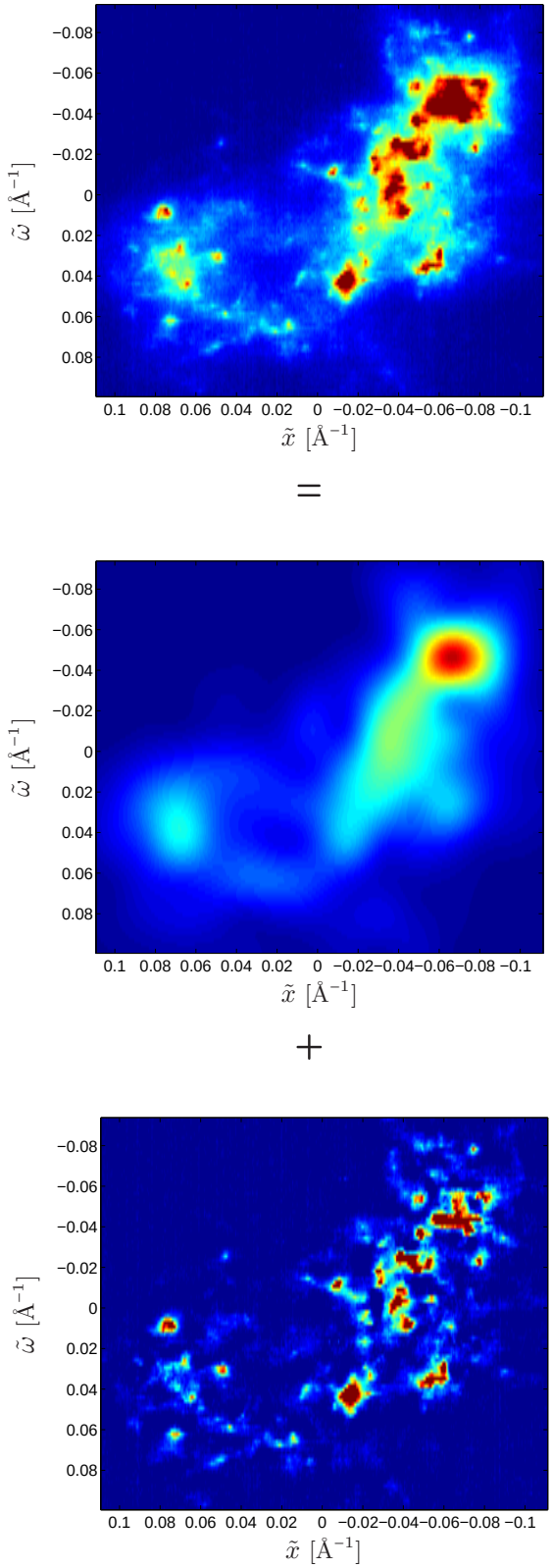

Figure 6.9: An example of an azimuthal map (top) from grain d2-1 and the corresponding wall component (center) and subgrain component (bottom). The color scale for the azimuthal map from the subgrain component is different from the color scale for the other azimuthal maps.

To check that it is reasonable to partition the reciprocal space maps one azimuthal layer at a time, one-dimensional profiles through single columns of voxels perpendicular to the azimuthal layers were calculated. These were all smooth, which indicates that the method produces a three-dimensional model of the intensity contribution from the walls which is smooth in all directions.

Finally, radial profiles were calculated from the subgrain and wall components as described for the entire reciprocal space maps in section 6.2. These will be called subgrain profiles and wall profiles, respectively.

6.4 Analysis of the individual sharp peaks

The individual sharp peaks in the reciprocal space maps were identified by searching for local maxima in the subgrain component produced by the partitioning method described in section 6.3. All local maxima (voxels for which the intensity was higher than the intensity in the 26 surrounding voxels) in the subgrain component were identified and sorted according to intensity.

Some of the maxima found by this method were caused by noise and did not represent subgrains, but the majority of these were removed by ignoring peaks that were very narrow (with a radial width (FWHM) smaller than $1.3{\cdot}10^{-3}$ Å^{-1}). A histogram of the width (FWHM) of all the sharp peaks (from all the reciprocal space maps) identified in this way is shown in figure 6.10. In the figure the red part represents the very narrow peaks which were ignored in the analysis. The majority of these narrow peaks are simply noise in the data, and the figure shows that it makes sense to use a cutoff around $\Delta q_{\mathrm{FWHM}} = 1.3 \cdot 10^{-3}$ Å^{-1}.

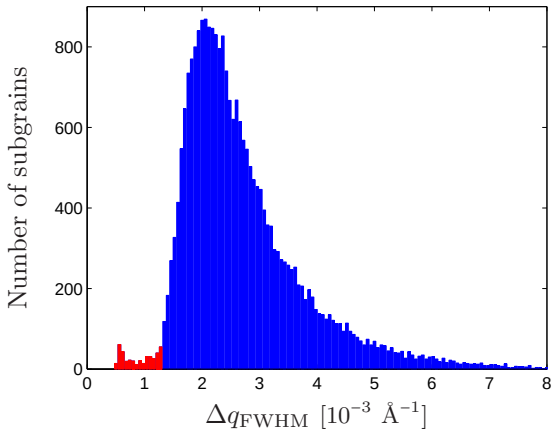

Figure 6.10: A histogram showing the number of identified sharp peaks with different radial widths (FWHM). The red part of the histogram shows the peaks that were ignored in the analysis.

The 80 most intense sharp peaks (measured by the maximum intensity) in each subgrain component were kept for further analysis and grouped into three groups according to the maximum intensity: Peaks number 1 to 10 in the first group, peaks number 11 to 30 in the second group and peaks number 31 to 80 in the third group. These groups will be called large subgrains, medium subgrains, and small subgrains, respectively. Figure 6.11 shows an example of the azimuthal position of the 80 most intense peaks for one reciprocal space map.

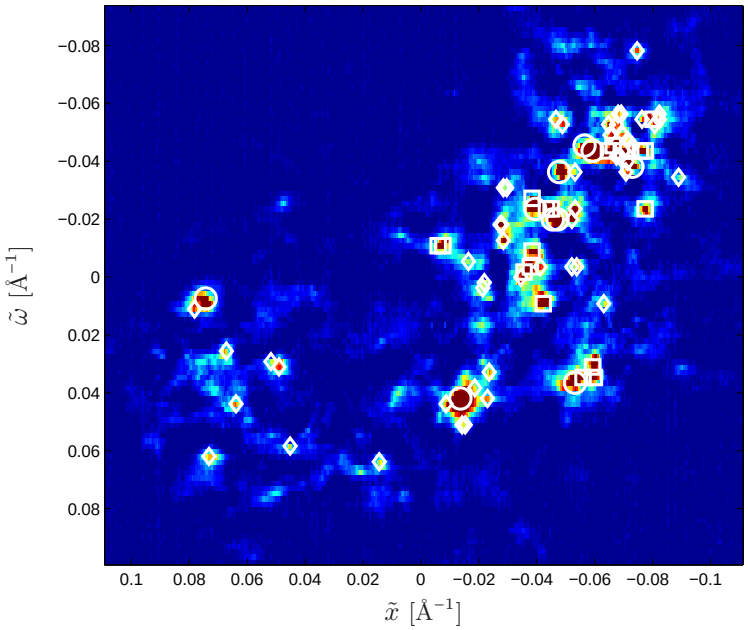

Figure 6.11: An example of an azimuthal map from the subgrain component from grain d2-1 (also shown in figure 6.9) with the position of the 80 most intense sharp peaks. The peaks are grouped according to maximum intensity: Peaks number 1 to 10 (large circles), peaks number 11 to 30 (medium squares), and peaks number 31 to 80 (small diamonds).

Because of the possibility of overlap between individual sharp peaks, it is possible that the 80 peaks do not correspond to the 80 largest subgrains in the grain. Some sharp peaks may represent a number of small subgrains diffracting in (almost) the same direction.

For each peak one-dimensional profiles were calculated from a single row or column of voxels through the center (the voxel with maximum intensity) along the $\tilde{x}$-direction, the $\tilde{\omega}$-direction, and parallel to the vertical detector direction (the latter will be called a radial profile despite the small deviation ($\sim \theta$) between the direction in reciprocal space corresponding to the vertical detector direction and the radial direction). These profiles will be called individual subgrain profiles even though some of the profiles may be composed of the diffracted intensity from more than one subgrain.

Each of the radial profiles were fitted with a split pseudo-Voigt profile and the position was characterized by the position of maximum intensity, $q^{\max}$, and the width by the sum of the half widths of the fitted profile, $\Delta q = \Delta_{\text{low}} + \Delta_{\text{high}}$. Some of the azimuthal profiles had a shape that was not suited for approximations with a split pseudo-Voigt profile, so for the azimuthal profiles the position was characterized by the position of the voxel with maximum intensity and the width was characterized by the FWHM, $\Delta\tilde{x}_{\text{FWHM}}$ and $\Delta\tilde{\omega}_{\text{FWHM}}$.

Three examples of profiles from individual peaks are shown in figure 6.12. The figure contains radial and azimuthal profiles from three different sharp peaks from grain d2-1. The figure shows both the profiles from the subgrain component (where the cloud model has been removed) and the profiles from the same voxels in the original reciprocal space map.

The profiles are rather sharp and the widths in all three directions of reciprocal space are

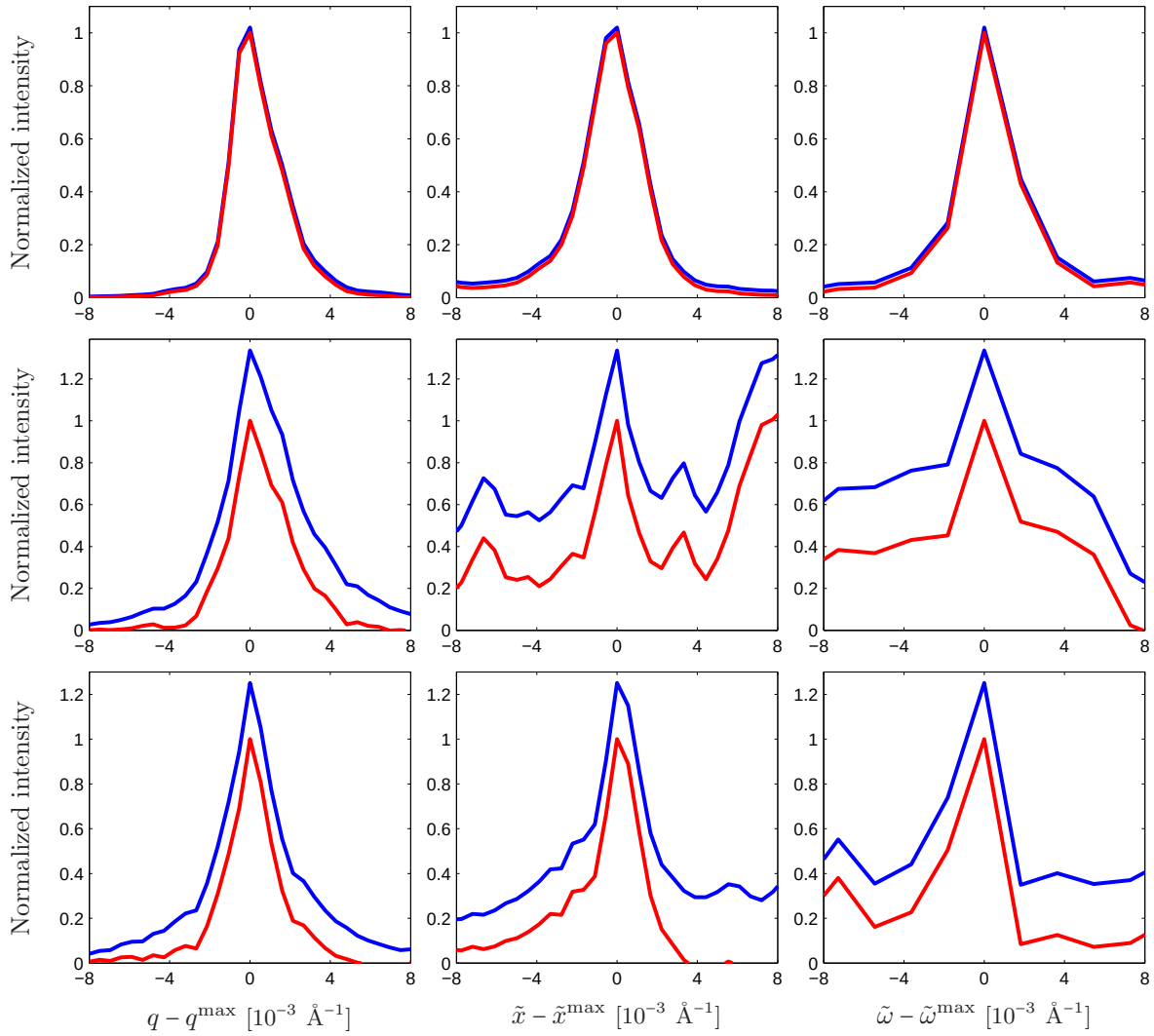

Figure 6.12: Three examples of profiles from individual peaks from grain d2-1. Radial profiles are shown on the left and azimuthal profiles in the center and on the right. The red profiles are from the subgrain component, and the blue profiles are from the same voxels in the original reciprocal space map. Measured by the absolute value of the maximum intensity, the profile shown in the top row is 5 times larger than the profile shown in the middle row and 7 times larger than the profile shown in the bottom row.

comparable. The figure shows that the partitioning is not perfect and that some of the peaks in the subgrain component (particularly the small ones) probably contain parts of the cloud. The radial peak shown in the top left part of the figure is asymmetric. This is the largest peak in the reciprocal space map, and the asymmetry can be interpreted as a sign that the peak is composed of a number of smaller peaks with slightly different radial positions.

The uncertainty in the position and the width of the peaks is estimated to be less than $5.3 \cdot 10^{-4}$ Å^{-1} (the q-width of one pixel) as for the grain profiles.

Furthermore, the profiles were only based on the intensity in a single line or column of voxels and not on integration of the entire intensity in the peaks. This means that the

intensity in the profile tails is underestimated, and if the entire intensity in the peaks were included in the profiles (which would be very difficult to do) they would be wider. The size of this effect depends on the exact shape of the peaks, but it is estimated that the width would be at most a factor of 1.5 larger.

Chapter 7

X-ray diffraction experiments: Results and discussion

In this chapter the results from the analysis described in chapter 6 are presented and discussed. The first section gives a qualitative overview of the evolution of the dislocation structures based on the azimuthal maps. The next three sections present the results from the analysis on three different levels: First the radial profiles from the entire reciprocal space maps, then the subgrain and wall components, and finally the profiles from the individual subgrains. The last section contains a summary and discussion of the results.

7.1 Azimuthal maps

Analysis of the azimuthal maps provide a convenient way to get an overview of the intensity distribution in the reciprocal space maps. The azimuthal maps show the distribution of the crystallographic direction corresponding to the mapped reflection, and the sharp peaks corresponding to subgrains can be easily identified. By analyzing the evolution of the azimuthal maps it is possible to study the evolution of the morphology of the dislocation structures during deformation. The azimuthal maps contain no information about the radial elastic strains, so in order to study the evolution of stresses and strains radial profiles must be analyzed.

Figures 7.1 to 7.8 show examples of the evolution of the azimuthal maps from seven grains as a function of the in situ strain, indicated in the top right corner of each azimuthal map. Apart from the azimuthal maps in figure 7.2, the color scale in each azimuthal map has been adjusted to make the details as clear as possible. This means that the intensity level can not be compared between the different azimuthal maps. The azimuthal maps in figure 7.2 are all shown with the same color scale to show the general effect on the intensity level. For each azimuthal map the horizontal axis shows the values of $\tilde{x}$ and the vertical axis shows the values of $\tilde{\omega}$, both in units of Å^{-1} (in order to save space in the figures this is not written explicitly on the azimuthal maps). The values of $\tilde{x}$ and $\tilde{\omega}$ were calculated from equations (5.5) and (5.7) and measured from a reference point with $\eta = 0\,^\circ$ and $\omega = 7.58\,^\circ$ (and corrected for any change in χ between the reciprocal space maps for each grain). In this way the absolute shift of the reflections in reciprocal space (caused by rotations of the grains) can be determined from the figures. The scale on the axes is the same for all azimuthal maps in each figure, making it easier to compare the different azimuthal maps from each grain.

Figure 7.1 shows six azimuthal maps from grain a1-1 for in situ strains between 0.2 % and 4.8 %. This grain is from a reference sample for which the in situ deformation axis was parallel to the pre-deformation axis ($\alpha = 1$). The reflection spreads in the azimuthal directions and shifts slightly in the $\tilde{x}$-direction. The changes from one azimuthal map to the next are gradual, although the strain steps for this grain are rather large, which makes it difficult to follow the details of the evolution. It is, however, clear that the relative position of the sharp peaks change, corresponding to relative rotations of the subgrains. It can also be seen that the sharp peaks get less intense relative to the cloud, corresponding to a decrease in the size of the subgrains. Due to the different color scale in the different azimuthal maps this can be difficult to see, and therefore the same azimuthal maps are shown in figure 7.2 with a constant color scale which clearly shows the decreasing intensity. In figure 7.1 the largest of the peaks present in the first five azimuthal maps seem to break up into a number of smaller peaks in the last azimuthal map (indicated by the lower arrow), but it is not clear whether this shows a break up of one large subgrain or if it is just caused by relative rotations of subgrains which were initially oriented such that their reflections overlapped. The upper arrow in the last azimuthal map points to a sharp peak which does not appear to be present in the earlier azimuthal maps. This could be interpreted as a sign of the intermittent dynamics reported by Jakobsen et al. (2006).

Figure 7.3 shows six azimuthal maps from grain a2-1 for in situ strains between 0.0 % and 1.0 %. This grain is from a reference sample for which $\alpha = 1$. For this grain the reflection also spreads in the azimuthal directions, but there is almost no azimuthal shift. The strain steps are smaller for this grain than for grain a1-1, which makes it possible to study the evolution of the dislocation structure in greater detail. There is almost no change between the first two azimuthal maps, and after that the changes are gradual without any signs of drastic changes in the morphology of the dislocation structure. For this grain the relative position of the sharp peaks also change, but it is less clear that the intensity of the sharp peaks decreases relative to the cloud, probably because the final level of the in situ strain is smaller for this grain than for grain a1-1. The azimuthal maps contain four large peaks, and two of those start to break up into smaller peaks after a strain of approximately 0.6 % (indicated by the arrows).

Figure 7.4 shows 18 azimuthal maps from grain a2-4 for in situ strains between 1.04 % and 1.56 %. In order to study the evolution in greater detail the strain steps between these azimuthal maps were small and in to save time only partial reciprocal space maps were acquired. This grain is from a reference sample for which $\alpha = 1$. The higher strain resolution shows that also for this grain the changes are gradual with no signs of drastic changes in the dislocation structure.

Figure 7.5 shows 22 azimuthal maps from grain c3-2 for in situ strains between 0.88 % and 1.48 %. As for grain a2-4 this grain was studied with small strain steps and only partial partial reciprocal space maps were acquired. The grain is a from a sample that was subjected to a strain path change with $\alpha = 0$. Again the changes in the azimuthal maps are gradual. An example of a peak splitting into two peaks can be seen after an in situ strain of 1.17 % (indicated by the arrow). A comparison with the azimuthal maps from grain a2-4 shows that there are no clear effects of the strain path change on the evolution of the dislocation structure (in this limited strain interval). The arrow in the azimuthal map corresponding to an in situ strain of 0.95 % points to a sharp peak which appears to suddenly become more intense. This is another example that could be interpreted as a sign of intermittent dynamics.

Figure 7.6 shows six azimuthal maps from grain d2-4 for in situ strains between 0.0 % and

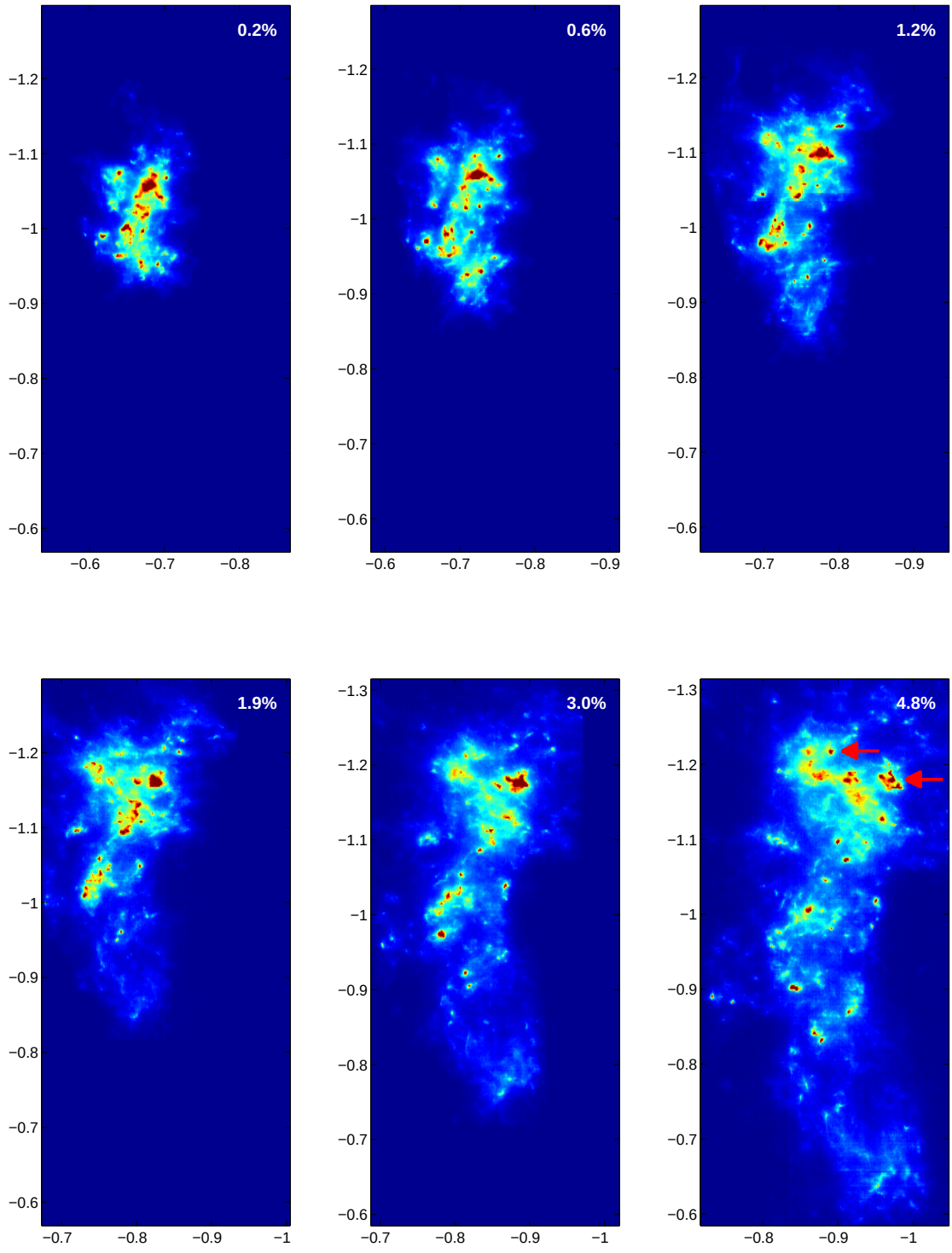

Figure 7.1: Six azimuthal maps from grain a1-1 ($\alpha = 1$) with the in situ strain indicated. The color scale is different for each azimuthal map. For an explanation of the axes and the arrows see the text.

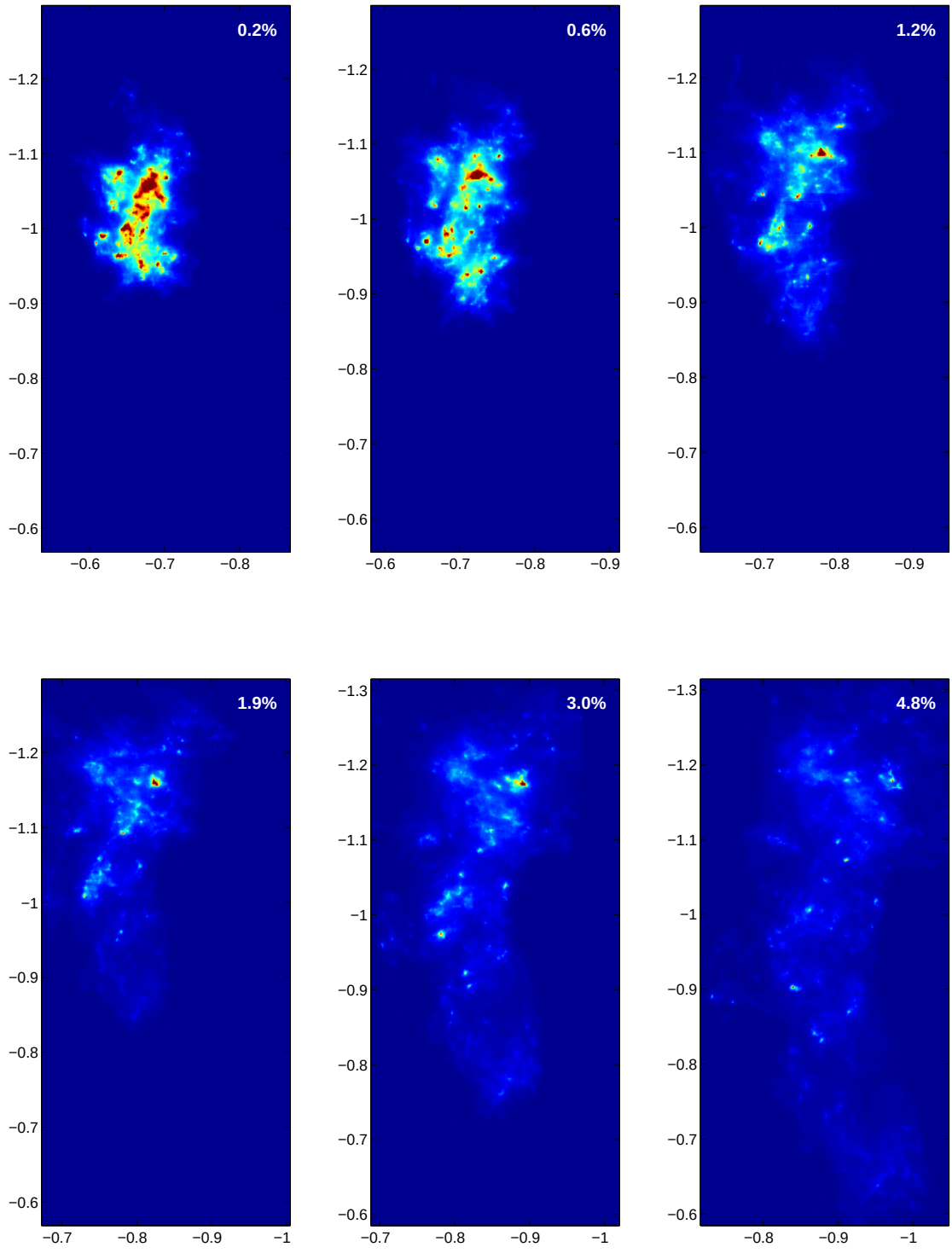

Figure 7.2: Six azimuthal maps from grain a1-1 ($\alpha = 1$) with the in situ strain indicated. The color scale is the same for each azimuthal map. For an explanation of the axes see the text.

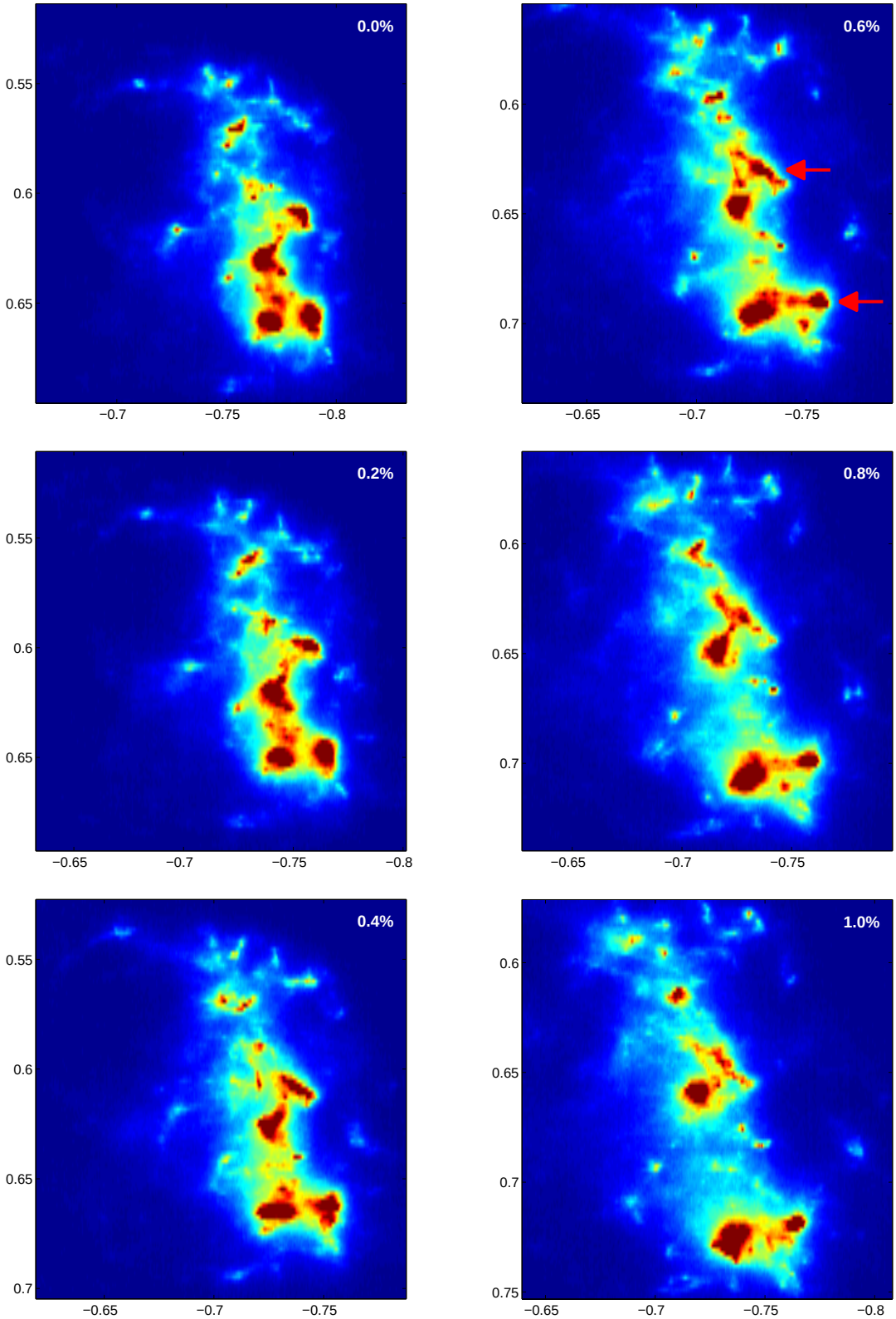

Figure 7.3: Six azimuthal maps from grain a2-1 ($\alpha = 1$) with the in situ strain indicated. The color scale is different for each azimuthal map. For an explanation of the axes and the arrows see the text.

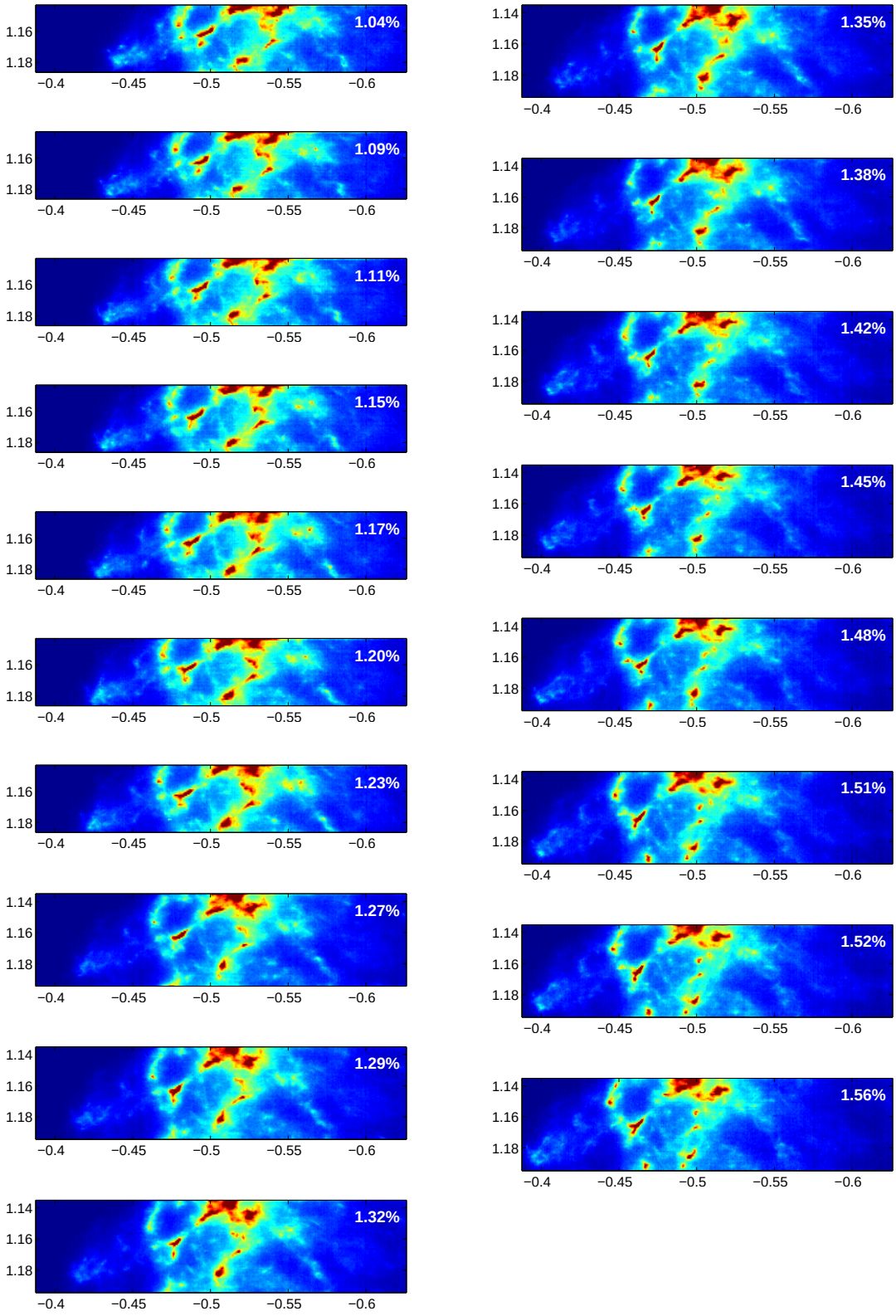

Figure 7.4: 18 azimuthal maps from grain a2-4 (α = 1) with the in situ strain indicated. The color scale is different for each azimuthal map. For an explanation of the axes see the text.

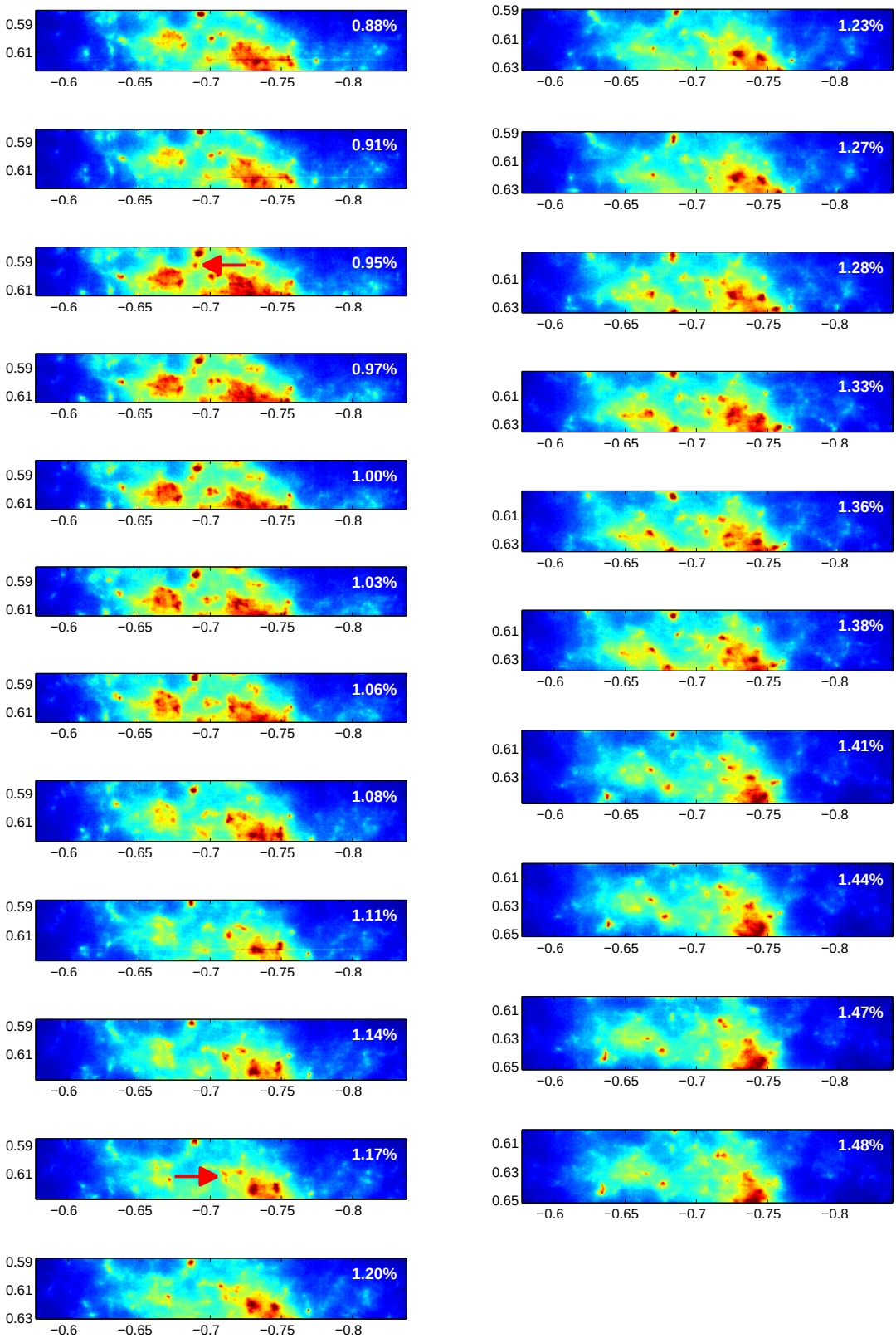

Figure 7.5: 22 azimuthal maps from grain c3-2 (α = 0) with the in situ strain indicated. The color scale is different for each azimuthal map. For an explanation of the axes and the arrows see the text.

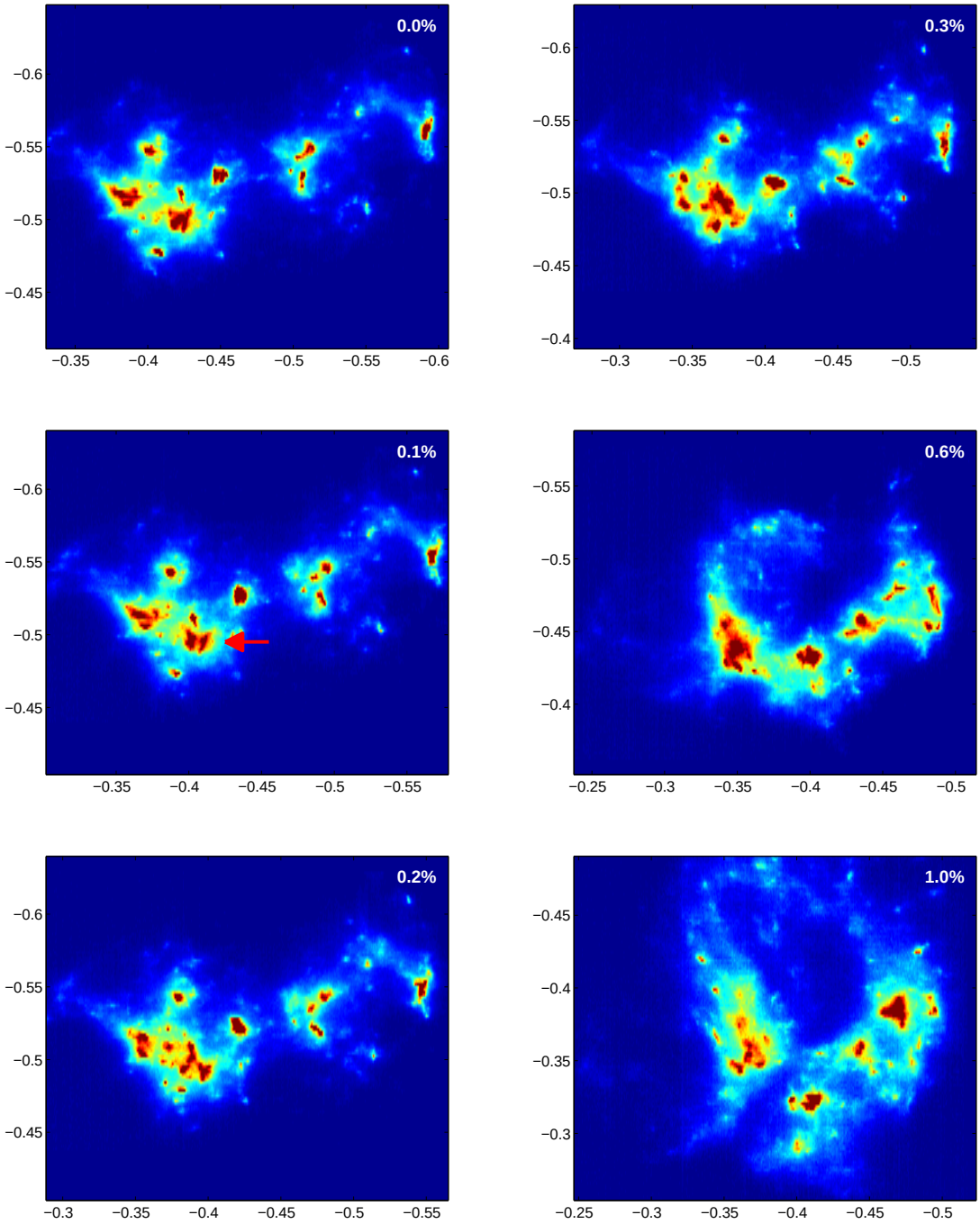

Figure 7.6: Six azimuthal maps from grain d2-4 ($\alpha = -1/2$) with the in situ strain indicated. The color scale is different for each azimuthal map. For an explanation of the axes and the arrow see the text.

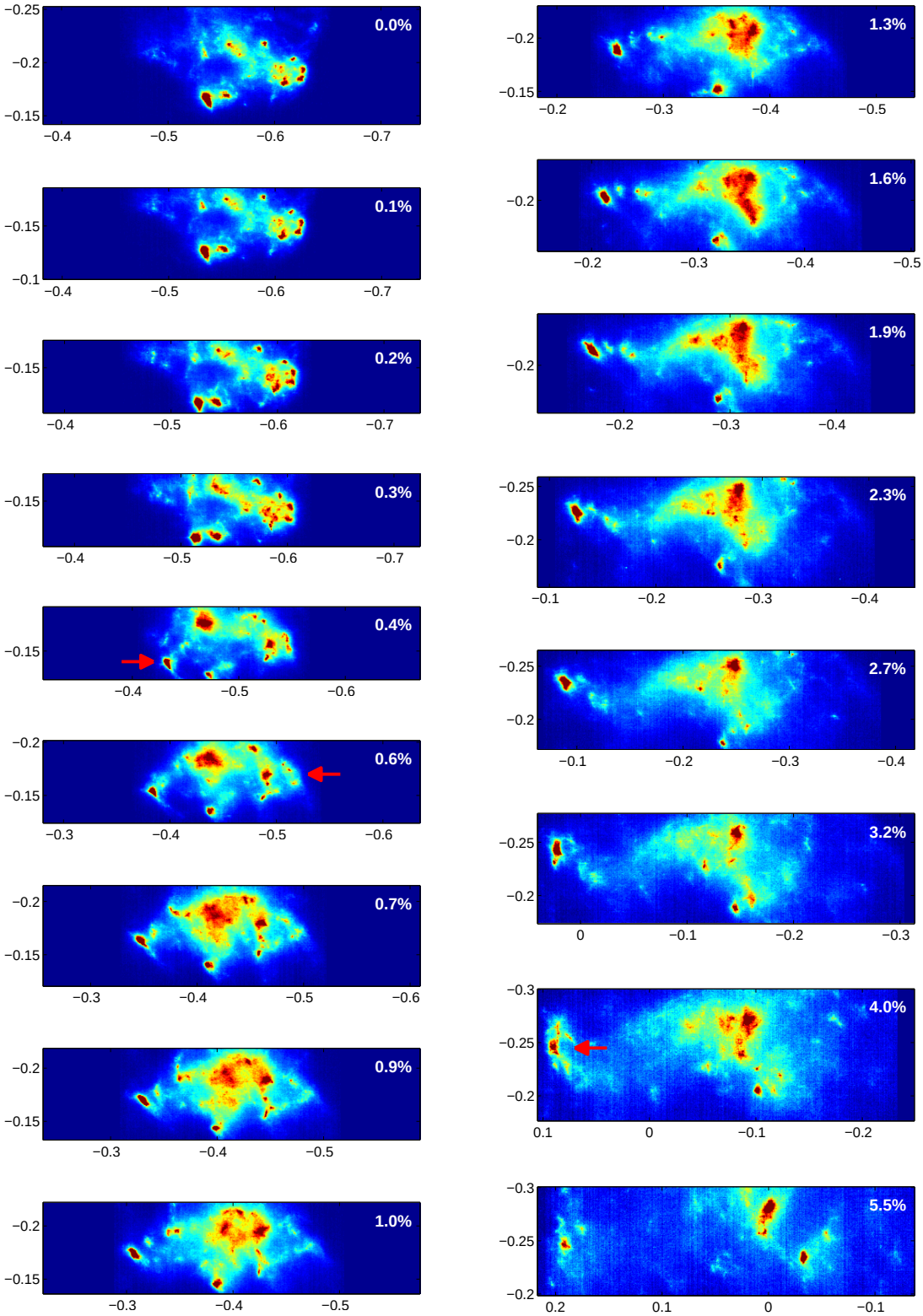

Figure 7.7: 17 azimuthal maps from grain e2-1 ($\alpha = -1/2$) with the in situ strain indicated. The color scale is different for each azimuthal map. For an explanation of the axes and the arrows see the text.

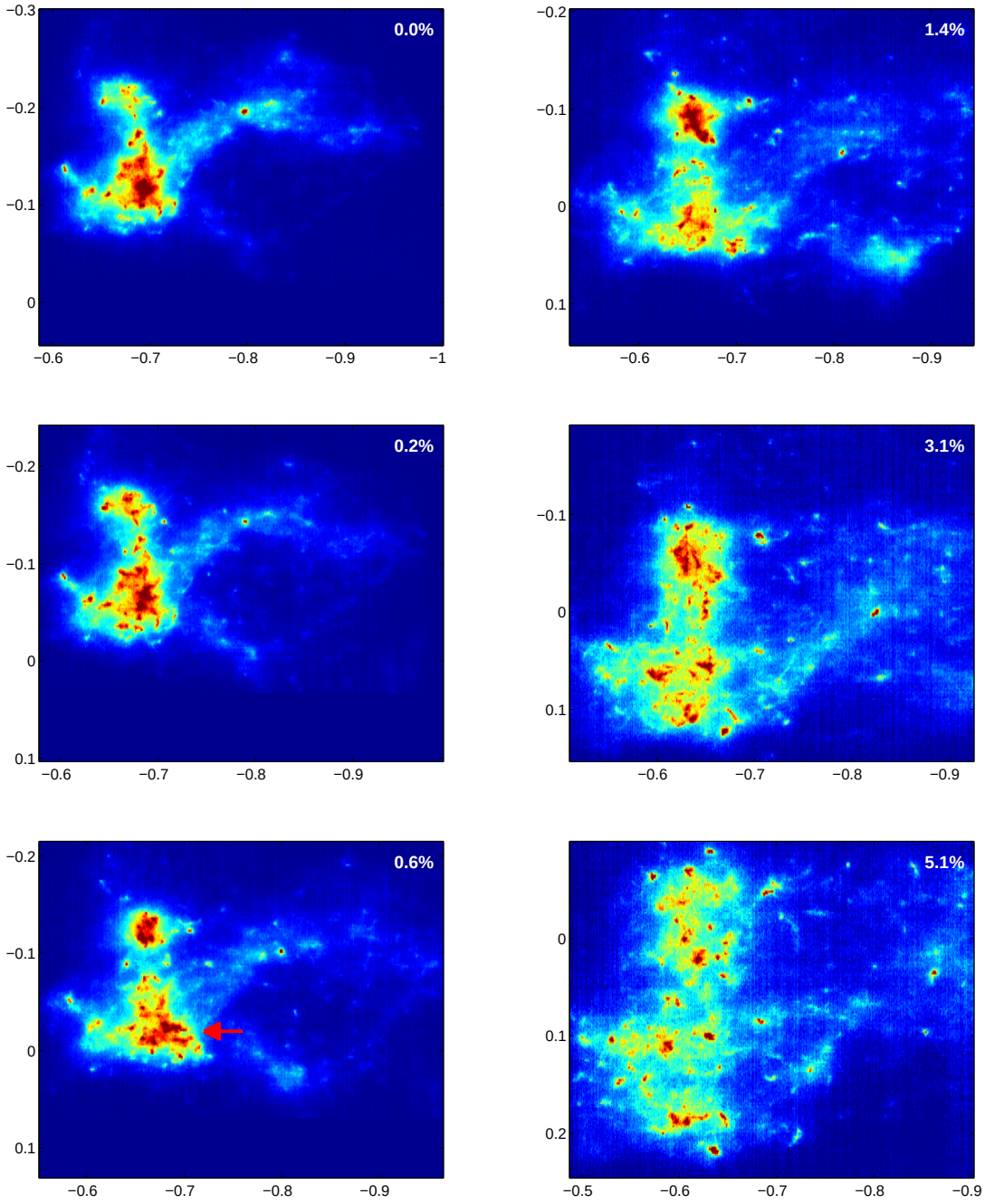

Figure 7.8: Six azimuthal maps from grain h1-1 ($\alpha = 1$, pre-deformation temperature -196 °C) with the in situ strain indicated. The color scale is different for each azimuthal map. For an explanation of the axes and the arrow see the text.

1.0 %. This grain is from a sample that was subjected to a strain path change with $\alpha = -1/2$. The reflection shifts in the azimuthal directions, but the azimuthal widths stay approximately constant. For this grain major changes do not occur before the strain reaches 0.3 %. However, small movements of the sharp peaks are observed already at a strain of 0.1 % leading to a breakup of one of the initially large peaks into smaller peaks at a strain of 0.2 % (indicated by the arrow). The changes are again gradual with no sign of any drastic changes caused by the strain path change.

Figure 7.7 shows 17 azimuthal maps from grain e2-1 for in situ strains between 0.0 % and 5.5 %. This grain is from a sample that was subjected to a strain path change with $\alpha = -1/2$ and the azimuthal maps are from a 222 reflection. For this grain only partial reciprocal space maps were obtained. The reflection spreads and shifts in the $\tilde{x}$-direction. The first four azimuthal maps are nearly identical, but after a strain of 0.3 % the azimuthal maps start to change. As in the previous figures the changes in the azimuthal maps occur gradually with no sign of any drastic changes in the dislocation structure caused by the strain path change. The figure shows an example of a subgrain which rotates much faster than the average rotation (indicated by the arrow on the azimuthal map for a strain of 0.4 %) and finally appears to break up into smaller peaks (indicated by the arrow on the azimuthal map corresponding to a strain of 4.0 %), some of which disappear into the cloud. On the other side of the reflection some of the sharp peaks which were well defined in the beginning are seen to slowly fade into the cloud (indicated by the arrow on the azimuthal map corresponding to a strain of 0.6 %).

Figure 7.8 shows six azimuthal maps from grain h1-1 for in situ strains between 0.0 % and 5.1 %. This grain is from a sample that was pre-deformed at a temperature of -196 °C and then deformed in situ along the same axis ($\alpha = 1$). The changes for this grain are similar to the changes observed for the reference grains that were pre-deformed at room temperature: The reflection spreads and shifts in the azimuthal directions, and the sharp peaks change their relative position and get less intense relative to the cloud. After a strain of 0.6 % one of the initially large peaks begins to break up into a number of smaller peaks (indicated by the arrow).

Based on the azimuthal maps shown in figures 7.1 to 7.8 and the azimuthal maps from the other grains, the conclusions about their evolution can be summarized as follows:

- There are only minor changes in the azimuthal maps for in situ strains below 0.3 %.
- For larger strains the reflections spread and shift in the azimuthal directions.
- The changes occur gradually with no signs of drastic changes in the dislocation structure.
- Very few examples of events that could be interpreted as intermittent dynamics were observed.
- As the strain is increased the sharp peaks shift relative to each other and generally get less intense relative to the cloud.
- There are examples of large peaks breaking up into smaller peaks and of small peaks disappearing into the cloud.
- From the visual inspection of the azimuthal maps there are no clear indications that a strain path change or a change in temperature has an effect on the evolution of the morphology of the dislocation structures.

The results show that for in situ strains below 0.3 % no significant changes occur in the morphology of the dislocation structures. According to figure 5.6, this strain value corresponds to a stress equal to or slightly above the yield stress. In the following a strain level of 0.2 % to 0.3 % will be taken as a limit between the micro-plastic range of deformation and the macro-plastic range of deformation.

For strains above 0.3 %, the changes in the morphology of the dislocation structures appear to occur in a gradual manner without any sudden major changes, which indicates that the dislocation structures are relatively robust. This impression of the evolution happening through gradual changes through relatively stable states is quite different from the picture of the dynamics controlled by intermittent dynamics suggested by Jakobsen et al. (2006). In the reciprocal space maps investigated in this work there are very few examples which may be interpreted as signs of intermittent dynamics (some of which were described above), and it seems that such processes do not play a major role in the evolution of the dislocation structures.

The azimuthal maps show no clear effects of either a strain path change or a change in temperature, and even in the cases where the dislocation structure may have to change its morphology to accommodate the new deformation conditions, the changes seem to occur gradually. For both the reference samples and the samples subjected to a change in loading conditions many of the azimuthal maps show signs of the cell size decreasing: Large sharp peaks appear to break up into smaller peaks and small sharp peaks appear to fade into the cloud. It is, however, difficult to say anything about the processes involved in this based on the azimuthal maps.

7.2 Radial profiles from individual grains

Radial profiles were calculated from each reciprocal space map and the evolution of the position and shape of the profiles was analyzed as described in section 6.2. The radial profiles calculated from the entire reciprocal space maps will be called grain profiles to distinguish

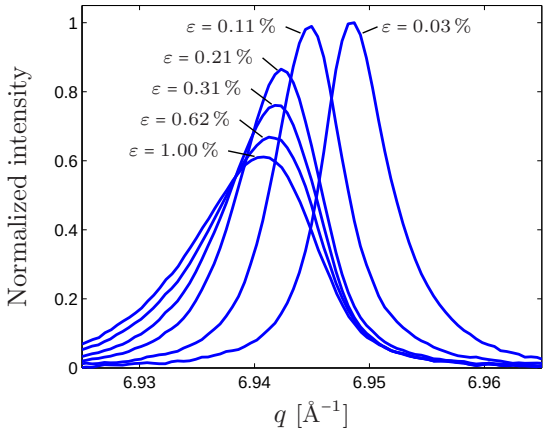

Figure 7.9: Radial profiles from grain d2-1 with corresponding values of in situ strain. As the strain increases the profiles shift to lower q-values and their width increases. The profiles have been normalized to have the same area.

them from the radial profiles calculated from the subgrain and wall components and the radial profiles from the individual subgrains.

To illustrate the typical changes observed in the grain profiles during deformation a series of profiles from grain d2-1 are shown in figure 7.9. As the grain is deformed, the position of the profiles shifts to lower q-values, and the width of the profiles increases. This general behavior was observed for all grains.

Below, results from the analysis of the position, width, asymmetry, and Lorentz fraction of the profiles, and from fitting the grain profiles with a Wilkens and a Gauss profile are presented and discussed.

7.2.1 Position of the grain profiles

From the mean profile position the mean radial elastic strain in the grains was calculated with the help of equation (3.8). The results are shown as a function of the applied stress in figure 7.10. The slope of the black line included in the figure corresponds to the value of Young's modulus (E = 105 GPa) determined from the mechanical tests described in section 4.3. For clarity the results for samples xa2, xc3, and xd2 are also shown in figure 7.11.

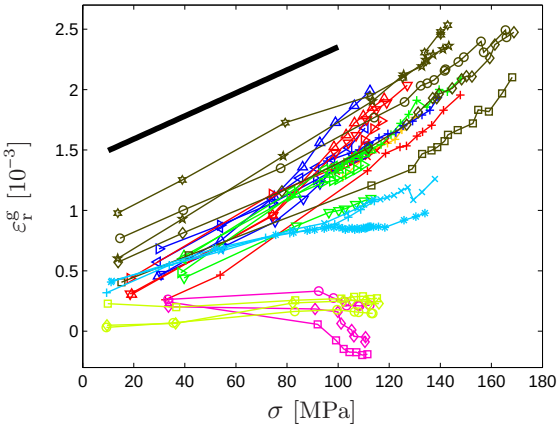

Figure 7.10: The mean radial elastic strain in the grains as a function of the applied stress. The slope of the black line corresponds to E = 105 GPa.

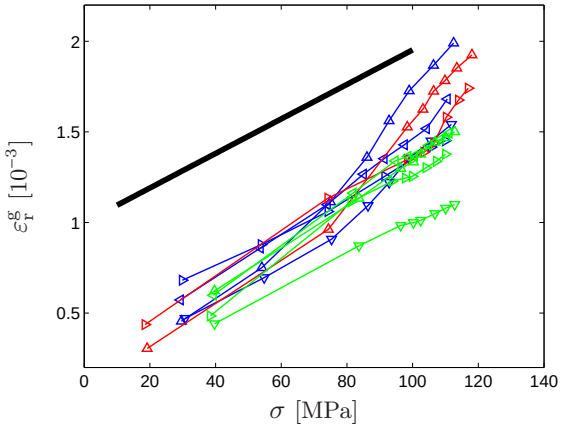

Figure 7.11: The mean radial elastic strain in the grains from samples xa2, xc3, and xd2 as a function of the applied stress. The slope of the black line corresponds to E = 105 GPa.

The radial elastic strain for grain groups A, B, C, D, E, and H increases approximately linearly with the applied stress (with a somewhat smaller slope for the curves for grain group E), and the slope of the curves is consistent with the value of Young's modulus determined from the characterization of the macroscopic mechanical properties. The radial elastic strain for grain groups F and G is close to zero, and for grain group G it even decreases for stresses above 90 MPa. There is significant variation both between curves from different samples and between curves from different grains in the same sample. In general, the curves show deviations from linear behavior, particularly for grain groups C, D, and G.

For grain groups A, B, C, D, and H the scattering vector and the in situ deformation axis were both parallel to a [100] direction, and for grain group E they were both parallel to a [111] direction. This explains the slightly lower slope of the curves for grain group E, because

Young's modulus is smaller along a [111] direction than along a [100] direction. The observed effect is not as strong as might be expected from the respective values of Young's modulus for the two directions, most likely because of a load transfer between the grains caused by the requirement for compatible deformation. The deviations from linear behavior for grain groups C and D is interpreted as a result of changes in inter-granular stresses as discussed below.

For grain groups F and G there was an angle of approximately 55 ° between the scattering vector and the in situ deformation axis. In this case the radial elastic strain, ε_r, is found from the elastic strains parallel, ε, and perpendicular, $\varepsilon_\perp$, to the deformation axis as

$$\varepsilon_r = \cos^2(55\,^\circ)\varepsilon + \sin^2(55\,^\circ)\varepsilon_\perp = (\cos^2(55\,^\circ) - \nu\sin^2(55\,^\circ))\varepsilon = 0.1\varepsilon. \tag{7.1}$$

This equation shows that the slope of the curves for grain groups F and G should be an order of magnitude smaller than the slope of the curves for the other grain groups, and this explains the low elastic strain observed for these grain groups. As discussed below, the decrease in radial elastic strain for stresses above 90 MPa for grain group G is interpreted as a result of changes in inter-granular stresses.

The variation between the curves in figure 7.10 indicates that the different grains experience significantly different elastic strains. To see if the differences could be due to wrong values of the grain-to-detector distance used in the calculation of some of the radial profiles, the size of such an effect was estimated. The detector position was calibrated with an error estimated to be less than 100 μm, the error in the position of the grain within the sample must be less than 150 μm (half the thickness of the samples), and the error caused by misalignment along the y-axis (such that a shift in y would change the grain-to-detector distance) was estimated from measurements on a few samples to be at most 50 μm. A worst case estimate of the effect of an error in the grain-to-detector distance was calculated by using a maximum value of 300 μm for the error and calculating the corresponding error in the radial elastic strain. The result was a shift of $8 \cdot 10^{-5}$ (which is also approximately the resolution in radial elastic strain corresponding to the size of a pixel), which is significantly smaller than the variations observed in the figures. Furthermore, for grains within the same sample, errors in the calibration of the detector position or misalignment of the sample would have a systematic effect and not give rise to variations between the corresponding curves. These arguments indicate that the variations between the curves in the figures represent real variations in elastic strain between the grains and show that inter-granular stresses (variations in the local stress between the different grains) exist in the samples. The deviations from linearity observed for some of the curves in the figures may be interpreted as changes in the inter-granular stresses during the deformation.

For each sample the horizontal difference between the curves can be used to give an estimate of the inter-granular stresses. The result is a value of ±10 MPa for the grains pre-deformed to a strain of 5 % at room temperature and ±30 MPa for the grains pre-deformed to a strain of 7.2 % at a temperature of -196 °C.

When interpreted in terms of inter-granular stresses, the significant departure from linearity of the curves for grain groups C, D, and G show that for the samples subjected to a strain path change, the inter-granular stresses change significantly when the stress reaches the yield stress. This can be understood as a consequence of changes in the local flow stress in the different grains. When the tensile axis is changed during the strain path change, the applied stress required for plastic deformation of each grain is altered because of the anisotropy of the

internal stresses and the activation of different slip systems. As a result there is a transfer of load from grains which were hard with respect to the pre-deformation but soft with respect to the second deformation to grains which were soft with respect to the pre-deformation but hard with respect to the second deformation. The grains in grain groups C and D, for which the elastic strain increases faster when the yield stress is reached, were pre-deformed along a direction different from [100] and deformed along a [100] direction during the in situ deformation. Contrary to this, the grains in grain group G, for which the elastic strain decreases when the yield stress is reached, were pre-deformed along a [100] direction and deformed along a different direction during the in situ deformation. This indicates that the local flow stress is highest for deformation along a [100] direction.

In conclusion, the measured radial elastic strain is consistent with the value of Young's modulus determined from the macroscopic measurements, and the different behavior of the different grain groups can be understood from the differences in orientation of the grains and the in situ deformation axis with respect to the scattering vector. The variation between curves from the same or similar grain groups can be explained by the presence of inter-granular stresses, and the magnitude of these stresses can be estimated. For the grains subjected to a strain path change, the results indicate that the load is redistributed between grains with different orientations when the yield stress is reached.

7.2.2 Width of the grain profiles

The integral width of the grain profiles is shown in figures 7.12 and 7.13 as a function of the in situ strain. For all the grains, the width increases with strain, and the rate of increase decreases after a strain of about 0.2 % to 0.3 %. For grain group E the width is only about half of the width for the other grain groups. For the other grain groups the width is smallest for grain groups F and G and largest for grain group H. A comparison of the curves for samples xa2, xc3, and xd2 (shown in figure 7.14) shows that the width is larger for the grains subjected to a strain path change. Figure 7.15 shows the integral width of the grain profiles for samples xa2, xc3, xd2, and xh1 as a function of the applied stress.

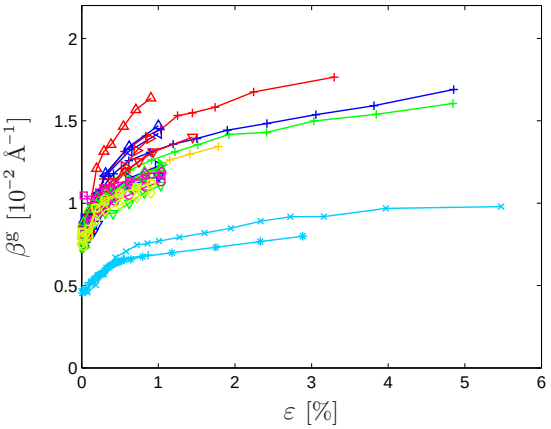

Figure 7.12: The integral width of the grain profiles for grain groups A, B, C, D, E, F, and G as a function of the in situ strain.

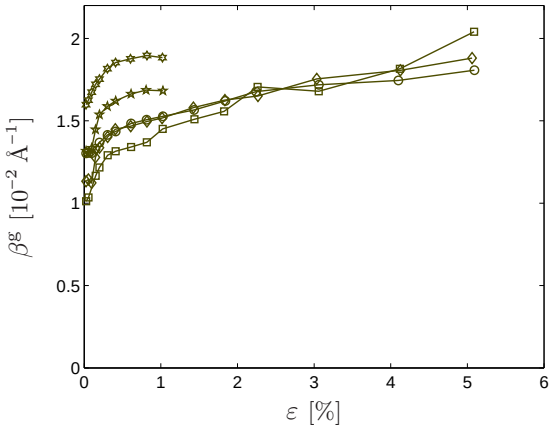

Figure 7.13: The integral width of the grain profiles for grain group H as a function of the in situ strain.

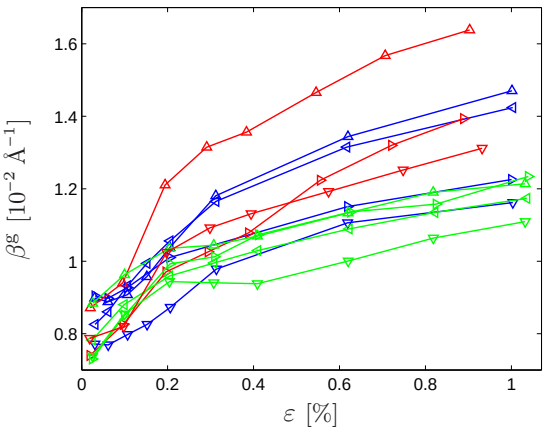

Figure 7.14: The integral width of the grain profiles for samples xa2, xc3, and xd2 as a function of the in situ strain.

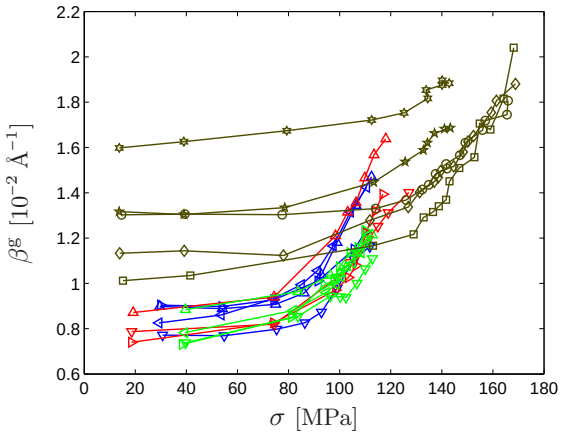

Figure 7.15: The integral width of the grain profiles for samples xa2, xc3, xd2, and xh1 as a function of the applied stress.

Because the grain profile is the sum of the subgrain profile and the wall profile, the width of the grain profile, if measured by the second central moment (the square of the standard deviation) is given by

$$\left(\sigma^{\mathrm{g}}\right)^2 = \left(1 - f^{\mathrm{s}}\right)\left(\sigma^{\mathrm{w}}\right)^2 + f^{\mathrm{s}}\left(\sigma^{\mathrm{s}}\right)^2 + \left(1 - f^{\mathrm{s}}\right) f^{\mathrm{s}} \left\langle q^{\mathrm{w}} - q^{\mathrm{s}} \right\rangle^2 , \tag{7.2}$$

where σ^{g}, σ^{w}, and σ^{s} are the standard deviations of the grain profile, the wall profile and the subgrain profile, respectively, f^{s} is the fraction of intensity in the subgrain profile (corresponding to the volume fraction of subgrains in the grain), and q^{w} and q^{s} are the position of the wall profile and the subgrain profile, respectively. The angled brackets denote the average value. It follows that the width of the grain profile is affected by the factors that influence width of the subprofiles or their relative position or intensity:

First, the dislocation density in the walls influences the width of the wall profile through strain broadening. The modified composite model assumes that for the subgrain profile and the radial profiles for the individual subgrains the effect of the dislocation density is negligible.

Second, the arrangement of the dislocations (quantified by the dislocation arrangement parameter M) influences the width of the wall profile. Because the modified composite model assumes a vanishing dislocation density in the subgrains, this factor is also assumed to be negligible both for the subgrain profile and for the radial profiles for the individual subgrains.

Third, the average intra-granular stress in the subgrains and in the walls shift the two subprofiles relative to each other, thereby increasing the width of the grain profile.

Fourth, the variation in the intra-granular stresses between the subgrains shifts the narrow profiles from the individual subgrains relative to each other, thereby increasing the width of the subgrain profile. Because of the high density of dislocations and the accompanying varying stress fields in the walls, the local stress is not as well defined in the dislocation walls as in the subgrains. Stress variations in the walls are thus most conveniently thought of as part of the strain broadening due to their dislocation content described above.

Fifth, the subgrain volume fraction determines the relative influence of the two subprofiles on the width of the total profile.

Based only on the data presented in figures 7.12 to 7.15 it is difficult to determine the relative influence of the different effects on the evolution of the grain profile width. However, the effects of both the average intra-granular stress and the variation in the intra-granular stresses would presumably lead to a constant or decreasing rate of increase in the width as a function of the applied stress. Figure 7.15 shows that from a certain stress level the width increases at a faster rate as a function of the applied stress. This implies that from this point on the effects of dislocation multiplication becomes important. The transition happens near the yield stress (which is larger for grain group H because of the larger pre-deformation), and for larger stresses the increase in the profile width appears to be controlled by the increase in dislocation density. For smaller stresses, in the micro-plastic range, the increase in the width is most likely caused by an increase in the average intra-granular stress or the variation in the intra-granular stresses or both.

Although the curves in figures 7.12 and 7.13 all show the same general behavior, there are significant differences between the different grain groups. As described in section 3.2.2, the profile width depends both on the length of the scattering vector and on the contrast factor, both of which are different for 222 reflections compared to 400 reflections, and this explains the smaller width for grain group E (for which 222 reflections were investigated). Ungár (2001) has measured the profile width for different reflections from copper and found that the integral width of the 400 reflection was slightly more that twice the integral width of the 222 reflection. This is about the same ratio as in figure 7.12, where the integral width for grain group E is approximately half the integral width for the other grain groups.

The grains in grain groups F and G were observed with an angle of approximately 55 ° between the scattering vector and the in situ deformation axis. The calculation performed in equation (7.1) show that axial stresses along the tensile direction lead to elastic strains along the direction parallel to the scattering vector which are an order of magnitude smaller than the elastic strains along the tensile direction. This means that purely tensile stresses (or variations therein) can not explain the increase in width of these profiles observed during the micro-plastic range. This suggests that there is a variation in the intra-granular stresses not only along the tensile axis but also in the perpendicular directions. The smaller width for these grains is discussed in relation to their symmetry below.

The larger width observed for grain group H can be explained by the larger pre-deformation and the corresponding larger dislocation density. It is likely that the low temperature of the pre-deformation contributed to an increase in the dislocation density due to suppression of thermally activated recovery processes.

The larger width for samples xc3 and xd2 compared to sample xa2 in figure 7.14 may be interpreted as an indication that in the grains subjected to a strain path change, processes operating during the micro-plastic range or in the beginning of the macro-plastic range lead to an increase in the width which remains during further deformation (of at least 0.7 % strain).

In conclusion, the increase in the width of the grain profiles falls in two ranges. In the micro-plastic range the increase in width can best be explained as a consequence of an increase in the average intra-granular stress or in the variation in the intra-granular stresses or both, also in directions perpendicular to the tensile axis. In the macro-plastic range the increase in width is dominated by the increasing dislocation density in the walls.

The variation in width between the different grain groups is explained by differences in the investigated reflections, the amount of pre-deformation, and the scattering geometry. Furthermore, the results suggest that a strain path change leads to a larger width for the grain profile compared to uniaxial deformation.

7.2.3 Asymmetry of the grain profiles

Figure 7.9 showed how the radial profiles from a single grain change with increasing deformation. A close look at the figure reveals that the asymmetry of the profiles changes from negative to positive. To illustrate this more clearly the first and last of the profiles from the figure are shown in figure 7.16, where the axes are scaled such that the profiles have the same maximum intensity, the same position of maximum intensity, and the same integral width. The asymmetry is indicated in the figure, showing that the first profile has a negative asymmetry (a longer tail on the high-q side) and the last profile has a positive asymmetry (a longer tail on the low-q side).

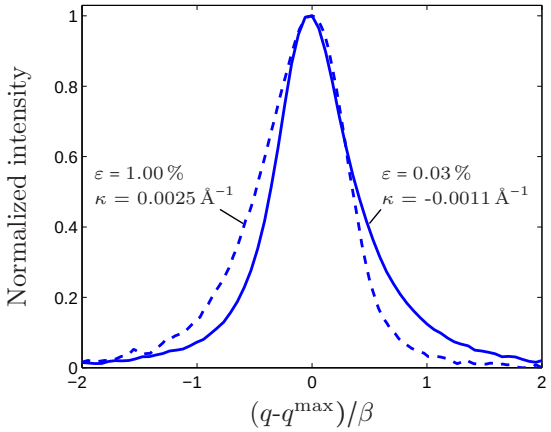

Figure 7.16: Illustration of the change in asymmetry between the first (solid line) and last (dashed line) profile in figure 7.9. The profiles are from grain d2-1, and the corresponding values of in situ strain and asymmetry are indicated.

The asymmetry for all the investigated grains is shown in figures 7.17 and 7.18 as a function of the in situ strain. For clarity the asymmetry for samples xa2, xc3, xd2, xe1, xe2, and xe3 is shown in figure 7.19, and the asymmetry for samples xf1, xg1, and xh1 is shown in figure 7.20 up to a strain of 1 %. To show that the results are generally independent of the chosen measure of asymmetry, figures 7.21 and 7.22 show the relative asymmetry for the same samples. There are only minor differences between the two sets of figures.

The figures show that the asymmetry varies considerably more during the first 0.2 % to 0.3 % of strain than for higher strains. For the reference grains in grain group A the asymmetry is positive and nearly independent of the in situ strain. However, figure 7.19 shows that the asymmetry is lower for the first point for some of the samples, and figure 7.17 shows that the asymmetry increases for higher strains.

A comparison of grain groups B, C, D, and E (which all consist of grains subjected to a strain path change) shows that the asymmetry for grain group E is lower than the asymmetry for the other grain groups, but for all the groups the asymmetry first increases from an initially low (negative in most cases) value and then becomes approximately constant after a strain of approximately 0.2 % to 0.3 %.

The asymmetry for grain group F is close to zero for all strains, and for grain group G it starts at positive values and then decreases to levels close to zero.

For grain group H the asymmetry decreases (for four out of five grains) during the first

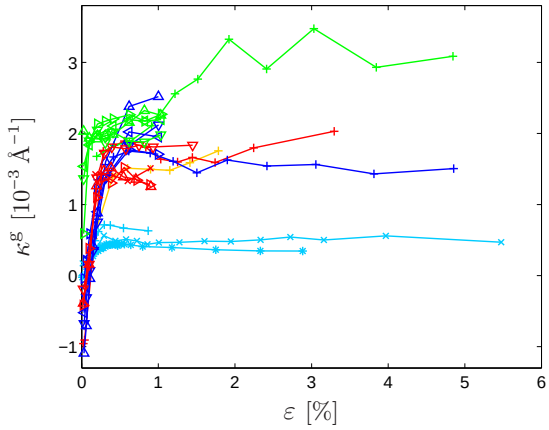

Figure 7.17: The asymmetry of the grain profiles for grain groups A, B, C, D, and E as a function of the in situ strain.

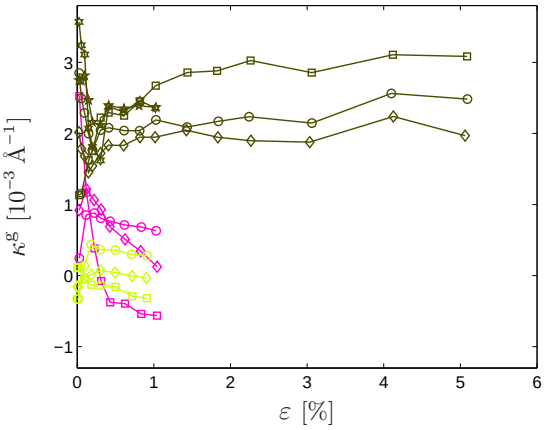

Figure 7.18: The asymmetry of the grain profiles for grain groups F, G, and H as a function of the in situ strain.

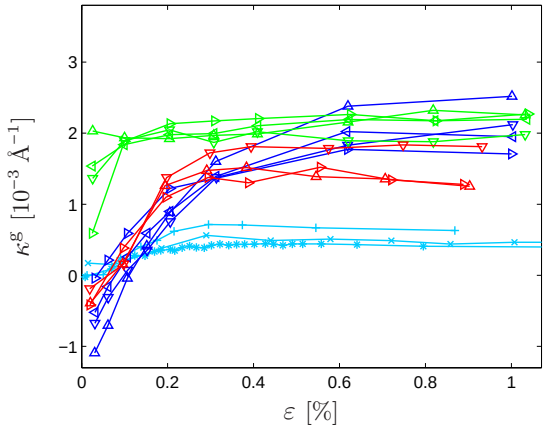

Figure 7.19: The asymmetry of the grain profiles for samples xa2, xc3, xd2, xe1, xe2, and xe3 as a function of the in situ strain.

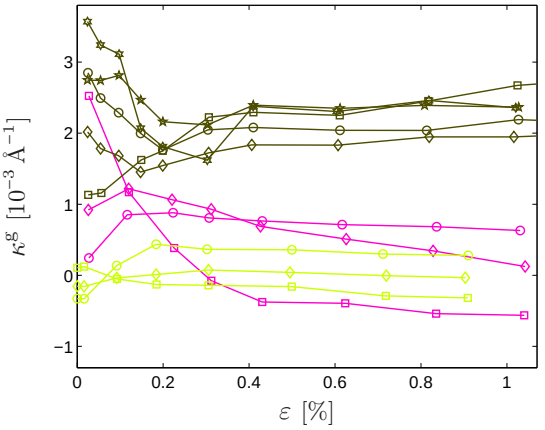

Figure 7.20: The asymmetry of the grain profiles for samples xf1, xg1, and xh1 as a function of the in situ strain.

0.2 % of strain before it increases slightly again and reaches an approximately constant level after a strain of approximately 0.3 %.

The modified composite model explains the asymmetry as a result of the relative shift of the subprofiles from the subgrains and the walls caused by intra-granular stresses. With this interpretation the initial positive asymmetry for grain group A can be understood as a result of the intra-granular stresses developed during the pre-deformation. These grains were investigated with the scattering vector parallel to the pre-deformation axes, corresponding to the axial case, which results in a positive asymmetry. Because the in situ deformation axis was parallel to the pre-deformation axis, the intra-granular stresses did not change significantly during the in situ deformation, and a positive asymmetry is observed for all strains. The lower asymmetry observed for the first point for some of the grains in figure 7.19 may be related to effects of unloading or to effects of recovery during storage or both. The increase in

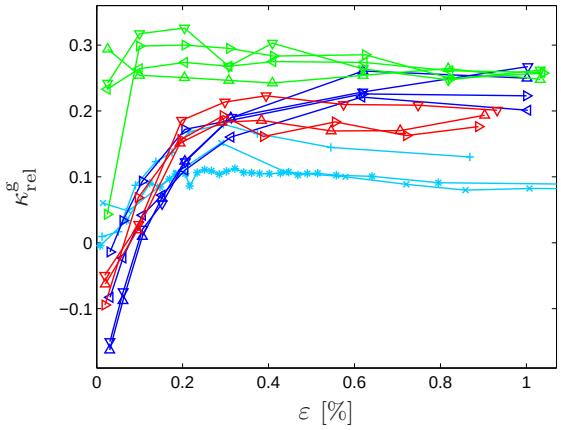

Figure 7.21: The relative asymmetry of the grain profiles for samples xa2, xc3, xd2, xe1, xe2, and xe3 as a function of the in situ strain.

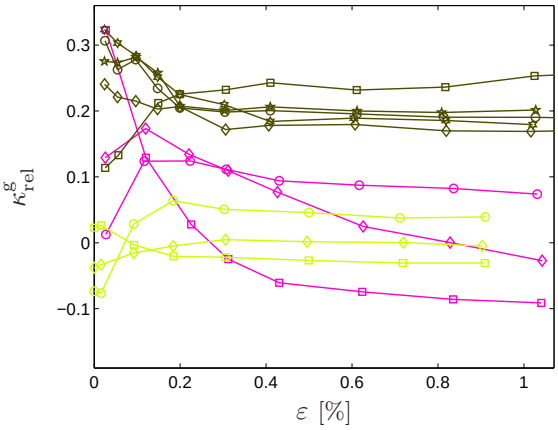

Figure 7.22: The relative asymmetry of the grain profiles for samples xf1, xg1, and xh1 as a function of the in situ strain.

asymmetry for grain a1-1 for larger strains shown in figure 7.17 may be explained as a result of an increase in the average intra-granular stress caused by work hardening in the walls.

For grain groups B, C, D, and E the scattering vector and the pre-deformation axis were not parallel. For grain group D the scattering vector was perpendicular to the pre-deformation axis, so these grains were initially observed in the side case, resulting in a negative asymmetry as observed for sample xd2 in figure 7.19. For grain groups B and C the situation was initially somewhere between the axial and the side case, resulting in a small asymmetry as shown for sample xc3 in figure 7.19. During the in situ deformation the intra-granular stresses developed during the pre-deformation gradually changed, leading to a larger and positive asymmetry along the new tensile axis. From figure 7.19 it is clear that the change in asymmetry primarily takes place during the micro-plastic range. From the figure it also appears that for sample xd2 the asymmetry continues to increase slightly after a strain of 0.3 % whereas for sample xc3 it remains constant. The lower asymmetry for grain group E may be related to the different orientation of these grains with respect to the tensile axis, as grains deformed with the tensile axis close to a [111] direction develop a different dislocation structure than grains deformed with the tensile axis close to a [100] direction as described in section 2.2.2.

For the grains in grain group F the in situ deformation axis and the pre-deformation axis were parallel and they were observed with an angle of approximately 55 ° between the scattering vector and the in situ deformation axis. Observed under this angle the intra-granular stresses produce almost no radial shift of the subprofiles, and this explains why the observed asymmetry is very low for all strains.

The grains in grain group G were initially observed in the axial case, and the asymmetry is initially positive. During the in situ deformation along a new axis the intra-granular stresses changed, and because of the angle of approximately 55 ° between the scattering vector and the in situ deformation axis the asymmetry along the scattering vector gradually decreases with increasing strain as the intra-granular stresses change.

The large initial asymmetry for the grains in grain group H may be a result of both the larger pre-deformation strain for these samples and the low pre-deformation temperature. Both lead to a larger flow stress during the pre-deformation and this may lead to larger intra-

granular stresses. The initial drop in asymmetry observed for most of these grains indicate that significant changes occur in the dislocation structure upon continued deformation at room temperature, resulting in a decrease of the average intra-granular stress.

The relative magnitude of the initial asymmetry in the axial case and in the side case is related to the Poisson effect. The initial positive asymmetry for sample xa2 is caused by intra-granular stresses along the direction of the pre-deformation axis and the resulting elastic strains along the same direction. The initial negative asymmetry for sample xd2 is caused by intra-granular stresses along the direction of the pre-deformation axis and the resulting perpendicular elastic strains caused by the Poisson effect. Because the asymmetry is expected to be roughly proportional to the mean radial elastic strain in the subgrains, this means that the ratio of the initial asymmetry for the two samples should be approximately equal to the negative of the Poisson ratio for copper, which is 0.34 (Noyan & Cohen 1987). As figure 7.19 shows this is indeed the case: For sample xa2 the initial asymmetry is approximately three times the initial asymmetry for sample xd2 and has the opposite sign.

A comparison of figures 7.14 and 7.19 suggests a correlation between the width and the asymmetry. Samples xc3 and xd2 were subjected to a strain path change and in figure 7.14 the curves for these samples show a shift from convex to concave behavior at the strain level where the asymmetry changes from negative to positive values. In contrast, the curves for sample xa2, for which the asymmetry is positive at all strains, show a concave behavior for all strains. This can be understood from the fact that the relative shift of the two subprofiles, which produces the asymmetry, also increases the width of the grain profile. This means that for strains around 0.1 %, where the grain profiles for samples xc3 and xd2 are nearly symmetric, their width is slightly reduced. This also explains why the grain profile width was relatively small for grain groups F and G (for which the asymmetry is close to zero) as shown in figure 7.12.

In conclusion, the evolution of the asymmetry of the grain profiles is quite different for the different grain groups. The asymmetry for the reference grains is nearly constant, but for the grains subjected to a strain path change, the asymmetry changes significantly during the micro-plastic range as a result of substantial changes in the intra-granular stresses. The asymmetry for most of the grains in the sample pre-deformed at a temperature of -196 °C decreases at the beginning of the in situ loading, indicating significant changes in the dislocation structure.

7.2.4 Lorentz fraction of the grain profiles

Because a Lorentz profile has longer tails than a Gauss profile, the Lorentz fraction of the pseudo Voigt profile fitted to the grain profiles gives a measure of the length of the profile tails. The Lorentz fraction is shown in figure 7.23 as a function of the in the situ strain up to a strain of 1 %. The Lorentz fraction is approximately constant for higher strains.

In general, the Lorentz fraction decreases during the first 0.2 % of strain and then becomes approximately constant. The decrease in the Lorentz fraction corresponds to a shortening of the profile tails, which can be interpreted in terms of building up of intra-granular stresses during the micro-plastic range.

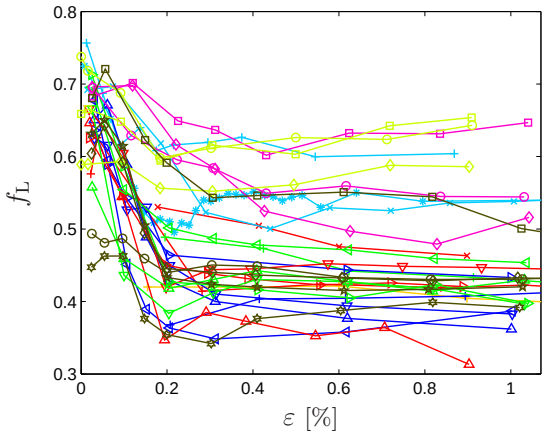

Figure 7.23: The Lorentz fraction of the grain profiles as a function of the in situ strain.

7.2.5 Fit with a Wilkens and a Gauss profile

The radial profiles (excluding the grains in grain group E because the investigated reflection from these grains was not a 400 reflection) were fitted with a single Wilkens profile as described in section 6.2.4. The results are shown in figures 7.24 and 7.25 as a function of the in situ strain up to a strain of 1 %. Figure 7.24 shows that, in general, the dislocation density first decreases and then increases again. Figure 7.25 shows that for many of the samples the dislocation arrangement parameter increases during the first 0.2 % of strain and then stays more or less constant.

As noted in section 6.2.4, the Wilkens profile is not a very good approximation to the asymmetric profiles, and Wilkens' model of radial profiles does not take into account heterogeneities in the dislocation structure and the resulting intra-granular stresses. For these reasons it may not be a reasonable approach to fit the asymmetric profiles with a single Wilkens profile and it is unclear how to interpret the results in figures 7.24 and 7.25. The higher dislocation density

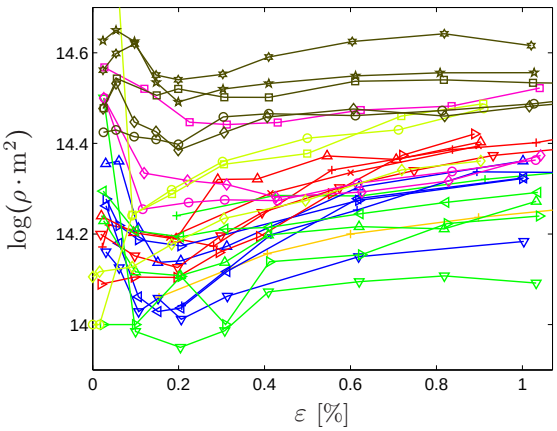

Figure 7.24: The logarithm of the dislocation density from a fit with a single Wilkens profile as a function of the in situ strain.

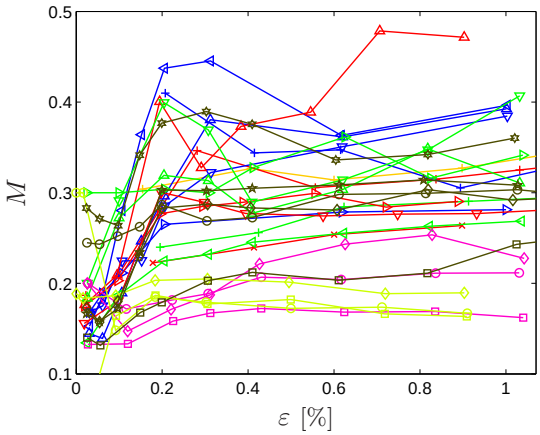

Figure 7.25: The dislocation arrangement parameter from a fit with a single Wilkens profile as a function of the in situ strain.

for grain group H can be understood as a result of the larger pre-deformation. The higher dislocation density and the lower value of the dislocation arrangement parameter for grain groups F and G (for which the profiles are nearly symmetric) indicate that the results do indeed depend on the profile asymmetry and confirms that a straightforward interpretation is problematic.

To take into account the heterogeneity of the dislocation structure, the profiles were also fitted with the sum of a Wilkens profile and a Gauss profile shifted with respect to each other (equation (6.5)). The results are shown in figures 7.26 to 7.30. In addition to the grains in grain group E, the grains in grain groups F and G are also excluded from these figures because the profiles from theses grains are nearly symmetric. The fit with two profiles is not very good in this case, and removing the grains from the figures make them easier to read without influencing the conclusions.

Figure 7.26 shows the Wilkens fraction, f_W, (calculated as the fraction of the integrated intensity of the Wilkens profile relative to the integrated intensity of the total profile) as a function of the in situ strain up to a strain of 1 %. This is a measure of the wall volume fraction in the investigated grains (the total volume of the walls in the grain divided by the total volume of the grain). For most of the grains it is nearly constant around 0.7. This is somewhat higher than the value around 0.45 obtained from TEM investigations by Göttler (1973), which indicates that the fit with a Wilkens and a Gauss profile is not able to perfectly separate the intensity contributions from the subgrains and the walls. The high values for grain groups B, C and D at strains around 0.1 % indicate that the fit with two profiles does not work well for symmetric profiles.

Figure 7.27 shows the position of the Wilkens and Gauss profiles (given by the coordinate $\delta q = q - \hat{q}^g$, which measures the position relative to the mean position of the grain profile) as a function of the applied stress. This corresponds to the position of the wall and subgrain profiles, respectively, and the figure shows that with increasing stress the two profiles move further apart as the intra-granular stresses increase. For grain groups C and D the curves for the two subprofiles cross each other corresponding to the change of sign in the asymmetry shown in figure 7.19.

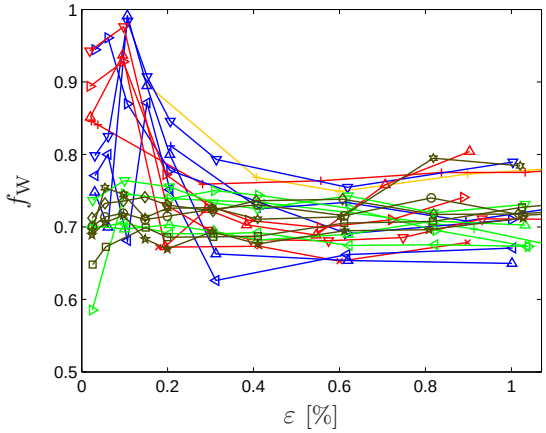

Figure 7.26: The Wilkens fraction from a fit with a Wilkens and a Gauss profile as a function of the in situ strain.

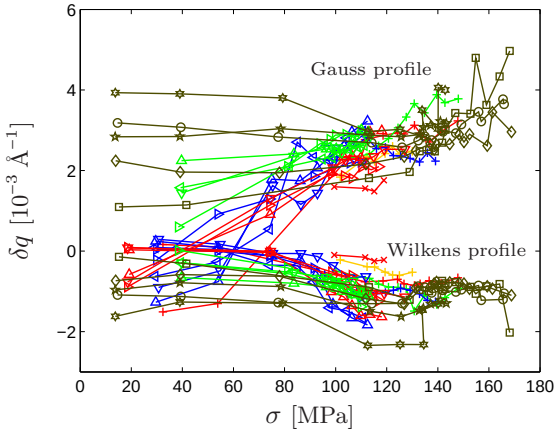

Figure 7.27: The position of the fitted Wilkens and Gauss profiles as a function of the applied stress.

Figure 7.28 shows the dislocation density for the Wilkens profile as a function of the in situ strain up to a strain of 1 %. For grain groups A, B, C, and D the dislocation density appears to increase from the onset of the in situ deformation. The lower dislocation density for grain groups B, C, and D at low strains may be related to the problems with symmetric profiles indicated by the high value of the Wilkens fraction for these grain groups, and therefore it is probably not a real effect. For grain group H the dislocation density starts at a higher level and appears to increase at a slower rate than for the other grain groups, which may be a result of the increased rate of thermally activated recovery processes at room temperature compared to the low pre-deformation temperature. For some of the grains in grain group H an initial drop in the dislocation density is observed. The larger dislocation density observed for grain group H may be a consequence of the larger pre-deformation for these grains.

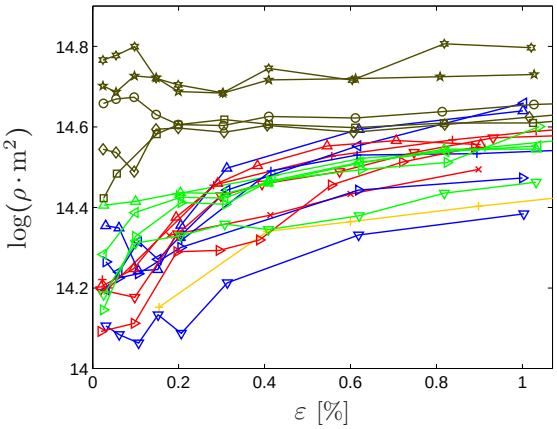

Figure 7.28: The logarithm of the dislocation density from a fit with a Wilkens and a Gauss profile as a function of the in situ strain.

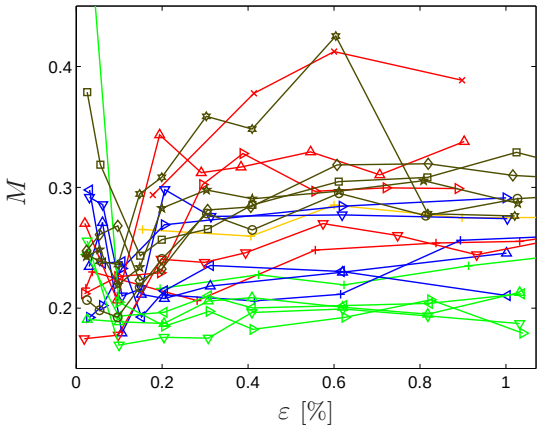

Figure 7.29: The dislocation arrangement parameter from a fit with a Wilkens and a Gauss profile as a function of the in situ strain.

Figure 7.29 shows the dislocation arrangement parameter for the Wilkens profile as a function of the in situ strain up to a strain of 1 %. For the reference grains in grain group A it is approximately constant, apart from a larger value for the first point for some of the grains which may be related to effects of unloading or recovery during storage.

For the grains in grain groups B, C, D, which were subjected to a strain path change, the dislocation arrangement parameter is generally larger than for the reference grains, which indicates that a strain path change leads to a less organized dislocation structure in the walls in which the screening is less effective. This interpretation may explain why the width of the grain profile is larger for samples xc3 and xd2 compared to sample xa2 as was shown in figure 7.14. For some of the grains the results indicate that the dislocation arrangement parameter increases during the micro-plastic range, but this is not a clear trend for all the grains, possibly because of the problems caused by the symmetry of the profiles in this strain interval.

For the grains in grain group H, which were pre-deformed at a low temperature, the dislocation arrangement parameter is initially larger than for the reference grains, and generally the value increases during the first 0.3 % of strain and then becomes approximately constant at a level higher than for the reference grains. The larger value before the in situ deformation can be interpreted as a sign of a more disordered dislocation structure caused by the suppres-

sion of thermally activated recovery processes at the low temperature. The increase of the dislocation arrangement parameter during the micro-plastic range shows that upon continued deformation at room temperature the dislocation structure becomes even more disordered and the screening of the dislocation strain fields become less effective.

Figure 7.30 shows the width (FWHM) of the Gauss profile as a function of the in situ strain up to a strain of 1 %. In general, the width increases with increasing strain. It is larger for grain groups B, C, D, and H than for the reference grains in grain group A. The larger width of the Gauss profile for these grain groups indicates that the variation in the intra-granular stresses is larger in these samples. This effect may also explain the larger grain profile width for samples xc3 and xd2 compared to sample xa2.

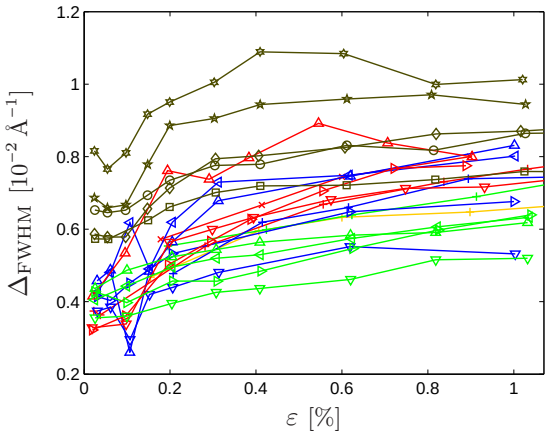

Figure 7.30: The width (FWHM) of the Gauss profile from a fit with a Wilkens and a Gauss profile as a function of the in situ strain.

In conclusion, the analysis indicates that the dislocation density increases with increasing strain, but less for the grains pre-deformed at a temperature of -196 °C. The results also indicate that a change in loading conditions leads to a less ordered dislocation structure in the walls and to an increase in the variation in the intra-granular stresses compared to a monotonic deformation. However, there are indications that the method of fitting with a Wilkens and a Gauss profile is not capable of perfectly partitioning the grain profile into subprofiles corresponding to the intensity contributions from the walls and the subgrains, and therefore the conclusions are somewhat uncertain.

7.3 Subgrain and wall components

With the use of the method described in section 6.3, the reciprocal space maps were partitioned into two components corresponding to the diffracted intensity from the subgrains and from the walls. By analyzing the radial profiles calculated from these two components it is possible to obtain information about the distribution of radial elastic strains in each of the two parts (subgrains and walls) separately. Examples of such radial profiles are shown in figures 7.31 and 7.32. Each figure shows an example of a grain profile (with the mean position and the position of maximum intensity indicated) and the corresponding subgrain and wall profiles. The two examples are from grain d2-1 at two different strain values.

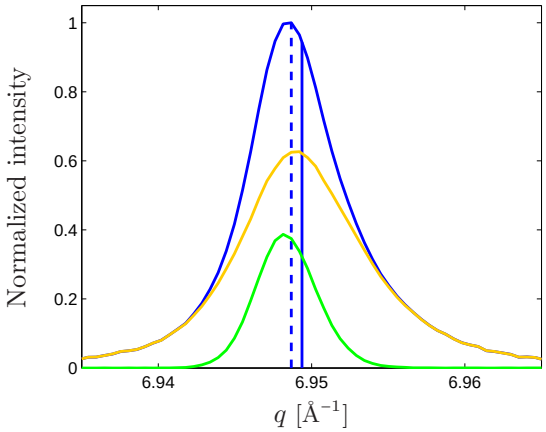

Figure 7.31: Radial profiles from grain d2-1 (blue) and the corresponding subgrain (green) and wall (yellow) profiles at an in situ strain of 0.03 %. The vertical blue lines indicate the mean position (solid line) and the position of maximum intensity (dashed line) of the grain profile.

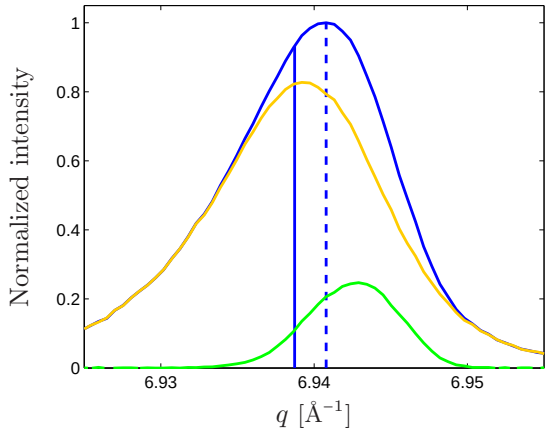

Figure 7.32: Radial profiles from grain d2-1 (blue) and the corresponding subgrain (green) and wall (yellow) profiles at an in situ strain of 1.00 %. The vertical blue lines indicate the mean position (solid line) and the position of maximum intensity (dashed line) of the grain profile.

The figures clearly show the shift in asymmetry of the grain profile which was also shown in figure 7.16. In figure 7.31 the grain profile has a negative asymmetry (the position of maximum intensity is positioned on the low-q side of the mean position), and in figure 7.32 the grain profile has a positive asymmetry (the position of maximum intensity is positioned on the high-q side of the mean position). In the case of a negative asymmetry the subgrain profile is shifted to low q-values relative to the wall profile, and in the case of a positive asymmetry the subgrain profile is shifted to high q-values relative to the wall profile. Furthermore, the figures show that the width of both subprofiles increase as the width of the grain profile increases, and that the subgrain profile is narrower than the wall profile. In both figures the subgrain profile contains less intensity than the wall profile, and the relative size of the subgrain profile decreases as the strain increases.

Below, results from the analysis of the relative size, position, width, and asymmetry of the subgrain and wall profiles are presented and discussed.

7.3.1 Subgrain intensity fraction

The ratio of the integrated intensity in the subgrain profile to the integrated intensity in the grain profile will be called the subgrain intensity fraction, and is denoted by f^{s}. This was calculated in order to determine the subgrain volume fraction in the investigated grains (the total volume of the subgrains in the grain divided by the total volume of the grain). If the partitioning method were able to completely separate the contributions from subgrains and walls in the reciprocal space maps, the subgrain intensity fraction would be a measure of the subgrain volume fraction. This was in large part the motivation behind the development of the partitioning method described in section 6.3. However, as explained below, other factors also influence the subgrain intensity fraction, which can therefore not be interpreted directly as the subgrain volume fraction.

Results from the first X-ray diffraction experiments indicated a systematic effect of the strain path change parameter on the evolution of the subgrain intensity fraction. These results were initially interpreted as evidence that the subgrain volume fraction decreased faster after a strain path change, which could be a sign that the subgrains become less well defined after a strain path change. Some of the later experiments were designed to verify this interpretation and investigate the effects of other parameters on the subgrain intensity fraction. The results of the later experiments, however, showed that there was no clear dependence of the strain path change parameter on the decrease of the subgrain intensity fraction, and that the interpretation of the subgrain intensity fraction was not as straightforward as initially thought.

Figures 7.33 and 7.34 show the subgrain intensity fraction as a function of the in situ strain. Generally, the subgrain intensity fraction decreases as the strain increases. For grains a2-1, a2-2, a2-3, and a2-4 (shown in figure 7.34) the subgrain intensity fraction is higher, and for grains h1-1, h1-2, h1-3, h1-4, and h1-5 (shown in figure 7.33) the subgrain intensity fraction is lower than for the other grains. The figures show no clear effect of a strain path change on the rate of decrease of the subgrain intensity fraction.

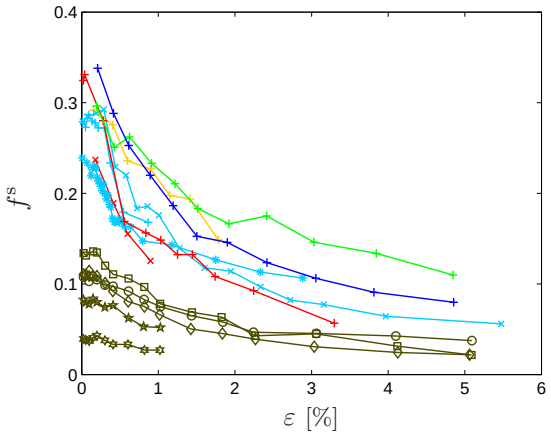

Figure 7.33: The subgrain intensity fraction for the grains from samples xa1, xb1, xc1, xc2, xd1, xe1, xe2, xe3, and xh1 as a function of the in situ strain.

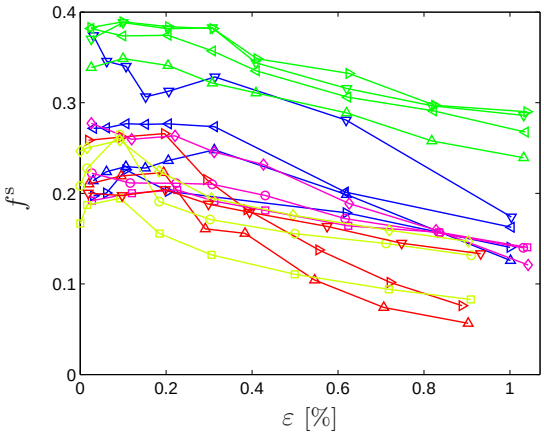

Figure 7.34: The subgrain intensity fraction for the grains from samples xa2, xc3, xd2, xf1, xg1 as a function of the in situ strain.

Figures 7.35 and 7.36 show the same results normalized to start at a value of 1, making it possible to compare the relative rate of decrease of the different curves. The fact that some of the red curves (corresponding to an orthogonal strain path change) fall below the other curves may indicate that the relative subgrain intensity fraction decreases faster after a strain path change, but the evidence is not very strong.

The general decrease of the subgrain intensity fraction can be understood as a consequence of the decreasing scale of the dislocation structures and the lack of ability of the partitioning method to separate small peaks from the cloud. As described in section 2.2.1, as the deformation is increased, the average subgrain size decreases. When the subgrains become sufficiently small, their intensity contribution is not included in the subgrain component by the partitioning method, and as a result the subgrain intensity fraction decreases. This effect also explains why the subgrain intensity fraction is smallest for grains h1-1, h1-2, h1-3, h1-4,

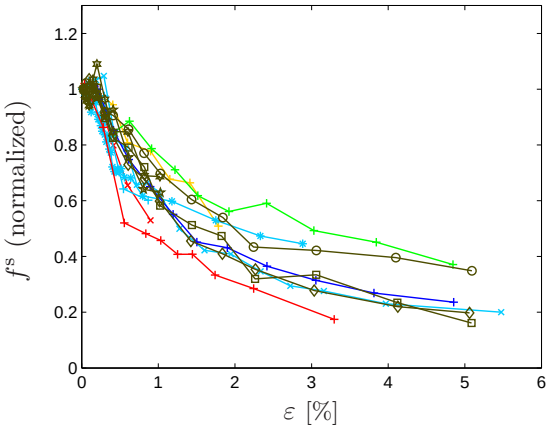

Figure 7.35: The normalized subgrain intensity fraction for the grains from samples xa1, xb1, xc1, xc2, xd1, xe1, xe2, xe3, and xh1 as a function of the in situ strain.

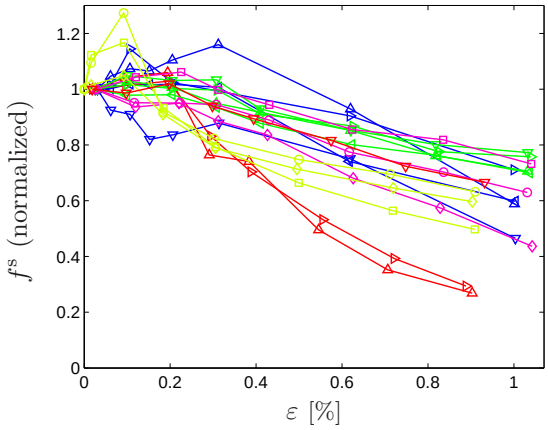

Figure 7.36: The normalized subgrain intensity fraction for the grains from samples xa2, xc3, xd2, xf1, xg1 as a function of the in situ strain.

and h1-5, because these grains were subjected to a larger pre-deformation than the other grains. Part of the reason could also be that the low-temperature pre-deformation may result in a less well defined dislocation structure as described in section 2.3.4.

However, the large subgrain intensity fraction for grains a2-1, a2-2, a2-3, and a2-4 can not be explained as a result of differences in pre-deformation, because the amount of pre-deformation was the same for grain groups A, B, C, D, E, F, and G. Furthermore, because the subgrain intensity fraction for these grains is already large before any significant in situ deformation, it can not be an effect of the strain path change, and because both grains a2-1, a2-2, a2-3, and a2-4 and grains g1-1, g1-2, and g1-3 were observed with the scattering vector parallel to the pre-deformation axis, it can not be explained by the orientation of the grains.

Further analysis of the data showed that the subgrain intensity fraction was influenced by the degree to which the intensity distribution is spread out in the azimuthal directions. The subgrain intensity fraction is larger for the azimuthal maps for which the intensity is concentrated in a few very intense peaks and smaller for the azimuthal maps for which the intensity is distributed in many smaller peaks. This is illustrated for the first azimuthal map from grains a2-2, a2-3, g1-1, and g1-2 in figures 7.37 to 7.40. The subgrain intensity fraction is 0.37, 0.38, 0.22, and 0.19 for the four azimuthal maps, respectively. The four azimuthal maps are all from grains subjected to the same amount of pre-deformation and observed with the scattering vector parallel to the pre-deformation axis before any in situ deformation. The angular scale and the color scale is the same in the four figures. The azimuthal maps for the grains with a high subgrain intensity fraction (a2-2 and a2-3) show a more concentrated intensity distribution than the azimuthal maps for the grains with low subgrain intensity fraction (g1-1 and g1-2).

To further show that the degree of azimuthal concentration of the intensity has a large influence on the subgrain intensity fraction, the azimuthal concentration was quantified by first calculating the integral width (for the azimuthal maps) in both the $\tilde{x}$-direction and the $\tilde{\omega}$-direction, and then calculating the inverse of the geometric mean of the two azimuthal integral widths. A large value of this parameter, $1/\sqrt{\langle\beta_{\tilde{x}}\rangle\langle\beta_{\tilde{\omega}}\rangle}$, corresponds to small azimuthal

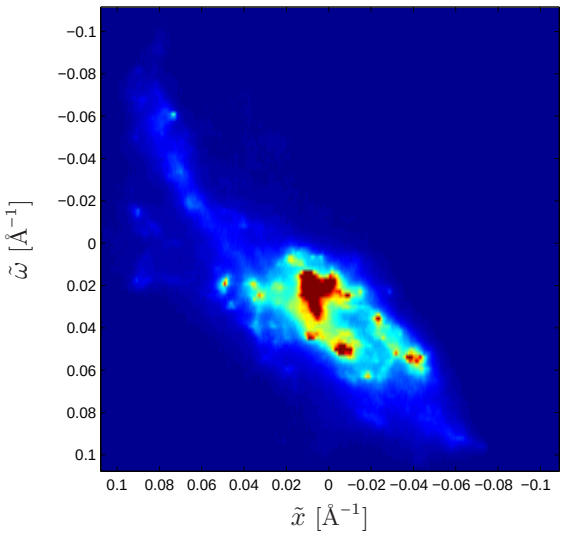

Figure 7.37: Azimuthal map from grain a2-2 at an in situ strain of 0.03 % showing a concentrated intensity distribution. The subgrain intensity fraction is 0.37.

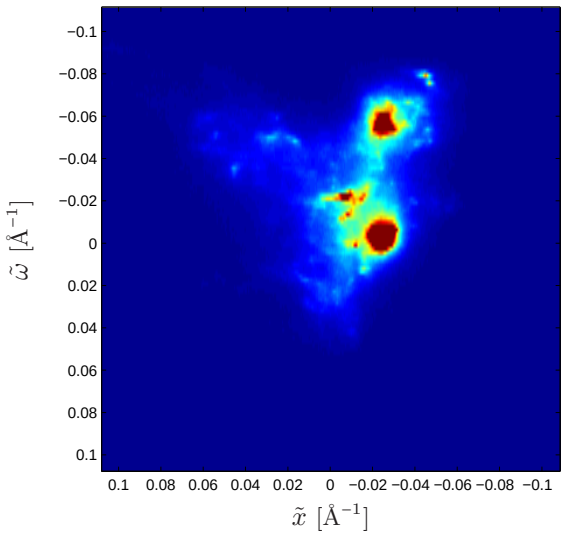

Figure 7.38: Azimuthal map from grain a2-3 at an in situ strain of 0.02 % showing a concentrated intensity distribution. The subgrain intensity fraction is 0.38.

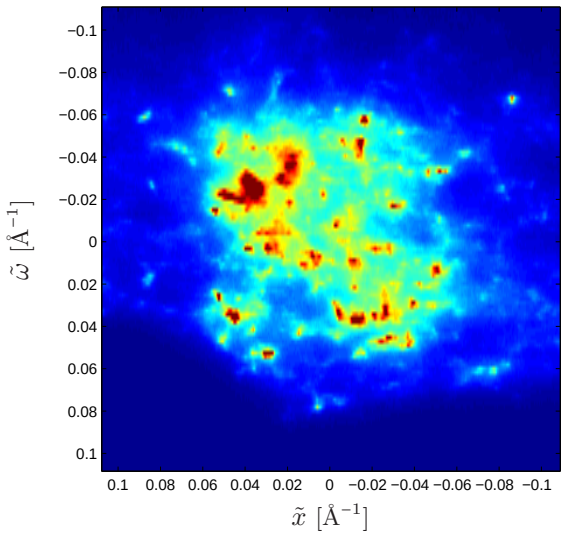

Figure 7.39: Azimuthal map from grain g1-1 at an in situ strain of 0.03 % showing a spread out intensity distribution. The subgrain intensity fraction is 0.22.

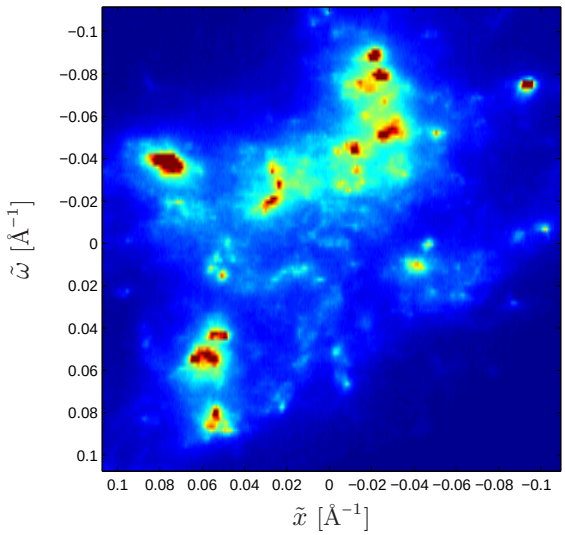

Figure 7.40: Azimuthal map from grain g1-2 at an in situ strain of 0.03 % showing a spread out intensity distribution. The subgrain intensity fraction is 0.19.

integral widths and therefore to a large degree of azimuthal concentration of the intensity. The results are shown as a function of the in situ strain in figure 7.41 for the samples whose subgrain component intensity fraction was shown in figure 7.34. The similarity between the two figures supports the idea that the degree to which the intensity is concentrated in a few peaks has a large influence on the subgrain intensity fraction. Figure 7.42 shows the parameter $1/\sqrt{\langle\beta_{\tilde{x}}\rangle\langle\beta_{\tilde{\omega}}\rangle}$ as a function of the subgrain intensity fraction. The correlation is not perfect, but the figure clearly shows that azimuthal maps with a large degree of azimuthal concentration of the intensity corresponds to reciprocal space maps with a large subgrain intensity fraction.

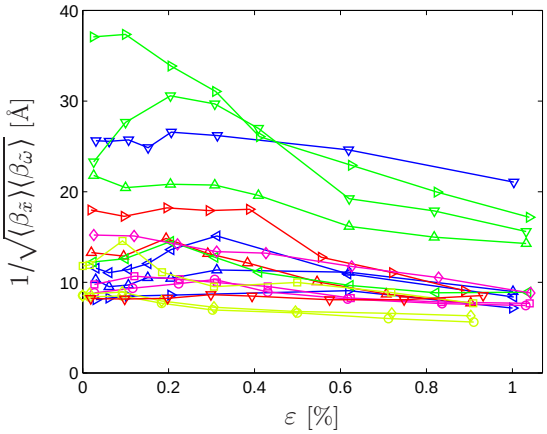

Figure 7.41: The inverse of the geometric mean of the integral width in the azimuthal directions for the grains from samples xa2, xc3, xd2, xf1, xg1 as a function of the in situ strain.

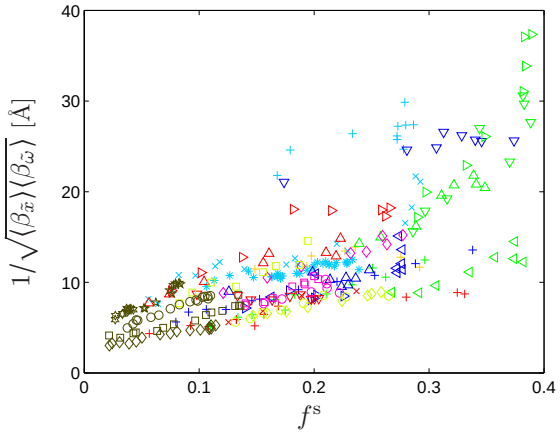

Figure 7.42: The inverse of the geometric mean of the integral width in the azimuthal directions as a function of the subgrain intensity fraction.

This effect can be understood from the description of the partitioning method given in section 6.3. Because of the asymmetric measure of misfit used in the method, the effect of a data point on the cloud model is independent of the intensity value as long as the intensity is above the value of the parameter s. This means that the level of the cloud model is affected equally by small and large peaks (as long as the widths of the peaks are equal and the peaks are above a certain minimum size), and that the level of the cloud model is pulled up less by one large large peak than by two smaller separated peaks. This explains why the total intensity in the subgrain component is larger when the intensity is concentrated in a few large peaks.

In conclusion, the subgrain intensity fraction can not be straightforwardly interpreted as a measure of the subgrain volume fraction. Both because very small peaks are not separated from the cloud by the partitioning method and because the degree of azimuthal intensity concentration significantly influences the subgrain intensity fraction. However, the azimuthal intensity concentration only affects the absolute value of the subgrain intensity fraction, and the results may indicate that the relative subgrain intensity fraction decreases faster after a strain path change.

7.3.2 Position of the subprofiles

For each reciprocal space map the position (relative to the position of the grain profile) of the subgrain profile and of the wall profile was calculated. The results are shown as a function of the asymmetry of the grain profile in figures 7.43 and 7.44. The coordinate $\delta q = q - \hat{q}^{\mathrm{g}}$ measures the position relative to the mean position of the grain profile. The straight line in each figure represents the position of maximum intensity of the grain profile.

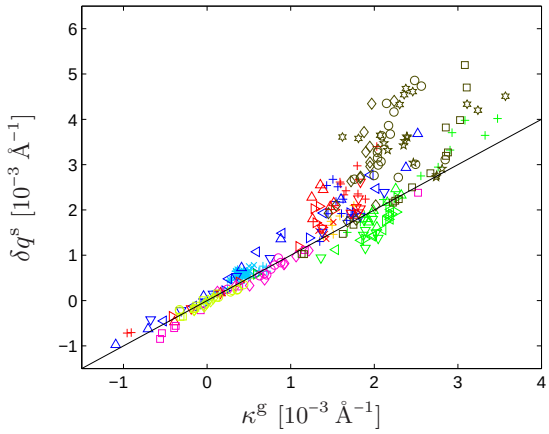

Figure 7.43: The position of the subgrain profile as a function of the asymmetry of the grain profile. The straight line represents the position of maximum intensity of the grain profile.

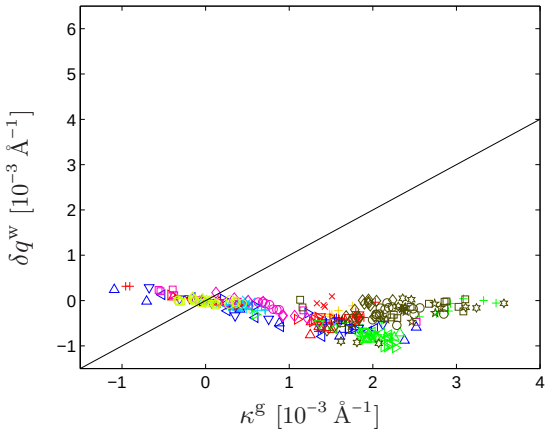

Figure 7.44: The position of the wall profile as a function of the asymmetry of the grain profile. The straight line represents the position of maximum intensity of the grain profile.

The position of the subgrain profile increases approximately linearly with κ^{g}. For κ^{g} smaller than 10^{-3} Å^{-1} the points follow the straight line in the figure, which means that the position of the subgrain profile is very close to the position of maximum intensity of the grain profile. For larger values of κ^{g} the points are significantly more scattered, but they generally lie above the straight line in the figure, which means that the subgrain profile is positioned at higher q-values than the position of maximum intensity of the grain profile. For grains a2-1, a2-2, a2-3, and a2-4 the subgrain profile is shifted to low δq-values compared to the general trend in the figure.

The position of the wall profile decreases approximately linearly with κ^{g} for κ^{g} smaller than 10^{-3} Å^{-1}. For larger values of κ^{g}, the position is approximately independent of κ^{g} and is very close to the mean position of the grain profile. For grains a2-1, a2-2, a2-3, and a2-4 the subgrain profile is shifted to low δq-values compared to the other grains.

The relative shift of the subprofiles observed in the figures is consistent with the modified composite model, which explains the asymmetry of the grain profile as a consequence of the shifts of the subprofiles from the subgrains and the walls caused by the average intra-granular stress. The shifts of the subprofiles were also shown in figure 7.27.

Figure 7.43 shows that the position of the subgrain profile is close to the position of maximum intensity for the grain profile, both in the case of compressive (positive values of δq) and tensile (negative values of δq) elastic back-strain. It follows from this and the fact that for the samples subjected to a strain path change the asymmetry changes substantially during the micro-plastic range (as was shown in section 7.2.3), that for most of the samples

subjected to a strain path change the average elastic back-strain in the subgrains changes from tensile to compressive during the micro-plastic range.

The fact that the subprofiles for grains a2-1, a2-2, a2-3, and a2-4 are shifted towards low δq-values compared to the subprofiles for the other grains can be understood from the discussion about the subgrain intensity fraction in section 7.3.1. For these grains the subgrain intensity fraction is higher than for the other grains, which means that the subgrain component contains a larger part of the intensity contribution from the walls (or from very small subgrains). For this reason the mean position is shifted towards the position of the wall component which is towards lower δq-values. This also means that the position of the wall profile is shifted towards lower δq-values, because, compared to the other grains, the wall profile contains less intensity at high δq-values.

The fact that the position of the wall profile is very close to the mean position of the grain profile for large κ^{g}-values can be understood from the fact that large κ^{g}-values generally correspond to large deformations and to dislocation structures with small subgrains and therefore to low values of the subgrain intensity fraction. In this case the wall profile is almost equal to the grain profile, and therefore the position of the wall profile is very close to the position of the grain profile.

In conclusion, figures 7.43 and 7.44 show that the subgrain profile is positioned close to the position of maximum intensity of the grain profile, and that the position of the subprofiles is correlated with the asymmetry of the grain profile. However, the position of the subprofiles is influenced by the lack of ability of the partitioning method to perfectly separate the intensity contributions from the subgrains and the walls.

7.3.3 Width of the subprofiles

The width of the subgrain and wall profiles is shown in figures 7.45 and 7.46 as a function of the width of the grain profile. For both subprofiles the width increases as the width of the grain profile increases.

As discussed in section 7.2.2 the width of the subgrain profile is determined by the variation in the intra-granular stresses between the subgrains. With this interpretation figure 7.45 shows

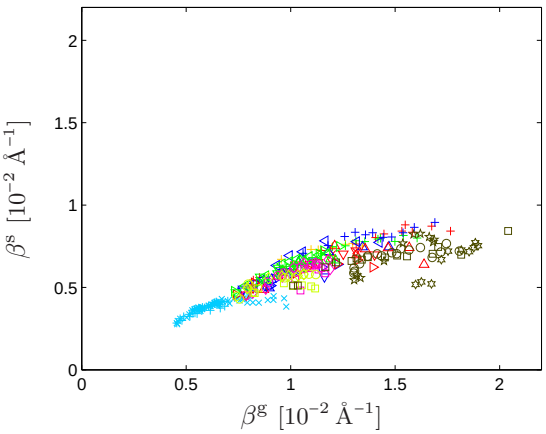

Figure 7.45: The width of the subgrain profile as a function of the width of the grain profile.

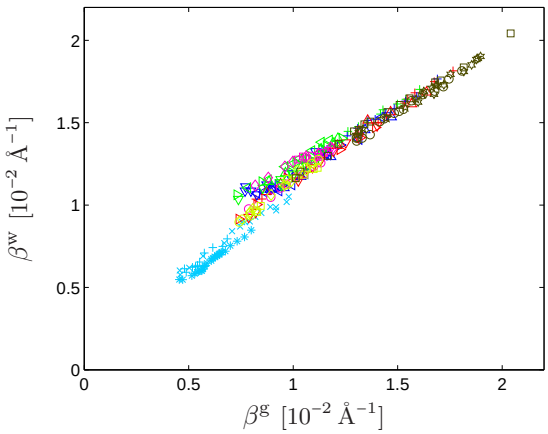

Figure 7.46: The width of the wall profile as a function of the width of the grain profile.

that with increasing deformation (corresponding to an increase in the width of the grain profile) the variation in the intra-granular stresses increases. The apparent saturation of the width of the subgrain profile may be related to the fact that the subgrain intensity fraction decreases with deformation. When the subgrain profile gets smaller (because the intensity contribution from the very small subgrains is not separated from the intensity contribution from the walls by the partitioning method), the width of the subgrain profile increases at a slower rate.

Because the subgrain intensity fraction decreases with increasing deformation, the wall profile is almost equal to the grain profile for large deformations, and therefore the data points in figure 7.46 lie almost on a straight line with a slope of 1 for large grain profile widths.

In conclusion, the width of both subprofiles increases as the width of the grain profile increases, but the width is affected by the problems with the partitioning method. The results indicate that the variation in the intra-granular stresses between the subgrains increases.

7.3.4 Asymmetry of the subprofiles

The asymmetry of the subgrain and wall profiles is shown in figures 7.47 and 7.48 as a function of the asymmetry of the grain profile. For both subprofiles the asymmetry tends to be of the same sign as the asymmetry of the grain profile. The asymmetry of the subgrain profile for samples a2-1, a2-2, a2-3, and a2-4 is significantly larger than for the other grains.

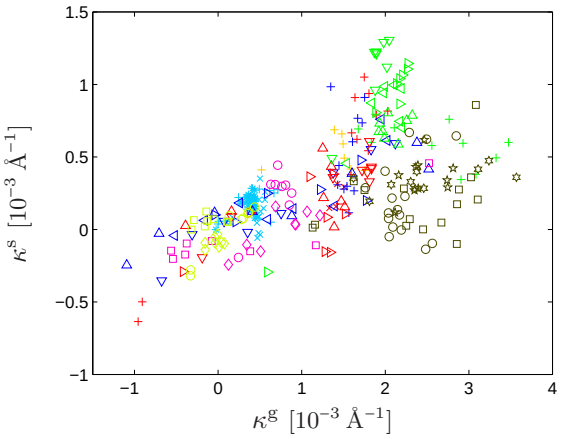

Figure 7.47: The asymmetry of the subgrain profile as a function of the asymmetry of the grain profile.

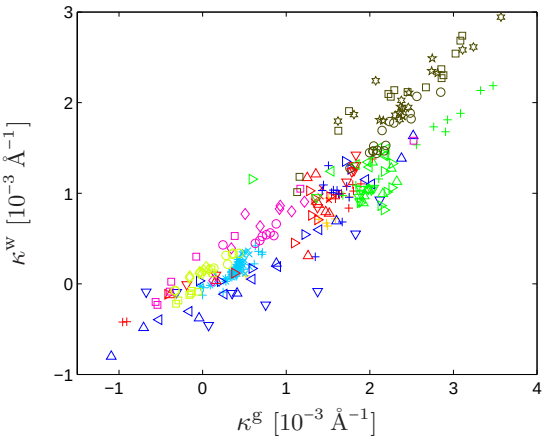

Figure 7.48: The asymmetry of the wall profile as a function of the asymmetry of the grain profile.

An asymmetric subgrain profile can be the result of a size effect in the elastic strains of the subgrains. If the larger subgrains experience a larger elastic back-strain than the smaller subgrains, the subgrain profile, which is the sum of the individual subgrain profiles, will be asymmetric, and the asymmetry will have the sign shown in figure 7.47: Negative in the case of a tensile elastic back-strain and positive in the case of a compressive elastic back-strain.

However, the results in figure 7.47 can also be understood as a result of the lack of ability of the partitioning method to perfectly separate the intensity contributions from the subgrains and the walls. If the contributions are not adequately separated, the subgrain profiles will contain part of the wall contribution, and this will tend to produce an asymmetric profile

with an asymmetry of the same sign as the asymmetry of the grain profile. As the grains a2-1, a2-2, a2-3, and a2-4 which have the largest subgrain intensity fraction also have the largest subgrain profile asymmetry, this is probably at least part of the explanation for the asymmetry of the subgrain profiles.

The asymmetry of the wall profiles is probably caused by the problems with the partitioning method. Because the intensity contribution from very small subgrains is part of the wall component, the wall profile is influenced by the intra-granular stresses in these subgrains, resulting in an asymmetric wall profile.

In conclusion, the analysis shows that both subprofiles are asymmetric, but the asymmetry can be explained as a results of problems with the partitioning method. However, the asymmetry of the subgrain profiles can also be interpreted as an indication of a size effect in the elastic strains in the subgrains. This will be investigated further in section 7.4.1.

7.4 Individual subgrain profiles

Section 6.4 described how the individual sharp peaks in the subgrain components were identified and characterized, and how profiles were calculated from a single row or column of voxels through the center of each peak. Analysis of the radial profiles give information about the elastic back-strain in the individual subgrains. Examples of such profiles from a few individual subgrains are shown in figures 7.49 and 7.50. The figures show the profiles for the entire grain, for the subgrain and wall components, and for the five largest subgrains (measured by the maximum peak intensity). The mean position and the position of maximum intensity of

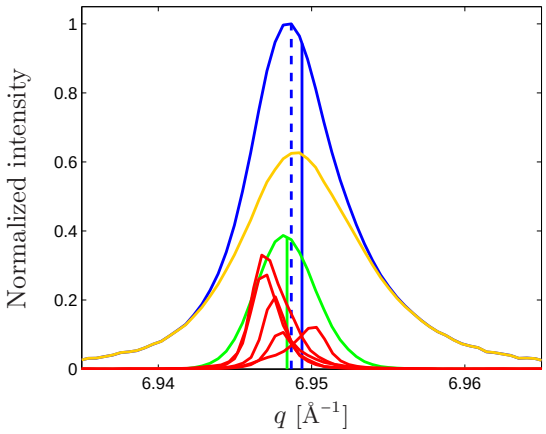

Figure 7.49: Radial profiles from grain d2-1 (blue) and the corresponding subgrain (green) and wall (yellow) components at an in situ strain of 0.03 %. Radial profiles from the five largest individual subgrains are shown in red scaled by a factor of 200. The vertical lines indicate the mean position (solid blue line) and the position of maximum intensity (dashed blue line) of the grain profile and the mean position (solid green line) of the subgrain profile.

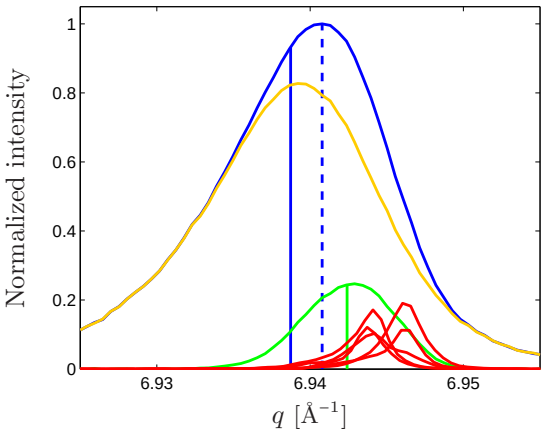

Figure 7.50: Radial profiles from grain d2-1 (blue) and the corresponding subgrain (green) and wall (yellow) components at an in situ strain of 1.00 %. Radial profiles from the five largest individual subgrains are shown in red scaled by a factor of 200. The vertical lines indicate the mean position (solid blue line) and the position of maximum intensity (dashed blue line) of the grain profile and the mean position (solid green line) of the subgrain profile.

the grain profile and the mean position of the subgrain profile are indicated in the figure. The individual subgrain profiles are scaled by a factor of 200 to make them clearly visible in the figures. The two examples are from grain d2-1 at two different strain values.

In figure 7.49 where the grain profile has a negative asymmetry, four out of the five largest individual subgrain profiles are positioned on the low-q side of the mean subgrain position (represented by the mean position of the subgrain profile and shown as a solid green line in the figures). In figure 7.50 where the grain profile has a positive asymmetry, the five largest individual subgrain profiles are positioned on the high-q side of the mean subgrain position. Furthermore, the figures show that the individual subgrain profiles are significantly narrower than the subgrain profiles.

The position and width of the individual subgrain profiles were analyzed for all the reciprocal space maps, and the results are presented and discussed below. As described in section 6.4, the terminology 'large subgrains' (and 'large individual subgrain profiles'), 'medium subgrains' (and 'medium individual subgrain profiles'), and 'small subgrains' (and 'small individual subgrain profiles') is used for the subgrains (and profiles) corresponding to the sharp peaks numbered 1 to 10, 11 to 30, and 31 to 80, respectively, when sorted according to maximum intensity. In total, more than 25000 individual subgrain profiles were analyzed by the methods described in sections 6.3 and 6.4. The analysis was also performed for different values of the parameters in the partitioning method, and it was verified that the conclusions presented below also hold for other parameter values and thus have a general validity.

7.4.1 Position of the individual subgrain profiles

The examples above (figures 7.49 and 7.50) indicate that the large subgrains experience a larger elastic back-strain than the average subgrain does. Such a size effect was mentioned in section 7.3.4, and to investigate this further, the mean of the position of the large individual subgrain profiles was calculated. The results are shown as a function of the position of the subgrain profile in figure 7.51. A straight reference line with a slope of 1 is included in the figure to make it easy to compare the mean of the position of the individual subgrain profiles to the position of the subgrain profile. The figure shows that the large individual subgrain profiles are positioned further away than the subgrain profile from the position of the grain profile, both for positive and negative values of δq^{s} (the position of the subgrain profile relative to the mean position of the grain profile). This supports the idea that the large subgrains experience a larger elastic back-strain than the average subgrain (in both the tensile and compressive cases).

To find further evidence for such a size effect, the mean of the position was also calculated for the medium individual subgrain profiles and for the small individual subgrain profiles. Figure 7.52 shows the results as a function of the position of the subgrain profile. Here the color indicates the size of the subgrains, with green points representing the large subgrains, red points representing the medium subgrains, and blue points representing the small subgrains. A straight reference line with a slope of 1 is included in the figure. This figure directly shows the size effect: For δq^{s} larger than $10^{-3}\,\text{Å}^{-1}$ the elastic back-strain experienced by the subgrains depends systematically on their size. It is largest for the large subgrains and smallest for the small subgrains. To see the effect more clearly, figure 7.53 shows parts of figure 7.52 and includes the best straight line fit for each group of subgrains.

The size effect can also be seen in figure 7.54, which shows the mean of the position of the large individual subgrain profiles as a function of the mean of the position of the small

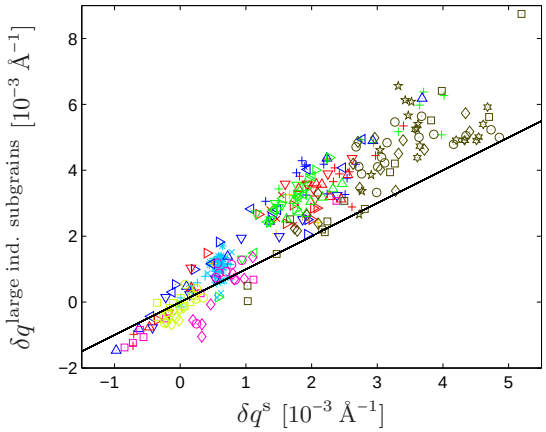

Figure 7.51: The mean of the position of the large individual subgrain profiles as a function of the position of the subgrain profile. The straight line has a slope of 1.

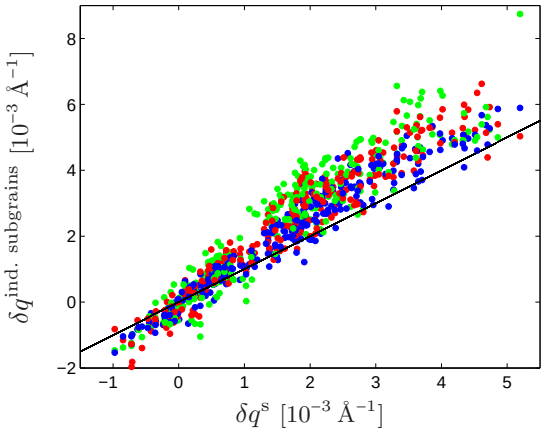

Figure 7.52: The mean of the position of the large (green), medium (red), and small (blue) individual subgrain profiles as a function of the position of the subgrain profile. The straight line has a slope of 1.

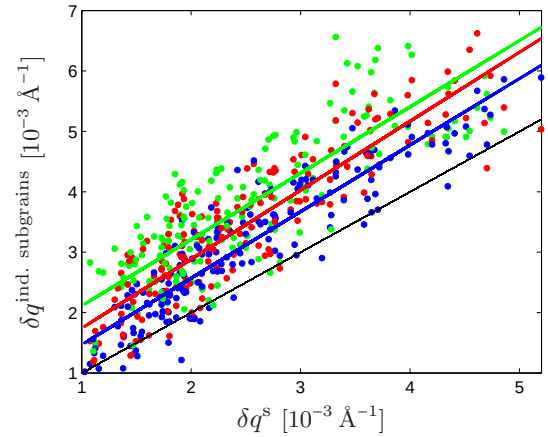

Figure 7.53: The mean of the position of the large (green), medium (red), and small (blue) individual subgrain profiles as a function of the position of the subgrain profile. The best straight line fit for each group is included. The straight black line has a slope of 1.

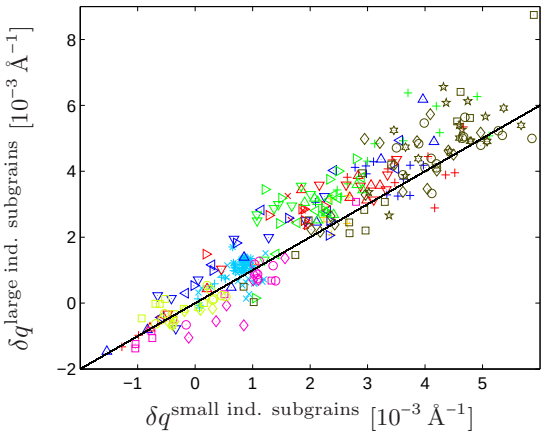

Figure 7.54: The mean of the position of the large individual subgrain profiles as a function of the mean of the position of the small individual subgrain profiles. The straight line has a slope of 1.

individual subgrain profiles. Again a straight reference line with a slope of 1 is included in the figure. For $\delta q^{\text{large ind. subgrains}}$ larger than 10^{-3} Å^{-1} the data points generally lie above the straight line, showing again that the large subgrains experience a larger elastic back-strain than the small subgrains.

According to the modified composite model the intra-granular stresses are built up because the subgrains are softer than the dislocation walls, and therefore they yield before the walls when the crystal is loaded. With this interpretation in mind, the size effect shown in the

figures above indicates that larger subgrains are softer and yield more easily than smaller subgrains.

The radial elastic back-strain, $\varepsilon_{\mathrm{r,rel}}^{\text{ind. subgrains}}$, experienced by the subgrains was calculated from the mean of the position of the 80 largest individual subgrain profiles with the use of equation (3.8) and the radial position of the grain profile as a reference position. Figure 7.55 shows the ratio of the average radial elastic back-strain to the average radial elastic strain in the entire grain, $\varepsilon_{\mathrm{r}}^{\mathrm{g}}$, as a function of the average radial elastic strain in the entire grain.

For small values of $\varepsilon_{\mathrm{r}}^{\mathrm{g}}$ there is a lot of variation of this ratio, particularly for grain groups F and G, for which the radial elastic strain in the grain is almost zero. For grain groups C and D the elastic back-strain is positive (tensile) for small values of $\varepsilon_{\mathrm{r}}^{\mathrm{g}}$ (corresponding to the observations made in the side case), but it becomes negative (compressive) for large values of $\varepsilon_{\mathrm{r}}^{\mathrm{g}}$ (as the intra-granular stresses change). When the average elastic strain in the entire grain becomes large, the ratio of the elastic back-strain to the elastic strain in the grain falls approximately between -40 % and -20 % (as it does for the reference samples in grain group A for all strain values). For comparison, Jakobsen (2006) reported ratios of the elastic back-strain to the average strain between -25 % and -10 %, Ungár, Mughrabi, Wilkens & Hilscher (1991) reported a ratio of the average intra-granular stress to the flow stress of -11 % (but their analysis was not based on the properties of individual subgrains), and Levine et al. (2006) reported a ratio of the average intra-granular stress to the flow stress of -17 %.

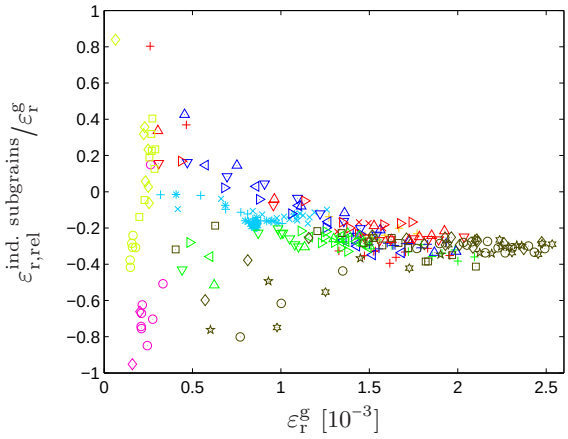

Figure 7.55: The ratio of the average radial elastic back-strain in the 80 largest individual subgrains to the average radial elastic strain in the entire grain as a function of the average radial elastic strain in the entire grain.

Figures 7.56 and 7.57 show the evolution of the mean of the position of the 80 largest individual subgrain profiles as a function of the in situ strain for the grains from samples xa2, xc3, xd2, and xh1 up to a strain of 1 %. The figures resemble figures 7.19 and 7.20, which showed the asymmetry of the grain profiles for the same samples, and they can be interpreted in the same way (as showing how the average intra-granular stress evolve), but in this case the interpretation is based on an analysis of individual subgrain profiles.

For sample xa2 the scattering vector and the in situ deformation axis were parallel to the pre-deformation axis, and the compressive elastic back-strain built up in the subgrains during the pre-deformation changed only slightly during the in situ deformation. The figure shows

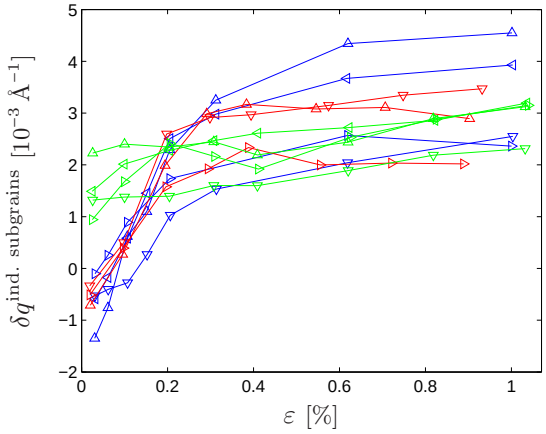

Figure 7.56: The mean of the position of the 80 most intense individual subgrain profiles for the grains from samples xa2, xc3, and xd2 as a function of the in situ strain.

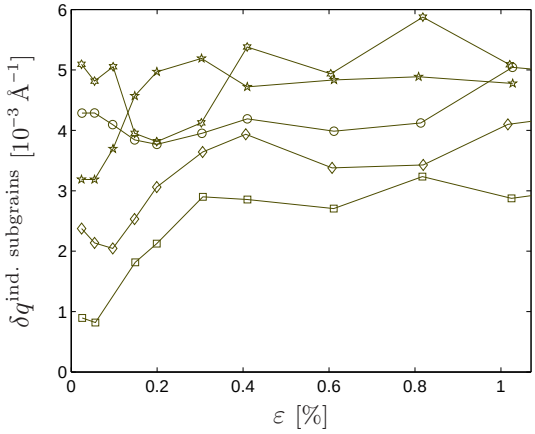

Figure 7.57: The mean of the position of the 80 most intense individual subgrain profiles for the grains from sample xh1 as a function of the in situ strain.

that during the deformation the intra-granular stresses increased slowly, leading to a shift of the position of the individual subgrain profiles.

For samples xc3 and xd2 the subgrains initially experienced a tensile elastic back-strain because of the angle between the scattering vector and the pre-deformation axis (55 ° for sample xc3 and 90 ° for sample xd2). Immediately upon application of an external load along an axis parallel to the scattering vector, a substantial redistribution of the intra-granular stresses took place during the first 0.2 % to 0.3 % of strain. As a result the elastic back-strain in the subgrains gradually changed to compressive, shifting the position of the individual subgrain profiles to the high-q side of the grain profile. The figure shows that for larger strains the shift of the profiles increases at a slower rate, and the continued shift appears to be slightly larger for sample xd2 than for sample xc3.

Figure 7.57 shows that for the grains in sample xh1 the evolution of the position of the individual subgrain profiles seems to fall in three phases: Initially (up to a strain of approximately 0.1 %) the profile position tends to shift towards the mean position of the grain profile or stay constant. This shows that for the grains pre-deformed at a temperature of -196 °C the evolution is different from that of the other grains in the initial part of the in situ deformation. For larger strains the profiles are shifted further away from the mean position of the grain profile indicating a build up of intra-granular stresses. Finally, after a strain of approximately 0.3 % the position stays approximately constant. As mentioned in section 7.2.3 the larger intra-granular stresses compared to the other samples may be a result of the larger pre-deformation and the low pre-deformation temperature.

In conclusion, the statistical analysis of the position of a large number of individual subgrain profiles shows that on average the individual subgrain profiles are positioned close to the mean of the subgrain profile, and that the large profiles are positioned further away from the mean position of the grain profile than the small profiles are. This shows the presence of a size effect in the elastic back-strain experienced by the individual subgrains. When the level of deformation is large enough that the effects of the pre-deformation no longer have any significant effect on the distribution of the intra-granular stresses, the average elastic

back-strain along the deformation axis in the subgrains is about 30 % of the average elastic strain along the deformation axis in the entire grain.

Furthermore, for the samples subjected to a strain path change the elastic back-strain in the subgrains changes from tensile to compressive during the micro-plastic range, and for the sample pre-deformed at a low temperature the elastic back-strain in the subgrains goes through a brief initial phase where it decreases or at least remains constant, indicating differences in the initial evolution of the dislocation structure compared to the other samples.

7.4.2 Spread in the position of the individual subgrain profiles

As indicated by figures 7.49 and 7.50 there is a significant spread in the position of the individual subgrain profiles. To investigate if the distribution of these positions can be approximated by a Gauss distribution, a Lilliefors test (which can be used to test whether a data set comes from a normally distributed population) with a 5 % significance level was performed on the positions of the 80 largest individual subgrain profiles from each reciprocal space map. Out of a total of 344 reciprocal space maps, 318 (corresponding to 92 %) passed the test (with no systematic trend in which ones passed or failed the test), showing that a Gauss distribution is a good approximation to the distribution of the position of the individual subgrain profiles. Figure 7.58 shows a normal probability plot of the position of the individual subgrain profiles for three reciprocal space maps from grain d2-1. For each reciprocal space map the data points approximately follow a straight line, showing that a Gauss distribution is a good approximation. The figure also shows that the slope of the straight lines decreases with increasing strain, which means that the spread in the position of the individual subgrain profiles increases with increasing strain.

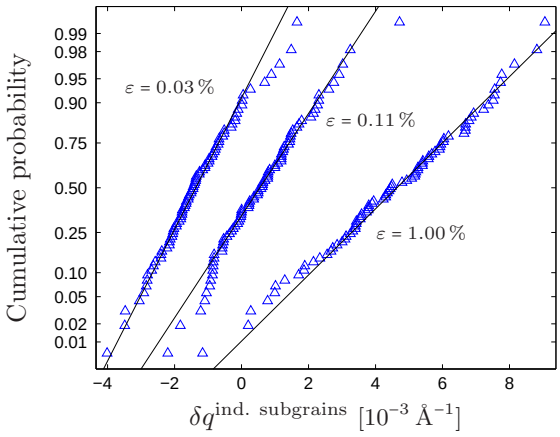

Figure 7.58: A normal probability plot of the position of the 80 largest individual subgrain profiles for three reciprocal space maps from grain d2-1. For each of the reciprocal space maps the best straight line fit is included and the in situ strain is indicated.

The spread in the positions can be characterized by the standard deviation, σ, of the distribution of the positions, which was calculated for the 80 largest subgrains. The results are shown in figure 7.59 as a function of the width of the grain profile. The figure shows an approximately linear relationship between the spread in the position of the individual subgrain profiles and the width of the grain profile.

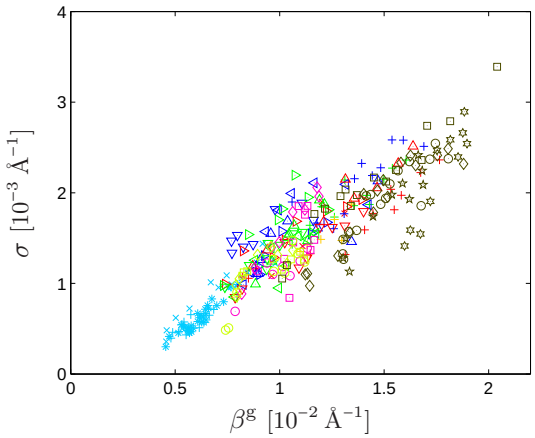

Figure 7.59: The standard deviation of the distribution of the position of the 80 largest individual subgrain profiles as a function of the width of the grain profile.

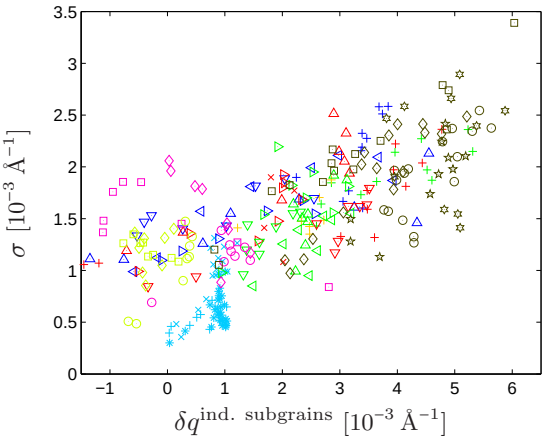

Figure 7.60: The standard deviation of the distribution of the position of the 80 largest individual subgrain profiles as a function of the mean of the position of the same profiles.

In figure 7.60 the spread in the positions is shown as a function of the mean of the position of the individual subgrain profiles (relative to the mean position of the grain profile). The figure shows that the spread is smallest when the shift in position is close to zero, and that the spread in the positions increases with increasing shift in position. This shows a correlation between the average intra-granular stress and the variation in the intra-granular stresses.

Figures 7.61 and 7.62 show the standard deviation of the distribution of the 80 largest individual subgrain positions as a function of the in situ strain up to a strain of 1 %. The rapid increase in the standard deviation during the first 0.2 % to 0.3 % of strain shows that the variation in the intra-granular stresses increases significantly during the micro-plastic range. For larger strains the variation seems to be approximately constant or slightly increasing.

Despite the variation between the curves in figure 7.61, there seems to be a tendency for the spread in the position of the individual subgrain profiles to be larger for the samples subjected to a strain path change (xc3 and xd2) than for the reference sample (xa2) for strains above 0.2 %. This indicates that the variation in the intra-granular stresses increases more after a strain path change, which was also suggested by the results of the fit with a Wilkens and a Gauss profile shown in figure 7.30.

Figure 7.62 shows that a significant spread in the position of the individual subgrain profiles is also observed for the samples observed with an angle of approximately 55 ° between the scattering vector and the in situ deformation axis (xf1 and xg1). As discussed in section 7.2.2, this shows that a significant variation exists in the intra-granular stresses also in the directions perpendicular to the tensile axis, because purely axial stresses would produce almost no radial elastic strain in this case. A comparison with the samples in figure 7.61 (which were observed with the scattering vector nearly parallel to the tensile axis) indicates that the variation in the intra-granular stresses in the perpendicular directions is smaller than the variation along the tensile axis.

Figure 7.62 also shows that for the grains in sample xh1 the variation in the intra-granular stresses decreases or remains constant during the first 0.1 % of strain, before it increases up to a strain of 0.3 %. This again shows that for the grains pre-deformed at a low temperature

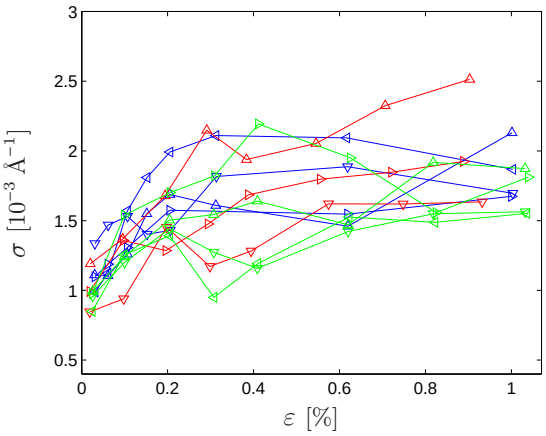

Figure 7.61: The standard deviation of the distribution of the position of the 80 largest individual subgrain profiles for samples xa2, xc3, and xd2 as a function of the in situ strain.

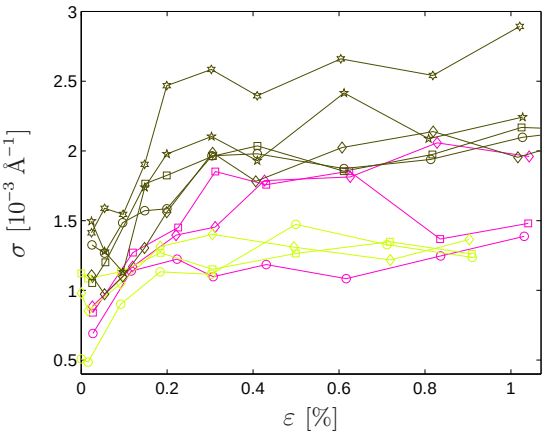

Figure 7.62: The standard deviation of the distribution of the position of the 80 largest individual subgrain profiles for samples xf1, xg1, and xh1 as a function of the in situ strain.

something different happens with the intra-granular stresses during the initial phase of the in situ deformation. As mentioned in section 7.2.3, the larger pre-deformation and the low pre-deformation temperature both result in a higher flow stress, and this may explain the larger variation in the intra-granular stresses for these grains compared to the other samples for strains above 0.3 %.

In conclusion, the distribution of the position of the 80 largest individual subgrain profiles can be well approximated by a Gauss distribution. The width of the distribution, which is a measure of the variation in the intra-granular stresses, increases with the shift of the distribution, which is a measure of the average intra-granular stress.

Furthermore, the analysis shows that the variation in the intra-granular stresses increases rapidly during the micro-plastic range, both along the direction of the deformation axis and in the perpendicular directions. For larger strains the variation appears to be larger for the grains subjected to a strain path change than for the reference grains, and for the grains pre-deformed at a low temperature the variation initially decreases or remains constant before it increases to larger levels than for the other grains.

7.4.3 Width of the individual subgrain profiles

The mean of the profile width was calculated for the large individual subgrain profiles. The results are shown as a function of the width of the grain profile in figure 7.63. The figure shows that the width is generally independent of the width of the grain profile, and therefore independent of the level of deformation. The width for grain group E (for which 222 reflections were investigated) is smaller than for the other grain groups because of differences in the length of the scattering vector and in the contrast factor.

The mean of the profile width was also calculated for the medium individual subgrain profiles and for the small individual subgrain profiles. Figure 7.64 shows the results for all three size categories, with green points representing the large individual subgrains, red points representing the medium individual subgrains and blue points representing the small individual subgrains. The grains in grain group E are not included in the figure. The figure

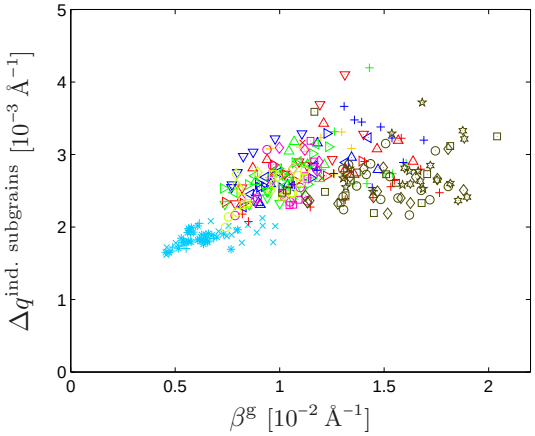

Figure 7.63: The mean of the width of the large individual subgrain profiles as a function of the width of the grain profile.

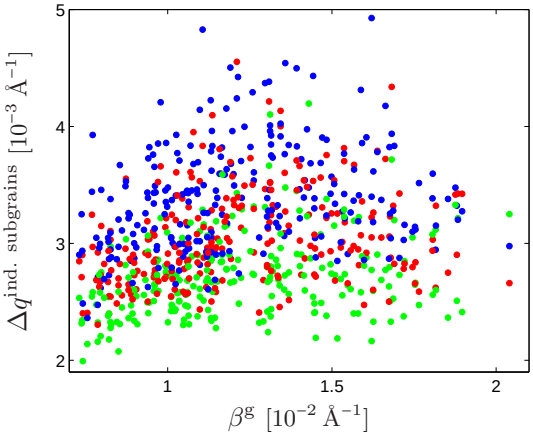

Figure 7.64: The mean of the width of the large (green), medium (red) and small (blue) individual subgrain profiles as a function of the width of the grain profile. Grain group E is not included in the figure.

shows that the width depends on the subgrain size: Large individual subgrain profiles are generally narrower than small individual subgrain profiles. This may be a an effect of size broadening caused by the small size of the individual subgrains. To get an estimate of the size of the effect of size broadening in the subgrains, a typical size of 2 μm was used for the large subgrains and a typical size of 0.5 μm was used for the small subgrains (based on the TEM images shown in section 4.2.2). Equation (3.9) with $k = 1$ then gives a difference in size broadening between the large and the small subgrains of $9.4 \cdot 10^{-4}$ Å^{-1}. This number fits very nicely with the differences shown in figure 7.64, and this suggests that the observed size effect is caused by the effects of size broadening.

The width of the individual subgrain profiles also contains an unknown instrumental contribution, and from the data it can not be ruled out that there is also a contribution from the dislocation content in the subgrains. However, even if such a contribution exists, the results in figure 7.63 show that it does not change with deformation. In other words, even though there may be a small non-zero dislocation density in the subgrains, there are no signs of an accumulation of dislocations during deformation. The dislocation density remains low.

As was shown in figure 6.10 the width of the individual subgrain profiles varies considerably with values between $1.3 \cdot 10^{-3}$ Å^{-1} and $8 \cdot 10^{-3}$ Å^{-1} and a mean around $3 \cdot 10^{-3}$ Å^{-1}. For comparison, Jakobsen et al. (2007) reported a mean width of the individual subgrain profiles of $2.0 \cdot 10^{-3}$ Å^{-1}. Their analysis was based on a manual selection of 14 sharp peaks in the reciprocal space maps and may not have included a large number of small profiles (which have a larger width), which may explain the lower mean width.

In units of strain, the widths reported above range from approximately $1.9 \cdot 10^{-4}$ to $1.2 \cdot 10^{-3}$ with a mean of $4.3 \cdot 10^{-4}$. For comparison, Levine et al. (2008) reported widths ranging from $7.2 \cdot 10^{-4}$ to $2.5 \cdot 10^{-3}$ with a mean of $1.58 \cdot 10^{-3}$ in units of strain. Their analysis was based on measuring the diffracted intensity from selected regions of the crystal in real space, and these selected regions may contain parts of the dislocation walls in addition to the almost dislocation-free subgrain which may explain the larger widths obtained with this method.

Figures 7.65 and 7.66 show the width (FWHM) of the individual subgrain profiles in the azimuthal directions as a function of the width of the grain profile. For most of the samples the resolution in $\tilde{\omega}$ was worse than the resolution in $\tilde{x}$ (see tables 5.2 and A.3), and this may explain the slightly larger width along the $\tilde{\omega}$-direction compared to the $\tilde{x}$-direction. Figure 7.66 shows that the profiles measured with a smaller ω-rocking interval (grains c1-1, e1-1, e2-1, and e3-1) have a smaller width along the $\tilde{\omega}$-direction than the other samples. Apart from the effects of the $\tilde{\omega}$-resolution, the figures show that the width is independent of the width of the grain profile and therefore independent of the level of deformation, and that it is comparable in the three reciprocal space directions (q, $\tilde{x}$, and $\tilde{\omega}$). Although not shown, the size effect discussed for the radial width above is also seen for the azimuthal widths.

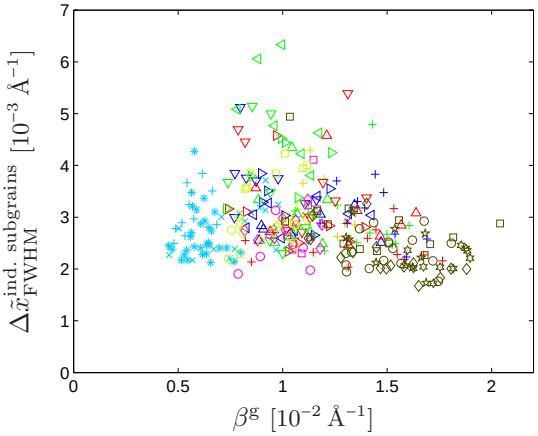

Figure 7.65: The mean of the width (FWHM) in the $\tilde{x}$-direction of the large individual subgrain profiles as a function of the width of the grain profile.

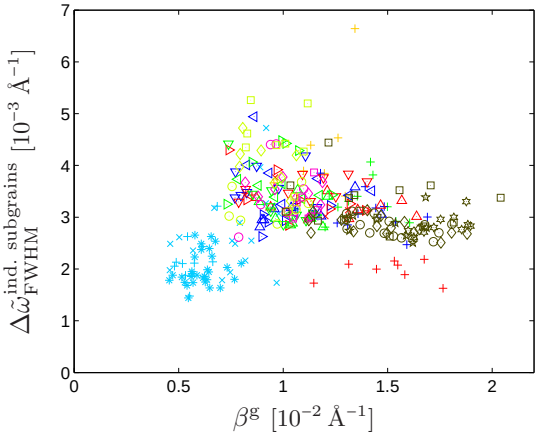

Figure 7.66: The mean of the width (FWHM) in the $\tilde{\omega}$-direction of the large individual subgrain profiles as a function of the width of the grain profile.

In conclusion, the width of the individual subgrain profiles is comparable in all directions in reciprocal space and the width is independent of deformation, showing that the low dislocation content of the subgrains remains constant during deformation. In all three directions in reciprocal space the profile width depends of the maximum intensity of the individual subgrain profile, and this may be interpreted as a result of size broadening.

7.4.4 Evolution of the position of the large individual subgrain profiles

The results presented in section 7.4.1 show that the elastic back-strain is larger in large subgrains than in small subgrains, and that after a sufficiently large strain path change, the elastic back-strain in the subgrains shifts from being tensile to being compressive during the micro-plastic range lasting up to a strain of approximately 0.2 % to 0.3 %. The results presented in section 7.1 show that the morphology of the dislocation structures remains (almost) unchanged during this strain interval, which implies in particular that the size of the subgrains remains constant. It follows that during the micro-plastic range the elastic back-strain in the large subgrains changes more than the elastic back-strain in the small subgrains, or equivalently that the large individual subgrain profiles are shifted more in position than the small individual subgrain profiles.

An attempt was made to see this effect for some of the investigated grains by following the evolution of the position of a number of large individual subgrain profiles. This was done by identifying the same sharp peak in a number of successive subgrain components. This was a challenging task, and in many cases it was very difficult to be sure that the same sharp peak was found in the next subgrain component. This was particularly a problem for the large peaks, which may in many cases be composed of a number of smaller peaks.

It was only possible to perform the analysis when the strain step between successive reciprocal space maps was very small (on the order of 0.05 % or less), and for this reason, and because the shifts in position are most clearly seen in grains with a large grain profile asymmetry, it was only carried out for grains d2-1 and d2-2 up to a strain of approximately 0.3 %. The analysis was attempted for other grains and larger strain values, but this was not fruitful.

For the two grains it was possible to follow nine and eight of the largest subgrains, respectively, in six successive subgrain components. The position of the corresponding individual subgrain profiles is shown in figures 7.67 and 7.68 as a function of the in situ strain.

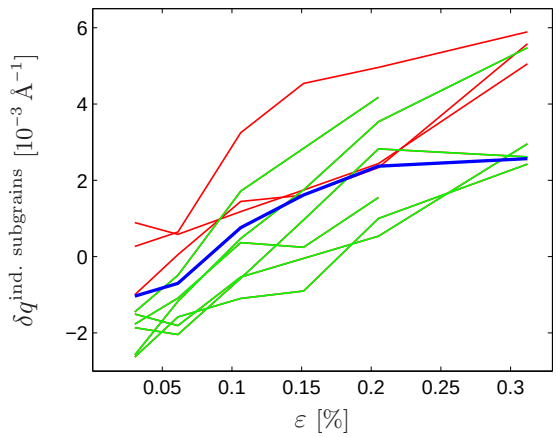

Figure 7.67: The position of nine individual subgrain profiles from grain d2-1 as a function of the in situ strain. The thick blue line indicates the mean of the position of the medium individual subgrain profiles. The red or green color of the thin lines indicates whether they are initially on the high-q or the low-q side of the blue line, respectively.

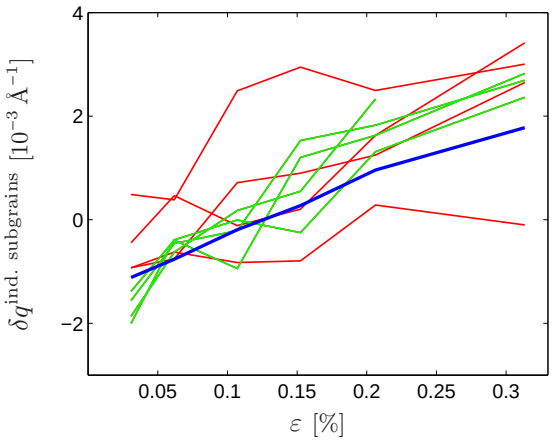

Figure 7.68: The position of eight individual subgrain profiles from grain d2-2 as a function of the in situ strain. The thick blue line indicates the mean of the position of the medium individual subgrain profiles. The red or green color of the thin lines indicates whether they are initially on the high-q or the low-q side of the blue line, respectively.

The figures also include the mean of the position of the medium individual subgrain profiles (thick blue line). This curve does not necessarily represent the same 20 subgrains in each map because the relative size of the profiles change from one subgrain component to the next. The red or green color of the thin lines indicates whether they are initially on the high-q or the low-q side of the blue line, respectively.

The figures show that during the micro-plastic range the large individual subgrain profiles have a tendency to be shifted further than the medium individual subgrain profiles. As discussed above, this means that in the grains subjected to a strain path change, the elastic back-strain changes more in larger subgrains than in smaller subgrains (from the largest

tensile elastic back-strain to the largest compressive elastic back-strain).

In conclusion, despite the difficulties with identifying the sharp peaks from one subgrain component to the next, when the strain steps are sufficiently small it is possible to follow the evolution of the elastic back-strain in individual subgrains, and the analysis shows that the stresses and strains in individual subgrains can change substantially without any drastic changes in the morphology of the dislocation structure.

7.5 Summary and discussion

This section contains a summary and brief discussion of the results about the properties and evolution of the dislocation structures that were presented in sections 7.1 to 7.4.

7.5.1 Gradual changes in the morphology of the dislocation structures

An analysis of the azimuthal maps revealed that the evolution of the morphology of the dislocation structures appears to take place through gradual changes without signs of drastic restructuring. During the first part of the in situ deformation, up to a strain of approximately 0.3 %, only minor changes occur in the morphology, and for larger strains the structure evolves without any sudden major changes and with no indications that intermittent dynamics plays a major role in the evolution.

From visual inspection of the azimuthal maps there are no clear indications of effects on the evolution of the morphology of the dislocation structures from a strain path change or a change in temperature. In all cases the azimuthal maps show signs of relative rotations of the individual subgrains and examples of decreasing cell sizes with large sharp peaks breaking up into smaller peaks and small sharp peaks disappearing into the cloud, consistent with a general decrease in the scale of the dislocation structure.

7.5.2 Properties of the individual subgrains

A statistical analysis of a large number of radial profiles from individual subgrains revealed that on average the profiles from the larger subgrains are positioned further away from the mean position of the grain profile than the profiles from the smaller subgrains are. In terms of elastic strains in the subgrains, this means that on average the larger subgrains experience a larger elastic back-strain than the smaller subgrains.

This can be explained if the larger subgrains deform more easily (at a lower local stress) than the smaller subgrains. Just as the dislocation walls experience an elastic forward-strain because they are harder than the subgrains, the smaller subgrains experience a reduced elastic back-strain because they are harder than the larger subgrains.

A simple explanation for why the larger subgrains are softer than the smaller subgrains can be given in terms of the stress required to bend a dislocation. Plastic deformation of subgrains requires that dislocations move through the subgrains. Because the dislocations can travel more easily through the dislocation-poor interior of the subgrains than through the dislocation-rich walls, a dislocation crossing a subgrain will be held back by the surrounding dislocation walls while it continues across the central part of the subgrain, curved by the applied stress. Because the stress required to bend a dislocation is inversely proportional to the radius of curvature, in a large subgrain, where the radius of curvature can be larger, a smaller stress is required to bend the dislocation sufficiently for it to cross the subgrain. On

the other hand, in a small subgrain the radius of curvature is necessarily smaller and a larger stress is required.

The statistical analysis also showed that the distribution of the position of the 80 largest individual subgrain profiles in each reciprocal space map (or equivalently the distribution of the elastic back-strain) can be well approximated by a Gauss distribution. On average, along the tensile axis the elastic back-strain in the subgrains tends to about 30 % of the average elastic strain in the entire grain when the level of deformation is increased.

The width of the individual subgrain profiles is comparable in all directions in reciprocal space, and the width is independent of deformation, which shows that the low dislocation density in the subgrains remains constant during deformation. In all three directions in reciprocal space the profile width depends on the maximum intensity of the individual subgrain profile, which may be interpreted as a sign of size broadening.

7.5.3 Evolution of the dislocation structures in the reference samples

Significant intra-granular stresses were produced by the pre-deformation in the reference samples. This can be seen from the asymmetry of the grain profile and the relative position of the individual subgrain profiles before the in situ deformation. The variation in the position of the individual subgrain profiles, observed for both the samples investigated with the scattering vector parallel to the pre-deformation axis and for the samples investigated with an angle of approximately 55 ° between the scattering vector and the pre-deformation axis, show that the intra-granular stresses varies considerably between the individual subgrains, and that there is a variation in the intra-granular stresses both along the pre-deformation axis and in the perpendicular directions.

As described by the modified composite model, the intra-granular stresses are produced because the subgrains are softer than the dislocation walls, and therefore, during the pre-deformation the subgrains begin to deform plastically before the walls. When this happens, dislocations accumulate against the walls, which results in a build up of intra-granular stresses until the stress experienced by the walls (the combination of the applied stress and the intra-granular stresses) becomes sufficiently high for them to deform plastically as well.

When an external load is applied during the in situ deformation, the average stress in the grains increases (as shown by the increase in the average elastic strain in the grains), but initially (during the micro-plastic range) the stress is not large enough for the dislocation walls to deform plastically. During this range of deformation the average intra-granular stress increase only slightly. However, as the increase in the spread of the position of the individual subgrain profiles shows, as the applied load increases, the variation in the intra-granular stresses (between the subgrains) increases both along the in situ deformation axis and in the perpendicular directions. This increase in the variation in the intra-granular stresses leads to an increase in the width of the grain profile through an increase of the width of the subgrain subprofile.

When the local stress in the dislocation walls reaches the local flow stress, the walls begin to deform plastically and the range of macro-plastic deformation is reached. When this happens, the intra-granular stresses continue to increase slowly (as shown by the slow shift in the position of the individual subgrains) as the flow stress in the walls increases due to local work hardening. The variation in the intra-granular stresses also appears to increase slowly, but this is less clear from the data. The fact that the width of the individual subgrain profiles is independent of deformation shows that the dislocation density in the subgrains remains

at a constant low level, and that the increase in dislocation density occurs in the dislocation walls.

The elastic strain in the subgrains can be measured directly from the reciprocal space maps, and the average intra-granular stress and the variation in the intra-granular stresses can be measured with a great deal of certainty. The properties of the dislocation walls are much less accessible. However, the results from the fit with a Wilkens and a Gauss profile and the rapid increase of the grain profile width as a function of stress in the macro-plastic range indicate that the dislocation density increases with deformation. The quantitative results for the dislocation arrangement parameter imply that in the reference samples the arrangement of the dislocations in the walls undergoes no significant changes during the in situ deformation.

7.5.4 Evolution of the dislocation structures in the samples subjected to a strain path change

Due to the change in deformation axis for the samples subjected to a strain path change, the load applied during the in situ deformation introduces stresses which may act in the same direction as the intra-granular stresses in the subgrains and opposite to the intra-granular stresses in the walls.

For this reason the local stress in the subgrains reaches the local flow stress at a lower applied stress compared to continued deformation along the pre-deformation axis, causing dislocations to move across the subgrains. In the walls, however, the applied stress is reduced by the intra-granular stresses, preventing plastic deformation of the walls (penetration of dislocations into the walls) until a sufficient number of dislocations have moved through the subgrains and been accumulated against the walls, thereby changing the intra-granular stresses.

These substantial changes in the intra-granular stresses which occur during the first 0.3 % of strain (the micro-plastic range) are evident in the evolution of the grain profile asymmetry and the relative position of the individual subgrain profiles. The increase in the spread of the position of the individual subgrain profiles show that the variation in the intra-granular stresses also increases during the same strain interval. The increase in the variation in the intra-granular stresses during the micro-plastic range appears to be slightly larger for the samples subjected to a strain path change than for the reference samples. This was also indicated by the increased width of the Gauss profile for these samples in the fit with a Wilkens and a Gauss profile, and this may be part of the explanation for the larger width of the grain profile observed for the samples subjected to a strain path change compared to the reference samples.

For higher strains, in the macro-plastic range, the average intra-granular stress increase slowly as for the reference samples (as shown by the slow shift in the position of the individual subgrains). For some of the grains the variation in the intra-granular stresses also appears to increase slowly, but this is less clear from the data. As for the reference samples, the dislocation density in the subgrains appears to remain constant.

With respect to the dislocation walls, the dislocation density appears to increase as for the reference samples. However, the results from the fit with a Wilkens and a Gauss profile indicate that the dislocation arrangement parameter is larger after a strain of approximately 0.2 % for the samples subjected to a strain path change. In these samples new slip systems are activated during the in situ deformation, and the interaction between the new dislocations and the old structure may lead to dislocation configurations in which the screening of the

dislocation strain fields is less effective. This may also be part of the explanation for the larger width of the grain profile observed for these samples compared to the reference samples.

7.5.5 Evolution of the dislocation structures in the samples subjected to a change in temperature

In the sample pre-deformed at a temperature of -196 °C the intra-granular stresses produced by the pre-deformation were larger than in the reference samples. This may be the result of the larger pre-deformation and the low pre-deformation temperature, since both effects increase the dislocation density and hence the flow stress.

Upon application of an external load during the in situ deformation, the average intra-granular stress and the variation in the intra-granular stresses appear to either decrease slightly or remain at a constant level up to a strain of approximately 0.1 % despite the increase in the applied load. This can be seen in the asymmetry of the grain profile, the relative position of the individual subgrain profiles and the variation in the position of the individual subgrain profiles. This is different from the behavior of both the reference samples and the samples subjected to a strain path change in which both the average intra-granular stress and the variation in the intra-granular stresses increase immediately when the external load is applied.

The decline or stagnation of the average intra-granular stress and the variation in the intra-granular stresses may be a result of the processes responsible for the work softening observed by Cottrell & Stokes (1955) and Adams & Cottrell (1955), and it may be interpreted as described in section 2.3.4: During deformation at a low temperature short-range dislocation interactions form immobile dislocation configurations which remain when the sample is unloaded and the temperature is increased. These dislocation segments act as barriers to dislocation motion, locking the mobile dislocations in place and supporting the intra-granular stresses. When an external load is applied at a higher temperature, the intra-granular stresses increase, but because of the higher temperature and the resulting increase in the rate of thermally activated processes, the barriers are gradually destroyed, and this enables the pinned dislocations to move, thereby reducing the intra-granular stresses. The combined effect may be that the intra-granular stresses remain at an almost constant level until no more immobile segments exist (or until the remaining immobile segments are all stable at the applied stress) and the intra-granular stresses can increase as in the samples pre-deformed at room temperature. When this point is reached, both the average intra-granular stress and the variation in the intra-granular stresses increase during the micro-plastic range just as for the other samples. Both reach levels higher than for the other samples, which, as mentioned above, may be due to the larger pre-deformation and the low pre-deformation temperature.

When the macro-plastic range is reached, the increase in both the average intra-granular stress and the variation in the intra-granular stresses continues at a slow rate (the variation in the position of the individual subgrains and the asymmetry of the grain profiles increase slightly as the strain is increased, but the increase is not very clear in the relative position of the individual subgrain profiles).

The results from the fit with a Wilkens and a Gauss profile indicate that in this sample the dislocation density increases at a slower rate than for the other samples. This may be explained in terms of the different rate of thermally activated recovery processes during the low-temperature pre-deformation and the in situ deformation at room temperature. During the pre-deformation the suppression of thermally activated processes resulted in a structure

with a larger dislocation density and less order. When the deformation is resumed at room temperature, thermally activated processes occur more frequently and clean up the dislocation structure produced at a low temperature, partly by removing some of the dislocations, which results in a slower increase in the dislocation density. It seems likely that a larger pre-deformation at a low temperature would increase the size of this effect and maybe even lead to a decrease in the dislocation density, and this may also be part of the explanation for the work softening observed by Cottrell & Stokes (1955) and Adams & Cottrell (1955).

The results from the fit with a Wilkens and a Gauss profile also indicate that for the sample pre-deformed at a low temperature the dislocation arrangement parameter is initially larger than for the reference samples, and that it increases further during the micro-plastic range. The initially larger value can be interpreted as a result of the suppression of thermally activated recovery processes during the low-temperature pre-deformation leading to a more disordered dislocation structure. The fact that the dislocation arrangement parameter increases further during the micro-plastic range shows that when the deformation is continued at room temperature the dislocation structure in the walls becomes even more disordered and the screening of the dislocation strain fields becomes less effective.

Chapter 8

Conclusions and outlook

The aim of the work presented in this thesis was to study the evolution of dislocation structures following a strain path change or a change in temperature. For this purpose copper samples were prepared with a dislocation cell structure produced by pre-deformation in tension to a strain of 5 % at room temperature or to a strain of 7 % at a temperature of -196 °C. The samples were used for TEM investigations, for mechanical characterization, and for X-ray diffraction experiments.

The TEM investigations of the morphology of the dislocation structures in grains deformed to different strain levels showed that with increasing strain the dislocation density in the walls increases and the walls appear sharper and more well defined. After an orthogonal strain path change the walls appear thicker and less well defined, and the structure looks more homogeneous.

The mechanical characterization of samples subjected to different tension-tension strain path changes (characterized by the strain path change parameter α) showed that for $\alpha = 1/2$ and $\alpha = 0$ the yield stress is increased, and for $\alpha = -1/2$, the yield stress is unchanged compared to the reference samples. In all three cases the strain path change is followed by a transient phase with a reduced work hardening rate.

To study the evolution of dislocations structures following a change in loading conditions the pre-deformed samples were further deformed in tension (along a different axis for some of the samples) at the APS synchrotron (the Advanced Photon Source at Argonne National Laboratory). The X-ray diffraction experiments constituted the main part of the work and a technique was employed with which it is it possible to obtain high-resolution reciprocal space maps from individual bulk grains in situ while deforming the samples in tension. The high-resolution reciprocal space maps contain features related to the dislocation structure in the grains: A spread-out cloud of low intensity caused by diffraction from the dislocation walls and a number of sharp high-intensity peaks caused by diffraction from the individual subgrains. For the analysis of the reciprocal space maps a mathematical method was developed to partition the intensity distribution into two components corresponding to the contributions from the subgrains and the walls. The main results from the X-ray diffraction experiments are summarized below:

- **Gradual changes in the morphology of the dislocation structures:** Analysis of the azimuthal maps showed that for in situ strains below 0.3 % only minor changes occur in the morphology of the dislocation structures.

  For larger strains the evolution occurs in a gradual manner without any sudden major changes and with no indications that intermittent dynamics plays a major role in the evolution of the dislocation structures.

- **Distribution of the elastic back-strain in the individual subgrains:** A statistical analysis of the position of a large number of radial profiles from individual subgrains showed a substantial variation in the elastic back-strain (and therefore in the intra-granular stresses) in the individual subgrains, both along the deformation axis and along the perpendicular directions. The analysis also revealed that the distribution of the elastic back-strain in the subgrains can be well approximated by a Gauss distribution.

  It was found that for levels of deformation where the pre-deformation no longer significantly influences the distribution of the intra-granular stresses, the average elastic back-strain along the deformation axis in the subgrains is about 30 % of the average elastic strain along the deformation axis in the entire grain.

- **Size effect in the elastic back-strain in the individual subgrains:** Based on the statistical analysis of the position of the individual subgrain profiles a size effect was found in the elastic back-strain in the subgrains. On average the larger subgrains experience a larger elastic back-strain than the smaller subgrains.

- **Evolution of the elastic back-strain in the individual subgrains:** The analysis showed that the variation in the intra-granular stresses increases, both along the deformation axis and along the perpendicular directions, when the externally applied stress is increased.

  In the samples subjected to a strain path change, the intra-granular stresses are substantially redistributed during the micro-plastic range (up to a strain of approximately 0.3 %) in order to ensure a compatible deformation along the new deformation axis. In a few individual subgrains it was possible to follow the evolution of the elastic back-strain from the tensile to the compressive case.

  In the sample pre-deformed at a temperature of -196 °C, the average intra-granular stress and the variation in the intra-granular stresses go through an initial phase of decrease or stagnation, which can be interpreted in terms of the destruction of immobile dislocation configurations formed during the low-temperature pre-deformation.

- **Evolution of the dislocation density in the individual subgrains:** The width of the radial profiles from the individual subgrains is small and appears to be independent of the deformation. This shows that the dislocation density in the subgrains remains constant at a low level during the deformation.

- **Evolution of the dislocation density and arrangement in the dislocation walls:** The results of fitting a Wilkens and a Gauss profile to the grain profiles indicate that the dislocation density in the walls increases with increasing strain, and that the increase is slower for the sample pre-deformed at a low temperature.

The evolution of the dislocation arrangement parameter indicates that a change in loading conditions (either a strain path change or a change in temperature) leads to a less ordered dislocation structure in the walls with a weaker correlation between the dislocations and a weaker screening of the dislocation strain fields.

The X-ray diffraction experiments presented in this thesis were limited by the lack of spatial resolution, by the use of only one reflection from each grain, and by the fact that the samples were only deformed to relatively small levels of strain. These limitations provide a natural starting point if the technique should be developed further.

First, the technique has no spatial resolution. The usefulness of the technique would be greatly increased if it was also possible to study the spatial arrangement of the subgrains. One way to accomplish this might be with the use of a box-scanning technique (which only requires two line scans of the X-ray beam and therefore is much faster than techniques that scans the sample surface in a grid). However, such a technique would require that sophisticated reconstruction algorithms are developed.

Second, as presented in this thesis the technique uses only a single reflection from each grain. By rotating the sample it would be possible to obtain reciprocal space maps of other reflections from the same grain. This would give access to more information about the orientation of the subgrains and about the elastic strain in the subgrains along different directions. For such a procedure to be feasible, it would probably require that an automated routine for finding different reflections from the same grain is developed. It should be mentioned that such an experiment has been performed with limited outcome by Jakobsen (2006) who acquired partial high-resolution reciprocal space maps from two reflections from a single grain in polycrystalline copper.

Third, use of the technique is restricted to relatively low levels of strain. This is both because overlap between reflections from different grains are more frequent at higher strains, but also because the subgrains become smaller at higher strains, and in the reciprocal space maps the sharp peaks overlap and blend into the cloud, resulting in a more homogeneous and featureless reciprocal space map in which the individual subgrains can not be identified. These problems might be overcome by reducing the volume of the sample that is illuminated. The extent of the illuminated volume along the X-ray beam could be reduced by using a thinner sample or a conical slit. To reduce the extent of the illuminated volume in the directions perpendicular to the X-ray beam would require a very narrow X-ray beam, and if the beam size is reduced below the grain size, the sample surface would have to be scanned in a grid. This would, however, greatly increase the acquisition time and make dynamic studies that require multiple reciprocal space maps unfeasible.

Even without any further development the technique could be used as it is to study the evolution of dislocation structures in other experiments than those presented in this thesis. Interesting candidates could be unloading-reloading sequences, fatigue or, with the inclusion of a furnace in the setup, recovery. Finally, it should be mentioned that the technique can of course also be used to investigate dislocation structures in other materials, e.g. steels.

Appendix A

Overview of the investigated samples and grains

The tables in this appendix contain an overview of the samples and grains described in the thesis. Table A.1 contains a summary of the properties of the samples prepared for TEM investigations, for mechanical characterization, and for X-ray diffraction experiments. Table A.2 contains an overview of the grain groups defined in section 5.3. Table A.3 contains an overview of all the grains investigated in the X-ray diffraction experiments. The meaning of the column names is as follows:

Table A.1:
Name: The name of the sample. The first letter in the sample name indicates the use for the sample: 't' for TEM investigations, 'm' for mechanical characterization, and 'x' for X-ray diffraction experiments. The color used to write the name of the 'x'-samples is the color used in the text in the thesis when referring to these samples.
Shape: The sample shape. Figure 4.2 showed the shape and dimensions of the samples.
ψ_1**:** The angle between the pre-deformation axis and the rolling direction.
ε_1**:** The (engineering) strain along the pre-deformation axis.
T_1**:** The temperature of the pre-deformation. 'RT' denotes room temperature and 'N2' denotes a temperature of -196 °C.
ψ_2**:** The angle between the second deformation axis and the rolling direction. This is not defined for samples that were only subjected to one deformation.
ε_2**:** The (engineering) strain along the second deformation axis. This is not defined for samples that were only subjected to one deformation.
T_2**:** The temperature of the second deformation. 'RT' denotes room temperature. This is not defined for samples that were only subjected to one deformation.
α**:** The strain path change parameter (see equation (2.5)). This is not defined for samples that were only subjected to one deformation.

Table A.1: Overview of the prepared samples. See the text for description of the column names.

Name	Shape	ψ_1	ε_1	T_1	ψ_2	ε_2	T_2	α
t1	Rectangular	0 °	5 %	RT	0 °	4 %	RT	1
t2	Rectangular	0 °	5 %	RT	90 °	1 %	RT	−1/2
t3	Rectangular	0 °	5 %	RT	90 °	2 %	RT	−1/2
t4	Rectangular	0 °	5 %	RT	90 °	5 %	RT	−1/2
t5	Rectangular	0 °	5 %	RT	90 °	10 %	RT	−1/2
m1	Rectangular	0 °	44 %	RT				
m2	Rectangular	0 °	33 %	RT				
m3	Rectangular	0 °	5 %	RT	0 °	10 %	RT	1
m4	Rectangular	0 °	5 %	RT	0 °	30 %	RT	1
m5	Rectangular	35 °	41 %	RT				
m6	Rectangular	35 °	38 %	RT				
m7	Rectangular	0 °	5 %	RT	35 °	4 %	RT	1/2
m8	Rectangular	0 °	5 %	RT	35 °	10 %	RT	1/2
m9	Rectangular	0 °	5 %	RT	35 °	34 %	RT	1/2
m10	Rectangular	55 °	39 %	RT				
m11	Rectangular	55 °	39 %	RT				
m12	Rectangular	0 °	5 %	RT	55 °	4 %	RT	0
m13	Rectangular	0 °	5 %	RT	55 °	10 %	RT	0
m14	Rectangular	0 °	5 %	RT	55 °	35 %	RT	0
m15	Rectangular	90 °	39 %	RT				
m16	Rectangular	90 °	31 %	RT				
m17	Rectangular	0 °	5 %	RT	90 °	4 %	RT	−1/2
m18	Rectangular	0 °	5 %	RT	90 °	32 %	RT	−1/2
xa1	Dog-bone	0 °	5 %	RT	0 °	4.8 %	RT	1
xa2	Dog-bone	0 °	5 %	RT	0 °	1.6 %	RT	1
xb1	Dog-bone	0 °	5 %	RT	35 °	4.4 %	RT	1/2
xc1	Dog-bone	0 °	5 %	RT	55 °	3.2 %	RT	0
xc2	Dog-bone	0 °	5 %	RT	55 °	4.9 %	RT	0
xc3	Dog-bone	0 °	5 %	RT	55 °	1.5 %	RT	0
xd1	Dog-bone	0 °	5 %	RT	90 °	4.9 %	RT	−1/2
xd2	Dog-bone	0 °	5 %	RT	90 °	1.0 %	RT	−1/2
xe1	Dog-bone	0 °	5 %	RT	90 °	0.9 %	RT	−1/2
xe2	Dog-bone	0 °	5 %	RT	90 °	5.5 %	RT	−1/2
xe3	Dog-bone	0 °	5 %	RT	90 °	2.9 %	RT	−1/2
xf1	Dog-bone	0 °	5 %	RT	0 °	0.9 %	RT	1
xg1	Dog-bone	0 °	5 %	RT	55 °	1.0 %	RT	0
xh1	Dog-bone	0 °	7 %	N2	0 °	5.1 %	RT	1

Table A.2:
Name: The name of the grain group. The color used to write the name is the color used in the text in the thesis when referring to the grain groups.
α: The strain path change parameter (see equation (2.5)).
ε_1: The (engineering) strain along the pre-deformation axis.
T_1: The temperature of the pre-deformation. 'RT' denotes room temperature and 'N2' denotes a temperature of -196 °C.
T_2: The temperature of the second deformation. 'RT' denotes room temperature.
Refl.: The type of reflection investigated.
ξ: The angle between the scattering vector and the in situ deformation axis.
 # samples: The number of samples with grains in the grain group.
 # grains: The total number of grains in the grain group.

Table A.2: Overview of the grain groups. See the text for description of the column names.

Name	α	ε_1	T_1	T_2	Refl.	ξ	# samples	# grains
A	1	5 %	RT	RT	400	0 °	2	5
B	1/2	5 %	RT	RT	400	0 °	1	1
C	0	5 %	RT	RT	400	0 °	3	5
D	−1/2	5 %	RT	RT	400	0 °	2	5
E	−1/2	5 %	RT	RT	222	0 °	3	3
F	1	5 %	RT	RT	400	55 °	1	3
G	0	5 %	RT	RT	400	55 °	1	3
H	1	7 %	N2	RT	400	0 °	1	5

Table A.3:
Grain: The name of the grain. The color used to write the name is the color used in the text in the thesis when referring to the grains.
Sample: The name of the sample. The color used to write the name is the color used in the text in the thesis when referring to the samples.
Grain group: The name of the grain group. The color used to write the name is the color used in the text in the thesis when referring to the grain groups.
Symbol: The symbol used for the grain in the figures in the thesis.
 # maps: The number of reciprocal space maps obtained from the map. Numbers in parenthesis indicate partial reciprocal space maps.
$\Delta\omega$: The rocking interval used for the reciprocal space maps for the grain. Numbers in parenthesis indicate the rocking interval used for the partial reciprocal space maps from that grain.
z^S: The position of the grain along the sample z-axis (described in appendix B). The absolute value of this number gives the distance from the center of the sample to the grain. The value was determined as described in appendix B.

Table A.3: Overview of the grains investigated with X-ray diffraction. See the text for description of the column names.

Grain	Sample	Grain group	Symbol	# maps	$\Delta\omega$	z^S
a1-1	xa1	A	+	11	0.015 °	-0.116 μm
a2-1	xa2	A	△	8	0.015 °	0.031 μm
a2-2	xa2	A	▽	8	0.015 °	
a2-3	xa2	A	▷	8	0.015 °	-0.097 μm
a2-4	xa2	A	◁	8 + (18)	0.015 ° (0.007 °)	0.041 μm
b1-1	xb1	B	+	11	0.015 °	0.097 μm
c1-1	xc1	C	+	(11)	0.005 °	-0.015 μm
c2-1	xc2	C	×	11	0.015 °	0.033 μm
c3-1	xc3	C	△	8	0.015 °	-0.074 μm
c3-2	xc3	C	▽	9 + (22)	0.015 ° (0.007 °)	0.123 μm
c3-3	xc3	C	▷	8	0.015 °	-0.137 μm
d1-1	xd1	D	×	11	0.015 °	-0.033 μm
d2-1	xd2	D	△	8	0.015 °	0.003 μm
d2-2	xd2	D	▽	8	0.015 °	-0.031 μm
d2-3	xd2	D	▷	6	0.015 °	0.014 μm
d2-4	xd2	D	◁	8	0.015 °	-0.075 μm
e1-1	xe1	E	+	(10)	0.005 °	
e2-1	xe2	E	×	(17)	0.007 °	
e3-1	xe3	E	✳	(30)	0.007 °	
f1-1	xf1	F	○	8	0.015 °	0.098 μm
f1-2	xf1	F	□	8	0.015 °	0.023 μm
f1-3	xf1	F	◇	8	0.015 °	0.004 μm
g1-1	xg1	G	○	8	0.015 °	0.123 μm
g1-2	xg1	G	□	8	0.015 °	-0.138 μm
g1-3	xg1	G	◇	8	0.015 °	0.067 μm
h1-1	xh1	H	○	16	0.015 °	-0.078 μm
h1-2	xh1	H	□	15	0.015 °	-0.102 μm
h1-3	xh1	H	◇	16	0.015 °	-0.104 μm
h1-4	xh1	H	☆	10	0.015 °	
h1-5	xh1	H	✡	10	0.015 °	0.127 μm

Appendix B

Determining the position of a grain within a sample

This appendix describes how the position of a grain within a sample and thereby the distance from the grain to the sample surface can be determined.

The position of the grains in the samples is described in a coordinate system, called the sample system, fixed with respect to the sample. This coordinate system is defined such that it coincides with the laboratory system when ω, χ and ϕ are zero. The axes of the sample system are denoted by x^S, y^S and z^S, and they are parallel to the axes of the translation stages. The transformation from the sample coordinates (x^S, y^S, z^S) to the laboratory coordinates (x, y, z) is given by

$$(x, y, z)^T = \boldsymbol{R}(\omega, \chi, \phi)(x^S, y^S, z^S)^T, \tag{B.1}$$

where

$$\boldsymbol{R} = \begin{pmatrix} \cos(\phi)\cos(\chi) & -\sin(\chi) & \sin(\phi)\cos(\chi) \\ \cos(\phi)\sin(\chi)\cos(\omega) - \sin(\phi)\sin(\omega) & \cos(\chi)\cos(\omega) & \sin(\phi)\sin(\chi)\cos(\omega) + \cos(\phi)\sin(\omega) \\ -\cos(\phi)\sin(\chi)\sin(\omega) - \sin(\phi)\cos(\omega) & -\cos(\chi)\sin(\omega) & -\sin(\phi)\sin(\chi)\sin(\omega) + \cos(\phi)\cos(\omega) \end{pmatrix} \tag{B.2}$$

is the transformation matrix, and the superscript T denotes transposition.

To determine the sample coordinates of a grain, the grain is first centered in the beam by measuring the intensity of a reflection as a function of the grain position. Because the center of rotation of the Euler cradle is centered with respect to the beam, this means that x and y for the grain are both zero:

$$(0, 0, z_1)^T = \boldsymbol{R}(\omega_1, \chi_1, \phi_1)(x^S, y^S, z^S)^T, \tag{B.3}$$

where the subscript 1 indicates that the parameter values correspond to the first position and orientation.

The orientation of the sample is then changed, which, in general, moves the grain out of the beam. If the grain satisfies the diffraction condition in the new orientation, the grain can be brought back to the center of the beam by translating the sample along the x^S-axis and the y^S-axis while measuring the diffracted intensity. The shifts necessary to do this are denoted by Δx^S and Δy^S. The sample coordinates of the grain after the translation are $(x^S + \Delta x^S, y^S + \Delta y^S, z^S)$, and they satisfy the equation

$$(0, 0, z_2)^T = \boldsymbol{R}(\omega_2, \chi_2, \phi_2)(x^S + \Delta x^S, y^S + \Delta y^S, z^S)^T. \tag{B.4}$$

where the subscript 2 indicates that the parameter values correspond to the second position and orientation.

Equations (B.3) and (B.4) contain the three equations:

$$\begin{aligned}
&x^S\cos(\phi_1)\cos(\chi_1) - y^S\sin(\chi_1) + z^S\sin(\phi_1)\cos(\chi_1) = 0\\
&x^S(\cos(\phi_1)\sin(\chi_1)\cos(\omega_1) - \sin(\phi_1)\sin(\omega_1)) + y^S\cos(\chi_1)\cos(\omega_1) + z^S(\sin(\phi_1)\sin(\chi_1)\cos(\omega_1) + \cos(\phi_1)\sin(\omega_1)) = 0\\
&(x^S + \Delta x^S)\cos(\phi_2)\cos(\chi_2) - (y^S + \Delta y^S)\sin(\chi_2) + z^S\sin(\phi_2)\cos(\chi_2) = 0.
\end{aligned} \tag{B.5}$$

If the angles ω_1, χ_1, ϕ_1, χ_2, and ϕ_2 are known and the shifts Δx^S and Δy^S are measured, this system of equations can be solved for the sample coordinates (x^S, y^S, z^S). z^S is the distance from the grain to the center of rotation along the z^S-axis, and when the position of the sample with respect to the center of rotation is known, the distance from the grain to the sample surface can be calculated.

In order to use the method, it is necessary to find a second orientation of the grain in which the used reflection satisfies the diffraction condition. If the angular coordinates of the reflection in the first orientation are $(2\theta,\eta)$, the corresponding reciprocal lattice vector, $\boldsymbol{G}$, has length

$$|\boldsymbol{G}| = 4\pi\sin(\theta)/\lambda \tag{B.6}$$

and laboratory coordinates

$$\boldsymbol{G}_1 = \big(G_{x,1}, G_{y,1}, G_{z,1}\big) = \big(-|\boldsymbol{G}|\cos(\theta)\sin(\eta), |\boldsymbol{G}|\cos(\theta)\cos(\eta), -|\boldsymbol{G}|\sin(\theta)\big). \tag{B.7}$$

The laboratory coordinates of $\boldsymbol{G}$ in the second orientation are

$$\boldsymbol{G}_2 = \boldsymbol{R}(\omega_2, \chi_2, \phi_2)\big(\boldsymbol{R}(\omega_1, \chi_1, \phi_1)\big)^{-1}\boldsymbol{G}_1. \tag{B.8}$$

Because of the geometry of the setup, the value of χ has no effect on the position of the grain with respect to the beam and need not be changed during the rotation. It is then straightforward, based on equation (B.8), to numerically calculate all the combinations of ω_2 and ϕ_2 for which the reciprocal lattice vector satisfies the diffraction condition:

$$G_{z,2} = G_{z,1} = -|\boldsymbol{G}|\sin(\theta). \tag{B.9}$$

Bibliography

Abbaschian, R., Abbaschian, L. & Reed-Hill, R. E. (2010), *Physical Metallurgy Principles*, fourth edn, Cengage Learning.

Adams, A. & Cottrell, A. H. (1955), 'Effect of Temperature on the Flow Stress of Work-Hardened Copper Crystals', *Philosophical Magazine* **46**, 1187–1193.

Aernoudt, E., Van Houtte, P. & Leffers, T. (1993), Deformation and Textures of Metals at Large Strain, *in* H. Mughrabi, ed., 'Plastic Deformation and Fracture of Materials', Vol. 6 of *Materials Science and Technology: A Comprehensive Treatment*, VCH Publishers Inc., chapter 3, pp. 89–136.

Als-Nielsen, J. & McMorrow, D. (2001), *Elements of Modern X-Ray Physics*, first edn, John Wiley & Sons Ltd.

Argon, A. S. & Haasen, P. (1993), 'A new mechanism of work hardening in the late stages of large strain plastic flow in fcc and diamond cubic crystals', *Acta Metallurgica et Materialia* **41**, 3289–3306.

Bandler, J. W., Chen, S. H., Biernacki, R. M., Gao, L., Madsen, K. & Yu, H. (1993), 'Huber Optimization of Circuits: A Robust Approach', *IEEE Transactions on Microwave Theory and Techniques* **41**, 2279–2287.

Basinski, Z. S. (1964), 'Dislocation Distribution in Deformed Copper Single Crystals', *Discussions of the Faraday Society* **38**, 93–102.

Bay, B., Hansen, N., Hughes, D. A. & Kuhlmann-Wilsdorf, D. (1992), 'Evolution of F.C.C. deformation structures in polyslip', *Acta Metallurgica et Materialia* **40**, 205–219.

Bouvier, S., Alves, J. L., Oliveira, M. C. & Menezes, L. F. (2005), 'Modelling of anisotropic work-hardening behaviour of metallic materials subjected to strain-path changes', *Computational Materials Science* **32**, 301–315.

Bulatov, V. V. (2002), 'Current developments and trends in Dislocation Dynamics', *Journal of Computer-Aided Materials Design* **9**, 133–144.

Christodoulou, N., Woo, O. T. & MacEwen, S. R. (1986), 'Effect of Stress Reversals on the Work Hardening Behaviour of Polycrystalline Copper', *Acta Metallurgica* **34**, 1553–1562.

Cottrell, A. H. & Stokes, R. J. (1955), 'Effects of temperature on the plastic properties of aluminium crystals', *Proceedings of the Royal Society of London. Series A, Mathematical and Physical Sciences* **233**, 17–34.

Cullity, B. D. & Stock, S. R. (2001), *Elements of X-Ray Diffraction*, third edn, Prentice Hall.

Essmann, U. (1963), 'Die Versetzungsanordnung in plastisch verformten Kupfereinkristallen', *Physica Status Solidi* **3**, 932–949.

Essmann, U., Rapp, M. & Wilkens, M. (1968), 'Die Versetzungsanordnung in plastisch verformten Kupfervielkristallen', *Acta Metallurgica* **16**, 1275–1287.

Fernandes, J. V., Gracio, J. J. & Schmitt, J. H. (1993), Grain size effect on the microstructural evolution of copper deformed in rolling-tension, *in* C. Teodosiu, J. L. Raphanel & F. Sidoroff, eds, 'Large Plastic Deformations: Fundamental Aspects and Applications to Metal Forming', Taylor & Francis, pp. 219–228.

Göttler, E. (1973), 'Versetzungsstruktur und Verfestigung von [100]-Kupfereinkristallen. I. Versetzungsanordnung und Zellstruktur zugverformter Kristalle', *Philosophical Magazine* **28**, 1057–1076.

Guinier, A. (1994), *X-Ray Diffraction: In Crystals, Imperfect Crystals, and Amorphous Bodies*, first edn, Dover Publications.

Haasen, P. (1993), 'On the region-iv hardening of fcc single-crystals', *Zeitschrift für Metallkunde* **84**, 387–390.

Hirth, J. P. & Lothe, J. (1992), *Theory of Dislocations*, Krieger Publishing Company.

Honeycombe, R. W. K. (1968), *The Plastic Deformation of Metals*, Edward Arnold Publishers Ltd.

Hosford, W. F. (1993), *The Mechanics of Crystals and Textured Polycrystals*, Oxford University Press.

Huang, X. (1998), 'Grain Orientation Effect on Microstructure in Tensile Strained Copper', *Scripta Materialia* **38**, 1697–1703.

Huang, X., Borrego, A. & Pantleon, W. (2001), 'Polycrystal deformation and single crystal deformation: dislocation structure and flow stress in copper', *Materials Science and Engineering* **A319-321**, 237–241.

Huang, X. & Winther, G. (2007), 'Dislocation structures. Part I. Grain orientation dependence', *Philosophical Magazine* **87**, 5189–5214.

Hughes, D. A. & Hansen, N. (2004), Plastic Deformation Structures, *in* G. F. Vander Voort, ed., 'Metallography and Microstructures', Vol. 9 of *AMS Handbook*, ASM International, pp. 192–206.

Hughes, D. A., Liu, Q., Chrzan, D. C. & Hansen, N. (1997), 'Scaling of Microstructural Parameters: Misorientations of Deformation Induced Boundaries', *Acta Materialia* **45**, 105–112.

Hull, D. & Bacon, D. J. (2001), *Introduction to Dislocations*, fourth edn, Butterworth-Heinemann.

Jakobsen, B. (2006), *In-situ* studies of bulk deformation structures: Static properties under load and Dynamics during deformation, Ph.d. thesis, Roskilde University.

Jakobsen, B., Poulsen, H. F., Lienert, U., Almer, J., Shastri, S. D., Sørensen, H. O., Gundlach, C. & Pantleon, W. (2006), 'Formation and subdivision of deformation structures during plastic deformation', *Science* **312**, 889–892.

Jakobsen, B., Poulsen, H. F., Lienert, U., Bernier, J., Gundlach, C. & Pantleon, W. (2009), 'Stability of disocation structures in copper towards stress relaxation investigated by high angular resolution 3d x-ray diffraction', *Physica Status Solidi A* **206**, 21–30.

Jakobsen, B., Poulsen, H. F., Lienert, U. & Pantleon, W. (2007), 'Direct determination of elastic strains and dislocation densities in individual subgrains in deformation structures', *Acta Materialia* **55**, 3421–3430.

Knoesen, D. & Kritzinger, S. (1982), 'Dislocation Cell Boundary Widths and Dislocation Cell Sizes in Deformed Copper', *Acta Metallurgica* **30**, 1219–1222.

Krivoglaz, M. A. & Ryaboshapka, K. P. (1963), 'Theory of X-ray scattering by crystals containing dislocations screw and edge dislocations randomly distributed throughout the crystal', *Fizika Metallov i Metallovedenie* **15**, 18–31.

Kubin, L. P. (1993), Dislocation Patterning, *in* H. Mughrabi, ed., 'Plastic Deformation and Fracture of Materials', Vol. 6 of *Materials Science and Technology: A Comprehensive Treatment*, VCH Publishers Inc., chapter 2, pp. 137–190.

Kubin, L. P. (1996), Dislocation Patterns: Experiment, Theory and Simulation, *in* A. Gonis and P. E. A. Turchi and J Kudrnovský, ed., 'Stability of Materials', NATO Science Series B: Physics, Plenum Press, pp. 99–135.

Kuhlmann-Wilsdorf, D. & Hansen, N. (1991), 'Geometrically Necessary, Incidental and Subgrain Boundaries', *Scripta Metallurgica et Materialia* **25**, 1557–1562.

Langford, J. I. & Wilson, A. J. C. (1978), 'Scherrer after sixty years: A survey and some new results in the determination of crystallite size', *Jounal of Applied Crystallography* **11**, 102–113.

Levine, L. E., Larson, B. C., Tischler, J. Z., Geantil, P., Kassner, M. E., Liu, W. & Stoudt, M. R. (2008), 'Impact of dislocation cell elastic strain variations on line profiles from deformed copper', *Zeitschrift fur Kristallograhie Supplement* **27**, 55–63.

Levine, L. E., Larson, B. C., Yang, W., Kassner, M. E., Tischler, J. Z., Delos-Reyes, M. A., Fields, R. J. & Liu, W. (2006), 'X-ray microbeam measurements of individual dislocation cell elsatic strains in deformed single-crystal copper', *Nature Materials* **5**, 619–622.

Madsen, K. & Nielsen, H. B. (1990), 'Finite Algorithms for Robust Linear Regression', *BIT Numerical Mathematics* **30**, 682–699.

Mughrabi, H. (1971), 'Elektronmikroskopische Untersuchung der Versetzungsanordnung am Ende von Bereich I', *Philosophical Magazine* **23**, 869–895.

Mughrabi, H. (1979), Microscopic Mechanisms of Metal Fatigue, *in* P. Haasen, V. Gerold & G. Kostorz, eds, 'Microstructural Characterization of Materials by Non-Microscopical Techniques', Proceedings of the Fifth International Conference on the Strength of Metals and Alloys, pp. 1615–1638.

Mughrabi, H. (1983), 'Dislocation wall and cell structures and long-range internal stresses in deformed metal crystals', *Acta Metallurgica* **31**, 1367–1379.

Mughrabi, H., Ungár, T., Kienle, W. & Wilkens, M. (1986), 'Long-range internal stresses and asymmetric X-ray line-broadening in tensile-deformed [001]-orientated copper single crystals', *Philosophical Magazine A* **53**, 793–813.

Nielsen, H. B. (1994), Fitting data from electrophoretic analysis of wheat, Technical report IMM-REP-1994-08, Institute of Mathematical Modelling, Technical University of Denmark.

Noyan, I. C. & Cohen, J. B. (1987), *Residual Stress – Measurement by Diffraction and Interpretation*, first edn, Springer-Verlag.

Pantleon, W., Wejdemann, C., Jakobsen, B., Lienert, U. & Poulsen, H. F. (2010), Advances in characterization of deformation structures by high resolution reciprocal space mapping, *in* N. Hansen, D. Juul Jensen, S. F. Nielsen, H. F. Poulsen & B. Ralph, eds, 'Challenges in materials science and possibilities in 3D and 4D characterization techniques', Proceedings of the 31st Risø International Symposium on Materials Science, pp. 79–100.

Peeters, B., Kalindindi, S. R., Van Houtte, P. & Aernoudt, E. (2000), 'A Crystal Plasticity Based Work-Hardening/Softening Model for B.C.C. Metals Under Changing Strain Paths', *Acta Materialia* **48**, 2123–2133.

Prinz, F. & Argon, A. S. (1980), 'Dislocation Cell Formation during Plastic Deformation of Copper Single Crystals', *Physica Status Solidi A* **57**, 741–753.

Raj, S. V. & Pharr, G. M. (1986), 'A Compilation and Analysis of Data for the Stress Dependence of the Subgrain Size', *Materials Science and Engineering* **81**, 217–237.

Scharfler, E., Simon, K., Bernstorff, S., Hanák, P., Tichy, G., Ungár, T. & Zehetbauer, M. J. (2005), 'A second-order phase-transformation of the dislocation structure during plastic deformation determined by in situ synchrotron X-ray diffraction', *Acta Materialia* **53**, 315–322.

Scherrer, P. (1918), 'Bestimmung der Grösse und der inneren Struktur von Kolloidteilchen mittels Röntgenstrahlen', *Nachrichten von der Königlichen Gesellschaft der Wissenschaften zu Gottingen, Mathematisch-Physikalische Klasse* **26**, 98–100.

Schmid, E. & Boas, W. (1935), *Kristallplasticität mit besonderer Berücksichtigung der Metalle*, Springer.

Schmitt, J. H., Aernoudt, E. & Baudelet, B. (1985), 'Yield Loci for Polycrstalline Metals without Texture', *Materials Science and Engineering* **75**, 13–20.

Schmitt, J. H., Fernandes, J. V., Gracio, J. J. & Vieira, M. F. (1991), 'Plastic behaviour of copper sheets during sequential tension tests', *Materials Science and Engineering* **A147**, 143–154.

Schmitt, J. H., Shen, E. L. & Raphanel, J. L. (1994), 'A Parameter for Measuring the Magnitude of a Change of Strain Path: Validation and Comparison with Experiments on Low Carbon Steel', *International Journal of Plasticity* **10**, 535–551.

Shastri, S. D. (2004), 'Combining flat crystals, bent crystals and compound refractive lenses for high-energy X-ray optics', *Journal of Synchrotron Radiation* **11**, 150–156.

Shastri, S. D., Almer, J., Ribbing, C. & Cederström, B. (2007), 'High-energy X-ray optics with silicon saw-tooth refractive lenses', *Journal of Synchrotron Radiation* **14**, 204–211.

Shastri, S. D., Fezzaa, K., Mashayekhi, A., Lee, W.-K., Fernandez, P. B. & Lee, P. L. (2002), 'Cryogenically cooled bent double-Laue monochromator for high-energy undulator X-rays (50-200 keV)', *Journal of Synchrotron Radiation* **9**, 317–322.

Staker, M. R. & Holt, D. L. (1972), 'The dislocation cell size and dislocation density in copper deformed at temperatures between 25 and 700 °C', *Acta Metallurgica* **20**, 569–579.

Steeds, J. W. (1966), 'Dislocation arrangement in copper single crystals as a function of strain', *Proceedings of the Royal Society of London. Series A, Mathematical and Physical Sciences* **292**, 343–373.

Swann, P. R. (1963), Dislocation Arrangements in Face-Centered Cubic Metals and Alloys, *in* G. Thomas & J. Washburn, eds, 'Electron Microscopy and Strength of Crystals', Interscience Publishers, chapter 3, pp. 131–181.

Ungár, T. (1999), The dislocation-based model of strain broadening in X-ray line profile analysis, *in* R. L. Snyder, J. Fiala & H. J. Bunge, eds, 'Defect and Microstructure Analysis by Diffraction', Oxford University Press, chapter 10, pp. 165–199.

Ungár, T. (2001), 'Dislocation densities, arrangements and character from X-ray diffraction experiments', *Materials Science and Engineering* **A309-310**, 14–22.

Ungár, T., Dragomir, I., Révész, A. & Borbély, A. (1999), 'The contrast factors of dislocations in cubic crystals: the dislocation model of strain anisotropy in practice', *Jounal of Applied Crystallography* **32**, 992–1002.

Ungár, T., Gubicza, J., Ribarik, G. & Borbély, A. (2001), 'Crystallite size distribution and dislocation structure determined by diffraction profile analysis: principles and practical application to cubic and hexagonal crystals', *Journal of Applied Crystallography* **34**, 298–310.

Ungár, T., Mughrabi, H., Rönnpagel, D. & Wilkens, M. (1984), 'X-ray line-broadening study of the dislocation cell structure in deformed [001]-oriented copper single crystals', *Acta Metallurgica* **32**, 333–342.

Ungár, T., Mughrabi, H. & Wilkens, M. (1984), Asymmetric X-ray line broadening due to long-range internal stresses in deformed [100]-orientated copper single crystals, *in* N. Hessel Andersen, M. Eldrup, N. Hansen, D. Juul Jensen, T. Leffers, H. Lilholt, O. B. Pedersen & B. N. Singh, eds, 'Microstructural Characterization of Materials by Non-Microscopical Techniques', Proceedings of the 5th Risø International Symposium on Metallurgy and Materials Science, pp. 539–544.

Ungár, T., Mughrabi, H., Wilkens, M. & Hilscher, A. (1991), 'Long-range internal stresses and asymmetric X-ray line-broadening in tensile-deformed [001]-orientated copper single crystals: the correction of an erratum', *Philosophical Magazine A* **64**, 495–496.

Warren, B. E. (1990), *X-Ray Diffraction*, first edn, Dover Publications.

Warren, B. E. & Averbach, B. L. (1950), 'The Effect of Cold-Work Distortion on X-ray Patterns', *Journal of Applied Physics* **21**, 595–599.

Wilkens, M. (1970*a*), 'The Determination of Density and Distribution of Dislocations in Deformed Single Crystals from Broadened X-Ray Diffraction Profiles', *Physica Status Solidi A* **2**, 359–370.

Wilkens, M. (1970*b*), Theoretical Aspects of Kinematical X-Ray Diffraction Profiles from Crystals Containing Dislocation Distributions, *in* J. A. Simmons, R. deWit & R. Bullough, eds, 'Fundamental Aspects of Dislocation Theory', Vol. II of *National Bureau of Standards*, VCH Publishers Inc., pp. 1195–1221.

Yang, W., Larson, B. C., Ice, G. E., Tischler, J. Z., Budai, J. D., Chung, K.-S. & Lowe, W. P. (2003), 'Spatially resolved Poisson strain and anticlastic curvature measurements in Si under large deflection bending', *Applied Physics Letters* **82**, 3856–3858.

Risø DTU is the National Laboratory for Sustainable Energy. Our research focuses on development of energy technologies and systems with minimal effect on climate, and contributes to innovation, education and policy. Risø has large experimental facilities and interdisciplinary research environments, and includes the national centre for nuclear technologies.

Risø DTU
National Laboratory for Sustainable Energy
Technical University of Denmark

Frederiksborgvej 399
PO Box 49
DK-4000 Roskilde
Denmark
Phone +45 4677 4677
Fax +45 4677 5688

www.risoe.dtu.dk